

Lecture Notes in Civil Engineering

Sireesh Saride  
B. Umashankar  
Deepti Avirneni *Editors*

# Advances in Geotechnical and Transportation Engineering

Select Proceedings of FACE 2019

 Springer

# Lecture Notes in Civil Engineering

Volume 71

## Series Editors

Marco di Prisco, Politecnico di Milano, Milano, Italy

Sheng-Hong Chen, School of Water Resources and Hydropower Engineering,  
Wuhan University, Wuhan, China

Ioannis Vayas, Institute of Steel Structures, National Technical University of  
Athens, Athens, Greece

Sanjay Kumar Shukla, School of Engineering, Edith Cowan University, Joondalup,  
WA, Australia

Anuj Sharma, Iowa State University, Ames, IA, USA

Nagesh Kumar, Department of Civil Engineering, Indian Institute of Science  
Bangalore, Bengaluru, Karnataka, India

Chien Ming Wang, School of Civil Engineering, The University of Queensland,  
Brisbane, QLD, Australia

**Lecture Notes in Civil Engineering** (LNCE) publishes the latest developments in Civil Engineering—quickly, informally and in top quality. Though original research reported in proceedings and post-proceedings represents the core of LNCE, edited volumes of exceptionally high quality and interest may also be considered for publication. Volumes published in LNCE embrace all aspects and subfields of, as well as new challenges in, Civil Engineering. Topics in the series include:

- Construction and Structural Mechanics
- Building Materials
- Concrete, Steel and Timber Structures
- Geotechnical Engineering
- Earthquake Engineering
- Coastal Engineering
- Ocean and Offshore Engineering; Ships and Floating Structures
- Hydraulics, Hydrology and Water Resources Engineering
- Environmental Engineering and Sustainability
- Structural Health and Monitoring
- Surveying and Geographical Information Systems
- Indoor Environments
- Transportation and Traffic
- Risk Analysis
- Safety and Security

To submit a proposal or request further information, please contact the appropriate Springer Editor:

- Mr. Pierpaolo Riva at [pierpaolo.riva@springer.com](mailto:pierpaolo.riva@springer.com) (Europe and Americas);
- Ms. Swati Meherishi at [swati.meherishi@springer.com](mailto:swati.meherishi@springer.com) (Asia—except China—and Australia/NZ);
- Ms. Li Shen at [li.shen@springer.com](mailto:li.shen@springer.com) (China).

**Indexed by Scopus and Compendex**

More information about this series at <http://www.springer.com/series/15087>

Sireesh Saride · B. Umashankar ·  
Deepti Avirneni  
Editors

# Advances in Geotechnical and Transportation Engineering

Select Proceedings of FACE 2019

 Springer

*Editors*

Sireesh Saride  
IIT Hyderabad  
Kandi, Sangareddy, India

B. Umashankar  
IIT Hyderabad  
Kandi, Sangareddy, India

Deepti Avirneni  
Mahindra Ecole Centrale  
Hyderabad, India

ISSN 2366-2557

ISSN 2366-2565 (electronic)

Lecture Notes in Civil Engineering

ISBN 978-981-15-3661-8

ISBN 978-981-15-3662-5 (eBook)

<https://doi.org/10.1007/978-981-15-3662-5>

© Springer Nature Singapore Pte Ltd. 2020

This work is subject to copyright. All rights are reserved by the Publisher, whether the whole or part of the material is concerned, specifically the rights of translation, reprinting, reuse of illustrations, recitation, broadcasting, reproduction on microfilms or in any other physical way, and transmission or information storage and retrieval, electronic adaptation, computer software, or by similar or dissimilar methodology now known or hereafter developed.

The use of general descriptive names, registered names, trademarks, service marks, etc. in this publication does not imply, even in the absence of a specific statement, that such names are exempt from the relevant protective laws and regulations and therefore free for general use.

The publisher, the authors and the editors are safe to assume that the advice and information in this book are believed to be true and accurate at the date of publication. Neither the publisher nor the authors or the editors give a warranty, expressed or implied, with respect to the material contained herein or for any errors or omissions that may have been made. The publisher remains neutral with regard to jurisdictional claims in published maps and institutional affiliations.

This Springer imprint is published by the registered company Springer Nature Singapore Pte Ltd. The registered company address is: 152 Beach Road, #21-01/04 Gateway East, Singapore 189721, Singapore

# Contents

<b>Estimation of PM<sub>2.5</sub>-Related Hospital Admissions and Its Monetary Burden in Hyderabad, India</b> . . . . .	1
N. Manojkumar, M. Manish Kumar, Shashank Kiran Somwanshi, M. Monish Raj and B. Srimuruganandam	
<b>Bi-directional Static Pile Load Test by S-Cell Method</b> . . . . .	11
Vijay Kumar Patidar, Suneet Kaur and Nitin Dindorkar	
<b>Soil Stabilization Using Bagasse Ash</b> . . . . .	21
Dharmesh Lal, M. Jeevan Kumar, K. Naresh Kumar, K. Sindhu and Ashok Kumar	
<b>Strength Behavior of Rammed Earth Stabilized with Metakaolin</b> . . . . .	29
S. K. Thiviya, Aswathi G. Krishnan, Monish Kalathuru, Anil Kumar Sharma and Sreevalsa Kolathayar	
<b>Geospatial-Based Coastal Risk Assessment of Gujarat Coastline</b> . . . . .	41
Minnu Abraham, R. S. Mahendra, Venkata Ravibabu Mandla, Chaithanya Sudha Merugu and Veerendra Satya Sylesh Peddinti	
<b>Development of Speed Prediction Models for Different Categories of Roads</b> . . . . .	59
Teja Tallam and Bhukya Bhadru	
<b>Numerical Analysis of Liquefaction and Settlement in Layered Soils</b> . . . . .	69
D. Nishanth Kiran, Mohammad Muzzaffar Khan, M. Madhusudhan Reddy, K. Raja Shekar Reddy and G. Kalayan Kumar	
<b>Evaluation of Lateral Capacity of Pile Foundation Using Finite Element Method in Layered Soil</b> . . . . .	79
B. K. Huchegowda, Munaga Teja and Gonavaram Kalyan Kumar	

<b>Impact Study on Desiltation of Water Tanks in Rural Areas Using Spatial Technology: A Case Study Work Under MGNREGA</b> .....	85
Venkata Ravibabu Mandla, Satyanarayana Prasad Nerella, Mithun Choudhary and Veerendra Satya Sylesh Peddinti	
<b>Calibration of Pedestrian Flow Model Using Greenshield's Macroscopic Stream Model for a Signalized Midblock</b> .....	101
Sai Prasanna Reddy, Teja Tallam and K. M. Lakshmana Rao	
<b>Evaluation of Physical and Environmental Parameters of the Indian Sundarbans</b> .....	113
Nilovna Chatterjee, Venkata Ravibabu Mandla, Ranadhir Mukhopadhyay, Nagaveni Chokkavarapu and Veerendra Satya Sylesh Peddinti	
<b>Development of Sustainable Community</b> .....	131
B. G. Jagadeesha Kumar, M. G. Prajwala, V. Vishal, Mohan and M. M. Pavithra	
<b>Cinder Coal-Aggregate Quality Index (AQI) Appraisal Based on Weighted Arithmetic Index Method and Fuzzy Logic</b> .....	153
Penki Ramu, J. Y. V. Shiva Bhushan, B. Shravani and I. Nagarani	
<b>Effect of Relief Shelves on Cantilever Retaining Walls</b> .....	165
Preethi Sekar, Satya Kiran Raju Alluri and S. Suganya	
<b>Heave Studies on Expansive Clay Beds Reinforced with Granular Pile Anchors and Geogrid-Encased Granular Pile Anchors</b> .....	179
Ammavajjala Sesha Sai Raghuram, B. R. Phanikumar, K. Purnanandam, Preethi Sekar and A. Sriramarao	
<b>Mathematical Modeling of Displacements in Building Frame Founded on Pile Groups Embedded in Sand</b> .....	193
C. Ravi Kumar Reddy, K. Ramesh, G. Srinivasulu and N. V. Mohan Krishna	
<b>Capacity and Level of Service of Roundabouts Using Indo-HCM</b> .....	199
Sadguna Nuli, Nagamani Gade and Kavya Beeravolu	
<b>Estimation of Arrival Time of Shear Waves in Fine-Grained Soils Using Bender Element Test</b> .....	213
Kannekanti Prithvi Chandra and Kadali Srinivas	
<b>Numerical Modelling of Lateral Deformation of the Cantilever Retaining Wall in Expansive Clays</b> .....	233
Santosh Sharma, N. Vinod Prabhu, Y. Naveen and S. Bhuvaneshwari	
<b>MASW Survey for Mapping Soil Profiles at Investigation Site</b> .....	249
Satya Sireesha, V. Padmavathi, V. Sai Venkata Harini and P. N. Rao	

<b>Analysis of Rice Crop Phenology Using Sentinel-1 and Sentinel-2 Satellite Data</b> .....	257
Radha Saradhi Inteti, Venkata Ravibabu Mandla, Jagadeeswara Rao Peddada and Nedun Ramesh	
<b>Life-Cycle Assessment of Various Synthesis Routes of Silver Nanoparticles</b> .....	267
Vantepaka Arundhathi, Sreeram Nagalakshmi Manasa, Suriseti Kalyani Lakshmi, Veeramaneni Varsha and Baranidharan Sundaram	
<b>Ground Response Analysis of Passighat Airport and Moga Bridge Sites</b> .....	279
Pabba Vinod Kumar Goud, Boya Manikanta Reddy and Madhav Madhira	
<b>Use of Waste Polypropylene Plastic in Geotechnical Applications</b> .....	291
Manisha Gajanan Ujankar and P. Hari Krishna	
<b>A Study on Influence of Organic Ligand on the Adsorption of Lead by Clayey Soil</b> .....	301
Sudheerkumar Yantrapalli and P. Hari Krishna	
<b>Numerical Analysis of Single Track Railway Tunnel in a Stratified Soil Condition</b> .....	317
Pallavi Badry, M. Venkateshwarlu, D. Sai Kiran Reddy, V. Prasad and M. Vishal Preetham	
<b>Effect of Interference on Ultimate Bearing Capacity of Strip Footings Resting on Reinforced Clay Overlying Sand</b> .....	325
Chandra Sekhar Jonnagiri, Venkata Balaiah Kami and Rabi Narayan Behera	
<b>Feasible Study for Allocation of Nodal Demands Through WaterGEMS</b> .....	339
Chekka V. S. S. Sudheer, Maddamsetty Ramesh and Gedela Venkata Ramana	



## About the Editors

**Dr. Sireesh Saride** is currently working as Professor and Dean Planning, Indian Institute of Technology Hyderabad. His expertise and research interests are in the area of pavement geotechnics, geosynthetics and ground improvement. He has graduated from JNTU College of Engineering, Kakinada in 2000 and earned his masters integrated with Ph.D. from Indian Institute of Science, Bengaluru in 2006. Before joining IIT Hyderabad in 2010, he was a post-doctoral research fellow at the University of Texas at Arlington, during 2006-2010. Dr. Sireesh has published more than 170 journal papers, conference articles, and technical reports. He is currently serving as an Associate Editor for the Journal of Ground Improvement (ICE) and Journal of Materials in Civil Engineering, ASCE. He is a member of ASCE, ICE, TRB and life member of IGS and IRC.

**Dr. B. Umashankar** is currently working as Associate Professor, Indian Institute of Technology Hyderabad. His expertise and research interests include reinforced earth structures, soil-structure interaction, foundation engineering, ground improvement techniques, and recyclable materials in geotechnics. He has graduated from Sri Venkateswara University, Tirupati, and earned his masters from the Indian Institute of Technology Kanpur. He received his doctorate from Purdue University, USA. Before joining IIT Hyderabad, he was a graduate research assistant at Purdue University. Dr. Umashankar has filed one patent and published more than 50 articles in journals and conference proceedings. He is an active member of the Indian Geotechnical Society and also a reviewer for various reputed journals.

**Dr. Deepti Avirneni** is currently working as Assistant Professor, Mahindra Ecole Centrale, Hyderabad. Her expertise and research interests include sustainable pavement materials, and pavement design. She has graduated from Acharya Nagarjuna University in 2006 and earned her masters from the Indian Institute of Technology, Roorkee in 2008. She received her doctorate from the Indian Institute

of Technology, Hyderabad. Before joining Mahindra Ecole Centrale Hyderabad in 2017, she worked as Associate Professor at VNR Vignana Jyothi Institute of Engineering and Technology, Hyderabad, during 2016-2017. Dr. Deepti has published more than 25 papers in journals and conference proceedings.

# Estimation of PM<sub>2.5</sub>-Related Hospital Admissions and Its Monetary Burden in Hyderabad, India



N. Manojkumar , M. Manish Kumar, Shashank Kiran Somwanshi, M. Monish Raj and B. Srimuruganandam 

**Abstract** Air pollution due to fine particulate matter (PM<sub>2.5</sub>) concentration in Indian cities is becoming a major threat to human health. The most common short-term effects of PM<sub>2.5</sub> are chronic obstructive pulmonary diseases (COPD). This COPD health effect is associated with high monetary burden on people residing in urban population. Thus, it is crucial to evaluate short-term COPD hospital admissions and monetary burden caused by PM<sub>2.5</sub>. In the present study, the Hyderabad city in India is chosen as a model city for evaluation. The AirQ+ software developed by World Health Organization is utilized for quantifying COPD hospital admission. Using AirQ+ software, the estimated attributable proportion (EAP), excess number of attributable cases (EAC), and estimated number of attributable cases per 1 lakh people (EACP) related to COPD hospital admissions are quantified. Further, the cost of illness (COI) method and value of statistical life (VSL) methods are adopted for estimating the monetary burden. The required annual mean PM<sub>2.5</sub> data is downloaded from Central Pollution Control Board website. Results showed that Hyderabad has an EAP of 7.12% in 2016 and 7.88% in 2017. Total EAC in our study period is found to be 2,97,848 cases, and the monetary burden in 2016 and 2017 are estimated to be 4998 and 5522 million INR, respectively. Also, the VSL<sub>Hyderabad</sub> is estimated to be 34,17,224 INR.

---

N. Manojkumar · M. Manish Kumar · S. K. Somwanshi · M. Monish Raj ·  
B. Srimuruganandam (✉)

School of Civil Engineering, Vellore Institute of Technology, Vellore, Tamil Nadu 632 014, India  
e-mail: [bsrimuruganandam@vit.ac.in](mailto:bsrimuruganandam@vit.ac.in)

N. Manojkumar  
e-mail: [manoj.ebet@gmail.com](mailto:manoj.ebet@gmail.com)

M. Manish Kumar  
e-mail: [manishkumar0916@gmail.com](mailto:manishkumar0916@gmail.com)

S. K. Somwanshi  
e-mail: [shankisk@gmail.com](mailto:shankisk@gmail.com)

M. Monish Raj  
e-mail: [monishraj36@gmail.com](mailto:monishraj36@gmail.com)

**Keywords** PM<sub>2.5</sub> · Hospital admissions · COPD · Monetary burden · Cost of illness · Value of statistical life

## 1 Introduction

Epidemiology evidence links the adverse effect of air pollution on human health [1–3]. India is one among the Asian countries which is having air pollution as the leading cause of deaths [4]. The health effects are found to be dominant among population living in urban area. Urban air pollution is a complex mixture of gaseous pollutants and particulate matter (PM) [5, 6]. These pollutants are significantly emitted from vehicular traffic, biomass burning, and industrial activities. Both gaseous and PM pollutants are found to have short-term and long-term human health effects [7, 8]. At global level, a total of 4.9 million deaths and 147 million disability-adjusted life year (DALY) are attributed to air pollution. Pollutants such as PM and ozone are found to be significant sources of air pollution-related deaths and DALYs. Ambient PM caused 2.9 million deaths and 83 million DALYs, whereas ozone contributed 0.47 million deaths and 7.3 million DALYs [9].

India is home for world's top-polluted cities by PM [10]. In India, the population-weighted mean PM<sub>2.5</sub> exposure increased from 74.3  $\mu\text{g m}^{-3}$  (2015) to 89.9  $\mu\text{g m}^{-3}$  (2017) [4, 11]. Respiratory diseases, cardiovascular diseases, and stroke are well documented by air pollution epidemiological studies [12–15]. With these health effects, several studies have estimated mortality, total years of life lost, and premature mortality [16–19]. It is also found that chronic obstructive pulmonary diseases (COPD) are highly associated with PM<sub>2.5</sub> [20, 21]. COPD is the blockage in human respiratory airways caused by inflammation due to PM<sub>2.5</sub> [22]. Hence, COPD-related hospital admissions are crucial.

Several models are available for estimating air pollution-related health effects. Widely adopted models are AirQ+, Environmental Benefits Mapping and Analysis Program—Community Edition (BenMAP-CE), Institute of Occupational Medicine—Life Table calculation (IOMLIFET), and FASST (TM5-FASST) [23]. AirQ+ software is developed by World Health Organization, Europe. This software quantifies hospital admissions and mortality caused by several air pollutants viz., PM<sub>2.5</sub>, PM<sub>10</sub>, black carbon, nitrogen dioxide, and ozone [24]. BenMAP-CE is developed by U.S. Environmental Protection Agency for estimating the health effects and monetary burden due to ambient air pollution. IOMLIFET calculates the loss or gain in life expectancy with respect to change in air pollution. TM5-FASST is an online tool used to evaluate air pollution effects on human health and crop yield [23]. Although several tools are available, hospital admissions caused by COPD can be quantified only in AirQ+. Therefore, AirQ+ model is adopted in the present study.

Air pollution monetary burden is widely estimated by the cost of illness (COI) method. COI estimates the monetary burden by accounting both direct and indirect costs viz., treatment cost, drug cost, transportation cost, productivity loss, etc., related

to the disease [25]. Value of statistical life (VSL) method assesses the monetary burden based on individual's willingness to pay for reducing premature mortality. Cost burden estimates from COI and VSL methods can be easily communicated to society and policymakers [26]. Also, it will be helpful for policymakers to add burden estimates in national gross domestic product. However, the studies on monetary burden caused by air pollution are scarce in India. Hence, this study aims to quantify hospital admissions caused by PM<sub>2.5</sub> and estimating the air pollution monetary burden using COI and VSL methods.

## 2 Methods

PM<sub>2.5</sub> data and population data are required for estimating hospital admissions. The annual mean PM<sub>2.5</sub> data for 2016 and 2017 is collected from Central Pollution Control Board (CPCB), India. Eight sampling locations from Hyderabad, India viz., Balanagar, Tarnaka, Uppal, Jubilee Hills, Paradise, Charminar, Zoo Park main road, and Jeedimetla are considered for the present study. The locations of all sampling stations are shown in Fig. 1. Annual mean PM<sub>2.5</sub> concentration of Hyderabad city in 2016 and 2017 is 49.25  $\mu\text{g m}^{-3}$  and 53.62  $\mu\text{g m}^{-3}$ , respectively. The population data is obtained from census of India website. After acquiring required data, the COPD hospital admissions are estimated using AirQ+ software. Several input parameters should be specified for running the software viz., health endpoint, incidence per 1 lakhs people per year, calculation method, relative risk, and cutoff value. The health endpoint of respiratory diseases admission is selected for the present study. With reference to the earlier studies, the incidence value of 20,465 is given as input for calculation [27]. Further relative risk and cutoff values are specified as per AirQ+ default values of 0.9982 and 10  $\mu\text{g m}^{-3}$ , respectively. Using all these parameters, estimated attributable proportion (EAP), excess number of attributable cases (EAC), and estimated number of attributable cases per 1 lakh people (EACP) related to COPD hospital admissions are quantified in this study. Apart from hospital admissions, AirQ+ software also estimates the years of life lost due to premature mortality, estimated life remaining, and mortality caused by stroke, heart diseases, and acute lower respiratory infection diseases. The monetary cost burden caused by PM<sub>2.5</sub> is estimated using COI and VSL methods. The protocol followed and the equations used for quantifying hospital admissions and monetary burden is presented in Fig. 2. Although AirQ+ has a range of application, and there are some limitations in using the software. Synergistic effects of multipollutant exposure cannot be determined in AirQ+. Further, PM chemical constituents are found to have influence on human health effects. But, in this software, the human health effects are quantified only based on the exposure concentration. By default, the relative risk and cutoff values are assumed to be same for any location in the world. However, the usage of location-specific values in AirQ+ leads to more appropriate results.

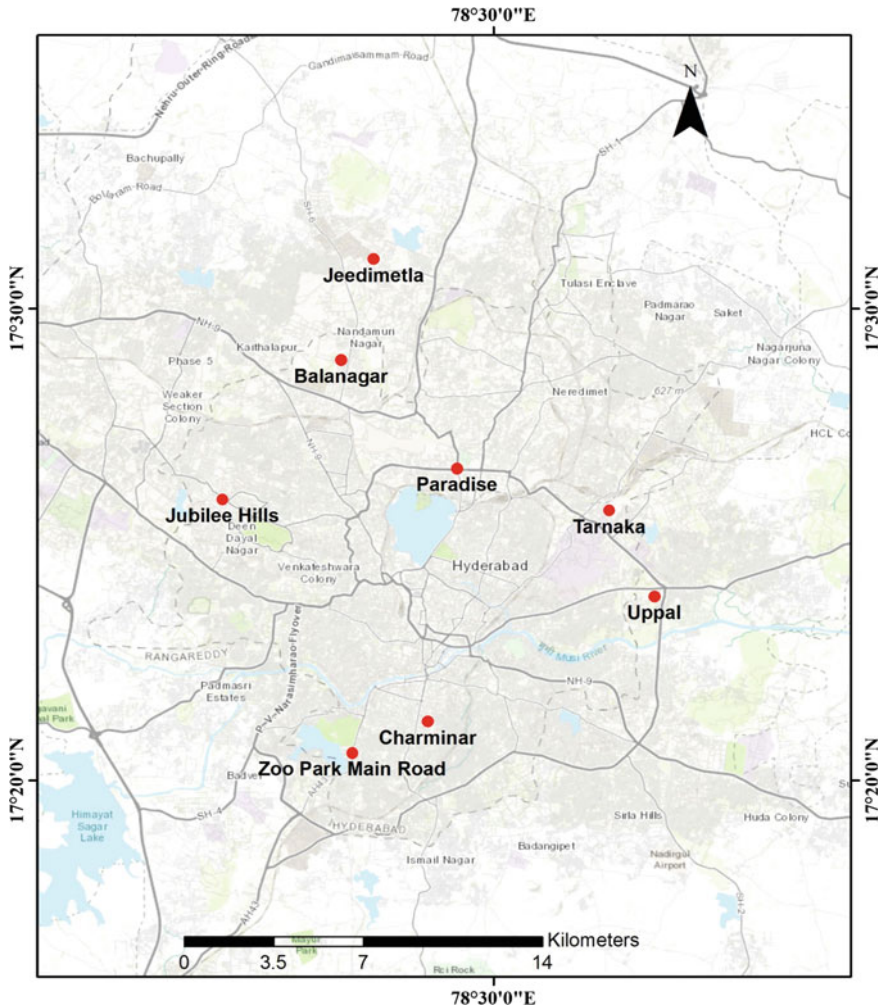
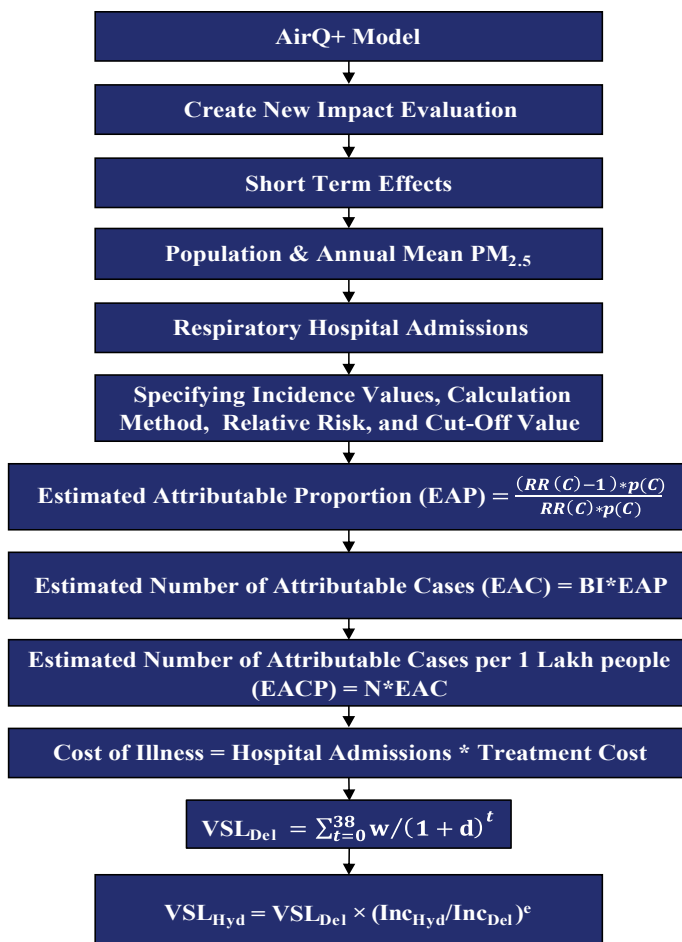


Fig. 1 Location of sampling stations

### 3 Results and Discussion

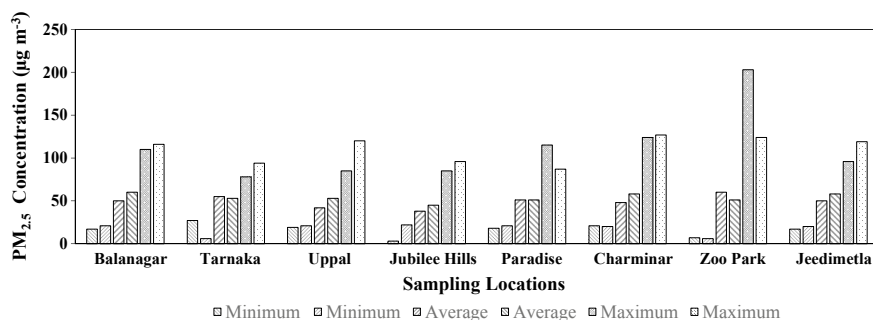
#### 3.1 $PM_{2.5}$ Concentration

The minimum, average, and maximum  $PM_{2.5}$  concentration values in eight sampling locations are shown in Fig. 3. It is observed that 2017 year has high  $PM_{2.5}$  concentration than in 2016. Places viz., Jubilee hills and Zoo Park are found to have lowest concentration in 2016 and 2017, respectively. The maximum concentration of 203 and 127  $\mu\text{g m}^{-3}$  is recorded in Zoo Park and Charminar stations. Also, the maximum



**Fig. 2** Protocol followed for estimating hospital admissions and monetary burden. *Note* RR(C)-relative risk,  $p(C)$ -population exposed in each category, BI-baseline incidence,  $N$ -population size,  $w$ -average annual income,  $t$ -life expectancy-average age of population,  $d$ -discount rate,  $VSL_{Hyd}$  = Value of statistical life of Hyderabad,  $VSL_{Del}$  = Value of statistical life of Delhi,  $Inc_{Hyd}$  = Income of Hyderabad,  $Inc_{Del}$  = Income of Hyderabad,  $e$  = elasticity coefficient

PM<sub>2.5</sub> concentration range in other stations varied from 78 to 124  $\mu\text{g m}^{-3}$  in 2016 and 87 to 124  $\mu\text{g m}^{-3}$  in 2017. Further, the highest PM<sub>2.5</sub> annual mean is found in Zoo Park (60  $\mu\text{g m}^{-3}$ ), Tarkana (55  $\mu\text{g m}^{-3}$ ), and Paradise (51  $\mu\text{g m}^{-3}$ ) during 2016, whereas places such as Balanagar (60  $\mu\text{g m}^{-3}$ ), Charminar (58  $\mu\text{g m}^{-3}$ ), and Jeedimetla (58  $\mu\text{g m}^{-3}$ ) are registered with maximum mean concentration in 2017. CPCB, India, has stipulated annual mean standard of 40  $\mu\text{g m}^{-3}$ . Except Jubilee hills, all other places have exceeded the CPCB standard value during the year 2016. In case of 2017, all stations have violated the standard limits.



Note: Bars in the figure follows the order of Minimum 2016, Minimum 2017, Average 2016, Average 2017, Maximum 2016 and Maximum 2017 at all locations

Fig. 3 PM<sub>2.5</sub> concentration in Hyderabad sampling locations.

### 3.2 Hospital Admissions

The estimates related to hospital admissions are summarized in Table 1. EAP is the fraction of the health outcome that can be related to PM<sub>2.5</sub> concentration exposure in a specified city population. AirQ+ software estimated an EAP of 7.12% and 7.88% in 2016 and 2017, respectively, at Hyderabad. The EAP is maximum in 2017 and it can be attributed to high PM<sub>2.5</sub> concentrations. Earlier study in Agra showed an average EAP of 8.58% [28]. A study in Kermanshah, Iran, found an EAP of 6.62% for PM<sub>2.5</sub> concentration above 10 µg m<sup>-3</sup> [29]. Another study in Yazd, Iran, has quantified the EAP of 6.54% with baseline incidence of 1260 cases [30]. EAC is the excess cases in the hospital admissions that are related to COPD. In the present study, a total EAC of 1,41,364 and 1,56,484 are estimated in 2016 and 2017, respectively. A similar study in Delhi showed the total EAC of 26,525 during the year 2010 [31]. Another study in Delhi estimated the EAC from 105 to 130 [32]. EAC in Chandrapur, Kolhapur, Navi Mumbai, Pune, and Solapur are also reported as 213, 540, 1236, 4303, and 705 cases, respectively [33]. A study in Ahvaz, Iran, has recorded COPD hospital admissions with range from 65 to 121 cases between 2009 and 2014 [34]. Another study in Yazd city of Iran has EAC of 401 cases with the relative risk of 1.008 [30]. Further, the lowest EAC of 39 cases is recorded in Kermanshah, Iran [29]. EAC findings of other studies are very low when compared to the present study and it may be due

Table 1 Estimates of COPD-related hospital admissions

Year	Estimated attributable proportion (EAP %)	Excess number of attributable cases (EAC)	Estimated number of attributable cases per 1 lakh people (EACP)
2016	7.12	1,41,364	1457
2017	7.88	1,56,484	1613



**Table 2** Monetary burden attributed to COPD hospital admissions

Year	Concentration ( $\mu\text{g m}^{-3}$ )	Treatment costs (per person/year in INR)	Total cost (million INR)	Total cost (million USD)
2016	49.25	35,290	4998	72.2
2017	53.62	35,290	5522	79.9

to variation in mean PM concentration, relative risks, and low population. EACP of Hyderabad is found to be 1457 and 1613 during 2016 and 2017, respectively.

### 3.3 Monetary Burden

Monetary burden estimates are given in Table 2. The treatment cost of 35,290 INR is considered from recent study [35]. COI results showed a total monetary burden of 4998 million INR (72.2 million US Dollars) and 5522 million INR (79.9 million US Dollars) in 2016 and 2017, respectively. Earlier study in Mumbai estimated a total burden of 92.23 million US dollars [36]. Similar study in Agra has quantified the monetary burden between 67 million and 254 million US dollars [28]. Another study in Pearl River Delta, China showed 4.35 billion US dollars burden due to air pollution [37]. The high monetary burden in present study is due to increased COPD incidence rate and treatment costs. It is observed that the year 2017 has highest monetary burden when compared to 2016. This could be reflection of high PM<sub>2.5</sub> concentration in the year 2017 than 2016.

### 3.4 Value of Statistical Life (VSL)

VSL is based on individual willingness to pay approach. VSL value gives information about the total money spent on increasing life expectancy. The equations utilized for quantifying VSL is given in Fig. 1. All these equations are adopted from earlier studies [28, 38]. Initially, the VSL of Delhi ( $VSL_{\text{Delhi}}$ ) is calculated using average annual income (3,29,093 INR), life expectancy (73.2 years), average age of population (38.25 years), and discount rate (5%). The  $VSL_{\text{Delhi}}$  is found to be 23,32,476 INR. Then with values of  $VSL_{\text{Delhi}}$ , annual average income of Hyderabad (4,82,142 INR), annual average income of Delhi (3,29,093 INR), the VSL of Hyderabad ( $VSL_{\text{Hyderabad}}$ ) are estimated. The  $VSL_{\text{Hyderabad}}$  is found to be 34,17,224 INR.

## 4 Conclusion

In this study, the COPD-related hospital admissions and monetary burden attributed to PM<sub>2.5</sub> are quantified. Hyderabad city in India is selected as a model city for the present study. AirQ+ software is adopted for estimating hospital admissions. The monetary burden is calculated using COI method. Results showed that the high EAP of 7.88% is in the year 2017. The average EAC and EACP in our study period are estimated to be 1,48,924 and 1535 cases, respectively. This leads to have average monetary burden of 5255 million INR. Further, the VSL<sub>Hyderabad</sub> is estimated to be 34,17,224 INR. Thus, by achieving World Health Organization annual standard of 10 µg m<sup>-3</sup>, the COPD hospital admissions and related monetary burden can be reduced significantly. In Hyderabad, the main sources of pollution can be linked with transport, industries, brick manufacturing, and waste burning sectors. Hence, mitigation measures related to these sources can significantly reduce PM<sub>2.5</sub> concentration and, therefore, results in reduced hospital admissions and monetary burden. The recommended mitigation measures are encouraging cycling, interconnection of city metro and roadways, ban on local waste burning, and efficient brick production technologies.

**Acknowledgements** We sincerely thank Central Pollution Control Board (CPCB), India, for providing the fine particulate matter (PM<sub>2.5</sub>) data for our research.

## References

1. Rohr, A. C., & Wyzga, R. E. (2012). Attributing health effects to individual particulate matter constituents. *Atmospheric Environment*, 62, 130–152.
2. Wu, C. F., Shen, F. H., Li, Y. R., Tsao, T. M., Tsai, M. J., Chen, C. C., et al. (2016). Association of short-term exposure to fine particulate matter and nitrogen dioxide with acute cardiovascular effects. *Science of the Total Environment*, 569–570, 300–305.
3. Luong, L. M. T., Phung, D., Sly, P. D., Morawska, L., & Thai, P. K. (2017). The association between particulate air pollution and respiratory admissions among young children in Hanoi, Vietnam. *Science of the Total Environment*, 578, 249–255.
4. Kalpana, B., Dey, S., Gupta, T., Dhaliwal, R. S., Brauer, M., Cohen, J. A., et al. (2018). The impact of air pollution on deaths, disease burden, and life expectancy across the states of India: The global burden of disease study 2017. *The Lancet Oncology*, 19, e26–e39.
5. Srimuruganandam, B., & Shiva Nagendra, S. M. (2011). Characteristics of particulate matter and heterogeneous traffic in the urban area of India. *Atmospheric Environment*, 45, 3091–3102.
6. Tyagi, S., Tiwari, S., Mishra, A., Hopke, P. K., Attri, S. D., Srivastava, A. K., et al. (2016). Spatial variability of concentrations of gaseous pollutants across the national capital region of Delhi, India. *Atmospheric Pollution Research*, 7, 808–816.
7. Zheng, S., Wang, M., Wang, S., Tao, Y., & Shang, K. (2013). Short-term effects of gaseous pollutants and particulate matter on daily hospital admissions for cardio-cerebrovascular disease in Lanzhou: Evidence from a heavily polluted city in China. *International Journal of Environmental Research and Public Health*, 10, 462–477.
8. Hadei, M., Saeed, S., Nazari, H., Yarahmadi, E., Kermani, M., & Yarah, M. (2017). Estimation of lung cancer mortality attributed to long-term exposure to PM<sub>2.5</sub> in 15 Iranian cities during 2015–2016; An AirQ+ modelling. *Journal of Air Pollution and Health*, 2, 19–26.

9. Jeffrey, D. S., Afshin, A., Gakidou, E., Lim, S. S., Abate, D., Abate, K. H., et al. (2018). Global, regional, and national comparative risk assessment of 84 behavioural, environmental and occupational, and metabolic risks or clusters of risks for 195 countries and territories, 1990–2017: A systematic analysis for the global burden of disease study 2017. *Lancet*, *392*, 1923–1994.
10. WHO—Global Ambient Air Quality Database 2018 Update. <https://www.who.int/airpollution/data/cities/en/>.
11. Cohen, A. J., Brauer, M., Burnett, R., Anderson, H. R., Frostad, J., Estep, K., et al. (2017). Estimates and 25-year trends of the global burden of disease attributable to ambient air pollution: An analysis of data from the global burden of diseases study 2015. *Lancet*, *389*, 1907–1918.
12. Pope, C. A., Burnett, R. T., Thurston, G. D., Thun, M. J., Calle, E. E., Krewski, D., et al. (2004). Cardiovascular mortality and long-term exposure to particulate air pollution: Epidemiological evidence of general pathophysiological pathways of disease. *Circulation*, *109*, 71–77.
13. Gong, H., Linn, W. S., Clark, K. W., Anderson, K. R., Geller, M. D., & Sioutas, C. (2005). Respiratory responses to exposures with fine particulates and nitrogen dioxide in the elderly with and without COPD. *Inhalation Toxicology*, *17*, 123–132.
14. Polichetti, G., Cocco, S., Spinali, A., Trimarco, V., & Nunziata, A. (2009). Effects of particulate matter (PM<sub>10</sub>, PM<sub>2.5</sub> and PM<sub>1</sub>) on the cardiovascular system. *Toxicology*, *261*, 1–8.
15. Stabile, L., Buonanno, G., Avino, P., & Fuoco, F. C. (2013). Dimensional and chemical characterization of airborne particles in schools: Respiratory effects in children. *Aerosol and Air Quality Research*, *13*, 887–900.
16. Rössli, M., Künzli, N., Braun-Fahrlander, C., & Egger, M. (2005). Years of life lost attributable to air pollution in Switzerland: Dynamic exposure-response model. *International Journal of Epidemiology*, *34*, 1029–1035.
17. Zhang, Y., Peng, M., Yu, C., & Zhang, L. (2017). Burden of mortality and years of life lost due to ambient PM<sub>10</sub> pollution in Wuhan, China. *Environmental Pollution*, *230*, 1073–1080.
18. Zeng, Q., Wu, Z., Jiang, G., Wu, X., Li, P., Ni, Y., et al. (2017). The association between ambient inhalable particulate matter and the disease burden of respiratory disease: An ecological study based on ten-year time series data in Tianjin, China. *Environmental Research*, *157*, 71–77.
19. Nikoonahad, A., Naserifar, R., Alipour, V., Poursafar, A., Miri, M., Ghafari, H. R., et al. (2017). Assessment of hospitalization and mortality from exposure to PM<sub>10</sub> using AirQ modeling in Ilam, Iran. *Environmental Science and Pollution Research*, *24*, 21791–21796.
20. Tsai, S. S., Chang, C. C., & Yang, C. Y. (2013). Fine particulate air pollution and hospital admissions for chronic obstructive pulmonary disease: A case-crossover study in Taipei. *International Journal of Environmental Research and Public Health*, *10*, 6015–6026.
21. Hwang, S. L., Lin, Y. C., Guo, S. E., Chou, C. T., Lin, C. M., & Chi, M. C. (2017). Fine particulate matter on hospital admissions for acute exacerbation of chronic obstructive pulmonary disease in southwestern Taiwan during 2006–2012. *International Journal of Environmental Health Research*, *27*, 95–105.
22. De Marco, A., Amoatey, P., Omidi, Y., Sicard, P., & Hopke, P. K. (2018). Mortality and morbidity for cardiopulmonary diseases attributed to PM<sub>2.5</sub> exposure in the metropolis of Rome, Italy. *European Journal of Internal Medicine*, *57*, 49–57.
23. Anenberg, S. C., Belova, A., Brandt, J., Fann, N., Greco, S., Guttikunda, S., et al. (2016). Survey of ambient air pollution health risk assessment tools. *Risk Analysis*, *36*, 1718–1736.
24. Bahrami Asl, F., Leili, M., Vaziri, Y., Salahshour Arian, S., Cristaldi, A., Oliveri Conti, G., et al. (2018). Health impacts quantification of ambient air pollutants using AirQ model approach in Hamadan, Iran. *Environmental Research*, *161*, 114–121.
25. Clabaugh, G., & Ward, M. M. (2008). Cost-of-illness studies in the United States: A systematic review of methodologies used for direct cost. *Value in Health*, *11*, 13–21.
26. Jo, C. (2014). Cost-of-illness studies: Concepts, scopes and methods. *Clinical and Molecular Hepatology*, *20*, 327–337.
27. Kumar, A., & Mishra, R. K. (2018). Human health risk assessment of major air pollutants at transport corridors of Delhi, India. *Journal of Transport and Health*, *10*, 132–143.

28. Maji, K. J., Dikshit, A. K., & Deshpande, A. (2017). Assessment of city level human health impact and corresponding monetary cost burden due to air pollution in India taking Agra as a model city. *Aerosol and Air Quality Research*, *17*, 831–842.
29. Goudarzi, G., Daryanoosh, S. M., Godini, H., Hopke, P. K., Sicard, P., De Marco, A., et al. (2017). Health risk assessment of exposure to the Middle-Eastern Dust storms in the Iranian megacity of Kermanshah. *Public Health*, *148*, 109–116.
30. Miri, M., Ebrahimi Aval, H., Ehrampoush, M. H., Mohammadi, A., Toolabi, A., Nikonahad, A., et al. (2017). Human health impact assessment of exposure to particulate matter: An AirQ software modeling. *Environmental Science and Pollution Research*, *24*, 16513–16519.
31. Nagpure, A. S., Gurjar, B. R., & Martel, J. (2014). Human health risks in national capital territory of Delhi due to air pollution. *Atmospheric Pollution Research*, *5*, 371–380.
32. Gurjar, B. R., Jain, A., Sharma, A., Agarwal, A., Gupta, P., Nagpure, A. S., et al. (2010). Human health risks in megacities due to air pollution. *Atmospheric Environment*, *44*, 4606–4613.
33. Maji, K. J., Dikshit, A. K., Deshpande, A., & Speldewinde, P. C. (2016). Human health risk assessment due to air pollution in ten urban cities in Maharashtra, India. *Cogent Environmental Science*, *12*, 1–16.
34. Maleki, H., Sorooshian, A., Goudarzi, G., Nikfal, A., & Baneshi, M. M. (2016). Temporal profile of PM<sub>10</sub> and associated health effects in one of the most polluted cities of the world (Ahvaz, Iran) between 2009 and 2014. *Aeolian Research*, *22*, 135–140.
35. Shah, M., Godbole, V., Patel, T. K., & Patel, T. R. (2017). Study of economic burden and health care resource utilization by chronic obstructive pulmonary disease patients in a tertiary care hospital in Western India. *National Journal of Community Medicine*, *8*, 535–540.
36. Patankar, A. M., & Trivedi, P. L. (2010). Monetary burden of health impacts of air pollution in Mumbai, India: Implications for public health policy. *Public Health*, *125*, 157–164.
37. Huang, D., Xu, J., & Zhang, S. (2011). Valuing the health risks of particulate air pollution in the Pearl River Delta, China. *Environmental Science and Policy*, *15*, 38–47.
38. Srivastava, A., & Kumar, R. (2002). Economic valuation of health impacts of air pollution in Mumbai. *Environmental Monitoring and Assessment*, *75*, 135–143.

# Bi-directional Static Pile Load Test by S-Cell Method



Vijay Kumar Patidar, Suneet Kaur and Nitin Dindorkar

**Abstract** Static load testing is a conventional technique for testing pile in which loads are applied on the top of the pile and generally known as ‘top-down testing’. This has been in practice from many years all over the world and has become a standard test for pile foundation. This method cannot be used when there is lack of space and high magnitude of load is to be applied for the pile test. There is a finite limit to the load capacity that can be applied with either kentledge, the use of reaction piles, or anchors, and as the load increases, the costs of whole assembly also increases. An attempt has been made in this study to adopt a new technique which would overcome all the large-scale problems associated with top-down testing technique. This method will divide the pile into two or more sections, and these can be loaded axially as required using a portion of the pile element as a reaction. Bi-directional static pile load test (S-Cell method) is economical and less time-consuming test as compared to conventional static load test. Therefore, bi-directional static pile load test can be considered as an alternative test for heavily loaded pile foundation in India.

**Keywords** Load test · Bi-directional static load test (BDSLTL) · Super cell · S-Cell · Foundation engineering · Equivalent curve

## 1 Introduction

Testing of pile plays an important role for the optimization of the pile design from a geotechnical point of view. Static load testing, where loads are applied vertically to the top of the pile and often referred to as ‘top-down testing’, has been used for many years and has become a ‘standard’ test for the world of foundation engineering. Bi-directional pile load test method attempts to overcome all the associated problems of conventional top-down static load testing techniques. The Super cell (S-Cell) load test is a bi-directional, axial, compressive, static load test conducted on deep foundations

---

V. K. Patidar (✉) · S. Kaur · N. Dindorkar  
MANIT, Bhopal, Madhya Pradesh, India  
e-mail: [cevijay2014@yahoo.in](mailto:cevijay2014@yahoo.in)

© Springer Nature Singapore Pte Ltd. 2020  
S. Saride et al. (eds.), *Advances in Geotechnical and Transportation Engineering*,  
Lecture Notes in Civil Engineering 71,  
[https://doi.org/10.1007/978-981-15-3662-5\\_2](https://doi.org/10.1007/978-981-15-3662-5_2)

to evaluate the soil–pile resistance [1]. This paper attempts to highlight some of the advantages of S-Cell over the conventional methods in Indian scenario.

## 2 Bi-directional Pile Testing Using S-Cell

### 2.1 About S-Cell

The S-Cell is a high-pressure hydraulic jack installed on the rebar cage and embedded into the foundation under test. The shaft above and below the S-Cell provides reaction for loading. The hydraulic working fluid is water for simplicity and environmental safety. If used in working pile, the S-Cell can be easily grouted after test completion. Multiple sizes of S-Cell are available based on test load capacity of the Pile. Any loading capacity is achieved by applying limited pressure up to 30 MPa by combining S-Cell in series as per the requirement. Each S-Cell is assembled in India and calibrated in-house for quality and reliability.

### 2.2 Method of Operation

In the conventional top-down testing, when load is applied at the pile head via a reaction system known as kentledge, force ( $P$ ) is applied downward to the pile. All of the load measured at the pile head is applied to the pile which is equivalent to the sum of mobilizing skin friction ( $F$ ) and the end bearing ( $Q$ ),  $P = F + Q$  (Fig. 1).

When S-Cell is installed at the toe of the pile, the load is transferred directly to the end bearing. The base resistance is used to mobilize the skin friction and vice versa. Therefore, the skin friction and the base resistance mobilized are equal until one or the other reaches ultimate capacity or the S-Cell system exceeds its capacity, i.e.  $P = F = Q$  (Fig. 1).

When the skin friction ( $F_1 + F_2$ ) is expected to be higher than the base resistance, the S-Cell can be placed at some balance point along the pile shaft where  $P = F_1 = F_2 + Q$ . The pile element above the S-Cell uses the friction ( $F_2$ ) and end bearing ( $Q$ ) below as a reaction (Fig. 1).

### 2.3 Installation of S-Cell

The S-Cell is calibrated before installation and provides an axial compressive load test as the jack is pressurized from the surface. Assembly is installed into the pile cage or carrying frame, either at or close to the pile toe or along the shaft at a level

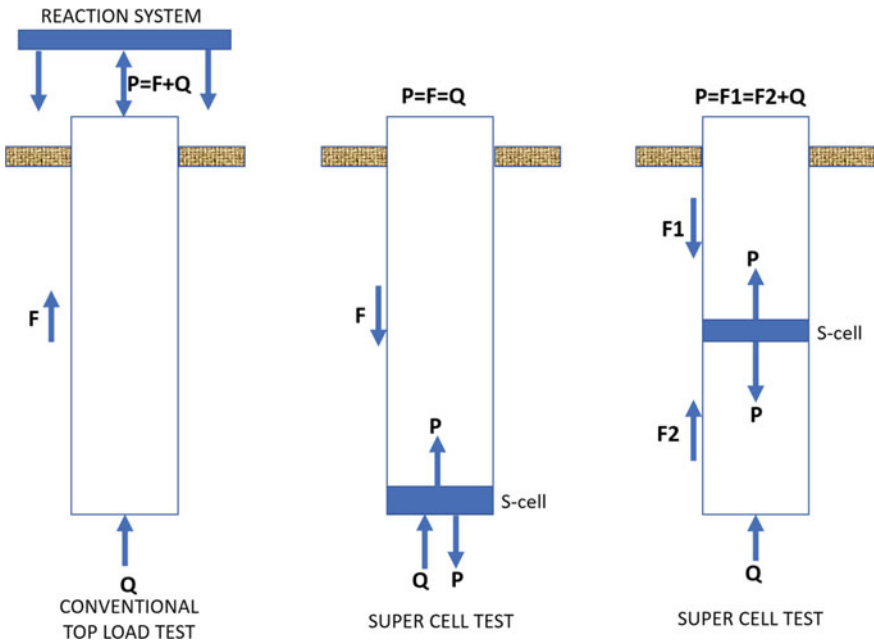


**Fig. 1** Test method comparison

where approximately equal capacity will be available above and below known as balancing point as explained in the previous section.

During the construction of pile, the cage of reinforcement is placed in the pile bore with S-Cell assembly welded during cage preparation as shown in Fig. 2. Strain gauges installation and hydraulic connections are made and cables and hoses are brought up to the pile head. A guide arrangement is constructed for insertion of the tremie into position wherever needed. Concrete is then pumped into the pile shaft and around the S-Cell assembly with proper pressure to avoid voids.

## 2.4 Testing Procedure

In conventional method ‘top-down’ testing, the safety considerations are very challenging, especially at high loads as very huge kentledge and reaction beam assemblies are needed to be assembled. In contrast to conventional method, bi-directional testing has all reactions generated from within the pile itself. The area required for testing work in both overhead and lateral direction is reduced drastically as compared to any other static load testing methods. Testing can be performed in limited space adjoining buildings, overpasses, and also at offshore locations.

**Fig. 2** Installation of S-Cell assembly in cage of diameter 1.5 m for test pile at foot over bridge construction in Sabarmati Riverfront Ahmedabad, Gujarat, India



Figure 3 shows the schematic diagram of S-Cell installation with the instrumentation provided for test. Figure 4a and 4b shows that on field these instrumentations need very less test areas, which are slightly more than the perimeter of pile shaft. Embedded jack assembly is used to apply the load on test pile. The resulting test load applied to the pile is twice the load measured in the jack assembly (Fig. 1). Structural capacity of the pile or the jack assembly should not be exceeded.

To avoid excessive creep and possible structural failure of cast-in-place concrete piles, the concrete should generally achieve uniform strength throughout the pile and should be at least 85% of the mix design compressive strength. Prior to performing the test, hydraulic fluid should be circulated through each jack to verify connectivity, saturate the system, and flush any blockages. Reference beam and LVDTs are set up in the tent to protect them against wind and heat.

Loading may be sustained or continued for a longer time interval to assess long-term creep and rebound behaviour after full unloading. Displacements are measured at each load increment intervals using LVDTs attached to reference beam. The readings can be displayed graphically as the test progresses. Thus, load/displacement data recorded above and below the S-Cell level is available for analysis (as that illustrated in Fig. 5). All the stored data will be analyzed after end of the test to calculate load



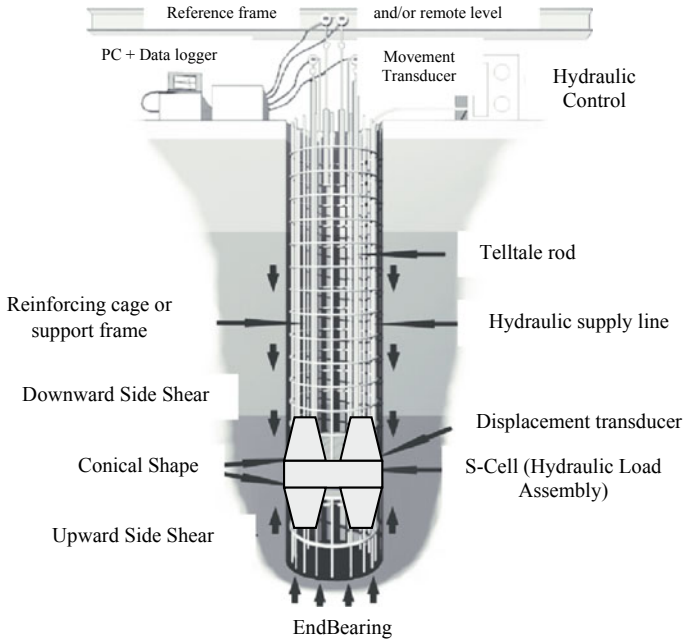


Fig. 3 Single-level S-Cell schematic diagram

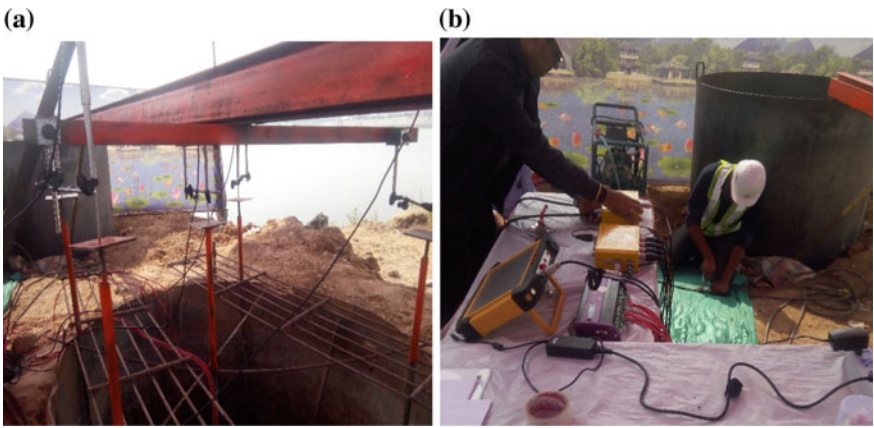
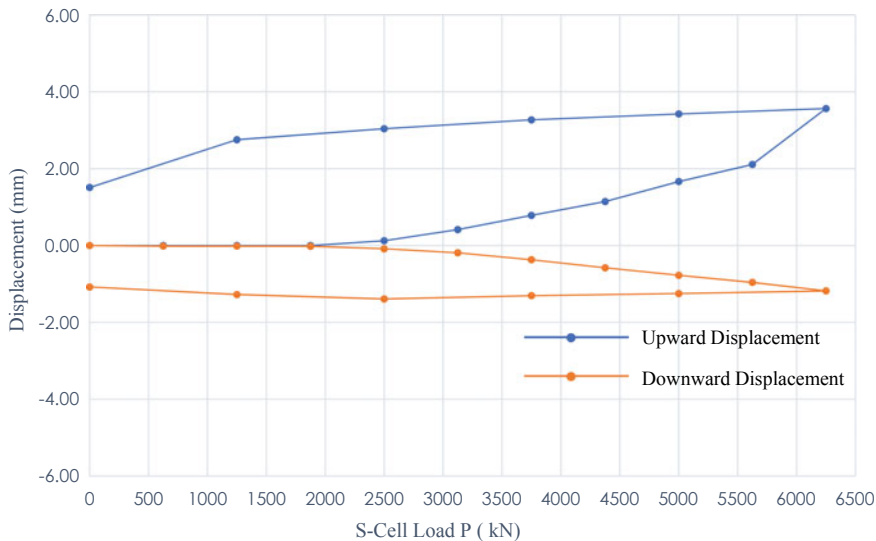


Fig. 4 Assembled setup for bi-directional static load test. a LVDT's with reference beam. b Data logger, data taker, control box, and pressure pump are connected together



**Fig. 5** S-Cell load versus displacement curve

distribution at strain gauge levels, ultimate skin friction, and end bearing at failure load or at maximum test load, for drawing equivalent top-load movement curve.

The total load mobilized in the pile is twice of that applied by the S-Cell system because the load is applied in two opposite directions (bi-directional) simultaneously. Self-weight (including buoyant force) of the pile is considered during calculation of balancing point. Therefore, the stresses within the concrete are half of the required stress by an equivalent top-down load test. Detailed analysis of the soil properties along the pile shaft can be done by embedded strain gauges or other devices.

### 2.5 Conversion of BDSLT Curve into Equivalent Top-Down Curve

Upward ( $Q^+$  vs.  $s^+$ ) and downward ( $Q^-$  vs.  $s^-$ ) curves from bi-directional static load test (BDSLT) need to be converted into conventional load–deformation curves ( $Q$ – $S$  curve) as shown Fig. 6 [2].

Conversion of pile top load versus displacement between BDSLT and conventional static test is based on synchronization principle of upward and downward displacement. Equivalent pile top load and pile top displacement after conversion can be computed by the formula as shown below.

$$Q = [(Q_u - W)/\gamma] + Q_d \tag{1}$$

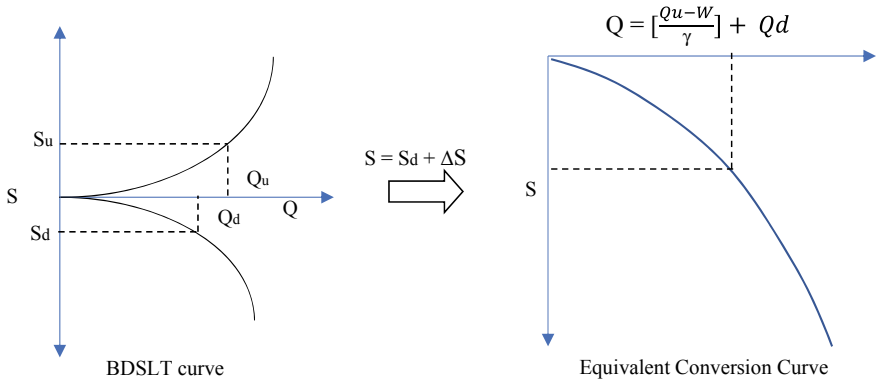


**Fig. 6** Conversion of BDSLT curve into equivalent top-down curve

$$S = S_d + \Delta S \quad (2)$$

where

$Q$  is equivalent pile top load after conversion

$Q_u$  Upper pile load when upper pile displacement absolute value equal to  $S_u$  in  $Q_u$  versus  $S_u$  curve, unit is kN

$W$  Test pile upper pile self-weight above load cell, unit is kN

$\gamma$  Correction factor; soil = 0.8, sand = 0.7, rock = 1.0

$Q_d$  is downward load value of the cell

$S$  is pile top displacement after conversion

$\Delta S$  is pile shaft compression,  $S_d$  is downward displacement.

Upper pile compression  $\Delta S$  is equal to the sum of elastic compression caused by upper pile and lower pile:

$$\Delta S = \Delta S_1 + \Delta S_2 \quad (3)$$

where

$\Delta S_1$  Elastic compression caused by the vertical load of the bottom compressed pile;

$\Delta S_2$  Elastic compression caused by friction resistance of the upper compressed pile.

$$\Delta S_1 = \frac{QdL}{E_p A_p} \quad (4)$$

$$\Delta S_2 = \frac{(Q_u - W)L}{2E_p A_p \gamma} \quad (5)$$

$$\Delta S = \Delta S_1 + \Delta S_2 = \frac{[(Q_u - W)/\gamma + 2Qd]L}{2E_p A_p} \quad (6)$$

where

- $L$  Upper pile length, unit is  $m$ ;  
 $E_P$  Pile shaft elasticity modulus, unit is  $kPa$ ;  
 $A_P$  Pile shaft cross-sectional area, unit is  $m^2$ .

It is useful to see the results of a bi-directional load test in the form of a curve showing the load versus settlement of the pile if it were top-loaded. There are some methods to find the equivalent top movement curve but generally, the test results can be combined by adding the loads mobilized at equal displacements. Some additional parameters like elastic shortening, buoyant force, modulus of elasticity of pile along the length of pile, etc. are needed to keep in consideration for calculating equivalent top-load movement curve. A smaller number of comparisons have been made between the equivalent pile head movement and top-loading test results around the world. England [3] compared static load results between top-down loading and bi-directional testing. He showed excellent correlation between the two.

### **3 Advantages of Bi-directional Static Load Test Over Conventional Methods**

The advantages of BDSLT are explained as follows.

#### **3.1 High-Quality Data**

Digital LVDTs and pressure transducers are used with least count 0.01 mm and 0.01 MPa, respectively to get high-quality data as these instrumentations have efficiency to record all the reading simultaneously during loading intervals.

#### **3.2 Higher Load Limit**

Lots of practical problems encountered during top-down load test, when load is more than 4 MN, i.e. approx. 400 ton [4]. Lots of space and machinery are required to make proper arrangement. By using S-Cell testing method, there is saving in terms of cost, transport, installation, and erection of kentledge, anchors, or anchor piles as well as the associated reaction system required above ground level. There is improvement in terms of safety, at the head of the pile as the assembly of a loading system is not required and the loads applied are through S-Cell embedded in the pile. The installation/welding of an S-Cell on an existing steel reinforcement cage typically takes one or two days with proper alignment. But the arrangement of kentledge for loads up to 4 MN may take over 20 days to make proper platform and reaction

arrangement with help of loading blocks. These features can make it preferable over top-down static load testing.

### ***3.3 Rock Socketed Pile***

It is difficult to evaluate skin friction in rock sockets because it not possible to ensure that the load applied has reached the area of interest. In top-down tests, it is found that the skin friction is often indistinguishable from the end bearing and extra sensors within the pile body are required to evaluate the friction distribution. Bi-directional tests can be arranged to apply the load directly into the rock sockets (or other zones of interest), and thereby, the resultant behaviour is more readily interpreted.

### ***3.4 Use of Test Pile as Working Pile***

In bi-directional tests, after fully grouting in and around the cell generally, the original stiffness is reverted with increase in base stiffness behaviour up to loads more than service load. Hence, it can be safely used as working pile.

### ***3.5 Testing Time***

Bi-directional statics load test takes less time as compared to conventional top-down test; hence, it is also known as quick static load test.

### ***3.6 Applications***

In several countries, up to 1% of the piles installed are static load tested and it appears more routinely to apply loads from top to down at the pile head. However, in many circumstances, the full-scale testing using top-down testing method is obstructed and bi-directional testing is becoming conventional. S-Cell test has been performed at various projects in India including offshore sites.

### ***3.7 Cost***

The current comparison between costs of top-down and bi-directional load tests in India shows that up to 7.5 MN loading costs per MN are same in both conventional and

bi-directional load tests. However, at higher loads, bi-directional tests become more cost-effective because only the cell cost increases, and the cost of instrumentation remains same. As the number of bi-directional tests increases, transportation cost and mobilization of instruments and personnel are also reduced. Hence, the overall cost of test gets reduced with increase in test load and number of tests.

## 4 Conclusion

- (a) The execution of top-down load tests has been optimized and made as cost-effective as possible; still, there is scope for further development in the practice of full-scale foundation testing using bi-directional tests.
- (b) Bi-directional static load test has unlimited loading capability, as compared to conventional techniques.
- (c) There are considerable costs savings at loads above approximately 7.5 MN.
- (d) Use of bi-directional S-Cell testing technique enables collection of full-scale data even under the most extreme and difficult conditions by providing significant advantages in terms of space and safety.
- (e) The bi-directional test is a static load test using automatic data acquisition techniques, load maintenance for accurate, efficient data processing, and analysis for calculating skin friction and end bearing separately.
- (f) The S-Cell test method excels in offshore testing environments as the top of the foundation element is not required to be cast above water.

**Acknowledgements** I would like to express my special thanks of gratitude to Er. Snehal Patel (P. Eng.) President and CEO of Super cell Bharat for giving golden opportunity for undergoing pile test using S-Cell technology at their ongoing project sites.

## References

1. Osterberg, J. O., & Hayes, J. A. (2002). The Osterberg load cell as a research tool. In *Proceedings of the International Conference on Soil Mechanics and Geotechnical Engineering* (Vol. 2, pp. 977–980). AA Balkema Publishers.
2. Kim, S. R., & Chung, S. G. (2012). Equivalent head-down load vs. movement relationships evaluated from bi-directional pile load tests. *KSCE Journal of Civil Engineering*, 16(7), 1170–1177. <https://doi.org/10.1007/s12205-012-1700-8>.
3. England, M. (2008). Review of methods of analysis of test results from bi-directional static load tests. In *Deep foundations on bored and auger piles* (pp. 235–239). Ghent: BAP V.
4. Fellenius, B. H. (2015). Analysis of results of an instrumented bidirectional-cell test. *Geotechnical Engineering Journal of the SEAGS & AGSSEA*, 46(2), 64–67.

# Soil Stabilization Using Bagasse Ash



Dharmesh Lal, M. Jeevan Kumar, K. Naresh Kumar, K. Sindhu  
and Ashok Kumar

**Abstract** Clay soils exhibit undesirable engineering properties like low shear strength, high compressibility and low permeability. The properties further deteriorate upon wetting or other physical disturbances. Hence, soil is stabilized before construction by soil stabilization techniques. Bagasse ash is a biodegradable waste material which can be effectively used as a stabilizer for soils after recycling or reprocessing. Bagasse ash has been found to improve the strength characteristics of soils. The main objective of this study is to investigate the use of bagasse ash in geotechnical applications to evaluate the effects of the waste powder on geotechnical characteristics of highly compressible clay soil deposits. The bagasse ash material is added to the soil in different proportions, i.e. 2, 4, 6 and 8%, to find the optimum percentage contributing to maximum strength development. The results obtained clearly indicate that the addition of the ash enhances the properties of the soil deposit.

**Keywords** Clay soils · Engineering properties · Bagasse ash · Stabilizer · Compressible clay · Optimum percentage

## 1 Introduction

Generally, clayey soil exhibits undesirable properties like low shear strength, low bearing capacity and high settlement. Clay soil is a mixture of several particles which are connected to each other. They rest on each other due to gravity and form grids based upon its properties. Each particle produces its own contact forces by the surrounding particle. These contact forces together hold all the individual particles at their place. The sudden water pressure leads to soil losing its cohesion. Once the soil loses its cohesive strength, it gets softened, weak and finally loses its solid properties. Due to these circumstances, it results in differential settlement, soil liquefaction and landslides. Also, black cotton soils encountered in many construction sites have poor engineering properties and become problematic because of their tendency to expand

---

D. Lal (✉) · M. J. Kumar · K. N. Kumar · K. Sindhu · A. Kumar  
Vardhaman College of Engineering, Shamshabad, Hyderabad, India  
e-mail: [dharmeshlal34@gmail.com](mailto:dharmeshlal34@gmail.com)

© Springer Nature Singapore Pte Ltd. 2020  
S. Saride et al. (eds.), *Advances in Geotechnical and Transportation Engineering*,  
Lecture Notes in Civil Engineering 71,  
[https://doi.org/10.1007/978-981-15-3662-5\\_3](https://doi.org/10.1007/978-981-15-3662-5_3)

during wet season and shrink during dry season. These problems can be solved by improving the strength of the soil by the process called soil stabilization.

Soil stabilization is the process of enhancing the stability of soil by the use of suitable admixtures, stabilizers or mechanical means. For many years, engineers have used additives such as cement, lime and cement kiln dust to improve the physical properties of soil [1–9]. Field and laboratory performance tests have confirmed that the addition of such additives can enhance the stability and strength of such soils. However, the cost of introducing these additives has also increased in recent years. This has opened the door widely for the development and introduction of other kinds of soil additives such as plastics, bamboo and liquid enzyme soil stabilizers.

In this present study, an attempt has been made to improve the properties of clay soil by stabilization technique using bagasse ash. Laboratory investigations were carried out to know the effect of bagasse ash as a stabilizer when mixed in different proportions. Properties of soil obtained with and without adding the stabilizer were compared. Bagasse ash (Fig. 1) is a waste product obtained from the sugar supplying industries. Bagasse ash improved the basic properties and shear strength characteristics of clayey soils [9].

Extensive experimental investigations were carried out on soil stabilization using bagasse ash by [10]. It was observed that bagasse ash can significantly enhance the properties of the soil used in the construction of road pavement. The soil was mixed with varying percentages (0.0, 0.2, 0.4, 0.6, 0.8%, etc.) of bagasse ash, and the soaked CBR value was noted. The optimum dosage of bagasse ash was obtained at 0.6%. At optimum, an improvement of about 26% was obtained. Also, a reduction of CBR value was observed at 0.2% bagasse content as a result of dispersed structure.

The main aim of this study is to find out the benefits of bagasse ash in geotechnical utilization to check out the holdings of the bagasse ash on geotechnical characteristics of highly compressible clay soil deposits. The bagasse ash material is mixed with the soil in various proportions, i.e. 2, 4, 6 and 8%, to find the optimum percentage

**Fig. 1** Bagasse ash





contributing to maximum strength development. Different tests such as Atterberg's limits, standard Proctor test and triaxial tests have been performed to find out the effect of bagasse ash on strength parameters of soil. Standard Proctor test results indicate that the optimum moisture content increases with increase in percentage of sugarcane bagasse ash and the maximum dry density decreases with increase in percentage of sugarcane bagasse ash. Also, an enhanced strength parameter values were obtained with the introduction of the ash. These results clearly show that sugarcane bagasse ash can be used as an effective stabilizer for reinforcing soil.

## 2 Materials and Methodology

### 2.1 Materials Used

#### Clay

Table 1 indicates the properties of black cotton soil used for the study.

#### Bagasse Ash

Bagasse ash (Fig. 1) is a waste product obtained from the sugar supplying industries. The composition of bagasse ash used for the study is enumerated in Table 2.

The triaxial tests were carried out by preparing the soil samples at maximum dry density condition with an aspect ratio of 2 (38 mm × 76 mm).

**Table 1** Basic properties of black cotton soil

S. no.	Property	Value
1	Specific gravity	2.125
2	Liquid limit	59%
3	Plastic limit	37.95%
4	Plasticity index	21.05%
5	OMC	24.27%
6	MDD	14.60 kN/m <sup>3</sup>
7	Cohesion	54.97 kPa
8	Angle of internal friction (degree)	10°
9	CBR	1.07%

**Table 2** Composition of bagasse ash

Constituents	Percentage (%)
Silicon dioxide (SiO <sub>2</sub> )	66
Aluminium oxide (Al <sub>2</sub> O <sub>3</sub> )	6
Ferric oxide (Fe <sub>2</sub> O <sub>3</sub> )	5
Calcium oxide (CaO)	2
Magnesium oxide (MgO)	2
Potassium oxide (K <sub>2</sub> O)	6.5
Sodium oxide (Na <sub>2</sub> O)	1
Phosphorous pentoxide (P <sub>2</sub> O <sub>5</sub> )	1
Sulphur trioxide (SO <sub>3</sub> )	0.18
Cl <sub>2</sub>	<0.1
Manganese oxide (MnO)	0.05
Titanium dioxide (TiO <sub>2</sub> )	0.25
Loss of ignition (LOI)	10

### 3 Results and Discussion

Triaxial test is conducted for clay without adding any additives. The stress–strain curve obtained is shown in Fig. 2. Based on results, modified shear strength parameters, i.e.  $p$  and  $q$  values, are obtained and listed in Table 3.

**Fig. 2** Stress versus strain curve for plain soil

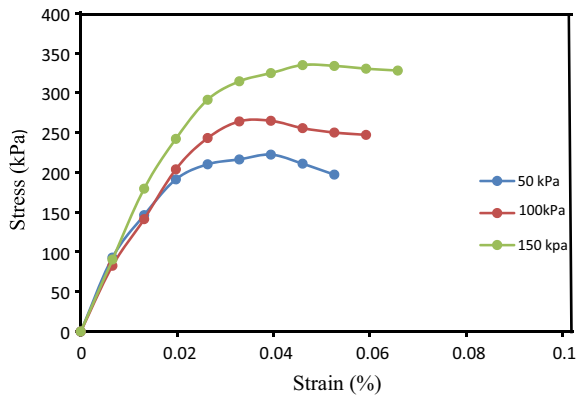


**Table 3** Modified shear strength parameters

$p$	$q$
164.745	114.745
222.81	122.81
280	130

**Fig. 3** Modified failure envelope

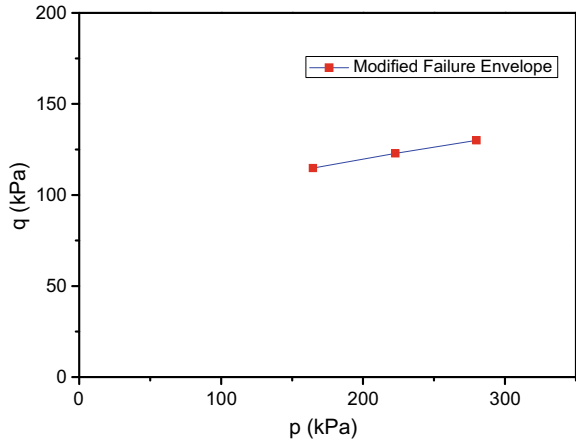


Figure 3 shows the plot between  $p$  and  $q$  which gives modified failure envelope, where  $p$  and  $q$  are given in Eq. (1)

$$p = \frac{\sigma_1 + \sigma_3}{2} \quad \text{and} \quad q = \frac{\sigma_1 - \sigma_3}{2} \tag{1}$$

- From the modified failure envelope, the intercept and the slope are found.
- By using these slope and intercept, the cohesion and the angle of internal friction are calculated.

For the normal soil, the shear parameters cohesion and angle of internal friction are found to be 54.97 kPa and 10°.

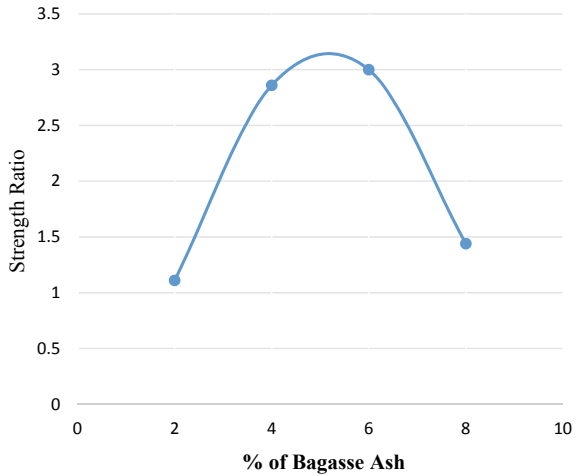
### 3.1 Strength Ratio

Strength ratio is the ratio of peak deviator stress of stabilized soil to the peak deviator stress of plain soil. The optimum percentage of plastic powder is obtained by plotting the graph between the % of bagasse ash and strength ratio. Table 4 shows the values of strength obtained for considered % of bagasse ash. Figure 4 shows the graph plotted between strength ratio and the % of bagasse ash.

**Table 4** Strength ratio with respect to % of bagasse ash

% of bagasse ash	Strength ratio
2	1.11
4	2.86
6	3
8	1.44

**Fig. 4** Strength ratio versus % of bagasse ash



From the strength ratio graph, it is observed that optimum % of bagasse ash was 6%.

### 3.2 Triaxial Test Results for 6% Bagasse Ash

Triaxial test was conducted for pure clay with addition of 6% of bagasse ash as the optimum was obtained at this percentage. Based on the observations, the stress–strain curve was obtained (Fig. 5). The  $C$  and  $\phi$  are found to be 164.46 kPa and  $10.2^\circ$  from the modified failure envelope (Fig. 6). The values of  $p$  and  $q$  are shown in Table 5.

**Fig. 5** Stress versus strain curve for 6% of bagasse ash

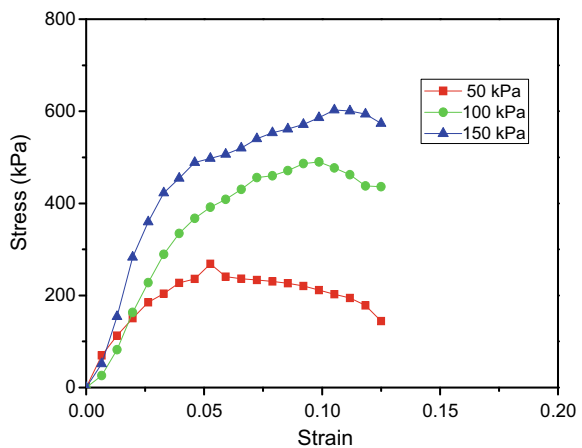


**Fig. 6** Modified failure envelope

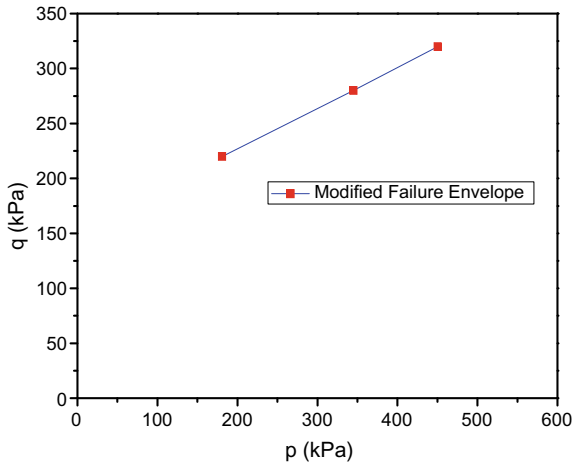


**Table 5**  $p$  and  $q$  values

$p$	$q$
180.80	220
344.99	280
450.33	320

From the results, it is clearly understood that value of cohesion increases and thereby increasing the strength and stiffness characteristics of soil. Similar conclusions were drawn by [10]. This is mainly because of the pozzolanic properties possessed by the ash. As indicated by the composition of ash in Table 2, it consists of various amounts of silica and other relevant oxides which enhance the pozzolanic activity of the soil [10].

## 4 Conclusion

Based on the above tests conducted in the present study, the following conclusions were drawn.

1. The optimum percentage of the bagasse ash which gave maximum strength and stiffness improvement was found to be **6%**.
2. The  $C$  and  $\phi$  values of the plain soil are 54.97 kPa and  $10^\circ$ , whereas the  $C$  and  $\phi$  values of the reinforced soil were found to be 164.46 kPa and  $10.2^\circ$ .
3. Overall it can be concluded that reinforced soil can be considered as a good ground improvement technique, especially in engineering projects on weak soils.
4. The use of bagasse ash is a cost-effective and sustainable method of soil stabilization.

## References

1. Suksun, H., Chayakrit, P., & Chinkulkijniwat, A. (2012). Soil stabilization by calcium carbide residue and fly ash. *Journal of Materials in Civil Engineering*, 24(2), 184–193.
2. Ramesh, H. N., Manoj, K. V., & Mamatha, H. V. (2010). Compaction and strength behavior of lime-coir fiber treated black cotton soil. *Geomechanics and Engineering*, 2(1), 19–28.
3. Gowtham, S., Naveenkumar, A., Ranjithkumar, R., Vijayakumar, P., & Sivaraja, M. (2018). Stabilization of clay soil by using glass and plastic waste powder. *International Journal of Engineering and Techniques*, 4(2), 146–150.
4. Harish, C., & Ashwini, H. M. (2016). Stabilization of soil by using plastic bottle strips as a stabilizer. *International Research Journal of Engineering and Technology*, 3(8), 1874–1877.
5. Temimi, M., Rahal, M. A., Yahiaoui, M., & Jaubertie, R. (1998). Recycling of fly ash in the consolidation of clay soils. *Conservation & Recycling*, 24, 1–6.
6. Cokca, E. (2001). Use of class C fly ash for the stabilization of an expansive soil. *ASCE Journal of Geotechnical and Geo-Environmental Engineering*, 127(7), 568–573.
7. Pandian, N. S., Krishna, K. C., & Leelavathamma, B. (2001). Effect of fly ash on the CBR behaviour of soils. In *Indian Geotechnical Conference* (Vol. 1, pp. 183–186). Allahabad.
8. Phanikumar, B. R., & Sharma, R. S. (2004). Effect of fly ash on engineering properties of expansive soil. *Journal of Geotechnical and Geo-Environmental Engineering*, 130(7), 764–767.
9. Senol, A., Etmnan, E., & Olgun, C. (2012). Stabilization of clayey soils using fly ash and homopolymer polypropylene. In *Geo Congress*, pp. 3929–3938.
10. Gandhi, K. (2012). Expansive soil stabilization using bagasse ash. *International Journal of Engineering Research & Technology (IJERT)*, 1(5), 28–31.

# Strength Behavior of Rammed Earth Stabilized with Metakaolin



S. K. Thiviya, Aswathi G. Krishnan, Monish Kalathuru,  
Anil Kumar Sharma  and Sreevalsa Kolathayar 

**Abstract** Rammed earth is an ancient construction technique practiced in India and in other parts of the world. The ancient traditional technique was of the un-stabilized method but incorporating suitable stabilizing materials will improve the strength of rammed earth construction. The main objective of the present study is to assess the behavior of the rammed earth with metakaolin. The suitability of the soil was tested based on sieve analysis and followed by mini compaction tests; optimum moisture content for the rammed earth construction for the selected soil was fixed for different proportions of binders with the soil. From the compaction results, the binder content was fixed for stabilization of rammed earth. The unconfined compressive strength of the sample was found for the samples at 7, 14, 28 days of curing, and microstructural studies of the samples were performed. The compression strength of rammed earth cubes was tested and also the durability of the cubes was determined by the spray erosion test.

**Keywords** Rammed earth · Sustainability · Metakaolin · Durability · Compressive strength

## 1 Introduction

Rammed earth (RE) is an old practice of construction. Archeological researchers have found an evidence of the rammed earth which dated to around 5000 BC. Many amusing structures such as the Great Wall of China, Egyptian Pyramids are all made of rammed earth construction. Later, concrete building took over the earth construction and also the non-availability of standard codebook reduced the RE construction

---

S. K. Thiviya · A. G. Krishnan · M. Kalathuru  
Amrita Vishwa Vidyapeetham, Coimbatore, India

A. K. Sharma  
National Institute of Construction Management and Research (NICMAR), Hyderabad, India

S. Kolathayar (✉)  
National Institute of Technology Karnataka, Surathkal, India  
e-mail: [sreevalsakolathayar@gmail.com](mailto:sreevalsakolathayar@gmail.com)

© Springer Nature Singapore Pte Ltd. 2020  
S. Saride et al. (eds.), *Advances in Geotechnical and Transportation Engineering*,  
Lecture Notes in Civil Engineering 71,  
[https://doi.org/10.1007/978-981-15-3662-5\\_4](https://doi.org/10.1007/978-981-15-3662-5_4)

in India. RE construction has a positive environmental concern such as low CO<sub>2</sub> emissions, good thermal performance, and cost-effectiveness when compared to modern building construction using concrete. According to the World Bank in 2015, 172 million people in India were in poverty which is 12.4% of the total world population. Hence, it is difficult for the people at extreme poverty to afford their own concrete houses. In recent years, rammed earth construction has been given prime consideration to overcome housing problems. A significant research has been done in the recent past to improve the strength of rammed earth by using various materials and techniques. Moreover, advancement in the instrumentation technique has increased the speed of construction and structural integrity of RE buildings.

The ancient constructions were of the un-stabilized method. But stabilizing the soil will improve its physical properties. Rammed earth construction is done by compacting the soil enough to hold together. Rammed earth construction is a long-term process as it has to ram tightly and it is also a labor-intensive process. The typical compressive strength of the un-stabilized earth block is in the range from 1 to 5.4 MPa [1]. Today rammed earth is topic of increased interest as sustainable construction practices become mainstream [2]. Stabilization is done to increase the durability and optimize the mechanical properties of soil to make it suitable for rammed earth construction [3]. The soil stabilization techniques fall into two broad categories—chemical stabilization and mechanical stabilization. Materials such as cement, lime, and fly ash can be used for soil stabilization. Lime is found to be a suitable treatment material for expansive soil works which acts on the clay minerals in the soil [1]. The optimum dosage of lime varies from 6 to 12% and after that the compressive strength decreases [4]. The cementitious compounds as a result of the pozzolanic reaction between lime and the clay fraction in the soil are mainly responsible for the improvement of strength and durability of RE [5]. Soil reinforcement can be done by using natural fibers such as straw, sisal fibers, and timber. The thermal performance, bending and tensile strength of soil can be improved by using fibers. Fiber stabilization is ideal for soil. A study found that there is an increase in the compressive strength of soil as with the increase in the fiber [6]. Sudhakaran et al. [7] demonstrated the performance improvement of areca fiber reinforced soil through experiments and reliability approach. Stabilization of cement is very common technique of RE construction currently since it significantly improves the strength of almost all types of soil.

The main objective of the present investigation is to study the behavior of the soil in rammed condition with the addition of metakaolin to the soil. The paper discusses the improvement of the properties of the locally available soil along with the determination of durability of the rammed earth cubes by spray erosion test. The microstructural behavior of UCS sample of high strength is also presented.



## 2 Materials

### 2.1 Soil

The soil was collected from a site at Coimbatore in the state of Tamil Nadu, India. Topsoil is unsuitable for the rammed earth because of the presence of organic matters in the soil which will absorb water and will perform high compressibility [8]. There are certain criteria to select the suitable soil for rammed earth; the soil should be well graded, so that it should contain gravel, silt, sand, and clay. Clay content should be comparatively more in the selected soil as it will act as binder. The specific gravity of soil is also calculated by using pycnometer as 2.67.

**Particle Size Distribution** Suitability of the soil is checked by the sieve analysis to find the particle size distribution. The study carried by Maniatidis and Walker [6] suggests that the soil should have a minimum of 20–25% of clay and silt together and a maximum of 30–35% sand should be minimum of 50–55% and a maximum of 70–75%. Figure 1 shows the grain size distribution curve of the soil. The soil used in this study is sandy soil with 10% of silt.

**Consistency Limits** If the soil is fine-grained, the water content plays a major role in the properties of the soil. Consistency limits thus help in determining the suitability of the soil for rammed earth construction. The basic properties of the soil are presented in Table 1.

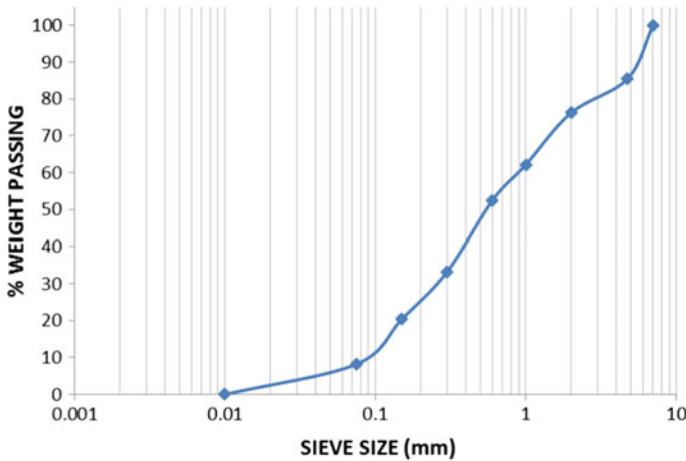


Fig. 1 Particle size distribution of soil

**Table 1** Properties of soil

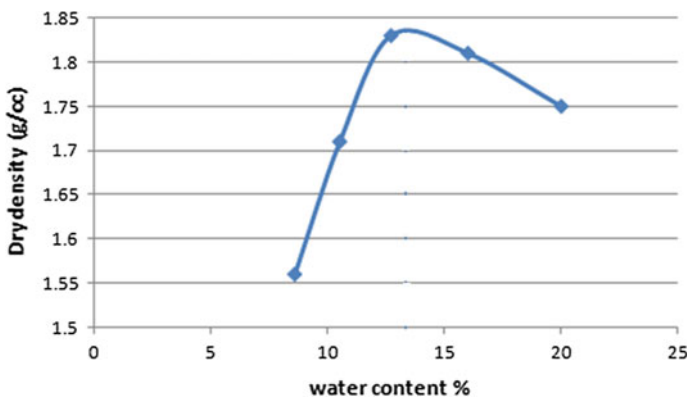
Liquid limit	26%
Plastic limit	16%
Plasticity index	10%

## 2.2 Metakaolin

Metakaolin is obtained by the calcination of kaolinite clay at temperature from 700 to 8000 °C. As kaolin does not contain any carbonates, no CO<sub>2</sub> is released during heating. Metakaolin is neither a by-product of industrial process nor it is natural. It is a mineral which is a dehydroxylated form of kaolinite.

## 2.3 Mini Compaction Test

The water added for rammed earth construction should be the optimum content to get maximum dry density as dry density is directly proportional to the compressive strength. The soil is filled in the mold of diameter 3.8 cm and height 10 cm in three layers and each layer is compacted by 36 blows [9]. The weight of the mold with the compacted soil is measured and moisture content of the soil is determined using the oven. A graph of water content and dry density was plotted. The highest point in the graph is the optimum moisture content after which any further addition of water decreases the dry density of the soil. Figure 2 shows the compaction curve for the soil. Similarly, the compaction test is done for soil with different proportions of metakaolin, and the optimum moisture content and maximum dry density are determined.

**Fig. 2** Compaction curve

The mini compaction test was done of 5, 10, and 15% of metakaolin combination with soil and optimum moisture content and maximum dry content was found. Figures 3 and 4 show the variation of OMC and MDD, respectively, with respect to metakaolin content.

From Figs. 3 and 4, it can be seen that both OMC and MDD increase with an increase in metakaolin content. This may be due to the fact that as the metakaolin panicles are finer than soil, it occupies the void spaces, and hence, as a result, the density is increased.

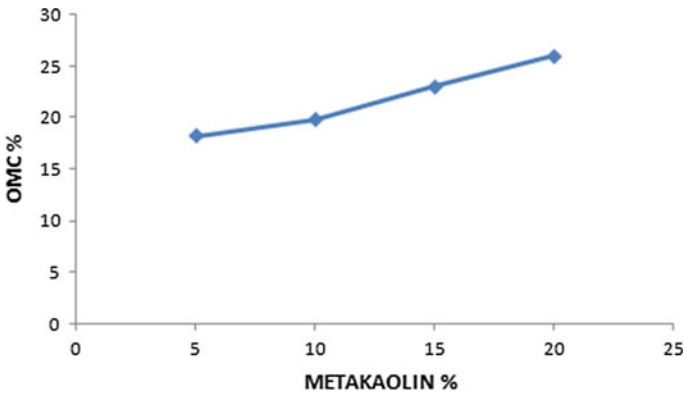


Fig. 3 Variation of OMC with metakaolin as a binder

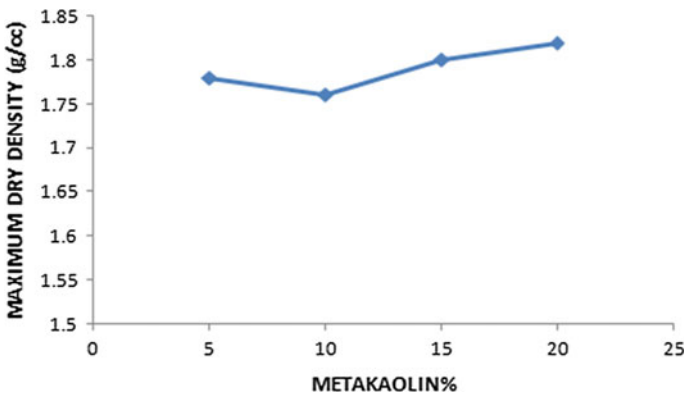
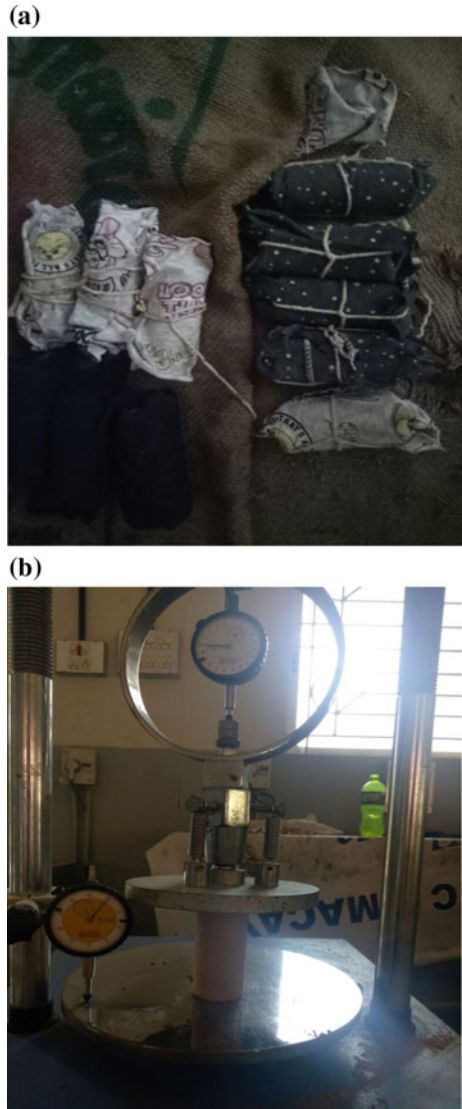


Fig. 4 Variation of MDD with metakaolin as a binder

### 3 Unconfined Compressive Strength

Cylindrical samples of soil with various proportions were prepared and kept for curing and these samples are tested for 7, 14, and 28 days curing (Fig. 5). The test was done according to IS: 2720, part 10. Figure 6 shows that soil with 15% metakaolin as a binder has more strength compared to 5 and 10% metakaolin in the soil. It can

**Fig. 5** a UCC samples kept for curing. b UCC test setup



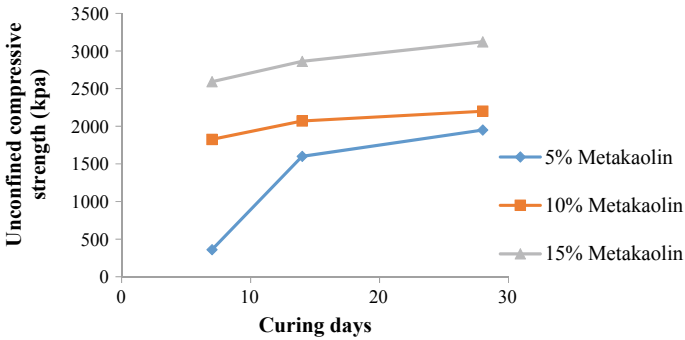


Fig. 6 Comparison of UCS of the different soil-binder mixture

be inferred that with the increase in binder content and number of curing days, the strength increases which is due to the pozzolanic reaction of metakaolin with soil.

#### 4 Cube Strength Test

The soil was mixed with optimum amount of 15% metakaolin to total dry weight of the soil. The prepared mixture was filled in a mold of size 150 mm × 150 mm × 150 mm in three layers and each layer was compacted with 25 blows. Demoulding of blocks was done after 24 h.

The compressive strength of blocks cured for 7, 14, and 28 days was determined in the laboratory by using compression testing machine (Fig. 7). The block was kept in the machine and tested for compression until it failed. The average compressive strength of the 2 tested cube specimens was then calculated. The average compressive strength of the blocks at 7, 14, and 28-day curing was obtained as 0.3 MPa, 0.7 MPa, and 1.2 MPa, respectively.

#### 5 Durability Test

The durability of rammed earth is quite excellent which makes them a good choice of over concrete structures. To determine the durability of the rammed earth, the spray erosion test is performed according to IS CODE 1725-1982 (Fig. 8).

The rammed blocks of 150 mm cubes are prepared for the spray erosion test. This test consists of a shower with 36 holes and each of 2 mm diameter. The water pump is used to maintain a constant pressure of about 1.5 kgf/cm<sup>2</sup> with the approximation of about 10%. Three rammed earth blocks are subjected to testing and the average value was considered. The blocks are placed at a distance of 18 cm from the showerhead and the water should be cleared out to avoid stagnation at the bottom of the blocks.

**Fig. 7** Compressive testing on rammed earth cubes



The period of exposure to water is usually limited to 2 h and the pits on the surface are examined. The pit developed should be within 1 cm diameter to pass the spray erosion test.

Spray erosion test results are presented in Table 2. The pits on the surface of the rammed earth block are found more than 1 cm in diameter, and it is beyond the advisable limits. Hence, it is advisable to increase the binder content or the addition of a small percentage of cement.

## 6 X-Ray Diffraction Test

X-ray analysis was done at the scattering angle  $2\theta$  ranging from  $10^\circ$  to  $70^\circ$  in both cases. Highly intense peaks are obtained in the case of sample 1 which indicates the presence of crystalline particles in the sand. The maximum intense peak is obtained for the  $2\theta$  value at  $26.4^\circ$  is 813 counts with a full width at half maximum (FWHM) 0.113. In the case of sample 2, the maximum peak height of 62 counts is obtained at  $20.70^\circ$  and FWHM 0.126. From the data, it is clear that in sample 2 intense prominent peaks are less when compared to sample 1 which indicates that the presence of less crystalline particles in a soil sample. There is a wide variation in the peak height also when compared to a sample of soil with metakaolin and soil sample (Fig. 9). Integration of the area under the curve will give a measure of the crystalline to the amorphous ratio between two samples.

**Fig. 8** **a** Spray erosion test setup. **b** Exposed face of the specimen after the test

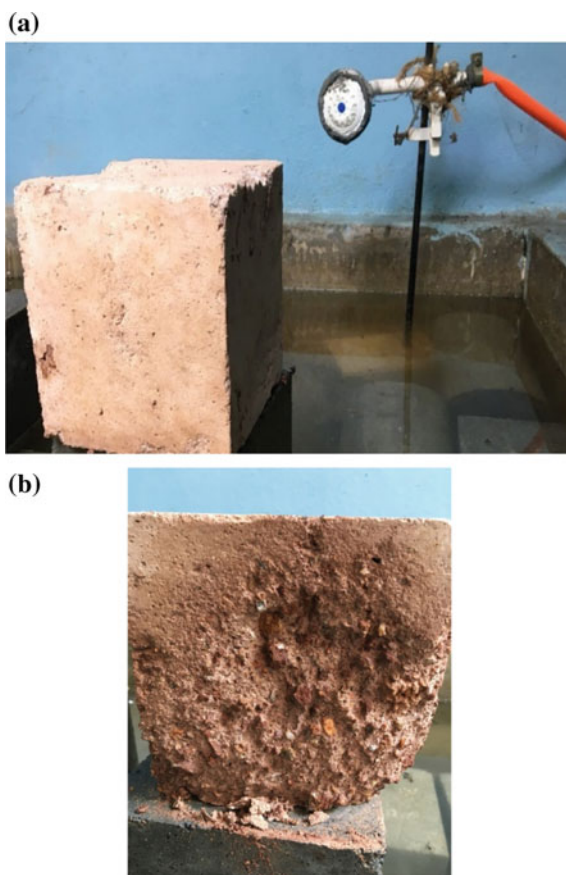


**Table 2** Spray erosion test results

Sample no.	Pitting depth (cm)
1	1.5
2	1.8
3	2.5

## 7 Scanning Electron Microscopy Analysis

Scanning electron microscopy is used in microanalysis of solid materials. The signals generated by SEM analysis give a 2D image and also information about the texture of the sample. SEM analysis of the soil-binder mixtures was done to analyze its microstructure to estimate the bond between particles and also to study the effect of binders. The SEM analysis of soil with metakaolin is illustrated in Fig. 10. The figure shows the microstructure of the soil when mixed with metakaolin.

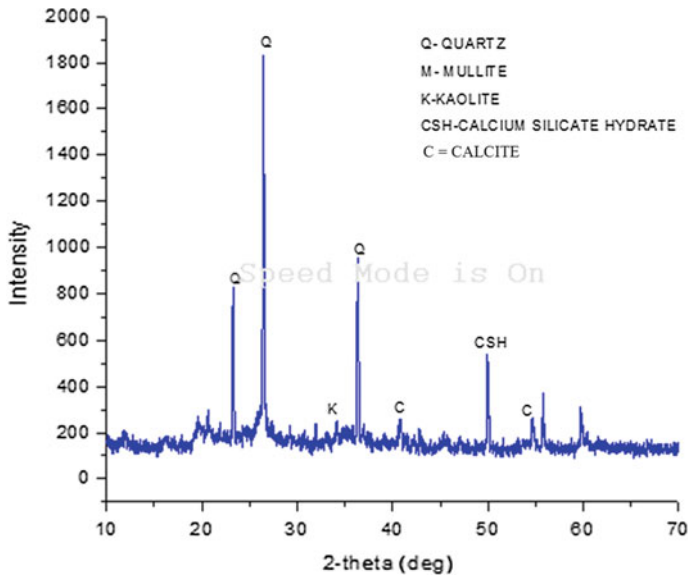


Fig. 9 X-ray diffraction test for metakaolin stabilized soil sample

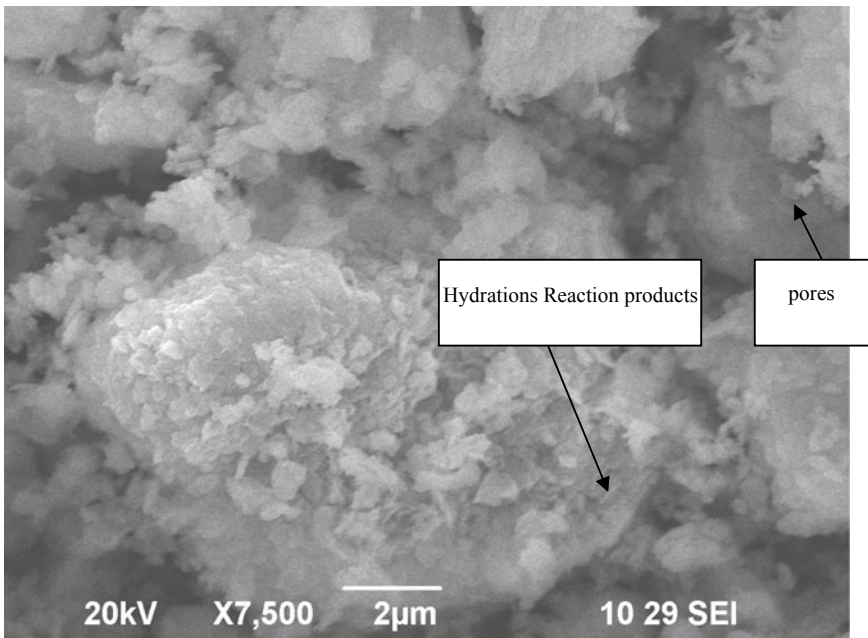


Fig. 10 SEM test for metakaolin stabilized soil sample



## 8 Summary and Conclusions

Mini compaction test was performed on the soil and the binder matrix to obtain the optimum moisture content and the quantity of the binders. The unconfined compression strength of the different mixtures of the soil and the binders are performed on the small cylinder specimens. Microstructural and the mineralogy studies for the optimum content of the binder with the soil were done. The following conclusions are drawn from the study:

1. Based on the compaction test done with different proportions of metakaolin, the optimum amount of metakaolin is recommended as 15%.
2. Both OMC and MDD have been found to increase with the addition of metakaolin.
3. UCS of soil stabilized with 15% metakaolin increases with increases in curing period
4. Microstructural and mineralogical studies using SEM and XRD served as an evidence for the increase in the strength of the specimen with the increase in the curing period due to the formation of the pozzolanic compounds.

## References

1. Reddy, B. V., & Jagadish, K. (1989). Properties of soil-cement block masonry. *Masonry International*, 3(2), 80–84.
2. Ciancio, D., Beckett, C. T. S., & Carraro, J. A. H. (2014). Optimum lime content identification for lime-stabilised rammed earth. *Construction and Building Materials*, 53, 59–65.
3. Walker, P., Keable, R., Martin, J., Maniatidis, V. (2005). Rammed earth: Design and construction guidelines. BRE Bookshop Watford.
4. Jayasinghe, C., & Kamaladasa, N. (2007). Compressive strength characteristics of cement stabilized rammed earth walls. *Construction and Building Materials*, 21(11), 1971–1976.
5. Silva, R. A., Oliveira, D. V., Miranda, T., Cristelo, N., Escobar, M. C., & Soares, E. (2013). Rammed earth construction with granitic residual soils: The case study of Northern Portugal. *Construction and Building Materials*, 47, 181–191.
6. Maniatidis, V., & Walker, P. (2003). A review of rammed earth construction. Innovation Project “Developing Rammed Earth for UK Housing”, Natural Building Technology Group, Department of Architecture & Civil Engineering, University of Bath.
7. Sudhakaran, S. P., Sharma, A. K., & Kolathayar, S. (2018). Soil stabilization using bottom ash and areca fiber: Experimental investigations and reliability analysis. *Journal of Materials in Civil Engineering*, 30(8), 04018169.
8. Morsy, M. S., Alsayed, S. H., & Salloum, Y. A. (2012). Development of eco-friendly binder using metakaolin-fly ash–lime-anhydrous gypsum. *Construction and Building Materials*, 35, 772–777.
9. Sridharan, A., & Sivapullaiah, P. V. (2005). Mini compaction test apparatus for fine grained soils. *Geotechnical Testing Journal*, 28(3), 240–246.

# Geospatial-Based Coastal Risk Assessment of Gujarat Coastline



Minnu Abraham, R. S. Mahendra, Venkata Ravibabu Mandla,  
Chaithanya Sudha Merugu and Veerendra Satya Sylesh Peddinti

**Abstract** Nowadays due to the change in climatic conditions and proliferation in sea level, the coastlines are under high threat. The Gujarat coastline is studied in the current work. It is the longest coastline in India and is highly vulnerable to cyclones, earthquakes, floods, landslides, etc. These facts show the relevance of the present research. The parameters based on which the coastal vulnerability index is laid include seven physical parameters and one social parameter. The seven physical parameters are rate of shoreline change, coastal slope, coastal elevation, geomorphology, significant wave height, tidal range, sea level rise, and the social parameter is population density. The additional parameters used in this study, to increase the accuracy of the vulnerability index are coastal elevation, rise in sea level, and population density. The study is done using geospatial data and various other models and is analyzed with the help of geospatial tools. The high-resolution Cartosat DEM data is used to analyze the coastal elevation and makes this study stand out from the previous studies. Using the risk rating of each parameter, the coastal vulnerability index is prepared and it divides the coast into four zones, that is, very highly vulnerable, highly vulnerable, moderately vulnerable, and low vulnerable. According to the analysis, about 43.5% of the coastline is under highly vulnerable zone and about

---

M. Abraham

National Center for Sustainable Coastal Management (NCSCM), Ministry of Environment, Forest and Climate Change (MoEF & CC), Anna University Campus, Chennai, Tamil Nadu 600025, India

R. S. Mahendra

Indian National Center for Ocean Information Services, Hyderabad, Telangana 500090, India

V. R. Mandla (✉) · V. S. S. Peddinti

CGARD, School of Science, Technology and Knowledge Systems, National Institute of Rural Development and Panchayati Raj (NIRDPR), Hyderabad, Telangana 500030, India  
e-mail: [ravi.mandla@gmail.com](mailto:ravi.mandla@gmail.com)

C. S. Merugu

VIT University, Vellore, Tamil Nadu 632014, India

V. S. S. Peddinti

Department of Civil Engineering, National Institute of Technology Warangal, Warangal, Telangana, India

© Springer Nature Singapore Pte Ltd. 2020

S. Saride et al. (eds.), *Advances in Geotechnical and Transportation Engineering*,  
Lecture Notes in Civil Engineering 71,

[https://doi.org/10.1007/978-981-15-3662-5\\_5](https://doi.org/10.1007/978-981-15-3662-5_5)

1% is under very highly vulnerable zone. The study shows that the area under high erosion is basically tidal flats and mangroves.

**Keywords** Shoreline change · Sea level rise · Geospatial data · Cartosat DEM · Population density

## 1 Introduction

Soon the world is going to be inundated due to global warming, and the present research work has been done to be a helping hand in the mitigation programs along the coastline. The wide variations in the climate have paved a way for many natural hazards and disasters in the environment. In the present scenario, coastlines are highly vulnerable to the change in climatic conditions, due to the presence of many natural resources like coral reefs, mangroves, and dense population along the shorelines. The present study analyzes and provides coastal vulnerability index for the whole Gujarat coastline based on eight parameters. The parameters include sea level rise, shoreline change rate (till 2016), elevation, geomorphology, slope, population density, tidal range, and significant wave height. The coastal vulnerability map is needed to protect the coastline from natural hazards.

As the decades are passing, more developments are taking place near coastline, and a study of United Nations in 1992 estimates that a greater number of people live within 60 km of a shoreline. The coastlines are being a major station for the rise of many megacities [1]. In 1990, the population occupying the space in the coastal floodplain was about 200 million and it is estimated that the number of people will reach about 600 million by 2100 [2].

The recorded data of sea level rise shows that there is an enormous rise in sea level during the twentieth century; the rise is about 1–2 mm/yr [3]. From the past decades' records, it is evident that the sea level rise has reached nearly 3 mm/yr [4]. The major noticed impact of climatic change combined with global warming is the rise in sea level [5]. In the long run, the shoreline will encounter the unfavorable impact in light of erosion, inundation, weakening of water quality in estuaries and aquifers, uneven tempest surge, and serious typhoon [6].

Many works have been done to calculate the coastal vulnerability index (CVI) of the coastlines, using the parameters landforms, geology, rate of change of sea level, coastline erosion or changes, wave and tide ranges [7–13]. The CVI can be estimated by geospatial techniques. The present work is done to get a more accurate CVI for the Gujarat coast. The previous work did not consider the elevation, sea level, and any of the social factors to determine the CVI. Hence, the present study is compensating all the limitations of the previous work.

## 2 Study Area

The area studied in this work is the coastline of Gujarat (Fig. 1). Gujarat is in the northwestern part of India. Some portion of the Gulf of Kutch region is not included in the study to avoid human inaccuracies. The Gujarat state lies between a geographical extend of  $20^{\circ}10' N$ – $24^{\circ}50' N$  latitudes and  $68^{\circ}40' E$ – $74^{\circ}40' E$  longitudes. The longest coastline in India is Gujarat (around 1600 km). The state has two Gulfs, i.e., Gulf

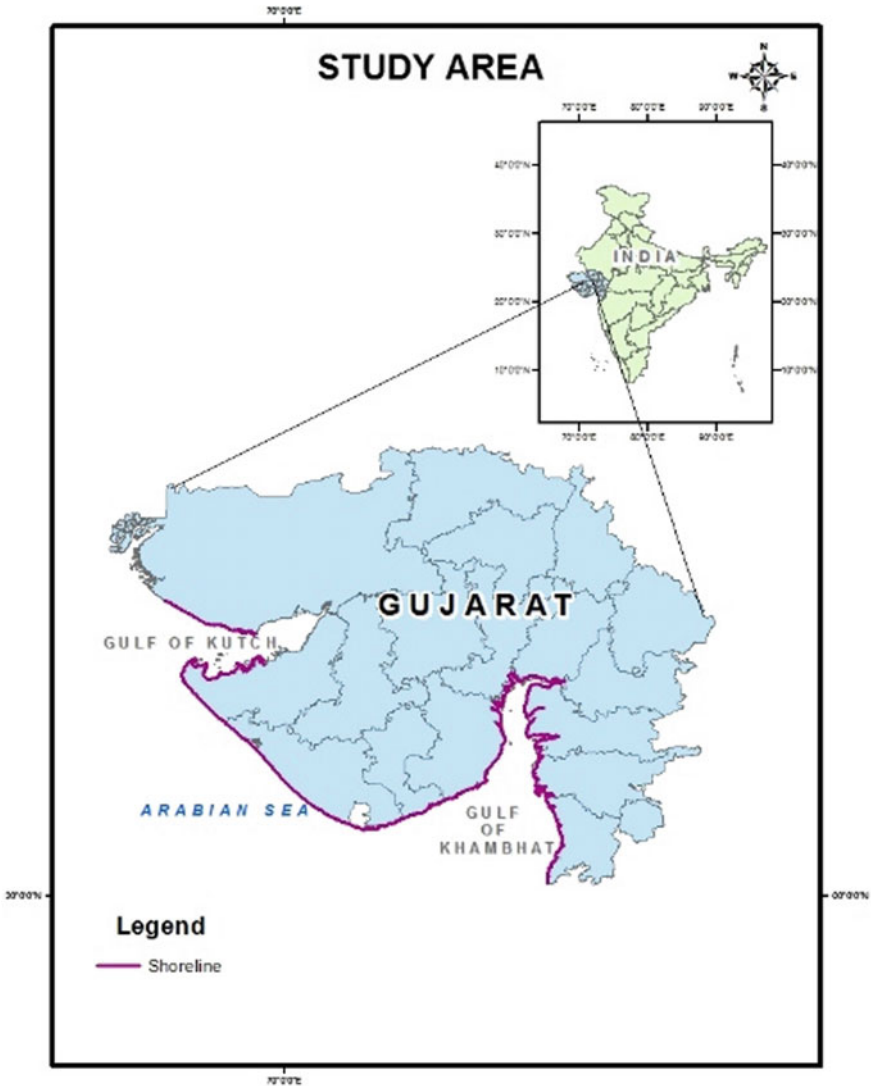


Fig. 1 Study area

of Kutch and Gulf of Khambhat. About 1300 km of the coastline is considered for this study. Some portions of Gulf of Kutch are avoided to reduce the human error. Gujarat has 16 coastal districts out of total 33 districts. Gujarat coastline has a very high variation in geomorphology and climate. Gulf of Kutch is a home to a wide variety of coral reefs and it has the first Marine National Park of India. Gujarat coastline is facing an assault of rapid urbanization and industrial development.

Two of the major ports of India are located in Gulf of Kutch, which allows the import of about 70% of India's crude oil. Gulf of Kutch also has two of the world's biggest refineries, quite a lot of blooming towns and industries, in addition to India's biggest salt industry. Gulf of Khambhat has extensive areas of tidal flats, salt marshes, and mangroves, mostly in the deltas of Mahi and Sabarmati rivers and it is one of the areas in Gujarat coastline with the largest intertidal mudflats (about 300 km). The population in the coastline is increasing by the decades.

### 3 Methodology

The risk assessment for the Gujarat coastline is done by developing a CVI index. The geospatial data are used majorly for the assessment of the CVI index and geospatial techniques are used to process the data. The parameters analyzed in the present study are the rate of change of shoreline, elevation, slope, population density, geomorphology, rate of change of sea level, tidal range, and significant wave height. The geospatial data is digitized by 1:25,000 scales. It gives more accurate results. Figure 2 shows the flowchart representing the methodology of the estimation of CVI index.

#### 3.1 *Shoreline Change Rate*

Shoreline is easily affected by the climatic changes and sea level ascent. The data is obtained from LANDSAT satellite (Table 1) and is processed using geospatial techniques and the shoreline change rate estimation is done using DSAS software, using the end point rate method (EPR). Till the latest year (2016), data is also used to get the accurate estimation for erosion rate along the Gujarat coastline. The shoreline shift for up to 4.3 decades is determined using the data. The near-infrared range of wavelength is used to analyze the data, as it is easy to distinguish land and water in that band. The permanent shoreline features were digitized along the coast associated with large tidal flats. The coastline is divided into five classes based on the EPR values, i.e., accreting area, no change area; low erosion area, moderate erosion area, and high erosion area and risk ratings are given for the coastline.

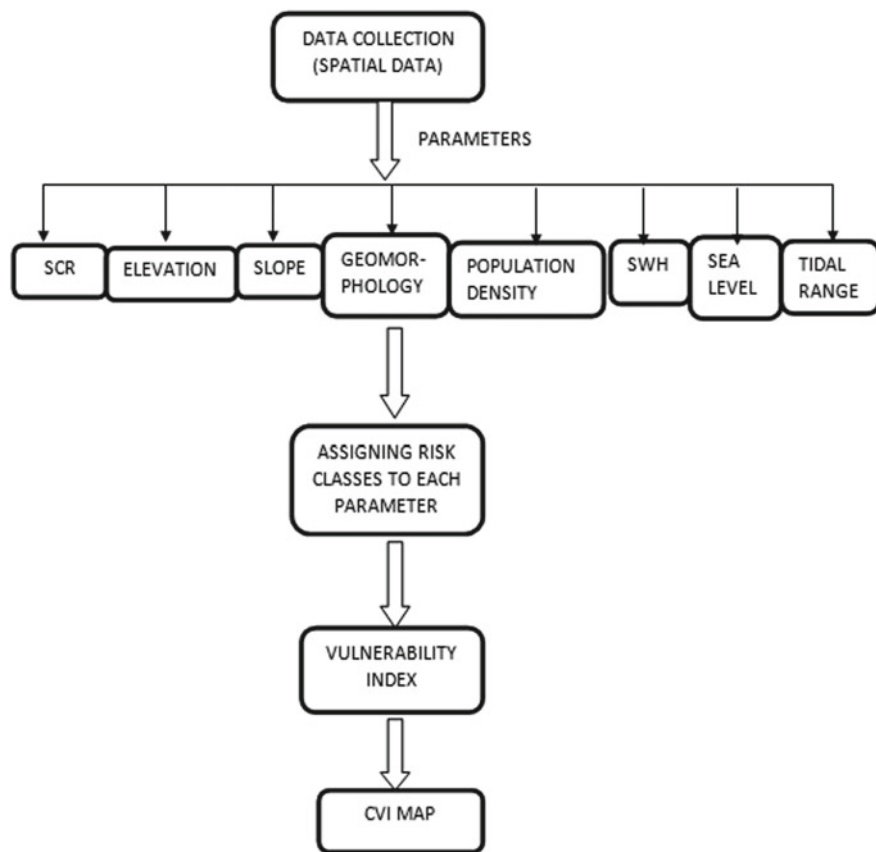


Fig. 2 Flowchart showing the methodology

Table 1 Data source of shoreline change estimation

Year	Data source	Band used
1973	LANDSAT MSS	Near IR
1991	LANDSAT TM	Near IR
2001	LANDSAT ETM	Near IR
2010	LANDSAT ETM	Near IR
2016	LANDSAT OLI	Near IR

### 3.2 Elevation

Regional elevation of the coastline is the average height of the coast above the mean sea level. Elevation is the major factor influencing the inundation of the land area

across the coastline. Data is collected from Bhuvan site. The data used is of CARTOSAT DEM images. The CARTOSAT DEM is a digital image of elevation and shows the land area of India. It is high-resolution data compared to SRTM, which is used mostly to analyze the elevation. The spatial resolution of CARTOSAT DEM is 2.5 m and its swath covers about 30 km. The data is processed using geospatial techniques. The data is mosaicked and clipped along the shoreline using the geospatial tool. The raster image is converted to points, and the elevation value is connected with the shoreline shapefile. The coastline is given the risk rating according to the fact that the area of the coastline with high elevation is less vulnerable to sea level ascent than low elevated area.

### ***3.3 Slope***

The steepness of the coastline is described using slope, and the slope is estimated in degrees in the present work. The gentle the slope, the more is the amount of inundation and shoreline erosion [17]. “General Bathymetric Chart of the Oceans (GEBCO)” data is used in the present work to estimate the regional slope of the coast. From the obtained data, the slope values are estimated using the geospatial tools. The image is clipped using the buffer and is converted to points. The values of slope from the points are given to the shoreline shapefile. Slope risk index is developed. The slope risk map is created using risk index. The slope index is given using natural break method. The coastline is divided into five classes based on the slope value.

### ***3.4 Geomorphology***

Geomorphology shows the landforms which are more prone to erosion and which can help in resisting erosion. The Gujarat coastline has a wide variety of landform. Build-up areas are also included in the analysis. The narrow beach area and marshy intertidal areas are under erosional risk at high waves. The LANDSAT data is used to analyze the geomorphology of Gujarat. The data is to be processed to categorize the geomorphological features. The geospatial tools are used to categorize the Gujarat coastline into different geomorphological classes. The risk is assigned based on the geomorphological classes. The risk index is classified based on natural break method. The map of coastal geomorphology is developed.

### ***3.5 Population Density***

Population density is the most important parameter of this study as it is the only socio-economic factor considered in the present study. Population is also included in

the economic parameter as people invest a lot of money to protect their buildings from the hazards [14–16]. The population density data is obtained from the 2011 census. The values are attached to the shoreline shapefile. And the population density risk index is given using the natural break method. The Gujarat coastline is classified into five classes based on the population risk value.

### 3.6 Significant Wave Height

The significant wave height helps to assess the area more vulnerable toward erosion, as the wave energy responsible for the sediment transportation increases with the square of significant wave height [17]. The data for the significant wave height analysis is obtained from INCOIS, Hyderabad. The entire image obtained is converted to points and then further processed to attach the values with the shoreline shapefile. The higher the value of significant wave height more will be the wave energy in that region.

### 3.7 Sea Level Changes

The main reasons for the sea level rise are the thermal expansion of the water in the sea and glacial melting. Sea level rise makes the coast more vulnerable toward storm surges and tsunamis. It affects shoreline change rate, geomorphology, and aquatic life. The data for the sea level change is obtained from NOAA Web site. The annual sea level change data is considered in the present study. The stations used are Kandla, Okha, Mumbai, and Karachi. Using the data obtained, the graph was drawn with year in *x*-axis and sea level (mm) in *y*-axis, and the annual sea level change rate is determined from the slope of the drawn graph (Table 2).

**Table 2** Data source of shoreline change estimation

Station	Latitude (radians)	Longitude (radians)	Sea level rise (mm/yr)
Kandla	23.017	70.217	2.129
Okha	22.467	69.083	1.974
Mumbai	18.917	72.833	0.795
Karachi	24.812	66.975	1.889



### 3.8 Tidal Range

The tidal range mainly relates to inundation and storm surges. Tidal range is defined as the vertical difference of high and low tide. The higher the tidal range, the more vulnerable is the coast. The data of 29 stations are considered for the analysis of tidal range. The data is obtained from the Web site of INCOIS. The data for the entire Gujarat coastline is obtained by interpolating the data using the method of kriging. The interpolated values are used to divide the coast into risk classes.

### 3.9 Coastal Vulnerability Index Calculation

The CVI can be estimated by either taking the square root of the geometric mean of the variables considered or as the sum of separately weighted parameters, based on the importance of each parameter. The coastal vulnerability index is calculated using the indices of all the parameters considered in the present study. The estimation is done using geospatial analysis tools. Equation (1) for finding the CVI for the whole coast is

$$CVI = \sqrt{\frac{(SCR \times Elevation \times Slope \times Geomorphology \times Population \times SWH \times Sealevel \times Tidalrange)}{8}} \quad (1)$$

## 4 Results and Discussions

### 4.1 Shoreline Change Rate

The present study shows that about 79 km of the 2333 km of coastline studied is under high risk of erosion. The 2333 km of the coastline is including the small creeks and estuaries. More area is under the category of accretion, i.e., about 627 and 605 km of the coast are safe with low erosion rate. The medium risk area is about 145 km. The area without any change from 4.3 decades is 877 km. The total of 3% of the coastline is highly eroding and according to geomorphological and sea level change maps of the present study, those are areas of tidal flats and mangroves with moderate sea level rise. The highly eroding portion is having erosion rate more than 10 m/yr.

### 4.2 Elevation

From the present study, it is revealed that 146 km is under very high risk and 1131 km of the Gujarat coastline is under high risk and only 5 km of the whole coastline is having very low risk class. The low risk areas are easily inundable portion of the Gujarat coastline. About 130 km is under low risk class and 921 km is under medium risk class. The districts coming under very high risk class are Valsad and Jamnagar and the very high risk region has elevation less than 9 m.

### 4.3 Slope

The present study found that 858 km of the coastline is under very high risk based on the slope parameter. Only 31 km is under very low risk class in the Gujarat coastline. Low risk portion includes about 180 km and high risk portion includes about 825 km. The medium risk area is about 438 km. Low slope area is having high vulnerability toward inundation. By analyzing the map prepared in the present study, it can be said that very low risk class is in the Bhavnagar district and except Jamnagar and Junagadh, all other districts have very high risk region (Figs. 3, 4, and 5).

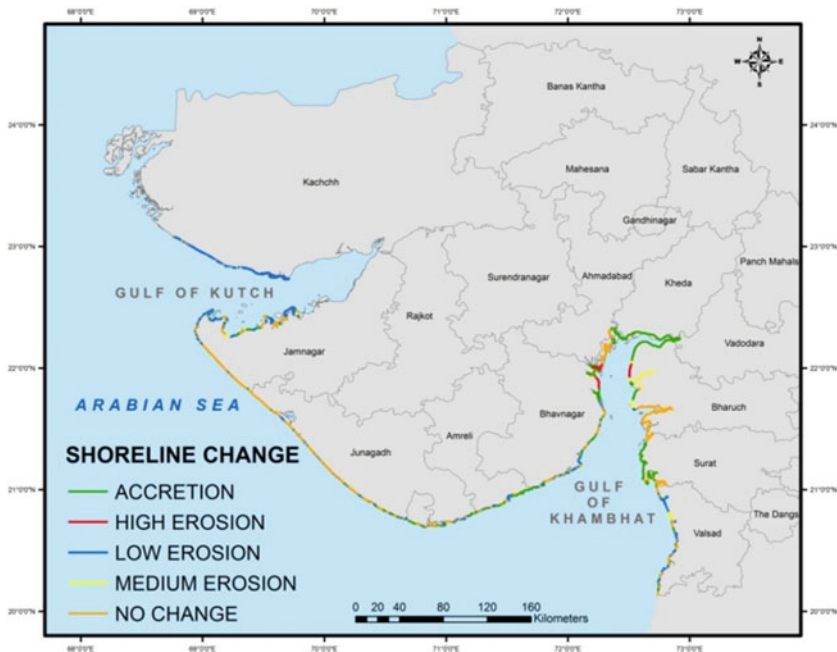


Fig. 3 SCR risk map

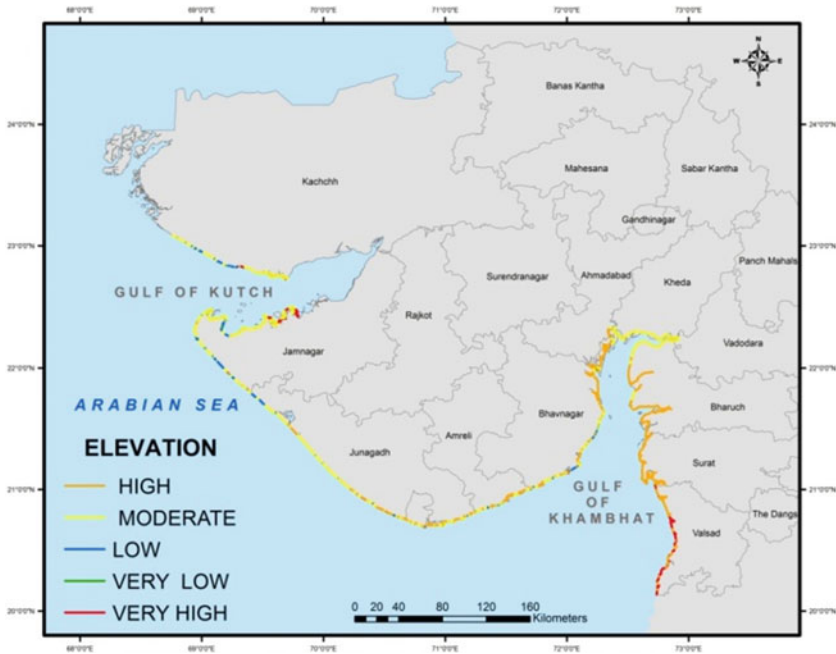


Fig. 4 Elevation risk map

#### 4.4 Geomorphology

The length of coastline under very high risk is 736 km and under very low risk is 105 km. The major portion of the coastline is under low risk, i.e., 901 km of the total Gujarat coastline. The high risk area is 149 km and moderate risk area is 441 km of the coastline. According to the study, most of the area is under very high risk class and more than 80% of Junagadh is in very high risk (Fig. 6).

#### 4.5 Population

About 240 km of the coastline is under very high risk class; i.e., Surat district is highly populated with 1376 per km<sup>2</sup> and is socioeconomically highly vulnerable toward hazards. Very low risk area is about 226 km and low risk area is 831 km of the coastline. Moderate risk area is about 730 km and high risk area is 306 km of the Gujarat coastline. Very low risk area constitutes Kachchh and the population density is 46 per km<sup>2</sup> (Fig. 7).

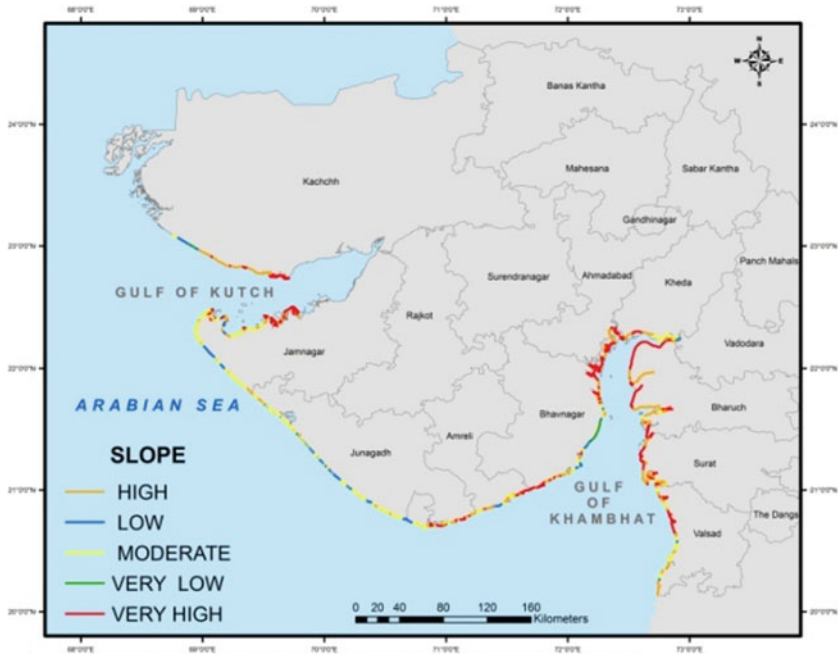


Fig. 5 Slope risk map

#### 4.6 Significant Wave Height (SWH)

Majority of the coastline is under SWH risk index 1. It comes under very low risk class and it is about 1031 km. The length of coastline under very high risk class is about 353 km and under high risk it is 80 km. The low risk stretch is 434 km and moderate risk stretch is 435 km. The highest value of SWH is 2.69. According to the map prepared using the present work, Junagadh is under very high risk based on the significant wave height value. Most of the area of Gulf of Khambhat is under very low risk.

#### 4.7 Sea Level Rise (SLR)

It is found from the present study that about 627 km of the Gujarat coastline is under low risk class and 545 km is under moderate risk class. The highest value of the sea level rise along the Gujarat coastline is 2.04 mm/yr. The stretch under high risk is 164 km, very low risk is 445 km, and very high risk is 552 km. The sea level rise along the Gulf of Kutch region is very high and this affects the geomorphology and population along that area.

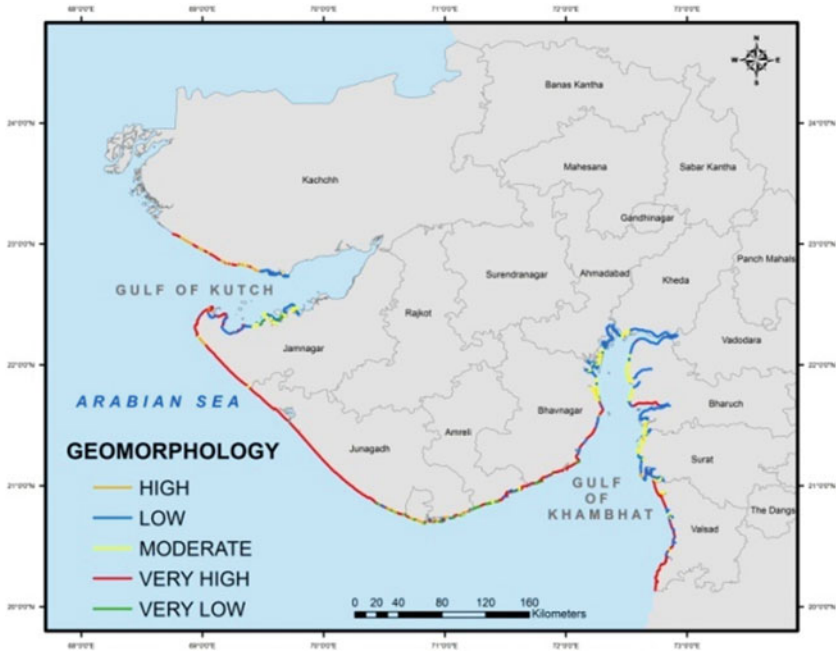


Fig. 6 Geomorphological risk map

### 4.8 Tidal Range

The coastline under very high vulnerability is about 718 km based on tidal range. The highest tidal range along the Gujarat coastline is 9.04 m and the lowest tidal range is 1.57 m. Tidal range is high along Gujarat coastline, while considering the other coastline states. Stretch of very low vulnerability is about 274 km and of low risk is 295 km. The moderate risk stretch is 405 km, and high risk stretch is 638 km (Figs. 8 and 9).

### 4.9 Coastal Vulnerability Index (CVI)

Based on the vulnerability values obtained by calculating using the equation, the coastline is divided into four classes, i.e., low, moderate, high, and very high risk class. Majority of the coastline is under high risk, i.e., about 1017 km of 2333 km is under high risk class and about 20 km is under very high risk. The very high risk region is in Valsad and it is one of the developed areas of the coastline. There are many built-ups in the very high risk region; hence, steps should be taken by the coastal zone management departments to protect those areas. The stretch under low CVI is about 428 km and moderate CVI is about 868 km (Figs. 10 and 11).

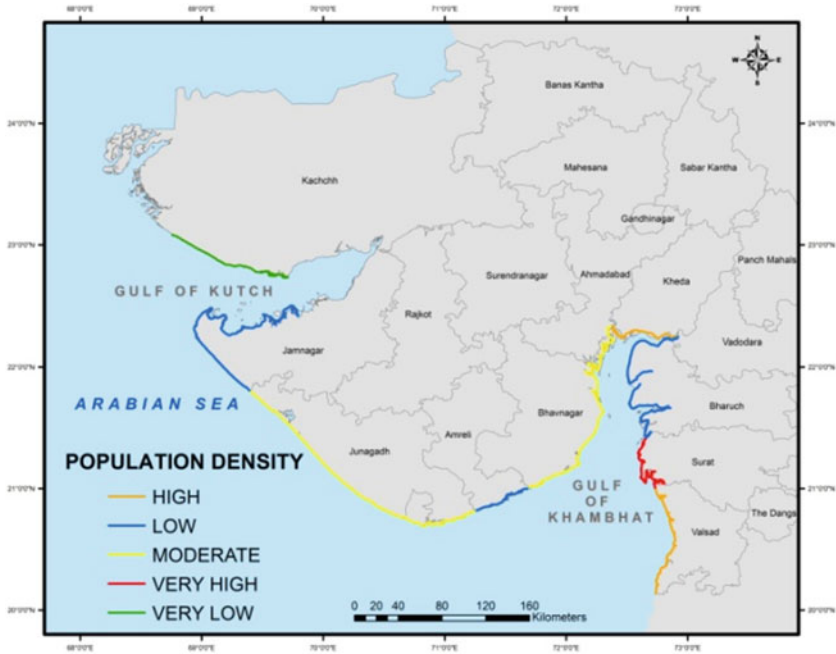


Fig. 7 Population density risk map

## 5 Conclusion

The present study found that remote sensing and GIS can be depended where field survey is not available. The spatial data can be effectively utilized to scrutinize the study area. This also saves a lot of time and money. The present work estimated the risk values for seven physical parameters and one socio-economic parameter. Table 3 shows the values of each parameter and its classification to each risk class.

Sea level rise is the main issue along Gujarat coastline; hence, there is a chance that in the future the erosion rate may increase more than 3%, which is estimated by this study. Hence, the present study is useful for the coastal zone managers as the estimation is more precise compared to the previous studies. The latest year data is used to find the shoreline change rate and also that almost 4.3 decades data (from 1973 to 2016) of the shoreline is studied. From Fig. 12, it can be seen that only 1% of the coastline is under very high risk toward natural hazards, while considering all the parameters. About 44% of the coastline is under high risk toward natural hazards. The scopes for future works are that more parameters can be utilized to determine the CVI, like storm surge and historical events. These factors are not considered in the present work.

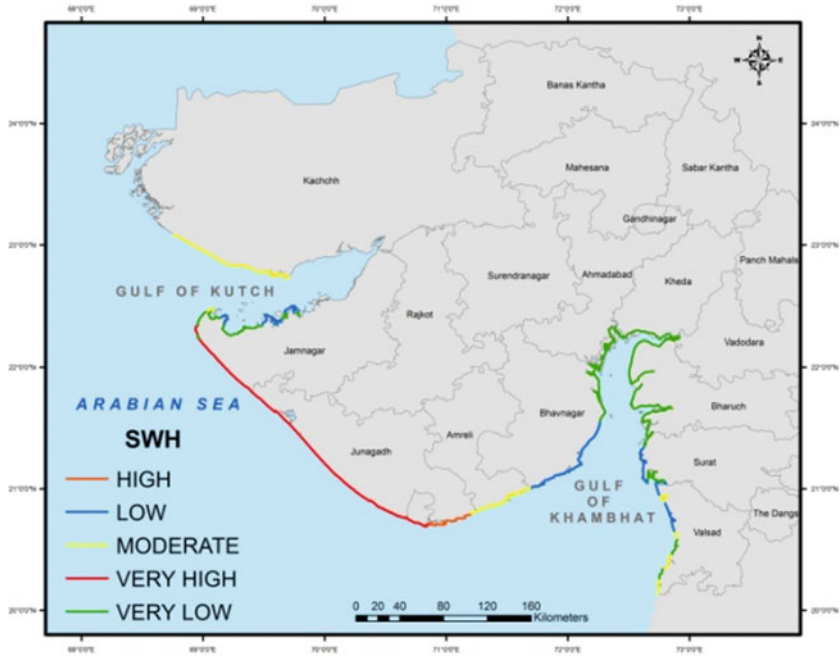


Fig. 8 SWH risk map

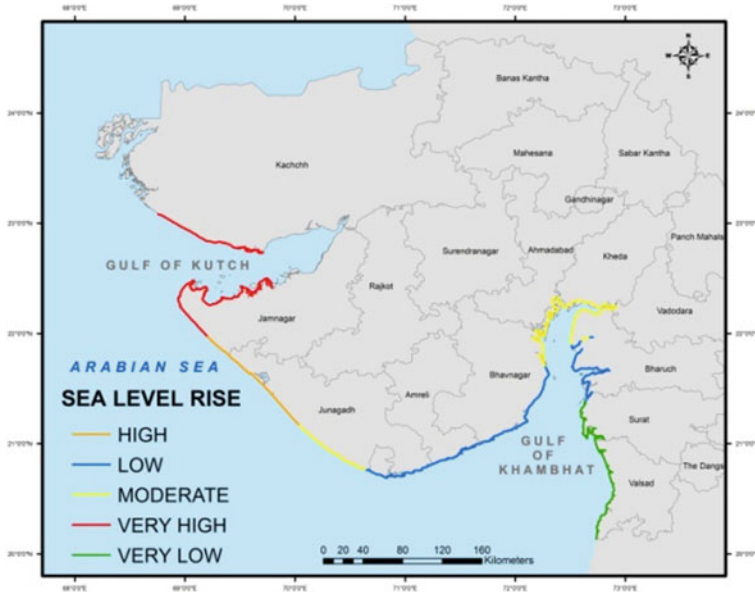


Fig. 9 Sea level rise risk map

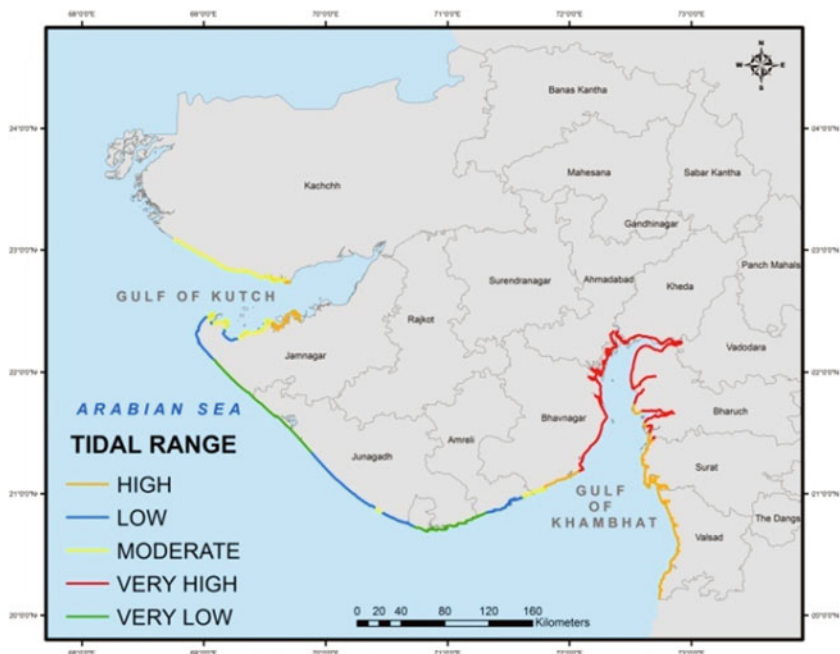


Fig. 10 Tidal range risk map

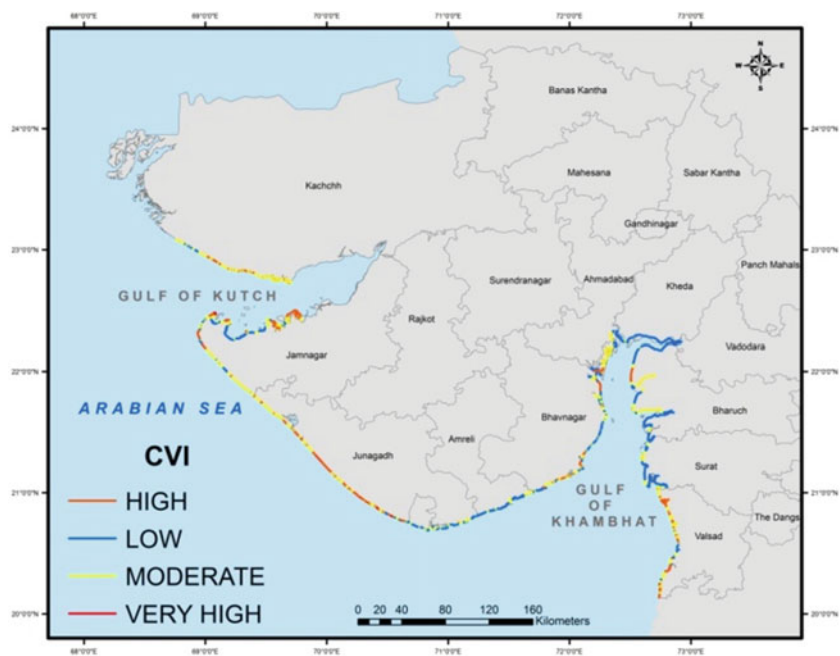


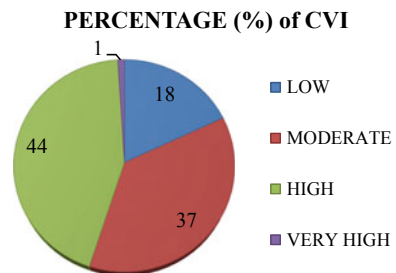
Fig. 11 CVI risk map



**Table 3** Data ranking

Parameter	Data ranking				
	Very low (1)	Low (2)	Medium (3)	High (4)	Very high (5)
Shoreline change rate (m/y)	>1 (accretion)	-1 to 1 (no change)	-1 to -5 (low erosion)	-5 to -10 (moderate erosion)	<-10 (high erosion)
Coastal slope (degree)	>0.47	0.31-0.46	0.18-0.30	0.092-0.17	0-0.091
Elevation (m)	>38	26-37	19-25	10-18	<9
Geomorphology	Rocky coasts	Mudflats/tidal flats, vegetation	Estuaries, mangroves, spit/estuary	Sea wall, wide beach	Built-ups, harbor, narrow beach
Sea level change rate (mm/y)	1.10-1.34	1.35-1.52	1.53-1.68	1.69-1.89	1.9-2.04
Mean significant wave height (m)	0-0.32	0.33-0.83	0.84-1.43	1.44-2.14	2.15-2.7
Tidal range (m)	1.56-2.50	2.51-3.32	3.33-4.53	4.54-6.48	6.49-9.04
Population density (no/km <sup>2</sup> )	0-46	47-238	239-310	311-561	562-1376

**Fig. 12** CVI risk percentage



**References**

1. Kumar, T. S., Mahendra, R. S., Nayak, S., Radhakrishnan, K., & Sahu, K. C. (2010). Coastal vulnerability assessment for Orissa state, East Coast of India. *Journal of Coastal Research*, 6, 523-534.
2. Mimura, N., & Nicholls, R. J. (1998). Regional issues raised by sea level rise and their policy implications. *Journal of Coastal Research*, 11, 5-18.
3. Yin, J., Yin, Z., Wang, J., & Xu, S. (2012). National assessment of coastal vulnerability to sea-level rise for the Chinese coast. *Journal of Coastal Conservation*, 16, 123-134.
4. Harvey, N., & Nicholls, R. (2008). Global sea-level rise and coastal vulnerability. *Sustainability Science*, 3, 5-7.

5. Allen, J. C., & Kumar, P. D. (2006). Climate controls on US west coast erosion processes. *Journal of coastal research*, 22, 511–529.
6. Islam, A., Hossain, S., & Murshed, S. (2015). Assessment of coastal vulnerability due to sea level change at Bhola island, Bangladesh: Using geospatial techniques. *Journal of the Indian Society of Remote Sensing*, 43, 625–637.
7. Gornitz, V. (1991). Global coastal hazards from future sea level rise. *Global and Planetary Change*, 89, 379–398.
8. Diez, P. G., Perillo, G. M. E., & Piccolo, M. C. (2007). Vulnerability to sea level rise on the coast of Buenos Aires province. *Journal of Coastal Research*, 23, 119–126.
9. Thieler, E. R., Hammar-Klose, E. S. (1999). National assessment of coastal vulnerability to future sea-level rise: Preliminary results for the U.S. Atlantic Coast, U.S.G.S. (pp. 99–593).
10. Pendleton, E. A., Thieler, E. R., Williams, S. J. (2004). Coastal vulnerability assessment of Cape Hettaras National Seashore (CAHA) to sea level rise, U.S.G.S. (pp. 1004–1064).
11. Rao, K. N., Subraelu, P., Rao, T. V., Malini, B. H., Ratheesh, R., Bhattacharya, S., et al. (2008). Sea-level rise and coastal vulnerability: An assessment of Andhra Pradesh coast India through remote sensing and GIS. *Journal of Coastal Conservation*, 12, 195–207.
12. Doukakis, E. (2005). Coastal vulnerability and risk parameters. *European Water*, 11, 3–7.
13. Abuodha, P., & Woodroffe, C. D. (2010). Assessing vulnerability to sea level rise using a coastal sensitivity index: A case study from southeast Australia. *Journal of coastal conservation*, 14, 189–205.
14. Dilley, R. S., & Rasid, H. (1990). Human response to coastal erosion: Thunder bay, Lake superior. *Journal of Coastal Research*, 6, 779–788.
15. Devoy, R. J. N. (1992). Questions of coastal protection and the human response to sea-level rise in Ireland and Britain. *Irish Geography*, 25, 1–22.
16. Rivas, V., Cendrero, A. (1994). Human influence in a low-hazard coastal area: An approach to risk assessment and proposal of mitigation strategies. *Journal of Coastal Research*, 289–298.
17. Mahapatra, M., Ratheesh, R., & Rajawat, A. S. (2015). Coastal vulnerability assessment of Gujarat coast to sea level rise using GIS techniques: A preliminary study. *Journal of coastal conservation*, 19, 241–256.

# Development of Speed Prediction Models for Different Categories of Roads



Teja Tallam and Bhukya Bhadru

**Abstract** Speed is one of the fundamental measures of traffic flow and level of service. It indicates the mobility of vehicle performance and quality of vehicles plying on roads. In the present scenario, due to increasing the more number of vehicles, the average stream speed of the traffic is becoming a bigger concern to traffic planners and engineers. For controlling traffic, optimizing vehicular operations and decreasing the conflicts and predicting the speeds of the vehicles under variable conditions help in better planning of the road network. In this paper, speed prediction equations were developed for different categories of roads network like National Highway (NH-44) at Kompally, State Highway (SH-6) at Gandimaisamma, arterial road at Himayath Nagar and sub-arterial road of Pragati Nagar, Hyderabad. Data was collected during peak hour with the help of the video camera. Vehicular volume and speeds were extracted for an interval of every 10 min. The vehicle speed varies with road geometry depends on different categories of roads. The percentile speed will also vary with functional characteristics of roads. The percentile speeds were calculated for all types of roads, i.e. 15th, 50th, 85th and 98th percentiles. The vehicle volumes are converted into passenger car unit (PCU) for each location. The vehicles classified into two-wheeler, three-wheeler; car, bus and light commercial vehicles. Graphs were drawn for each location by using Greenshield's model to obtain maximum speed capacity of roads. Regression technique is used to develop an equation for predicting speeds at each location.

**Keywords** Greenshield's model · Percentile speeds · Speed prediction · Different categories of roads

---

T. Tallam (✉) · B. Bhadru  
Department of Civil Engineering, VNR Vignana Jyothi Institute of Engineering and Technology,  
JNT University, Hyderabad, India  
e-mail: [tnteja@gmail.com](mailto:tnteja@gmail.com)

B. Bhadru  
e-mail: [bhanunaik295@gmail.com](mailto:bhanunaik295@gmail.com)

© Springer Nature Singapore Pte Ltd. 2020  
S. Saride et al. (eds.), *Advances in Geotechnical and Transportation Engineering*,  
Lecture Notes in Civil Engineering 71,  
[https://doi.org/10.1007/978-981-15-3662-5\\_6](https://doi.org/10.1007/978-981-15-3662-5_6)

## 1 Introduction

Speed is one of the principal proportions of traffic execution of roadway frameworks. It shows the versatility of vehicle execution on streets and nature of vehicle employing on streets. In the present situation, because of increment in the quantity of vehicles, the vehicle portability is influenced the most prompting substantial traffic issues. In the past inquires, speed was used as a fundamental parameter for evaluating the traveller vehicle unit (PCU) for different vehicles on a road. In this way, speed models have been created by analysts to work out the working velocity on a roadway. In this exploration, speed forecast of various characterizations of streets like national highway, state highway, arterial road and sub-arterial road is talked about.

The speed of the vehicles varies with different locations depends on the category of the road and functional characteristics like lane width, number of lanes, type of median, shoulder width, side walking, pedestrian facilities, etc. Generally, in national highways, the vehicles are plying with their design speed, and no restriction takes place on highways when compared with other roads. In some cases, the speed is influenced by driver behaviour, improper geometric design and heavy truck loads. In state highways, the vehicles speed is influenced by the volume of vehicles, geometric parameters like number of lanes, width of lanes, shoulder width and functional characteristics. In arterial road, speed is influenced by volume of vehicles, width of road, type of median, size of population, number of junctions, pedestrian crosswalks and un-necessary parking on roads.

## 2 Literature Review

Many researchers have focuses the study on speed prediction model, especially homogeneous traffic condition.

Donnell et al. [1] developed speed prediction model for trucks on two-lane rural highways. A series of regression model was developed using a combination of field data and simulation data. Finally, a series of regression model was developed to predict 85th percentile truck operating speeds of upstream along with down streams on horizontal curve.

Crisman et al. [2] developed speed prediction model for two-lane rural roads. They studied to overcome the problem of decreasing accident rates at horizontal curves for the previous research.

Abbas et al. [3] presented the empirical research and empirical model to predict the 85th percentile operating speed models for the horizontal curves on two-lane rural highway condition and they developed multiple linear regressions to predict the 85th percentile speed of vehicles on horizontal curves in two-lane rural highways.

Dhamaniya and Chandra [4] proposed that speed information might possibly pursue the typical conveyance relying on the extent of moderately slower vehicles

like three-wheelers in the rush hour in traffic stream. They introduced a new term called speed spread ratio (SSR) for predictor of normality in the speed data.

Dhamaniya and Chandra [5] developed the equations for relating speed with density of individual category of vehicles. These equations are then analyzed for the composition of traffic stream for fixed values of traffic volumes and for varying volumes levels at fixed traffic composition. As the solution is based on iterative process, a mathematical program has been developed in MATLAB software to solve this equation.

Razzaq [6] developed a model to predict free-flow speed for multi-lane highways and created a model for evaluating normal free-flow speed and for recognizing the appropriation of individual free-flow speed.

### 3 Objectives

The main objectives of the study are

1. To analyze the variation of 15th, 50th, 85th and 98th percentile speeds for different types of roads.
2. To predict speeds in different classifications of the roads like national highway, state highway, arterial road and sub-arterial road.

### 4 Methodology

The methodology adopted in this study is shown in Fig. 1.

### 5 Study Locations

Four locations were selected for this research involving various categories of roads like National Highway (NH-44), State Highway (SH-6), arterial road and sub-arterial roads are shown in figures (Figs. 2, 3, 4 and 5).

Video recording method was done for capturing traffic flow and its volume at peak hour for each. Each individual vehicular volume (2w, 3w, car, bus, LCV) and speed was extracted from the videos for an interval of every 10 min.

**Fig. 1** Methodology adopted for the present research

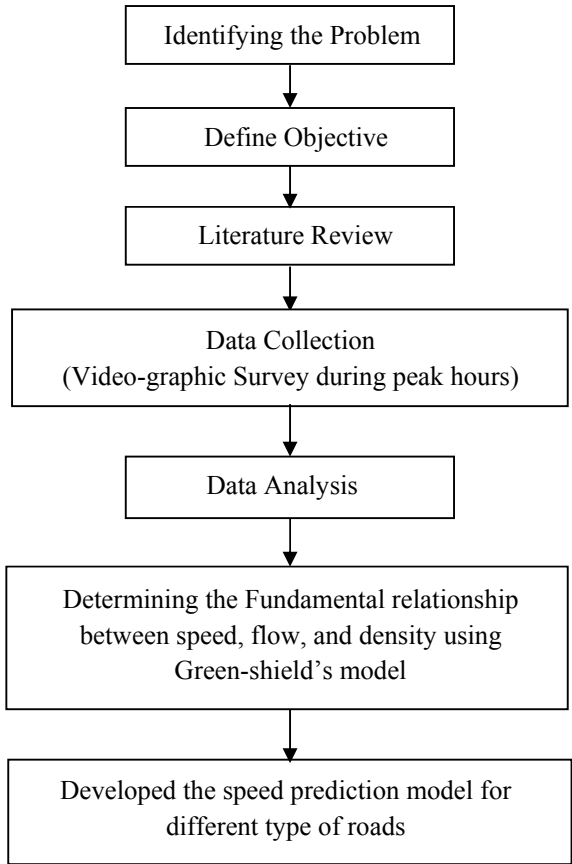


**Fig. 2** Kompally (NH-44)



**Fig. 3** Gandimaisamma  
(SH-6)



**Fig. 5** Himayath Nagar  
(arterial road)

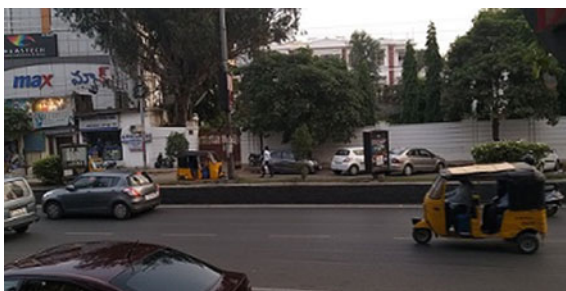


**Fig. 4** Pragati Nagar  
(sub-arterial road)



## 6 Data Analysis

A cumulative frequency curve is being plotted between speeds and percentage of vehicles for each location to obtain variation of speeds and is shown in Table 1.

From the table, it can be observed that design speeds (98th) are higher for NH, followed by sub-arterial road instead of arterial road due to higher vehicular volume on arterial roads.

**Table 1** Percentile speeds for each location

Type of speed	National highway (NH-44 Kompally) (kmph)	State highway (SH-6 Gandimaisamma) (kmph)	Arterial road (Himayath Nagar) (kmph)	Sub-arterial road (Pragati Nagar) (kmph)
98th percentile	80	35	45	59
85th percentile	58	29	31	44
50th percentile	42	21	22	32
15th percentile	30	16	16	26

Also, to understand the relation between category of road and maximum vehicular speeds, graphs were plotted between vehicular speed and density and are shown (Figs. 6, 7, 8 and 9).

Using Greenshield’s Eq. (1), free-flow speed ( $V_f$ ) and jam density ( $K_j$ ) were calculated for all the locations and are shown in Table 2.

$$v = V_f - (V_f / K_j)k \tag{1}$$

**Fig. 6** Speed versus density for NH

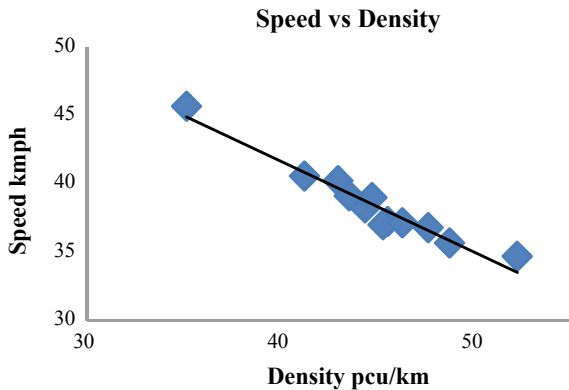


**Fig. 7** Speed versus density for SH

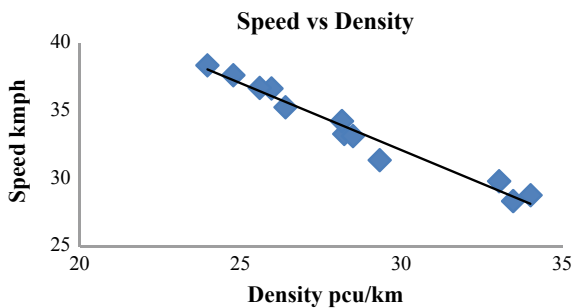




**Fig. 8** Speed versus density for arterial road

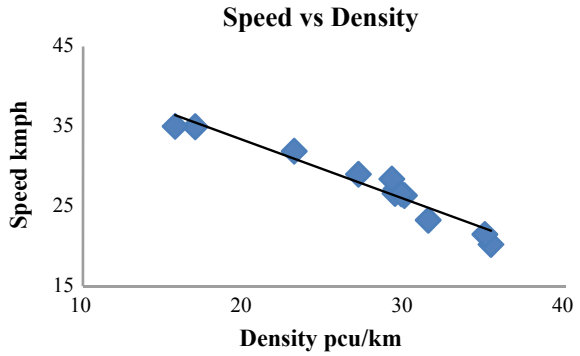


**Fig. 9** Speed versus density for sub-arterial road

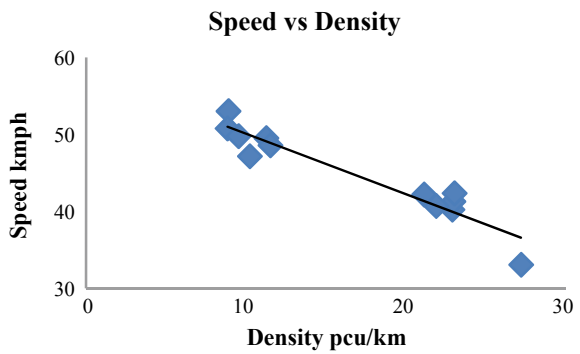


**Table 2** Free-flow speed and jam density

Type of road	Free-flow speed ( $V_f$ ) (kmph)	Jam density ( $K_j$ ) (veh/km)
National highway	68.39	102.21
State highway	45.70	62.47
Arterial road	47.98	61.21
Sub-arterial road	57.93	73.89

where

- $V$  = mean vehicular speed in kmph
- $K$  = vehicular density in veh/km
- $V_f$  = free-flow speed in kmph
- $K_j$  = jam density in veh/km

Based on above data, the speed prediction models were developed for four locations, i.e. National Highway (NH-44), State Highway (SH-6), arterial road and sub-arterial road. The classification of vehicles and their individual volumes ( $X$ ) were considered as speed predicting ( $Y$ ) variables of this research. The speed prediction equations obtained using regression technique are shown in the below equations.

For national highway

$$Y = 73.36899 - 2W (0.06856) - 3W (0.11931) - \text{Car} (0.09371) - \text{Bus} (0.37164) - \text{LCV} (0.18644) \{ R^2 = 0.925 \} \quad (2)$$

For state highway

$$Y = 58.54719 - 2W (0.11143) - 3W (0.15076) - \text{Car} (0.25703) - \text{Bus} (0.26644) - \text{LCV} (0.35085) \{ R^2 = 0.951 \} \quad (3)$$

For arterial road

$$Y = 48.11562 - 2W (0.09134) - 3W (0.1459) - \text{Car} (0.08444) - \text{Bus} (0.60622) - \text{LCV} (0.31714) \{ R^2 = 0.913 \} \quad (4)$$

For sub-arterial road

$$Y = 61.72965 - 2W (0.09554) - 3W (0.17866) - \text{Car} (0.11342) - \text{Bus} (1.04777) - \text{LCV} (0.046675) \{ R^2 = 0.932 \} \quad (5)$$

The equation can be used for predicting the average vehicular speeds for the respective category of road.

## 7 Conclusion and Discussion

From the collected speed data, *S*-curves were drawn between vehicular speeds and % of cumulative frequencies, from that the percentile speeds of 15th, 50th, 85th and 98th speed for different types of roads were obtained.

Based on extracted data of vehicular speed, density and flow from four locations, the graphs were generated using the Greenshield's Eq. (1) to predict free-flow speeds and jam densities.

Based on individual vehicular volumes at each location, using multi-linear regression technique equations were developed to predict the average vehicular speeds. Their  $R^2$  values for predicted speed equations for national highway ( $R^2 = 0.925$ ), for state highway ( $R^2 = 0.951$ ), for arterial road ( $R^2 = 0.913$ ) and for sub-arterial road ( $R^2 = 0.932$ ). This means  $R^2$  values were best fit for all the above equations which are more than 90% of accuracy.

## References

1. Donnell, E. T., NI, Y., Adolini, M., & Elefteriadou, L. (2001). Speed prediction models for trucks on two-lane rural highways. *Transportation Research Record, 1751*, 44–55. Transportation research board, Washington, D.C.
2. Crisman, B., Marchionna, A., Perco, P., & Roberti, R. (2004). Operating speed prediction model for two lane-rural roads. In *Proceedings of the SIV International Conference*. Florence, Italy.
3. Abbas, S. K. S., Adnan, M. A., & Endut, I. R. (2011). Exploration of 85th percentile operating speed model on horizontal curve: A case study of two-lane rural highways. *6th International Symposium on Highway Capacity and Quality of Service*, Stockholm, Sweden.
4. Dhamaniya, A., & Chandra, S. (2013). Speed characteristics of mixed traffic flow on urban arterials. *World Academy of Science, Engineering Technology International Journal of Civil and Environmental Engineering*, 7(11).
5. Dhamaniya, A. & Chandra, S. (2013). Speed prediction models for urban arterials under mixed traffic conditions. In *2nd Conference of Transportations Research Group of India (2nd CTRG)*. Department of Civil Engineering. Indian Institute of Technology, Roorkee-247 667, India.
6. Razzaq, A. K. (2017). *Model development to predict free flow speed for multi-lane highways*. Research & Reviews: Journal of engineering technology. Civil Engineering Department, Faculty of Engineering, University of Kufa, Iraq.

# Numerical Analysis of Liquefaction and Settlement in Layered Soils



D. Nishanth Kiran, Mohammad Muzzaffar Khan, M. Madhusudhan Reddy, K. Raja Shekar Reddy and G. Kalayan Kumar

**Abstract** Liquefaction is the phenomena when there is a loss of strength in saturated and cohesionless soil because of increased pore water pressures and hence effective stress is reduced due to the dynamic loading. Liquefaction may cause failure of foundations, resulting in the collapse of the structure. Liquefaction depends on the characteristics of subsurface soil. Study area considered was Amaravati, de facto capital city of the Indian state of Andhra Pradesh. It is essential to evaluate the liquefaction potential and settlement analysis of the soil as the constructions are on the rise in the new capital area. Based on the borehole data collected from the study area, it is seen that the soil profile consists of the sandy layers sandwiched between two silty clay layers in many of the boreholes up to 15 m depth. In the present study, Idriss and Boulanger method (new criteria for distinguishing between silts and clays that are susceptible to liquefaction versus cyclic failure. 2005, [1]) was used and the analysis carried out by using LiqIT software. It was found from the present study that the range for the factor of safety against liquefaction is varying from 1.5 to 5.0 in few boreholes. Based on the results, the soils are not susceptible to liquefaction, and the settlements are within the permissible limits.

**Keywords** Liquefaction · Idriss and Boulanger method · Settlement · Factor of safety

---

D. N. Kiran · M. M. Khan (✉) · G. K. Kumar  
Department of Civil Engineering, National Institute of Technology Warangal, Warangal,  
Telangana 506004, India  
e-mail: [mdkhan27@gmail.com](mailto:mdkhan27@gmail.com)

G. K. Kumar  
e-mail: [kalyan@nitw.ac.in](mailto:kalyan@nitw.ac.in)

M. M. Reddy · K. R. S. Reddy  
Department of Civil Engineering, KL University, Guntur 522502, India

© Springer Nature Singapore Pte Ltd. 2020  
S. Saride et al. (eds.), *Advances in Geotechnical and Transportation Engineering*,  
Lecture Notes in Civil Engineering 71,  
[https://doi.org/10.1007/978-981-15-3662-5\\_7](https://doi.org/10.1007/978-981-15-3662-5_7)

## 1 Introduction

The loss of ability to bear the loads by the soil underneath is due to rapid loading like that of an earthquake is liquefaction. It is more of a fact that the soil underneath acts like liquid, mathematically explained by equating total stress and pore water pressure, thereby a zero effective stress. Liquefaction is prominent in soils of mediocre density with amounts of saturation. History shows a colossal damage is transpired due to causes of liquefaction in the mode of ground settlements, landslides, etc. [2]. Assessing the effect in prior to its occurrence can render necessary actions at times of earthquake. Many instances of liquefaction are noticed right from Niigata earthquake (1964), Alaska earthquake (1964), Loma Prieta earthquake (1989), Kobe earthquake (1995), Chi-Chi earthquake (1999), Bhuj (2001) to recent Christchurch (2010) and Canterbury (2011) earthquakes. Countries like India got stretchy coastal line, with a high probability of liquefaction taking place. Also, the country got chances of over 50% susceptible to the earthquakes [3]. The Bhuj earthquake (2001) got incidents of failures due to liquefaction, causing sand boils, rail-road and highway damage. The areas that are placed near water bodies like rivers, oceans, etc., are found to be more open to liquefaction from the observations from the past earthquakes, damaging structures like bridges, retaining walls at the sites. Generally, the effect of liquefaction is observed in loose (rarely dense) cohesionless soils, as the concept of generating negative pore pressure while in shear may help dense soils. This effect of liquefaction is predominant up to a depth of 15 m based on the literature as well as observed in the history. The present study area covering the new capital region of Andhra Pradesh is predominantly having high water table, which varies from ground surface to 5 m depth at various locations, Krishna river is flowing in the middle of the proposed area, based on the seismic Zone III as per IS 1893: 2002, and based on the Geological Survey of India, seismotectonic map (2000), which shows more than 20 faults and lineaments in this region, with major thrust from Gundlakamma fault near Ongole, and Addanki-Nujiveedu fault, which is passing through the capital region. Also at present, the population is 2 million and identified as the most futuristic state capital of India, with the expectation of 3 million population in the next 5 years with major infrastructural facilities such as Government offices, high rise structures for both commercial and residential purposes and industries in this region.

By keeping in view the importance as given above, the borehole data is collected from 24 locations from various organisations and estimated the liquefaction potential based on the well-established cyclic stress approach developed by Idriss and Boulanger [1].

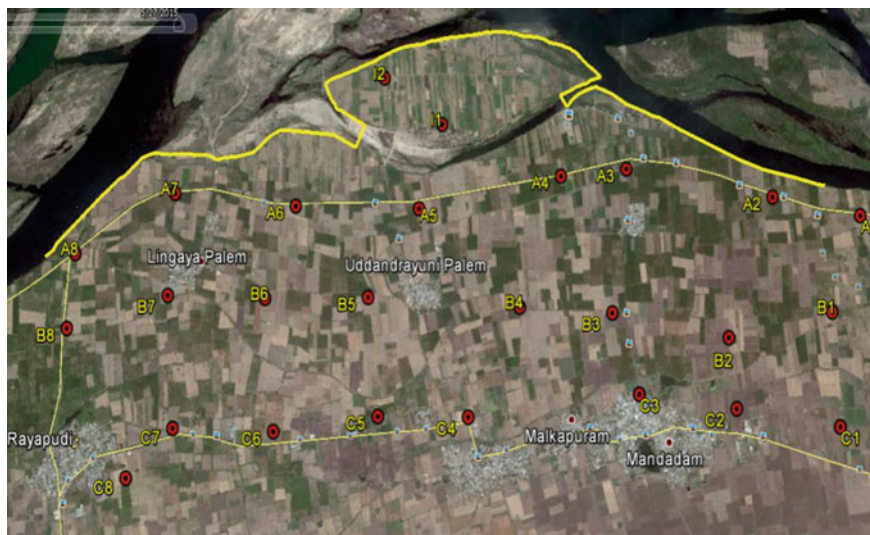


**Fig. 1** Map view of study area with borehole locations

## 2 Study Area

The study area under scope is a location having an area of 16.5 km<sup>2</sup> in the villages of Lingayapalem, Udandarayapalem, Thalayapalem in Thullurmandal of Guntur district, and map view of area is shown in Fig. 1 representing the locations of boreholes. It is located between 80°33'3.19" E, 16°31'15.03" N and 80°29'2.31" E, 16°32'37.37" N. It is the third most populous district in Andhra Pradesh. River Krishna also partly flowing in the district and there are other small rivers and channels flowing in the district. There are hills in surrounding areas and can be found forest reserves in the north-east region. Guntur will come in Zone 3 according to IS 1893 part-I (2016) makes moderate earthquake having magnitude from 4.9 to 6 Mw. For detailed estimation of liquefaction, geotechnical data is collected from SPT test conducted at the study area up to a depth of 15 m.

## 3 Geotechnical Details

In the study area, SPT test was performed at different locations as shown in Fig. 1. Bedrock was observed at 15 m depth in few locations and extended to 30 m others. Site was characterised with different soils like silty clay (residual soils), silty sand, sand (alluvial soils) and stiff clay were mostly found the in eastern side and with addition to this soil, pebbles and yellowish soft disintegrated rock can be found in the western side of the area. Undisturbed and disturbed samples were collected from

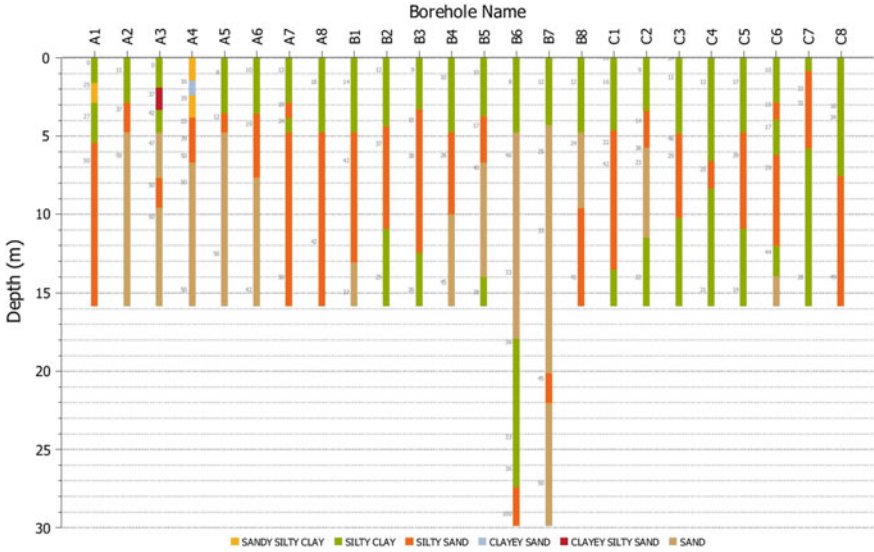


Fig. 2 SPT-N values along depth

test site and analysed in laboratory. SPT-N values for every strata of entire soil depth were given in Fig. 2. Groundwater table influences the site effects which should be considered. Water table levels are shallow having depth up to 3–4 m at all the boreholes. It infers that their location is at the upstream side of the river.

### 4 Methodology

Using SPT-based empirical formulas, the quantitative assessment of liquefaction potential for study region [4] has been carried out. From IS 1893 [5], an earthquake magnitude and the site-specific surface peak ground acceleration values are taken. The adopted methodology is illustrated in Fig. 3.

**Idriss and Boulanger approach:**

The relationship given by Idriss and Boulanger [6] for CSR caused due to earthquake ground motion is given in Eq. (1)

$$CSR_{M=7.5} = 0.65 \left( \frac{\sigma_{vo}}{\sigma'_{vo}} \right) \left( \frac{a_{max}}{g} \right) \frac{r_d}{MSF} \frac{1}{K_\sigma} \tag{1}$$

where  $a_{max}$  is the maximum horizontal acceleration at the ground surface;  $\sigma_{vo}$  and  $\sigma'_{vo}$  are total and effective overburden stress in vertical direction, respectively;

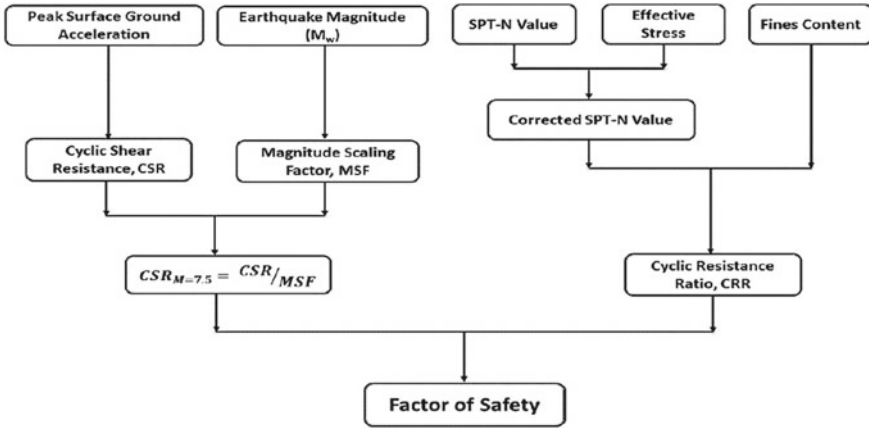


Fig. 3 Flowchart for the liquefaction analysis

MSF = magnitude scaling factor;  $r_d$  = reduction factor for depth-dependent stress; and  $K_\sigma$  = overburden correction factor (OCF).

**Coefficient of stress reduction ( $r_d$ )** is represented as a function of earthquake magnitude ( $M$ ) and depth ( $z$ ):

$$\ln(r_d) = \alpha(Z) + \beta(Z)M \tag{2}$$

$$\alpha(z) = -1.012 - 1.126 \sin\left(\frac{z}{11.73} + 5.133\right) \tag{3}$$

$$\beta(z) = 0.106 + 0.118 \sin\left(\frac{z}{11.28} + 5.142\right) \tag{4}$$

where  $M$  is earthquake magnitude;  $z$  is depth (in metre).

Equations (2), (3) and (4) were reliable if depth,  $z \leq 3$  m. Equation (5) is used if the depth,  $z > 3$  m.

$$r_d = 0.12 \exp(0.22M) \tag{5}$$

The ratio of induced CSR during an earthquake of any magnitude to that of an equivalent CSR corresponding to a magnitude of 7.5 ( $M = 7.5$ ) gives the magnitude scaling factor (MSF).

$$MSF = \left(\frac{CSR_M}{CSR_{M=7.5}}\right) \tag{6}$$

Idriss [7] modified Eq. (6) as follows:

$$MSF = 6.9 \exp\left(\frac{-M}{4}\right) - 0.058 \tag{7}$$



Boulanger and Idriss [8] found that overburden stress effects on the cyclic resistance ratio (CRR). The recommended  $K$  curves are expressed as follows:

$$K_{\sigma} = 1 - C_{\sigma} \ln\left(\frac{\sigma'_{vo}}{P_{\alpha}}\right) \leq 1.1 \quad (8)$$

The coefficient  $C_{\sigma}$  is expressed in terms of  $(N1)_{60}$

$$C_{\sigma} = \left(\frac{1}{18.9 - 2.55\sqrt{(N1)_{60}}}\right) \leq 0.3 \quad (9)$$

where  $(N1)_{60}$  is the overburden stress corrected blow count.

### Evaluation of Cyclic Resistance Ratio (CRR):

To get the CRR value, the following parameters are required.

- Percentage of fines in soil mass.
- The number of blows obtained in SPT test  $(N1)_{60}$  corrected to standard penetration resistance value  $(N1)_{60cs}$  to an equivalent clean sand.

Equation (10) for calculation of CRR for cohesionless soils having fines is given by Idriss and Boulanger [6].

$$CRR = \exp\left\{\frac{(N1)_{60cs}}{14.1} + \left(\frac{(N1)_{60cs}}{126}\right)^2 - \left(\frac{(N1)_{60cs}}{23.6}\right)^3 + \left(\frac{(N1)_{60cs}}{25.4}\right)^4 - 2.8\right\} \quad (10)$$

where

$$(N1)_{60CS} = (N1)_{60} + \Delta(N1)_{60} \quad (11)$$

$\Delta(N1)_{60}$  is the correction for per cent of fines (FC) present in the soil and is mentioned in Eqs. (12) and (13),

$$\Delta(N1)_{60} = \exp\left(1.63 + \frac{9.7}{FC} - \left(\frac{15.7}{FC}\right)^2\right) \quad (12)$$

$$(N1)_{60} = C_N(N)_{60} \quad (13)$$

$N_{60}$  is the 'N' value after correction to an equivalent 60% hammer efficiency,  $C_N$  is the OCF for penetration resistance and  $(N1)_{60}$  is the blow count corrected to overburden stress.

### Estimation of Factor of Safety ( $FS_{Liq}$ ):

Quantification of liquefaction potential can be done by using the factor of safety against liquefaction ( $FS_{Liq}$ ) which can be defined by

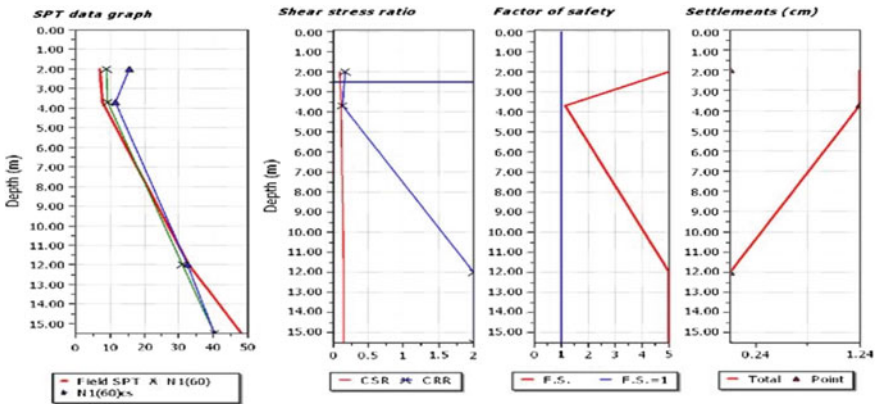
$$FS_{Liq} = \left( \frac{CRR_M}{CSR_M} \right) \tag{14}$$

During an earthquake, liquefaction can occur if CRR is less than cyclic stress ratio (CSR). Soil is susceptible to liquefaction if  $FS_{Liq} \leq 1.0$ . The higher the factor of safety, the more resistant against liquefaction. Liquefaction susceptibility has to be evaluated at the required depth in the soil mass, as the CSR and CRR will vary with the depth of the soil bed.

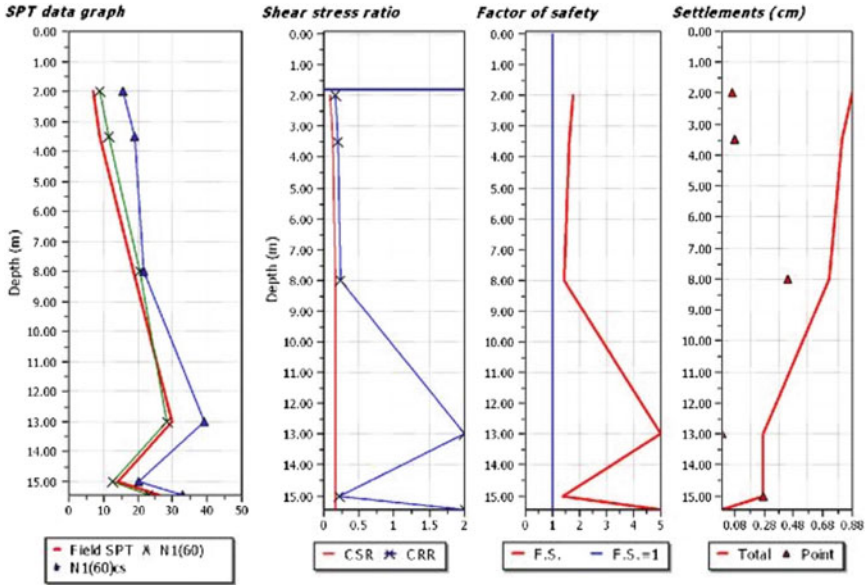
### 5 Results and Discussions

The seismic moment magnitude scale ( $M_w$ ) and peak ground surface acceleration (PGA) values are the essential seismic input parameter in the liquefaction hazard analysis. In this study, Chamoli earthquake of magnitude 5.4 is taken. PGA at surface was taken at different boreholes by ground response analysis using DEEPSOIL software. Liquefaction analysis was carried out in LiqIT software which gives deterministic values considering SPT-N values at different locations. From the collected bore log data, the water table is observed very high (<3 m from ground surface) in nearby areas of Krishna river. In such situations, it becomes essential to identify the liquefiable soil layers within upper 15 m strata, especially with sandy soils, which can be susceptible to liquefy in future. The following are results obtained at different boreholes in the study area.

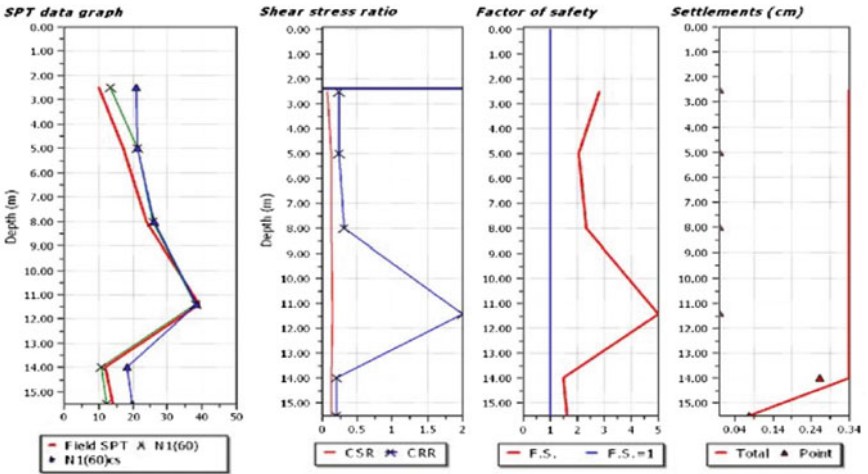
A-5 BOREHOLE:



**B-3 BOREHOLE:**



**C-5 BOREHOLE:**



From results, it is observed that factor of safety obtained is greater than 1 and it goes to 5 at greater depths indicating that soil is not probable to liquefy and the settlements obtained are 12.4 mm at A-5, 8.8 mm at B-3 and 3.4 mm at C-5 boreholes, respectively, which is in permissible limits (25 mm). Due to high SPT-N value ( $>10$ ) the sandy soil is not probable to liquefy which is observed in the soil profile of each borehole. Though, the water table is below the 2 m from surface in all the boreholes the soil is having high density to resist the earthquake vibrations against liquefaction.

## 6 Conclusions

1. Analysis of liquefaction is attempted using SPT-based method Idriss and Boulanger [4]. Liquefaction analysis at various boreholes has been prepared which show the maximum depth of liquefaction is around 15 m by using LiqIT software.
2. It is observed that the boreholes such as A-5, B-3, C-5 in three different grids of our study area are not liquefied due to high SPT-N values. Looking at the scenario of soil profile of the study area, the sites can resist the vibrations of earthquake against liquefaction.
3. Settlements at A-5, B-3, C-5 boreholes are within permissible limits (25 mm). The soils can withstand against huge deformations which indicates that structures are safe against earthquake induce settlement.

## References

1. Boulanger, R. W., & Idriss, I. M. (2005). New criteria for distinguishing between silts and clays that are susceptible to liquefaction versus cyclic failure. In *Proceedings Technologies to Enhance Dam Safety and the Environment, 25th Annual United States Society on Dams Conference* (pp. 357–366).
2. Borcherdt, R. D. (1991). On the observation, characterisation, and predictive GIS mapping of strong ground shaking for seismic zonation: A case study in the San Francisco Bay region, California. *Bulletin of the New Zealand National Society for Earthquake Engineering*, 24(4), 287–305.
3. Kolathayar, S., Sitharam, T. G., & Vipin, K. S. (2014). Probabilistic liquefaction potential evaluation for India and adjoining areas. *Indian Geotechnical Journal*, 44(3), 269–277.
4. Idriss, I. M., & Boulanger, R. W. (2010). SPT-based liquefaction triggering procedures. *Rep. UCD/CGM-10, 2*, 4–13.
5. Bureau of Indian Standards. (2002). Criteria for earthquake resistant design of structures. IS 1893(Part 1).
6. Idriss, I. M., & Boulanger, R. W. (2006). Semi-empirical procedures for evaluating liquefaction potential during earthquakes. *Soil Dynamics and Earthquake Engineering*, 26(2–4), 115–130.
7. Idriss, I. M. (1999). An update to the Seed-Idriss simplified procedure for evaluating liquefaction potential. *Proc., TRB Workshop on New Approaches to Liquefaction, Publ. n. FHWA-RD-99-165, Federal Highway Administration*.
8. Boulanger, R. W., & Idriss, I. M. (2004). State normalization of penetration resistance and the effect of overburden stress on liquefaction resistance. In *Proceedings 11th SDEE and 3rd ICEGE*. Berkeley, CA: University of California.
9. Seed, H. B., & Idriss, I. M. (1971). Simplified procedure for evaluating soil liquefaction potential. *Journal of Soil Mechanics & Foundations Div.*
10. Kramer, S. L. (2003). *Geotechnical Earthquake Engineering*. New Delhi: Pearson Education (Singapore) Private Ltd.
11. Satyam, N. D., & Towhata, I. (2016). Site-specific ground response analysis and liquefaction assessment of Vijayawada city (India). *Natural Hazards*, 81(2), 705–724.
12. Putti, S. P., & Satyam, N. (2018). Ground response analysis and liquefaction hazard assessment for Vishakhapatnam city. *Innovative Infrastructure Solutions*, 3(1), 12.
13. Rao, G. V., Subba, R., & Sai, B. U. (2018). Seismic liquefaction analysis of capital region of Andhra Pradesh State, India. *Civil Engineering Journal-stavebni Obzor*, 2.

# Evaluation of Lateral Capacity of Pile Foundation Using Finite Element Method in Layered Soil



B. K. Huchegowda, Munaga Teja and Gonavaram Kalyan Kumar

**Abstract** The behavior of the pile subjected to lateral load depends on subsoil condition, sectional properties of pile, boundary condition of pile at top and bottom, and rigidity of the structure. Early attempts have been made to understand the response of the pile subjected to lateral loads using finite difference method (FDM) to obtain non-dimensional curve. Such curves are being used for determination of ultimate horizontal capacity as well as deflection, shear force, bending moment, soil reaction, etc., under design horizontal load. In the current study, an effort was made to determine the lateral load capacity using finite element method (FEM) for pile diameter, varying from 0.15 to 2.0 m in layered soil. The performance of the pile–soil system depends on the properties of soil and pile. The results obtained from the study indicated that the lateral capacity of pile foundation depends on cross-sectional area and material of pile, boundary conditions of the pile at top and bottom, and horizontal subgrade modulus of top soil ( $6D$ , where  $D$  is diameter of pile). For an increase in the diameter of pile ( $D-2D$ ), lateral capacity of pile is increased by 2.5 times.

**Keywords** Lateral loaded pile · FEM · FDM · Pile–Soil interaction and subgrade modulus

---

B. K. Huchegowda  
Department of Civil Engineering, Indian Institute of Technology Hyderabad, Hyderabad,  
Telangana, India  
e-mail: [gowdakambaiah42@gmail.com](mailto:gowdakambaiah42@gmail.com)

M. Teja · G. Kalyan Kumar (✉)  
Department of Civil Engineering, National Institute of Technology Warangal, Warangal,  
Telangana, India  
e-mail: [kalyan@nitw.ac.in](mailto:kalyan@nitw.ac.in)

M. Teja  
e-mail: [mteja@student.nitw.ac.in](mailto:mteja@student.nitw.ac.in)

© Springer Nature Singapore Pte Ltd. 2020  
S. Saride et al. (eds.), *Advances in Geotechnical and Transportation Engineering*,  
Lecture Notes in Civil Engineering 71,  
[https://doi.org/10.1007/978-981-15-3662-5\\_8](https://doi.org/10.1007/978-981-15-3662-5_8)

# 1 Introduction

## 1.1 General

Piles are used to transfer loads (vertical and lateral loads) to the surrounding soil when poor soil is encountered at shallow depth. Piles are used to support high-rise buildings, television and communication towers, tall chimneys, offshore structures, etc., and are subjected to lateral loads. These pile groups resist considerable magnitude of vertical and lateral movements. A major concern for engineering is not only finding the lateral capacity but also to check the magnitude and depth of occurrence of maximum bending moment. In case of soft clay deposits, deflection will be large which can cause structural damage to foundation and superstructure, so it is essential to restrict lateral movement.

Several theories were proposed by investigators stating the behavior of piles subjected to lateral loads. Generalized solutions were proposed earlier for laterally loaded vertical piles [1]. The combined effect of lateral and vertical loads was evaluated in terms of non-dimensional parameters by Davisson [2]. Different approaches were proposed by several researchers [3–5] for solving the problem of laterally loaded piles. Brom's method is based primarily on limiting values of soil resistance. Poulos and Davis method [5] is based on the theory of elasticity. These methods are applicable to only uniform layer of soil. In this study, an attempt was made to determine the lateral behavior of pile in layered soil. Numerical solutions to analyze the behavior of a laterally loaded pile in two layered soil were proposed by Yang and Jeremić [6] and Yang and Liang [7] using a variational approach.

## 1.2 Finite Element Method

PLAXIS 3D Foundation is FEM modeling software used for 3D analysis of deep foundations like piles and pile–rafts. Foundations form the interaction between the upper structure and the soil on which they are constructed. In case of pile–rafts, interaction between pile, raft, and soil plays major role in determining the settlement. In these cases where interaction plays major role, three-dimensional finite element calculations are essential to account for soil behavior and soil–structure interaction.

The dimensions of the model are chosen based on recommendations of Kim and Jeong [8]. Hence, a model of width  $22D$  and height  $1.7L$  is chosen, where  $D$  is diameter and  $L$  is length of the model pile. These dimensions were considered adequate to eliminate the influence of boundary effects on the pile's performance. The 3D model of mesh generated for foundation is shown in Fig. 1. The mesh generation in PLAXIS 3D Foundation involves generation of 15-node wedge elements which are composed of six-node triangular faces in work planes. These elements contain six stress points which are used in calculation kernel. The model also comprises six-node

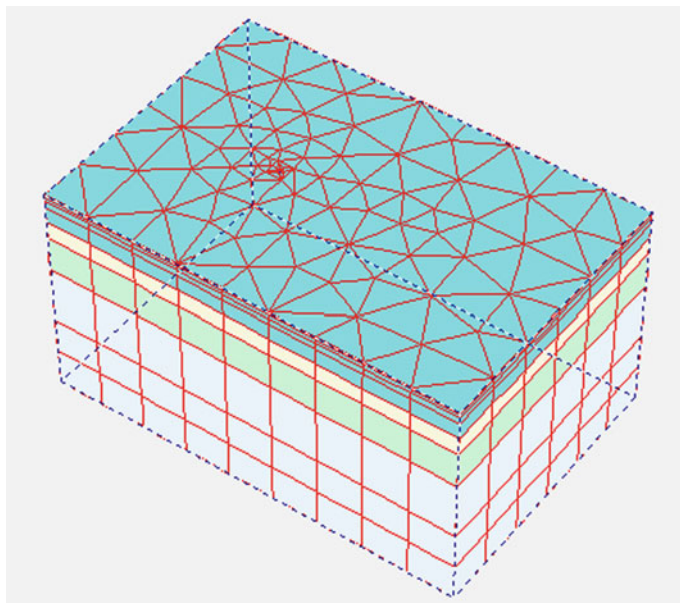


**Fig. 1** 3D mesh generated from PLAXIS 3D foundation

plate elements and 16-node interface elements to model soil–structure interaction and structural behavior of the soil–pile model.

## 2 Methodology

### 2.1 Properties of Soil and Pile

The soil strata for analysis were selected based on the borehole data. For this soil profile, lateral load carrying capacity was calculated using FEM analysis. The detailed parameters used in layered soil are given in Table 1. The length of the concrete pile

**Table 1** Properties of layered soil

Depth (m)	Soil type	Safe bearing capacity (kPa)	Modulus of soil (kPa)	Poisson's ratio	$K_h$ (kN/m <sup>3</sup> )
0.00–1.70	Clay	90	11,000	0.45	12,000
1.70–3.00	Sand	SPT = 24	36,000	0.35	40,000
3.00–5.70	Clay	210	21,000	0.45	24,000
5.70–15.45	Sand	SPT = 45–50	60,000	0.35	70,000

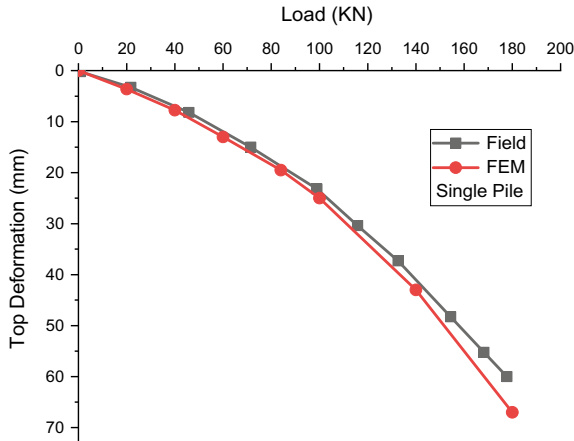


**Fig. 2** Load versus top deformation of the pile

used in this analysis is considered as 10 m with a diameter varying from 0.15 to 2.0 m with an elastic modulus of  $22.5 \times 10^6$  kPa. Free-head pile is used in this analysis.

## 2.2 Validation

The FEM was validated using the available field test data [8]. The variation of load with lateral deformation is given in Fig. 2. Lateral capacity was measured corresponding to 12-mm settlement. The results indicated that up to 30 mm deformation, the deviation of FEM analysis with field results is found to be negligible. It indicates that PLAXIS 3D Foundation results are in good agreement with the results of field test.

## 3 Results and Analysis

Pile was modeled in PLAXIS 3D Foundation, and load was applied 0.3 m above the ground surface. The lateral capacity of single pile was determined corresponding to a pile head deflection of 12 mm by varying the diameter of pile. It is observed that with an increase in the diameter of the pile, load carrying capacity increases. However, increase in the length of flexible pile resulted in no change in the lateral load capacity. The variation of lateral load with deflection for different diameters of pile is given in Fig. 3. From these curves, it can be observed that the load deflection curve is initially linear and further increase in the load leads to rapid increase in the pile head deflection.



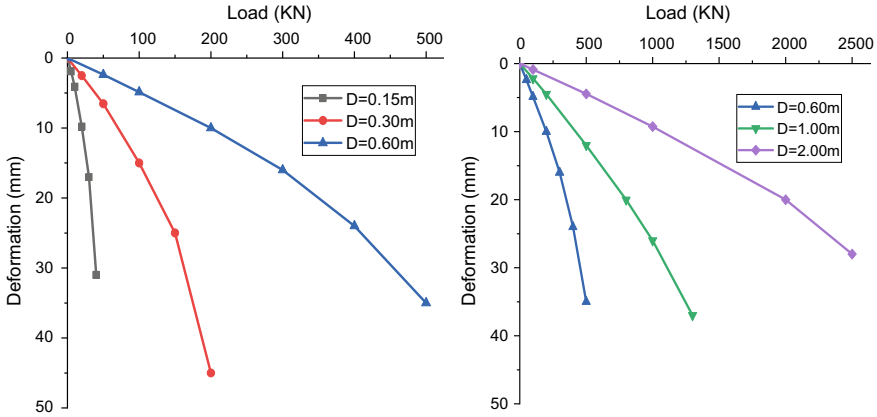


**Fig. 3** Load versus pile head deformation at ground level for different diameters of pile

It is also evident that pile head deflection is dependent on the properties of top layer of soil up to a depth of  $6D$  ( $D$  is diameter of the pile). Further increase in the length of the pile lead to little or no change in the pile head deflection. Figure 4 shows the difference between the flexible behavior and rigid behavior. The lateral load carrying capacity corresponding to 12 mm deformation was found to be 35 kN, 95 kN, 235 kN, and 1250 kN for pile diameters of 0.15 m, 0.3 m 0.6 m, 1.0 m, and 2.0 m, respectively. With an increasing in the diameter of pile by two times, the load carrying capacity increased by an average of 2.3–2.5 times.

The variation of deformation over the depth was analyzed using FEM analysis as shown in Fig. 4. It clearly shows that deformation of the pile is almost negligible beyond certain depth. Hence, it can be inferred that deformation of the pile is dependent on the top soil layer. In case of rigid pile, the load is distributed throughout the

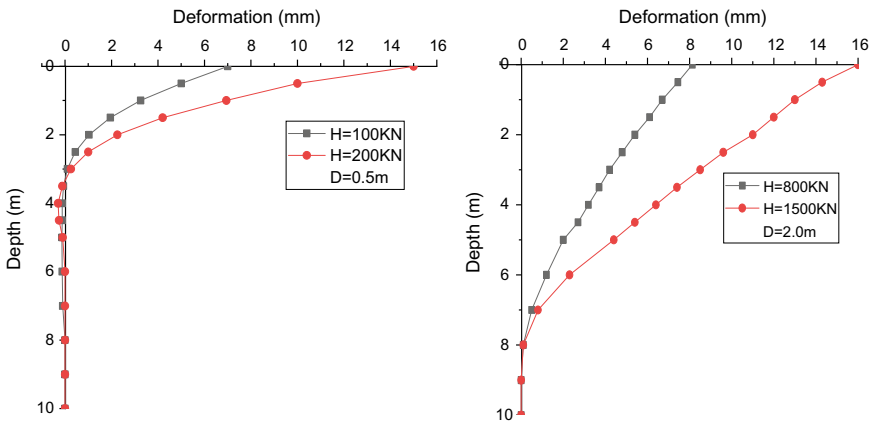


**Fig. 4** Deformation over the depth for different diameters of pile **a**  $D = 0.5$  m **b**  $D = 2.0$  m

length of pile; however, in case of flexible pile, pile reaction is limited only to the top portion. It can also be observed that the depth of occurrence of zero deformation is constant for all the loads. But, with an increase in the diameter of the pile, the depth of occurrence of zero deformation shifted downward. Hence, the depth of maximum bending moment also shifts downward.

## 4 Conclusions

In this study, finite element analysis was performed to study the behavior of laterally loaded piles in layered soil. Based on this study, the following conclusions have been drawn.

- Lateral capacity of the pile is dependent on the properties of soil up to a depth of  $6D$  ( $D$  is diameter of the pile).
- Increasing in the diameter of pile by two times increases the lateral load capacity by 2.3–2.5 times.
- For a flexible pile, increase in the length of pile leads to no change in the lateral load capacity.
- With an increase in the diameter of the pile, the depth of occurrence of zero deformation, i.e., depth of maximum bending moment, shifts downward.

## References

1. Matlock, H., & Reese, L. C. (1960). Generalized solutions for laterally loaded piles. *Journal of the Soil Mechanics and Foundations Division*, 86(5), 63–94.
2. Davisson, M. T. (1960). Behavior of flexible vertical piles subjected to moment, shear, and axial load. Doctoral dissertation, University of Illinois at Urbana-Champaign.
3. Broms, B. B. (1964). Lateral resistance of piles in cohesive soils. *Journal of the Soil Mechanics and Foundations Division*, 90(2), 27–64.
4. Broms, B. B. (1964). Lateral resistance of piles in cohesionless soils. *Journal of the Soil Mechanics and Foundations Division*, 90(3), 123–158.
5. Poulos, H. G., & Davis, E. H. (1980). Pile foundation analysis and design. Rainbow-Bridge Book Co.
6. Yang, Z., & Jeremić, B. (2002). Numerical analysis of pile behaviour under lateral loads in layered elastic-plastic soils. *International Journal for Numerical and Analytical Methods in Geomechanics*, 26(14), 1385–1406.
7. Yang, K., & Liang, R. (2006). Numerical solution for laterally loaded piles in a two-layer soil profile. *Journal of Geotechnical and Geoenvironmental Engineering*, 132(11), 1436–1443.
8. Kim, Y., & Jeong, S. (2011). Analysis of soil resistance on laterally loaded piles based on 3D soil–pile interaction. *Computers and Geotechnics*, 38(2), 248–257.

# Impact Study on Desiltation of Water Tanks in Rural Areas Using Spatial Technology: A Case Study Work Under MGNREGA



Venkata Ravibabu Mandla, Satyanarayana Prasad Nerella,  
Mithun Choudhary and Veerendra Satya Sylesh Peddinti

**Abstract** This study was conducted under the Mahatma Gandhi National Rural Employment Guarantee Scheme (MGNREGS) in Gural Mandal, Vizianagaram District, Andhra Pradesh, to identify the improvement around irrigation tanks which were desilted under this programme. In rural areas, small tanks serve as the major source for irrigation and groundwater. Improper soil management has led to a significant reduction in water tank surface spread area and depth due to the accumulation of the sedimentation process. Desiltation of these selected tanks would improve the water spread area, thus improving total volume. Remote sensing and GIS support continuous analysis of the study tanks using satellite images and Modified Normalized Difference Water Index (MNDWI) before and after desiltation work. This index has supported the seasonal water storage/spread area, crop pattern change and income level in rural villages.

**Keywords** MNDWI · MGNREGA · Desiltation · Water spread area · Remote sensing

---

V. R. Mandla (✉) · S. P. Nerella · V. S. S. Peddinti  
CGARD, School of Science, Technology and Knowledge Systems, National Institute of Rural Development and Panchayati Raj (NIRDPR), Ministry of Rural Development, Government of India, Hyderabad, Telangana 500030, India  
e-mail: [mvravibabu.nird@gov.in](mailto:mvravibabu.nird@gov.in)

S. P. Nerella  
e-mail: [nsrprasad.nird@gov.in](mailto:nsrprasad.nird@gov.in)

V. S. S. Peddinti  
e-mail: [pvssylesh.nird@gov.in](mailto:pvssylesh.nird@gov.in)

M. Choudhary  
Department of Civil Engineering, Malaviya National Institute of Technology (MNIT), Malviya Nagar, Jaipur, Rajasthan 302017, India  
e-mail: [mithun.mnit@gmail.com](mailto:mithun.mnit@gmail.com)

© Springer Nature Singapore Pte Ltd. 2020  
S. Saride et al. (eds.), *Advances in Geotechnical and Transportation Engineering*,  
Lecture Notes in Civil Engineering 71,  
[https://doi.org/10.1007/978-981-15-3662-5\\_9](https://doi.org/10.1007/978-981-15-3662-5_9)

## 1 Introduction

Monitoring small water tanks with 1–14 hectares is essential to improve agriculture in rural areas. Often these tanks are small in size but a quite large number in rural areas with the highest agriculture potential support. Landsat images with the optimal spatial resolution are suitable for small water tank surface area mapping and land cover change analysis for long-term analysis. The importance of small agriculture water tanks due to their number and geographical distribution in rural areas has gained wide importance in India due to water storage and infiltration in the form of base flow, thus improving groundwater. In Andhra Pradesh, minor tanks are traditional water storage reservoirs designed to capture monsoon run-off and store rainfall. The tanks are designed to store water, based on the seasonal and inter-annual rainfall at a particular spatial extent. The irrigation system supported by tanks exists from Vedic times [1]. The tank systems were created with indigenous technology which harvests the rainfall run-off from unpredictable monsoon with wide distribution.

The irrigation tanks contribute as a major source of water for agriculture support. These tanks are presently being monitored by local governmental authorities and departmental officers with the support of local people participation. Small irrigation tanks lose their storage capacity due to sedimentation, which results in a reduction in storage capacity and storage volume at different elevations. To improve the tank storage capacity and irrigation system, tank rehabilitation/restoration/renovation was undertaken by the water management groups. The rehabilitation is a term which is used for dysfunctional tanks which are brought to normal functioning [2]. The maintenance of irrigation tanks with a command area of 40–2000 ha is undertaken by the Minor Irrigation Department (DMI). The tanks with command area less than 40 ha are maintained by District and Panchayat Raj of villages. Identification of water surface spread area at various storage levels would help in estimating current storage and pattern of water spread in the selected irrigation tanks. Satellite remote sensing plays a vital role because of its synoptic and repetitive coverage.

Measurements from satellite remote sensing provide a means of observing and quantifying land hydrological variables over a geographic area and their temporal description. Temporal fluctuation in water tanks happens seasonally with great variation in water spread area during pre-monsoon to post-monsoon. A conventional technique helps to identify and measure these changes on a regular basis to maintain the systematic inventory. Remote sensing satellite data at multiple spatial resolutions and at regular time intervals and surface water bodies can be mapped and monitored in terms of the occurrence of water spatial extent and volume. There are many traditional image classification methods using multispectral data, namely supervised, unsupervised and pixel-based spectral indices like Modified Normalized Difference Water Index (MNDWI) to extract water bodies. These methods are effective to delineate different land classes and surface water bodies like large lakes, reservoirs, rivers, streams, etc. The automatic extraction algorithm for water body extraction using AWIFS and LISS data was developed by many researchers. Venkatesan et al. [3]

estimated surface area and volume of the small tanks using GPS field data by developing a relationship between SRTM DEM 90 m and GCP data. The small tanks with 0.2–7.8 ha area were extracted by using high-resolution imagery from Google Earth, Bing maps and Sentinel-2 to extract flooded lakes based on visual interpretation. The desiltation work was under process in the study area from 2016. Total 17 tanks work was started initially and completed by April 2017.

Changing climate and poor water harvesting techniques have resulted in a serious problem to the ecological balance, surface area and volume of water bodies in rural India. GIS and satellite images have proven to be strong investigating tools to monitor changing water distributed area for proper and effective planning of surface water resources. Landsat and Sentinel images of 30 and 20 m spatial resolution are freely available for land cover classification with frequent revisit period. This paper has been carried using Landsat images from 2010 to 2018 to provide a great possibility to understand the local water resources like tanks in Gurla Mandal. These images were used to identify water tanks using spectral indices which were more effective like MNDWI using GREEN and SWIR bands to differentiate water and land area.

## 2 Methodology

Landsat 5 and 8 images of 2010, 2011, 2015, 2016, 2017 and 2018 images were used for the MNDWI index. Study area water tanks were occupying a very small area, where images with 30 m resolution would be bigger than a tank. Hence, these images were resampled to 10 m pixel. Landsat has receptivity for every 16 days for data collection. The images with less than 20% cloud cover were selected for atmospheric correction and dark object subtraction. All objects on earth interact with incoming solar radiation thus emitting a specific wavelength of radiation back to the sensor. Landsat green (G) and shortwave infrared (SWIR) bands were used for the extraction of water pixels enabling the identification of water tanks and surface spread area. The surface water is delineated using MNDWI index Eq. (1) [4].

$$\text{MNDWI} = \frac{\rho_{\text{GREEN}} - \rho_{\text{SWIR}(2)}}{\rho_{\text{GREEN}} + \rho_{\text{SWIR}(2)}} \quad (1)$$

Modification of Normalized Difference Water Index (MNDWI) is a water index and is developed by Xu [4]. For Landsat 5,  $\text{MNDWI} = \text{Band } 2 - \text{Band } 7 / \text{Band } 2 + \text{Band } 7$ . Similarly for Landsat 8,  $\text{MNDWI} = \text{Band } 3 - \text{Band } 7 / \text{Band } 3 + \text{Band } 7$  Table 1.

**Table 1** Green and SWIR band wavelengths for Landsat 5 and 8

Band ( $\mu\text{m}$ )	Landsat 5	Landsat 8
Green	0.52–0.60	2.09–2.35
Shortwave infra red	0.53–0.59	2.10–2.29

### 3 Study Area and Data Collection

Gurla is one of the Mandal in Vizianagaram district. The total geographical area of the Mandal is 163 km<sup>2</sup>. There are 39 revenue villages consisting of 37 Grama Panchayats, and the total households in the Mandal are 15,571 with 64,695 population. The average annual rainfall of the Gurla Mandal is 1039 mm with predominantly south-west monsoon. Major crops grown in the Mandal are paddy, maize but area under mango is increasing gradually. The study area is situated in between 83° 27' 8'' and 83° 32' 00'' E longitudes, 18° 10' 35'' and 18° 16' 40'' N latitudes. The study area includes 13 Panchayats, namely Garida, Tettangi, Polayavalasa, Badaripeta, Jammu, Jammupeta, Kella, Vallapuram, Gudem, Achutapuram, Chukkapeta, Gujjangivalasa and Meesalapeta which covers 64 km<sup>2</sup> of geographical area (Fig. 1). In the study area, most of the tanks were filled with water during the monsoon season, i.e. from

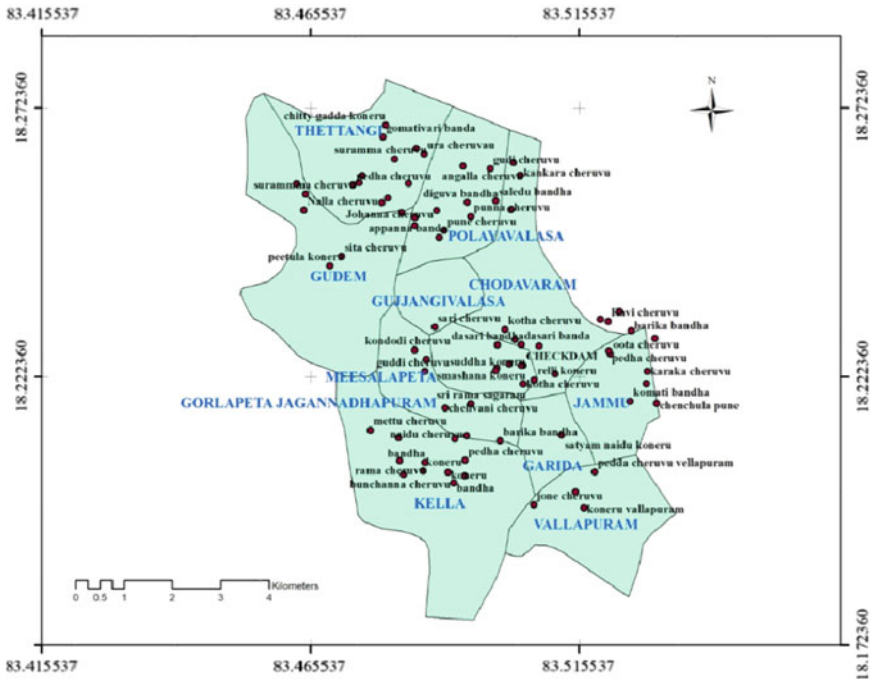


**Fig. 1** Gurla Mandal at village level map with proposed tanks for renovation work

**Table 2** Dates of Landsat images collected

2010	2011	2015	2016	2017	2018
26-Jan	13-Jan	24-Jan	11-Jan	13-Jan	16-Jan
11-Feb	29-Jan	9-Feb	12-Feb	29-Jan	1-Feb
27-Feb	14-Feb	25-Feb	15-Mar	2-Mar	5-Mar
3-Jun	2-Mar	13-Mar	31-Mar	18-Mar	21-Mar
22-Aug	6-Jun	29-Mar	16-Apr	3-Apr	6-Apr
23-Sep	26-Sep	30-Apr	2-May	19-Apr	8-May
28-Dec		23-Oct	19-Jun	5-May	9-Jun
		8-Nov	21-Jul	21-May	25-Jun
		10-Dec	7-Sep	10-Sep	29-Sep
		26-Dec	25-Oct	28-Oct	31-Oct
			10-Nov	13-Nov	16-Nov
				29-Nov	
				15-Dec	
				31-Dec	

August to November. This water supports Rabi crop which is sown in the ending of the monsoon season. Few tanks support 2–3 crops per annum. Almost all tanks fall under 40 ha catchment area. These water bodies have been observed from different sources like toposheets from a survey of India (1:50,000), memoirs of minor irrigation tank, etc., identified and digitized the tank boundaries from the topo map. Satellite images were collected for different months as shown in Table 2.

#### 4 Modification of Normalized Difference Water Index (MNDWI)

The objective of this MNDWI index is to identify the water body with existing water at different seasons and months. Total water tank boundary is taken from SOI toposheet, and the available water extent is identified with the help of MNDWI. The absorption and reflection of light between water and land use features show variation in different wavelengths. The reflection of water is very low in infrared than visible bands. The water occupied cells were automatically extracted by MNDWI. MNDWI values range between  $-1$  and  $1$ . Theoretically, these values for water regions will be larger than  $0$  in MNDWI but due to surface parameters and vegetation influence MNDWI varies for some images smaller or larger than actual range. These pixels overestimate the water tank boundaries due to residual soil moisture within the tank boundary. To avoid such type of interferences, the threshold values are adjusted manually. To get more accurate boundary of the tank spread area, visual interpretation technique of images in FCC is adopted to adjust the boundaries (Fig. 2). Total 19 tanks were

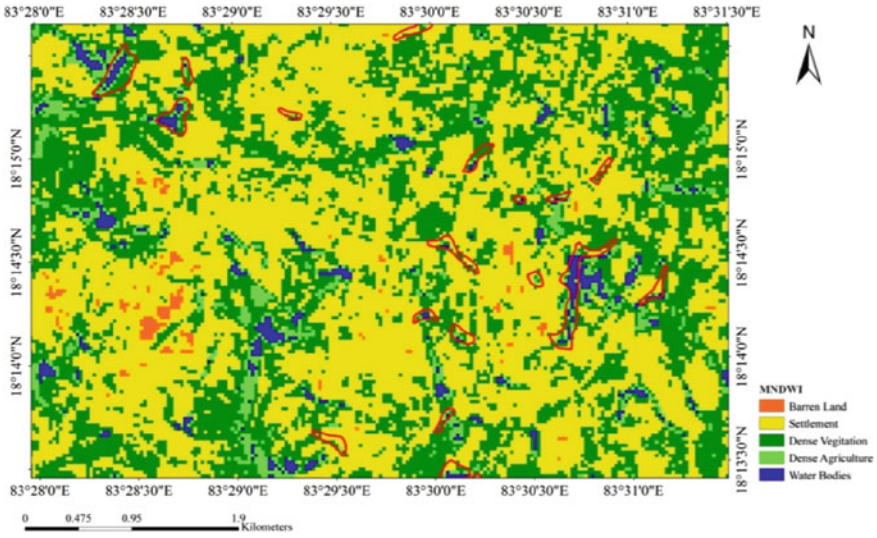


Fig. 2 MNDWI coverage of the study area with few water bodies (red shapes)

considered in this analysis of MNDWI variation for 2010, 2011, 2015, 2016, 2017 and 2018 Table 3. Rainfall data are shown in Table 4.

These tanks are explained cluster wise based on their geographical distribution and elevation. Each cluster contains three or more than three tanks.

**Cluster 1** It includes three tanks named as Komati Banda, Poonu Cheru and Vura Cheru. Komati Banda and Vura Cheru (Fig. 3) come under Chodavaram Panchyat, while Poonu Cheru comes under Garida Panchayat. The average slope of this area is 3% which is an almost flat surface with first- and second-order stream network. The annual average rainfall is 915.412 mm. Poonu Cheru and Komati Cheru have two sluice outlets, whereas Vura Cheru has four sluices to irrigate water into agriculture area. For the year 2015 and 2016, MNDWI values (Fig. 4) were between  $-0.2$  and  $+0.4$ . Lower and negative values show the absence of water during the dry season from February to June. Positive values show an increasing trend from the beginning of the monsoon season, i.e. from July to October. Poonu Cheru for 2015 and 2016 almost continues with positive values which gives an indication of sufficient water availability during the dry season. Komati Banda and Vura Cheru MNDWI values were very low till  $-0.15$  for 2015 and 2016 which further continued till 2018 reaching  $-0.2$ . After desiltation work, MNDWI values have raised between  $0.22$  and  $0.27$  during the rainy season for the three tanks Table 5.

Komati Banda shows drastic improvement from 2016 to 2018, i.e.  $0.10-0.27$ . Other two tanks also show improvement after desiltation.

**Cluster 2** It includes four tanks named as Yerra Cheru, Pilakavani Cheru, Uppada Banda and Rayi Cheru (Fig. 5). Yerra Cheru and Uppada Banda come under Achyutapuram Panchayat, and Pilakavani Cheru and Rayi Cheru come under Chodavaram



**Table 3** Tank names with associated command area and hydraulic details

Tank name	Latitude	Longitude	Catchment area (acres)	Tank water spread area (ha)	Length of tank bund (m)	Top width of tank bund (m)
Uppada Banda	18.2218008	83.5091633	18	2	210	3
Komati_Banda	18.2429733	83.5091633	12	3.2	250	3
Guddi_Cheruvu	18.2605033	83.4988317	10	6	600	3.5
Poonu_Cheru	18.2384567	83.517155	15	6	450	3
Pilakavani_Cheru	18.246315	83.509965	15	1.2	200	3
Yerra_Cheru	18.2485217	83.5027867	5	1.2	360	2.5
Laxmana_Cheru	18.2229133	83.5004133	4	1.2	650	3
Lankavane_cheruvu	18.2372767	83.499565	25.87	2.4	200	3
Jaganna_cheruvu	18.25482	83.4793233	26	2.8	685	3
Seera_Banda	18.23492	83.5024333	8.09	1.6	230	3
Pedda_Cheruvu	18.2584767	83.4741333	8	5.2	930	3
Modiavane_cheruvu	18.2236817	83.5006483	28	7.36	490	3.5
Patha_Cheruvu	18.24093	83.50271	6	1.6	510	3
Rayi_cheruvu	18.2474767	83.5136483	16	4.8	320	3
Sudha_cheruvu	18.2229133	83.5004133	2	0.1	215	2.5
Vura_Cheru	18.2406033	83.5113433	82	14.4	700	4
Dasari_Banda	18.2276667	83.49996	20	4	210	3
Seetha_Cheru	18.22766	83.50873	5	2.4	420	3
Joganna_Cheru	18.253355	83.4889217	15	4	300	3

Panchayat. The average slope of this area is 3%. Pilakavani Cheru has two, and Rayi Cheru has one sluice outlet. Yerra cheru has resulted in with least MNDWI values during February to May and the highest values in September month. Table 6 shows maximum MNDWI values in each year. Yerra cheruvu recorded the lowest value in October 2017, whereas monthly rainfall for that month was 1.4 mm. May to August months of 2018 received below average rainfall. October month shows the highest MNDWI value with 0.16 after removal of silt and encroachment. Among the four years, 2015 October recorded with lowest MNDWI value with 0.14 because October month normal rainfall is 181 mm and actually received is 33.60 mm and 2018 September with 0.19. 2016 and 2017 have shown 0.11 and 0.14. Land encroachment is identified as 3 acres occupying water surface area which has contributed increased value even though annual precipitation was below normal. Uppada Banda shows a gradual increase in values from 2016 to 2018 from 0.13 to 0.23 (Fig. 6).

**Table 4** Rainfall (mm) from 2015 to 2018 of the study area

Year	Jan	Feb	Mar	Apr	May	Jun	Jul	Aug	Sep	Oct	Nov	Dec	Annual mean
Normal	5.0	11.0	11.0	24.0	95.0	119.0	167.0	183.0	154.0	181.0	84.0	5.0	1039
2015	0.00	0.00	0.00	20.80	10.00	252.80	139.00	329.80	178.80	33.60	46.60	0.00	1011.4
2016	0	0.0	0.0	20.8	10.0	252.8	139.0	329.8	178.8	46.6	0	0	977.8
2017	0.0	0.0	0.0	0.0	162.6	166.9	188.0	168.9	339.7	1.4	0.0	0.0	1027.5
2018	0	0.0	82.2	0	40.0	123.1	70.3	-	-	-	-	-	315.6

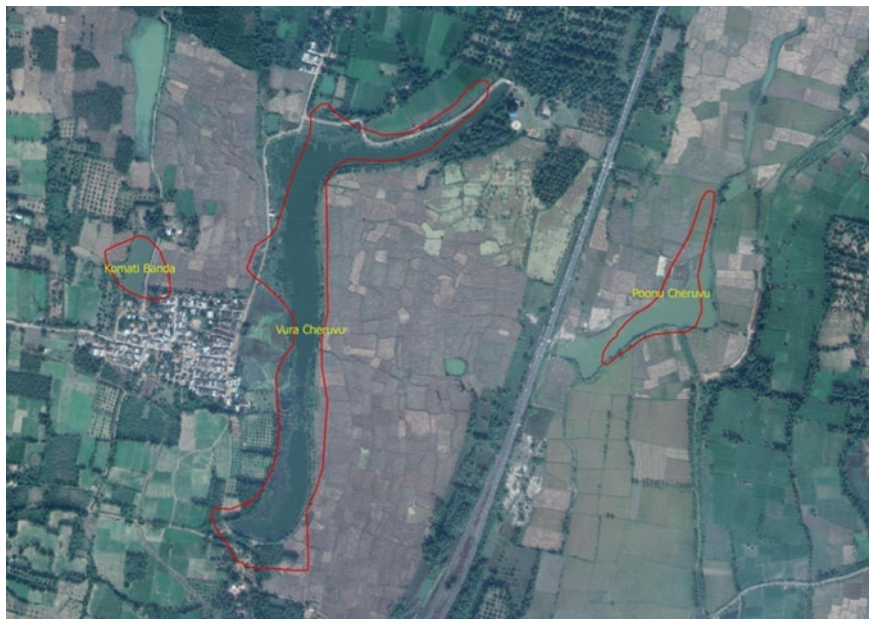


Fig. 3 Google image of Komati Banda, Vura Cheruvu and Poonu Cheruvu

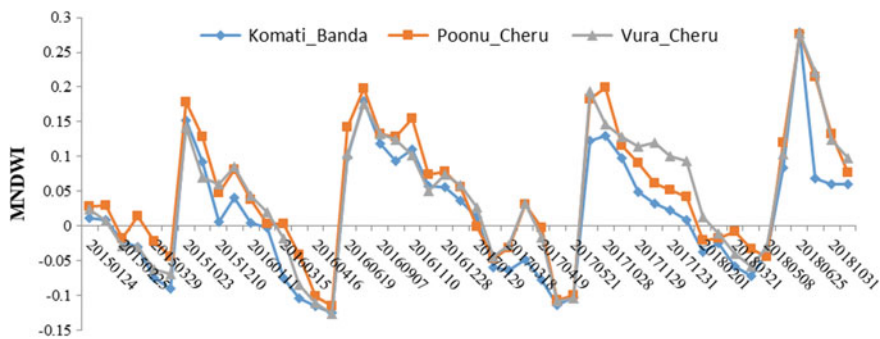


Fig. 4 Cluster 1 MNDWI values from 2015 to 2018

Table 5 MNDWI maximum values for cluster 1

Year	Komati_Banda	Poonu_Cheru	Vura_Cheru
2015	0.151351	0.178938	0.142824
2016	0.109442	0.154547	0.124111
2017	0.129212	0.198624	0.145793
2018	0.277994	0.214623	0.221091



Fig. 5 Google image of study cluster 2

Table 6 MNDWI maximum values for cluster 2

Year	Yerra_Cheru	Pilakavani_Cheru	Uppada_Banda	Rayi_cheruvu
2015	0.144105	0.141745	0.174252	0.145985
2016	0.177201	0.113043	0.131552	0.197692
2017	0.144045	0.141143	0.185383	0.197279
2018	0.162992	0.191975	0.235064	0.181184

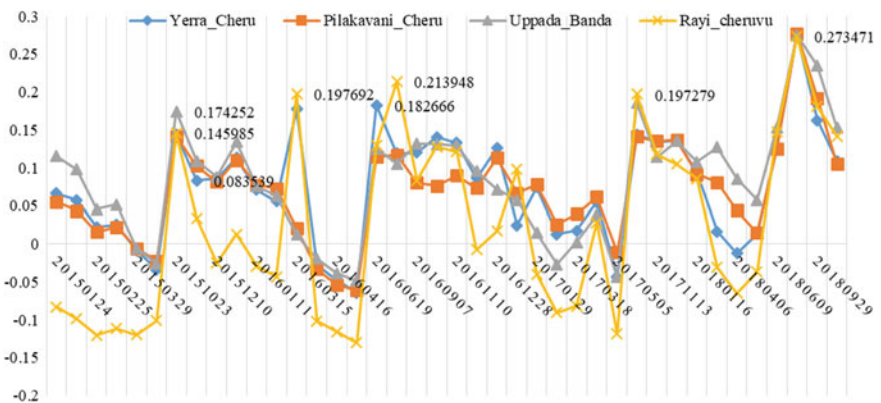


Fig. 6 Cluster 2 MNDWI values for 2015 and 2018

Desiltation significantly improved MNDWI values with 1027.5 mm rainfall in 2017 and below normal level precipitation in 2018 from the month of June onwards. Yerra Cheruvu with the least encroached area could able to maintain the same values irrespective of low annual rainfall. This can be attributed to effective groundwater recharge, proper maintenance of sluice and filling water from the upper tank connected in a cascading system

**Cluster 3** It shows three tanks, namely Patha Cheruvu, Lankavani Cheruvu and Seera Banda (Fig. 7). Three of these tanks belong to Chodavaram village, in the Gurla Mandal. Average annual rainfall is 915.12 mm. Water spread area of Patha Cheruvu and Seera Banda is 1.6 ha and Lankavani Chruvu is 2.4 ha. These tanks often suffer from weed spread above 50% of the tank surface. These tanks support single and double crops in their command area. Compared to 2010 and 2011 tank, MNDWI values show variations due to siltation. Figure 8 clearly shows that 2015 MNDWI values are comparatively lesser than 2010 which has led to shrinking of the lake in terms of depth and surface area. Table 7 gives maximum MNDWI values for all three tanks. Among them, all tanks are showing gradual improvement in values.

**Cluster 4** It includes four tanks named as Modiavane\_cheruvu, Dasari\_Banda, Sudha\_cheruvu and Seetha\_Cheru (Fig. 9). All the four tanks come under Garida Panchayat. The average slope of this area is 3%. Modiavane\_cheruvu, Dasari\_Banda and Seetha\_Cheru have three sluices outlets. Moidavani Cheruvu comes under the above medium irrigation tank with 7.36 ha with 50% weed infestation. For October



**Fig. 7** Google image of cluster 3 tanks

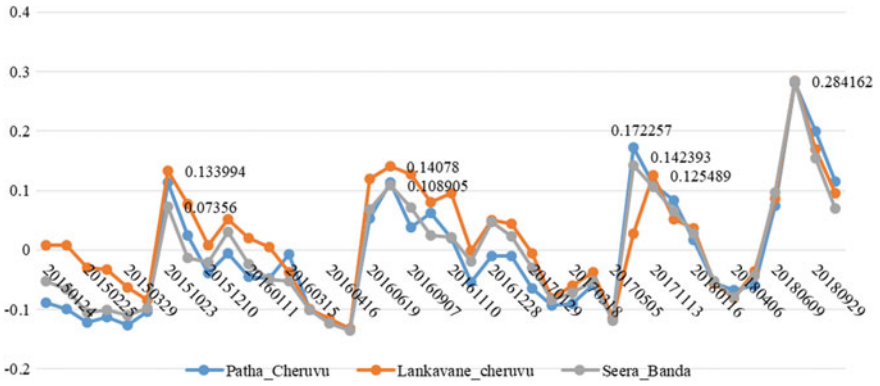


Fig. 8 MNDWI values of cluster 3 tanks for 2015–2018

Table 7 MNDWI maximum values for cluster 3

Year	Patha_Cheruvu	Lankavane_cheruvu	Seera_Banda
2015	0.114319	0.133994	0.07356
2016	0.114403	0.140781	0.108905
2017	0.172257	0.125489	0.142393
2018	0.200107	0.170119	0.153863



Fig. 9 Google image of cluster 4 tanks

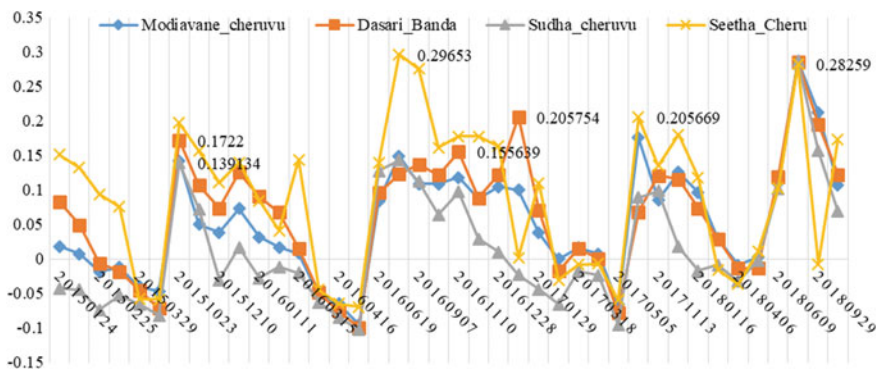


Fig. 10 Cluster 4 MNDWI variation from 2015 to 2018

Table 8 MNDWI maximum values for cluster 4 tanks

Year	Modiavane_cheruvu	Dasari_Banda	Sudha_cheruvu	Seetha_Cheru
2015	0.142681	0.172200	0.139134	0.197554
2016	0.149461	0.155639	0.143015	0.296530
2017	0.175677	0.185136	0.171618	0.205669
2018	0.287357	0.285708	0.284059	0.282410

month from 2015 to 2018, MNDWI values increase in all the four tanks like for Mo-davani Cheruvu it raised from 0.10 to 0.21 after desiltation work. It can be attributed to the removal of 3 acres of encroached land and desiltation. Dasari Banda is situated in Meesalapeta village with 12.48 acres of Ayacut area with 15 farmers cultivating this land. This tank was taken for renovation works as the reconstruction of three sluices and inlet waterway from Laxmana Cheruvu. Surplus course widening and desiltation work improved MNDWI values gradually from 2016 to 2018 (Fig. 10). Sudha Cheruvu and Seetha Cheruvu also show changed MNDWI values with tank renovation work Table 8.

**Cluster 5** It includes five tanks named as Pedda Cheru, Jaganna Cheru, Laxmana Cheru, Joganna\_Cheru and Guddi Cheru (Fig. 11). All the five tanks come under Polayavalasa Panchayat. Pedda cheruvu and Jagganna Cheruvu are relatively bigger tanks. Due to siltation of tanks, farmers could able to irrigate Ayacut area only for one month. During the rainy day, these two tanks easily get full level but not sufficient volume. Pedda Cheruvu surplus water moves into Jagganna cheruvu and Laxmanna cheruvu. Desiltation work in these tanks supports more water accumulation. Table 9 and Fig. 12 show the changing MNDWI values in all the five tanks. Removal of encroached area and silt can retain more water in monsoon season thus recharging more water into the ground level. Ayacut area farmers can irrigate through bore wells/wells during less water in tanks.



Fig. 11 Google image of cluster 4 tanks

Table 9 Year wise maximum MNDWI values in each tank

Year	Pedda_Cheruvu	Jaganna_cheruvu	Laxmana_Cheru	Joganna_Cheru	Guddi_Cheruvu
2015	0.172	0.163	0.121	0.129	0.155
2016	0.219	0.170	0.155	0.144	0.168
2017	0.225	0.152	0.189	0.182	0.190
2018	0.291	0.289	0.288	0.286	0.273

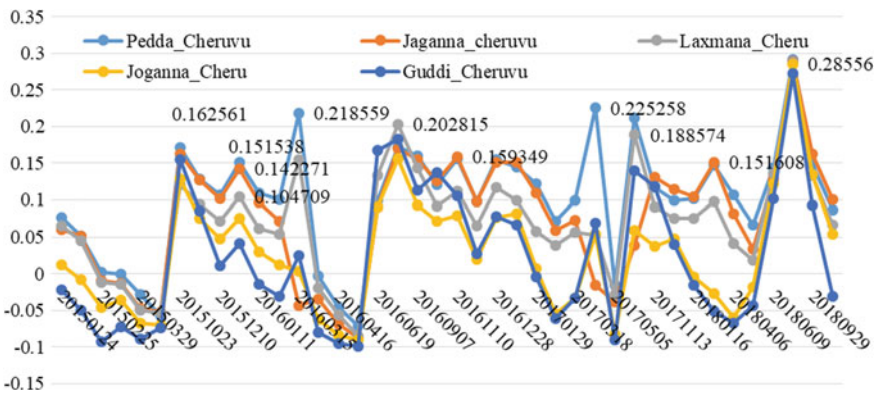


Fig. 12 Cluster 5 MNDWI variation among tanks for 2015 and 2018



## 5 Conclusions

With increasing remote sensing and geospatial technology in the recent past years made easy of monitoring land cover type and water resources. Monitoring lakes and ponds at the local and regional level requires high-quality maps accompanied by field data and ground truth. The present study has taken water tanks lesser than 20 ha which needs high-resolution data. The present study is carried out using 30 m satellite image which was resampled to 10 m with a proper atmospheric correction to improve the quality of the image. Data were collected with a low cloud cover percentage. MNDWI index functions based on the reflectance of ground features and automatically derives water pixels. This method allowed water surface separation from other surfaces.

Tanks after desiltation from 2017 onwards could be able to give high MNDWI values when compared to before desiltation period. The range of the water pixel values varied before and after desiltation which is a significant factor to prove that the depth of the lake has been improved. Almost all tanks are connected in a cascading system with one upper and one lower tank. Surplus water filling in lower tanks also resulted in varied MNDWI values in other than the rainy season. Overall desiltation work has improved water during dry season, i.e. April and May months in larger tanks. Farmers are now using this water for mango tree plantation and coconut plantation in the offshore area of the tanks. A single crop is grown in Rabi season because of sufficient water supply. Further improvement of tanks depth could assist the second crop in the Kharif season also.

**Acknowledgements** Authors would like to thank the Dhan Foundation and GIZ for funding and field support on this project.

## References

1. Oppen, M. V., Subba Rao, K. V. (1980). Tank irrigation in semi-arid tropical India. II. Technical features and economic performance. *Progress report-International Crops Research Institute for the Semi-Arid Tropics*, 2475.
2. Rajeswari, Y. R., Rao, N. B. (2018). Hydrological viability analysis for minor irrigation tanks—a spatial approach. In *Proceedings of International Conference on Remote Sensing for Disaster Management* (pp. 189–197).
3. Venkatesan, V., Balamurugan, R., Krishnaveni, M. (2012). Establishing water surface area-storage capacity relationship of small tanks using SRTM and GPS. *Energy Procedia*, 16, 1167–1173.
4. Xu, H. (2006). Modification of normalised difference water index (NDWI) to enhance open water features in remotely sensed imagery. *International Journal of Remote Sensing*, 14, 3025–3033.

# Calibration of Pedestrian Flow Model Using Greenshield's Macroscopic Stream Model for a Signalized Midblock



Sai Prasanna Reddy, Teja Tallam and K. M. Lakshmana Rao

**Abstract** Walking is one of the most important modes of travel, so pedestrian facilities are presenting attracting the interest of diverse researchers. However, because of speedy urbanization, traffic congestion has turn out to be a chief problem for secure pedestrian motion. It is important to objectively quantify how nicely roadways accommodate pedestrian movement. Because of more urbanization and also huge distance among the successive intersections, people are forced to cross at midblock. This paper goals in expertise pedestrian characteristics that is a fundamental in pedestrian plans system, by developing a model together with basic parameters (speed, flow and density) which fits best for the collected data. Pedestrian data required are retrieved using videography technique during morning and evening peak hours of a day at Kukatpally and Nizampet cross-road signalized midblocks in Hyderabad city. Greenshields's macroscopic stream model was used to find the important parameters like free-flow speed ( $v_f$ ), max flow ( $Q_{\max}$ ) and jam density ( $k_j$ ). Then, a statistical flow model using normal distribution (which best fitted the data) is developed using the basic parameters speed and density in R software. From the results, it was found that log normal distribution fits best for the collected data and pedestrian flow can be found from the equation using pedestrian speed and density.

**Keywords** Signalized midblock · Greenshield's model · R software · Pedestrian crosswalk · Macroscopic

---

S. P. Reddy (✉)  
VNR VJIET, Hyderabad, India  
e-mail: [prasannajilkapally@gmail.com](mailto:prasannajilkapally@gmail.com)

T. Tallam · K. M. Lakshmana Rao  
JNTU, Hyderabad, India  
e-mail: [tnteja@gmail.com](mailto:tnteja@gmail.com)

K. M. Lakshmana Rao  
e-mail: [kmlraoin@yahoo.com](mailto:kmlraoin@yahoo.com)

## 1 Introduction

Generally, transportation is the basic source for the transfer of goods and persons from one place to the other. Transportation is broadly classified as private, public and walk. Of the entire medium, pedestrians are the most neglected mode of transportation in terms of safety, at intersections as well as midblocks. Generally, pedestrians in view of safety are allowed to cross near the intersections where the vehicles approaching intersections must stop, giving way for the pedestrians. Due to controlled conditions at the intersections, the probability of occurring hazardous situations between vehicle and the pedestrian is less. These days, people started crossing at different midblock locations because of the large distance between the successive intersections, to save their crossing time. At these locations, pedestrians are responsible for their own safety.

In India, according to the accidents that are recorded in the year of 2014, number of people expired was about 141,573 and 488,730 people have been wounded. Statistics show about 37% of road accident victims in the city are pedestrians. As per police records, around 272 pedestrians were either killed or critically injured on the outskirts of Hyderabad city, most of them are due to pedestrians, crossing the road. According to the data released by the Cyberabad police in 2015, at least three pedestrians were hit everyday and the number of deaths of pedestrians is three times higher than deaths among any other category of road users. It is revealed that Hyderabad, Mumbai and New Delhi have the worst pedestrian infrastructure.

This paper studies the basic parameters like flow ( $q$ ), density ( $k$ ) and speed ( $v$ ) of the pedestrians at signalized midblock using Greenshield's macroscopic stream model and develops a new model that best suits the collected pedestrian data. Generally, Greenshield's model is used for the calibration of traffic flow, but in this paper, it is used for the modelling of pedestrian flow. The data required for the analysis (flow, speed and density) are retrieved manually from the videos and the data obtained is put in the Greenshield's macroscopic formulae to calculate jam density ( $K_j$ ), max flow ( $Q_{\max}$ ) and free-flow speed ( $V_f$ ), and their respective graphs are plotted.

The main aim is to develop a facile, fundamental model consisting of the basic parameters, which is used in the design of signalized pedestrian midblocks. The data obtained is put in R software (programming language in which statistical simulation is done), from which a model is developed using the best fit distribution (Weibull, gamma, normal and lognormal) in terms of independent variables speed and density.

## 2 Literature

This present paper studies the macroscopic stream model for the pedestrians at signalized midblocks and develops a new model consisting the basic parameters speed, density and flow. Based on Boltzmann-like gas kinetic model, in the year 1998, a fluid dynamic model was developed by Helbing for the collective pedestrian's

movement. In [1], Cui and Nambisan evaluated the safe of pedestrian at midblock crossings and compared with the safety at intersections using Wilcoxon signed rank test. It was observed that pedestrians cross safely at intersections compared to mid-blocks. In [2], Polus stated that pedestrians at midblocks move at small gaps and creates risk for themselves. Serag [3] developed a binary logit model to examine the effects of various parameters on the decision of pedestrians to cross the street or not. Daamen [4] applied the obtained pedestrian data in the macroscopic stream model equations and the free-flow speed, maximum flow and jam density are determined and the fundamental diagrams are derived from the cumulative flow plots. Rastogi et al. [5] explained pedestrian speeds at midblock crossings. Videography technique is used to collect the pedestrian data, and the percentile speeds were calculated from cumulative S-shaped curve. It was observed that as age increases, speed of the pedestrian decreases and females cross at low speed compared to males. Lyons et al. [6] explained signalized midblock pedestrian crossing is a general method of resolving conflicts between pedestrian and vehicular traffic. ANN models are developed to enhance the operation of signalized midblock pedestrian crossings. This research has proposed a high-performance pedestrian gap acceptance model for pedestrian crossing opportunities implemented with the ANN software simulation. Hamed [7] presented methodology for studying the behaviour of pedestrians at midblock crossings in Jordan city using survival models and Poisson's regression model. This paper concluded that pedestrians behave differently from one side of the street to refuge and from refuge to the other side. Hoogendoorn et al. [8] proposed a new approach to estimate basic model parameters for microscopic pedestrian models using individual trajectory data. The implications of these findings in the microscopic description of pedestrian flows are considered by studying the predicted flow operations at a narrow bottleneck. Axler [9] suggested more warrants and other considerations for grade-separated pedestrian crossings based on pedestrian hourly volume, vehicle volume, any physical barrier-like underpass, overpass and the elevation difference, etc. Kormanová [10] in this paper provided several approaches to pedestrian modelling. A hydrodynamic model was developed based on its similarity with the fluids and gases using conservation equations.

### 3 Objectives

The objectives of the study are as follows:

- To apply Greenshield's macroscopic model for pedestrian modelling.
- To develop a model for predicting the pedestrian flow based on pedestrian speed and density.

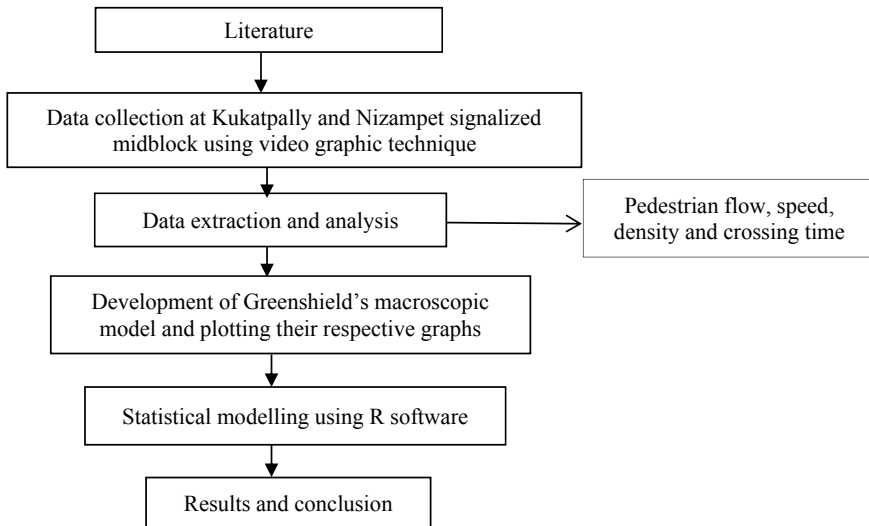


**Fig. 1** Flow chart showing methodology adopted in the study

## 4 Methodology

The methodology adopted for the study is shown in Fig. 1.

## 5 Study Location

Kukatpally (latitude  $17.4948^\circ$  N, longitude  $78.3996^\circ$  E) and Nizampet ( $17.5197^\circ$  N,  $78.3779^\circ$  E longitude) of Hyderabad, Telangana were considered as the study locations, as they have high pedestrian and traffic volume involved and are shown in Figs. 2 and 3.

The pedestrian crossing patterns observed at these locations are two types, one step crossing and two step crossing. In the first type, pedestrians cross the road without waiting at the refuge island, and in the second type, they have to wait at the island in order to cross the next half portion of the road.

## 6 Data Collection and Analysis

A 2 h's pedestrian information is gathered at the selected locations, both the locations have a carriage way of 21 m wide each. The information was gathered from 9 am to 11 am in the morning and 4 pm to 6 pm at evening utilizing videography procedure,



Fig. 2 Kukatpally signalized midblock



Fig. 3 Nizampet signalized midblock

**Table 1** Study location and data collection

S. No	Site identity	Flow (ped's/hour)	Mean speed (m/s)	Max speed (m/s)	Min speed (m/s)	Mean crossing time in sec (CT)	Max CT (s)	Min CT (s)
1	KM	3671	1.35	1.73	1.06	16.13	19.83	12.12
2	KE	4868	1.22	1.67	0.97	19.13	23.49	14.28
3	NM	2263	1.16	1.42	0.92	19.77	24.92	15.99
4	NE	2768	1.31	2.29	1.06	18.41	21.01	16.44

mounted at a raised position in order to acquire the general perspective on area and the information required, i.e. flow, speed and crossing time are extracted physically for each 5 min interim. The data collected is as follows (Table 1).

KM and KE represents the data collected at morning (9 am to 11 am) and evening (4 pm to 6 pm) for the Kukatpally location. Similarly, NM and NE represent the morning and evening data for the Nizampet location. Pedestrian crossing speed ( $v$ ) is determined as the time taken for the pedestrians to cross the midblock divided by the length of crosswalks. The average green time accommodated the walkers at the two areas is 32 s, and the red time accommodated the people on foot is 125 s.

## 7 Results and Discussion

### 7.1 Calibration of Greenshield's Macroscopic Model

Macroscopic models are utilized to determine the reliance of the basic traffic parameters (flow, speed and density) on each other. The most significant relation among them is speed and density. The simplest relation between them is first proposed by Greenshield. A linear relationship is developed between speed ( $v$ ) and density ( $k$ ) using the Eq. 1:

$$v = v_f - [v_f/k_j].k \quad (1)$$

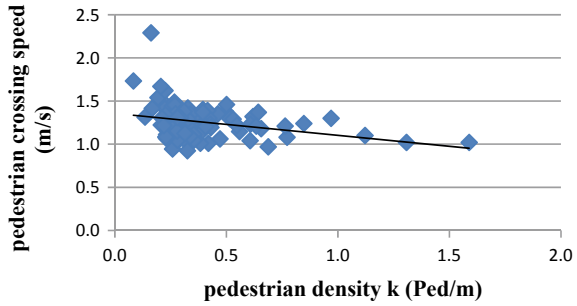
A parabolic relation is developed between flow ( $q$ ) and density ( $k$ ), shown in Eq. 2:

$$q = v_f.k - [v_f/k_j].k^2 \quad (2)$$

The relation between speed ( $v$ ) and flow ( $q$ ) is again parabolic in shape, shown in Eq. 3:

$$q = k_j.v - [k_j/v_f].v^2 \quad (3)$$

**Fig. 4** Pedestrian crossing speed versus pedestrian density



$v_f$  is the free-flow speed and  $k_j$  is the jam density.

Utilizing the pedestrian data, a graph is plotted as appeared in Fig. 3, between speed and density from which the basic regression equation is acquired as

$$y = -0.2544x + 1.357 \tag{4}$$

In Eq. 4 written above,  $x$  is the density of the pedestrian which is considered as the independent variable and  $y$  is the crossing speed of the pedestrian considered as the dependent variable.

According to the calibration of Greenshield’s model, jam density is obtained as 5.33 ped/m and free-flow speed as 1.36 m/s. The respective Greenshields graphs are plotted as appeared beneath in the Figs. 4 and 5.

According to IRC 103 guidelines, max free-flow speed is 1.2 m/s. From the study, it is revealed that free-flow speed for the midblocks is 1.36 m/s which is slightly higher than IRC guidelines.

## 7.2 Calibration of New Model

From the data collected, 75% data is used to train (prepare) the model and remaining 25% is used to validate (approve) the model. A different analysis is accomplished for both test and train data, and their respective observed, predicted graphs variation is shown.

75% of the collected data is utilized for the analysis in the R programming software for ‘goodness-of-fit statistics’, i.e. Kolmogorov–Smirnov statistic, Cramer–von mises statistic, Anderson information criteria, and for ‘goodness-of-fit criteria’, i.e. Akaikes information criteria, Bayesian information criteria based on normal, log normal, Weibull and Gamma distributions. The values and the histogram developed from the software are shown (Tables 2 and 3).

From the graph shown in Fig. 6, it is clear that, on developing a model log normal distribution fits best for the collected pedestrian flow data. Lognormal distribution is a continuous distribution of a random variable whose logarithm is distributed



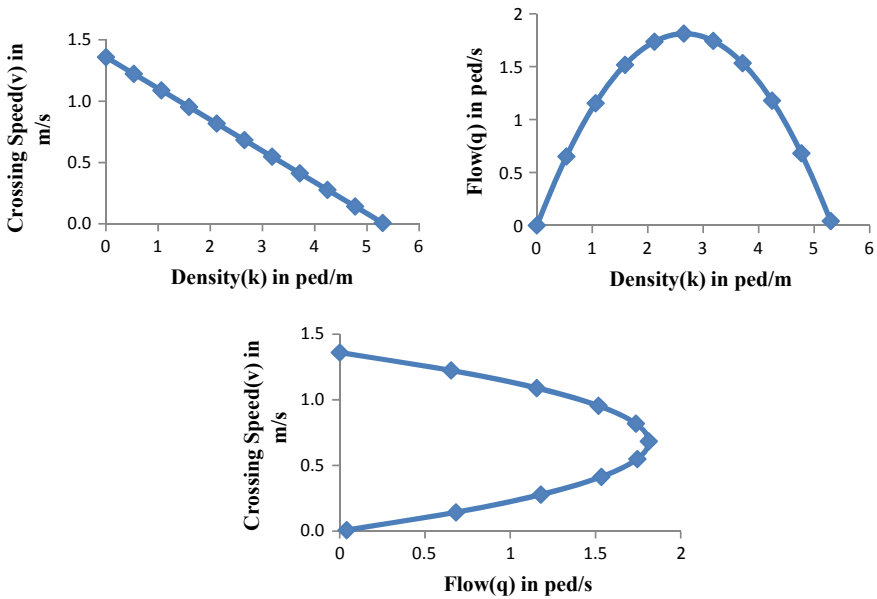


**Fig. 5** Greenshield’s graphs showing relation between basic parameters for the collected pedestrian data

**Table 2** Goodness-of-fit statistics

	Normal	Lognormal	Weibull	Gamma
Kolmogorov—Smirnov statistic	0.1842832	<b>0.09709108</b>	0.1487354	0.1263592
Cramer—von Mises statistic	0.5202339	<b>0.10607810</b>	0.3674822	0.2030137
Anderson—Darling statistic	3.0132593	<b>0.66979575</b>	2.1772533	1.1896710

**Table 3** Goodness-of-fit criteria

	Normal	Lognormal	Weibull	Gamma
Akaike’s information criterion	15.94316	<b>-11.097450</b>	4.087418	-6.245606
Bayesian information criterion	19.92113	<b>-7.119482</b>	8.065386	-2.267638

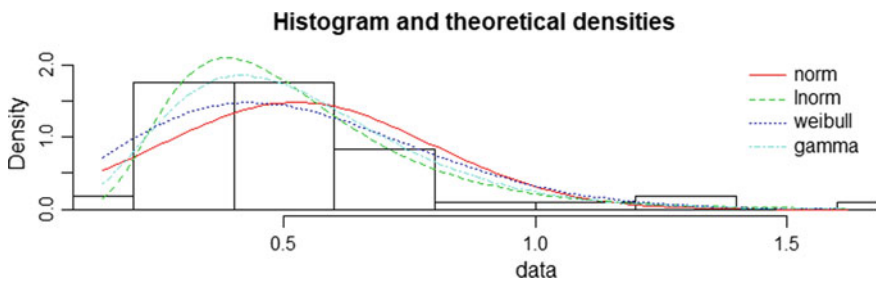


**Fig. 6** Histogram for the observed flow at the midblock from R software

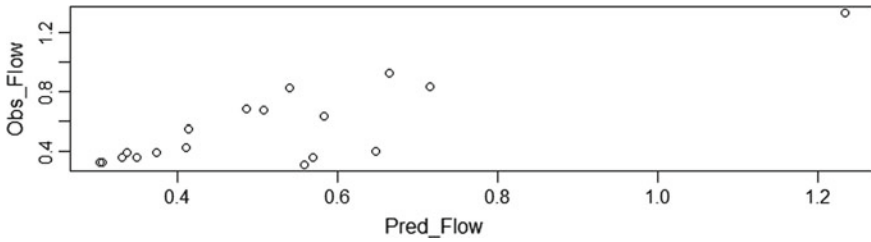


**Fig. 7** Observed versus predicted flow graph for the calibrated model

**Table 4** Model coefficients for the flow equation from lognormal distribution

	Estimate	Std. error	<i>t</i> value	Pr(>  <i>t</i>  )	Significance
Intercept	-0.4058	0.3423	-1.186	0.24146	
Density	1.9199	0.6244	3.075	0.00344	**
Speed	0.4193	0.2552	1.643	0.10669	
Density: speed	0.9754	0.5091	-1.916	0.06125	.

Significance codes: 0 '\*\*\*' 0.001 '\*\*' 0.01 '\*' 0.05 '.' 0.1 ' ' 1

normally. For the calibrated model, observed and predicted flow graph is shown as Fig. 7.

The chi square value observed for the calibrated is 0.74 which is very much less than chi critical value of 4.61 for 99% confidence interval. The root mean square value is noted as 0.15. The reliability ( $R^2$ ) obtained is 0.67 which tells 67% is predicted properly.

The flow equation is obtained for the model considering flow as dependent and speed, density as the independent variables, from the R software using the values from Table 4.

From the values, flow equation is written as shown in Eq. 5:

$$\text{Pedestrian flow, } q = -0.4058 + 1.9199 k + 0.4193 v + 0.9754 * k * v \quad (5)$$

In Eq. 5,  $v$  is the crossing speed of the pedestrian in m/s and  $k$  is the density of pedestrians in ped/m. The above equation is used to find the pedestrian flow if the density and speed of the pedestrians at the locations are known.

### 7.3 Validation or Testing of Developed Model

The 25% of data is used to carry this analysis to assess the performance of developed model. This data is put in the software and similar analysis is carried out, considering the lognormal distribution which best fitted the data.

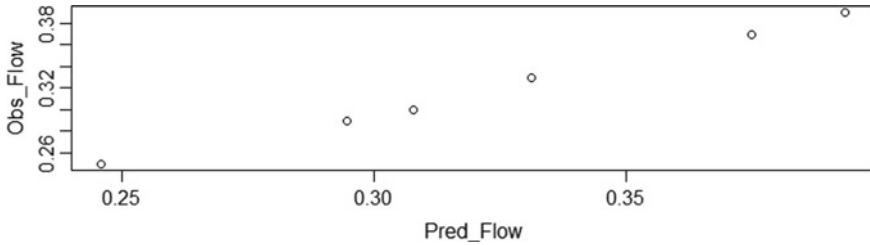


**Fig. 8** Observed versus predicted flow for the validation of developed model

The chi-squared value obtained from the chi-squared test is 0.0004 which is less than chi critical for 99% confidence interval. The  $R^2$  value calculated from the observed and predicted values is 0.97, which means 97% of the data set can be predicted accurately.

The root mean square error (RMSE) calculated is 0.0047, which approximates zero, indicates that the lognormal distribution better fits the data set. Lognormal distribution is a continuous distribution of a random variable whose logarithm is distributed normally (Fig. 8).

## 8 Conclusion

- Greenshield's model is the most adaptable and effective technique for the data analysis. This model is fundamentally used to set up the relation between traffic stream parameters, yet in this examination it is utilized for the pedestrian analysis at signalized midblocks.
- The obtained observed pedestrian flow distribution is used for predicting pedestrian flow based on pedestrian crossing speed and density from the equation generated. This study can be further continued to calculate pedestrian LOS at the signalized midblock.
- The reliability obtained for the calibrated model is 0.67, which means 67% of the data is predicted properly. Also, the chi square value is very much less than the chi critical value for the developed model, which tells the above developed model is accurate and best suits for the locations.
- The above developed model is transferrable to other cities, but with the new data set depending on the location.

## References

1. Cui, Z., & Nambisan, S. S. (2003). Methodology for evaluating the safety of midblock pedestrian crossings. *Transportation Research Record*, 1828(1), 75–82.
2. Polus, A. (1983). Gap acceptance characteristics at unsignalised urban intersections. *Traffic Engineering and Control*, 24(5), 255–258.
3. Serag, M. S. (2014). Modelling pedestrian road crossing at uncontrolled mid-block locations in developing countries. *International Journal of Civil and Structural Engineering*, 4(3), 274.
4. Daamen, W. (2004). Modeling Passenger Flows in Public Transport Facilities. Dissertation thesis.
5. Rastogi, R., Chandra, S., Vamsheedhar, J., & Das, V. R. (2011). Parametric study of pedestrian speeds at midblock crossings. *Journal of urban planning and development*, 137(4), 381–389.
6. Lyons, G., Hunt, J., & McLeod, F. (2001). A neural network model for enhanced operation of midblock signalled pedestrian crossings. *European Journal of Operational Research*, 129(2), 346–354.
7. Hamed, M. M. (2001). Analysis of pedestrians' behavior at pedestrian crossings. *Safety Science*, 38(1), 63–82.
8. Hoogendoorn, S. P., Daamen, W., Landman, R. (2005). Microscopic calibration and validation of pedestrian models—Cross-comparison of models using experimental data. *Pedestrian and Evacuation Dynamics*, 253–265.
9. Axler, E. A. (1984). *Warrants for pedestrian over and underpasses* (No. FHWA-RD-84-082). United States. Federal Highway Administration.
10. Kormanová, A. (2014). Hybrid model for pedestrian movement simulation. In *The 10th International Conference on Digital Technologies 2014* (pp. 152–158). IEEE.

# Evaluation of Physical and Environmental Parameters of the Indian Sundarbans



Nilovna Chatterjee, Venkata Ravibabu Mandla, Ranadhir Mukhopadhyay, Nagaveni Chokkavarapu and Veerendra Satya Sylesh Peddinti

**Abstract** Deltas and associated coastlines are amongst the most rapidly changing landscape features, as these are subjected to physical, geological, biological and environmental threats. One of the largest deltas of the world, Sundarbans is undoubtedly a vulnerable area from both the ecosystem and human sustainability angles. To protect such a sensitive ecosystem, a comprehensive strategy and action plan is therefore needed to ensure conservation of the environment while guaranteeing the inhabitants an adequate living standard. Such rigorous planning must follow reliable and scientific data and information. The present study aims to evaluate the primary physical and environmental parameters affecting the Indian Sundarbans, and it will help to assess the amount of erosion and accretion over the southern islands of Indian Sundarbans that directly faces the onshore tidal currents.

**Keywords** Sundarbans · Sea surface temperature · Local sea level rise · Salinity · MODIS

## 1 Introduction

Global climate changes have affected the coastal communities all over the world. Many of these communities are already vulnerable to potential threats like increased

---

N. Chatterjee

Department of Agronomy and Horticulture, University of Nebraska-Lincoln, Lincoln, USA

V. R. Mandla (✉) · V. S. S. Peddinti

CGARD, School of Science, Technology and Knowledge Systems, National Institute of Rural Development and Panchayati Raj (NIRDPR), Ministry of Rural Development, Government of India, Hyderabad, Telangana 500030, India

e-mail: [ravi.mandla@gmail.com](mailto:ravi.mandla@gmail.com)

R. Mukhopadhyay

National Institute of Oceanography, Dona Paula, Goa, India

N. Chatterjee · N. Chokkavarapu

VIT University, Vellore, Tamil Nadu 632014, India

© Springer Nature Singapore Pte Ltd. 2020

S. Saride et al. (eds.), *Advances in Geotechnical and Transportation Engineering*,

Lecture Notes in Civil Engineering 71,

[https://doi.org/10.1007/978-981-15-3662-5\\_11](https://doi.org/10.1007/978-981-15-3662-5_11)

sea level, tidal surges, tidal inundation, increased cyclonic activities, saltwater intrusion inland and rising water table [1]. These changes have affected the livelihood of people living around these coastal areas. Clart [2] stated that the scale of this impact on the coastal communities is unevenly distributed around the globe. Vulnerability is a function of susceptibility and coping mechanism. To understand the vulnerability associated with the coastal communities with changing climate, one needs to clearly understand the concepts of adaptation and adaptability. The term adaptation has been defined several times in several ways. Adaptation means any adjustment, whether passive, reactive or anticipatory, that is proposed for improving the anticipated adverse consequences associated with climate change [3, 4]. Adaptation is mainly a compromise to the changing climatic conditions in order to survive, and never a choice. According to Climate Change Vulnerability Index (CCVI) report, India is the second most vulnerable to climate changes, after Bangladesh. Vulnerability assessment involves understanding potential threats that might arise in the future and assessing the present threat and its impact on the ecosystem. It also includes analysis of adaptations that have taken place over an ecosystem to cope up with the present threats. The present study aims at identifying the primary physical and environmental parameters affecting the Indian Sundarbans, and it will help to assess the amount of soil removal over the southern islands of Indian Sundarbans that directly faces the onshore tidal currents. The proposed results can help policymakers and other statutory planning bodies/authorities to effect changes in policies and also increase safety measures to protect this fragile ecosystem.

## 2 Study Area

The Sundarbans lie at the southern gangetic plains where rivers Ganga, Brahmaputra and Meghna meet before emptying themselves into the Bay of Bengal. Several intricate rivers and creeks intersect this region bordered by latitude  $21^{\circ} 39' 0''$  N to  $22^{\circ} 14' 41''$  N and longitude  $88^{\circ} 03' 0''$  E to  $89^{\circ} 08' 26''$  E. The Indian Sundarbans consists of 102 islands spread over  $9630 \text{ km}^2$  spread over 19 blocks-thirteen in South 24-Parganas and six in North 24-Parganas (Centre for Science and Environment). The administrative blocks and the various islands under Reserve Forest, Wildlife Sanctuary and National Parks of Indian Sundarbans are shown in Fig. 1. Criss-crossed by several rivers, rivulets and tidal creeks, the Indian Sundarbans is a highly fertile alluvial plain.

Rivers in the Sundarbans are meeting places of salt water and freshwater. Thus, it is a region of transition between the freshwater of the rivers originating from the Ganges and the saline water of the Bay of Bengal [5]. It is a natural delta formed by the sediment deposition of several rivers. Sunderban consists of 102 islands with 2–3 m elevation and 48 of these are not populated with human existence. It is a highly tide-dominated area, with several mudflats and tidal flats, beaches and spits all along the island shores. Several marshy lands and tidal sandbars can also be observed all over the inland region. The rivers and creeks carry salt water inland, and thus several

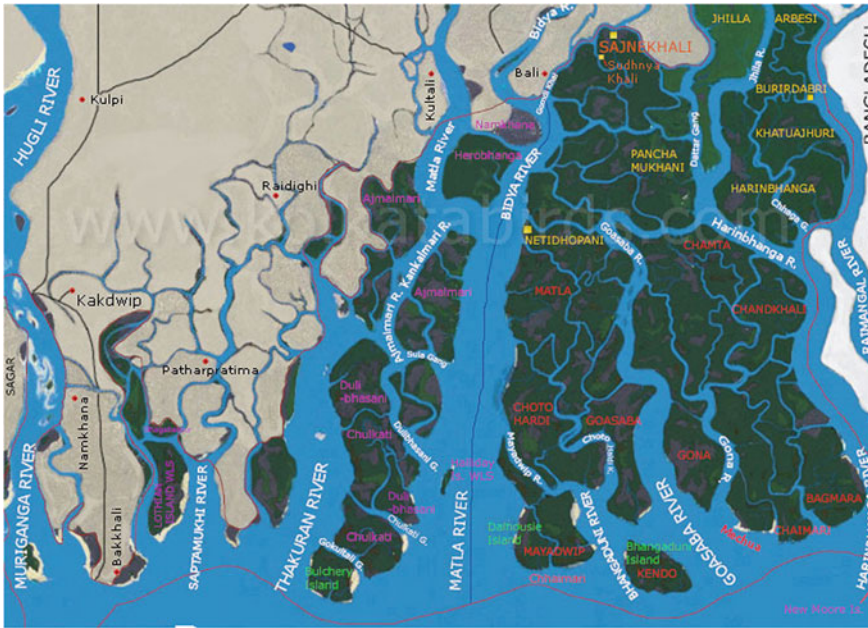


Fig. 1 Study area of Indian Sundarbans

mangrove patches can be observed even in the inland regions. The biotic and abiotic factors together make up the physiographic features of this region. The mangroves in this region assist in the formation of new land masses with their morphological features that accumulate sediments from rivers. These sediments get accreted over the years to form a substratum for new mangroves to develop. Due to its proximity to the Bay of Bengal, the area is highly humid especially over the southern islands. April and May are the hottest seasons with mercury soaring to 35 °C. November to January are the coldest months when temperatures fall to 12.7 °C. This part of delta is under severe threat, as the Indian Sundarbans lie in the low elevation coastal zone (LE CZ) with elevations reaching up to only 3 m, leaving this area vulnerable to climatic changes. The ecosystem is highly fragile and vulnerable. Rise in sea level has been a major threat to this area. The local sea level rise was reported to be 5.22 mm/year which is much higher than the average sea level rise over the Bay of Bengal [6]. If this trend continues, then the entire Sundarbans will sink by 2030. Moreover, the area is highly underdeveloped and the inhabitants live mostly below poverty line (BPL). In addition to this, the southern islands of the Indian Sundarbans are facing rapid erosion. Almost 81 km<sup>2</sup> of land has been lost to the sea over the past 32 years. Islands like Lohachara and Suparibhanga have already been submerged. Rapid erosion has affected the livelihood of the inhabitants. Seawater intrusion into land has led to an increase in top soil salinity and rendered several acres of land unfit for paddy cultivation. In the background of the discussion made above on the threat perception and consequent vulnerability of Sundarbans, this study highlights

to identifying the forcing parameters that threaten the environment of the Indian Sundarbans, between 1979 and 2011, for the important vulnerable islands.

### 3 Environmental Parameters

Studies have revealed that in the past several years, changes in air quality, humidity and water vapour have not been varying. The relative humidity data has been 80–85% during April–September and 70–75% in October–March [7]. Therefore, in our evaluation, these parameters remain a constant factor with little variations and can be considered as of secondary significance. The geographical position of Sundarbans makes it highly vulnerable to cyclonic activities, as it lies perpendicular to the approaching cyclone [8]. Depressions occurring over mid-Bay of Bengal tend to affect Sundarban delta more due to its perpendicular location. Research has proved a linear relationship between maximum potential intensity of tropical cyclones and sea surface temperature [9]. In their study, they have showed that maximum potential intensity largely depends upon the sea surface temperature. Duration of cyclones/storms over the Bay of Bengal would be about four days from the beginning to ending. This has increased SST by 0.1 °C in the past ten years. Cyclones occurring before and after monsoon are more violent in nature.

The Sundarban is one of the finest examples of tide-dominated delta system. High tidal range of Sagar Island in India, at the head of the Bay of Bengal, has a range of 17.4 ft (5.3 m). Due to tidal dominance, the sea water enters up to several metres inside land rendering intrusions of salt water into freshwater aquifers and also affecting the salinity of region. Salinity of the oceans is a measure of amount of dissolved salt in sea water and is measured in practical salinity units (psu). Several studies conducted over the region show that the salinity over Indian Sundarbans is increasing continuously. Increasing temperature over the open sea/ocean surface will lead to raise in rate of evaporation. This increases water salinity in the open water surfaces. However, salinity of water is always subjected to freshwater inflow, amount of rainfall and run-off [10]. The increase in salinity is primarily due to the barrage constructed at Farakka in West Bengal, which has reduced the inflow of freshwater in this region.

Drying of several small rivers and rivulets has also been one of the major causes for reduction of freshwater flow over the region. The Bengal basin is reported to be tilting which another important reason that has increased the salinity [11]. The western station showed a significant and continuous decrease in salinity (1.67 psu/decade), whereas the eastern sector showed an increase in salt ~6 psu over thirty years. Another effect of salinity is excess salinity retards growth of mangroves. Central part of the Sundarban delta is recorded high salinity during the last 5 years [12]. Based on physiological studies, he concluded that mangroves are salt-tolerant and not salt lovers. Increased saline condition retards seed germination and impedes growth. Salinity therefore becomes an important parameter since it has a direct effect on



growth of the mangroves as well as has been accounted for a reason behind the climatic changes in the Sundarban deltaic regions.

River water influences the salt concentration in estuaries due to the continuous supply of freshwater. Most of the estuaries have become salty, most of the year except monsoon season as they receive water from Brahmaputra and Ganges rivers. This area has only six rivers flowing with freshwater. Those estuaries which were disconnected from this freshwater supply are showing sedimentation and gradually silted. High tide along the Bay of Bengal raises above four metres along the shores. The region experiences a subtropical monsoonal climate with an annual rainfall of 1600–1800 mm and severe cyclonic storms [13]. Major factors which force agriculture are amount of precipitation and humidity [14]. The Sundarbans island regions are most vulnerable to sea level rise due to climatic changes. The data on physical parameters studied were collated from various secondary databases available in public domain, satellite imageries and most importantly through cruise data conducted by National Institute of Oceanography, Goa.

## 4 Evaluation of Identified Parameters

### 4.1 Wind Speed

The cruises made by ships of the Goa-based National Institute of Oceanography (NIO) and also the station at Sagar Island set over the Bay of Bengal gives the wind speed over this geographical location. The average wind speed taken every month has been tabulated for Sagar Island for the year 2010 (Table 1). The highest wind speed is observed over the months of June and July. This is marked by the

**Table 1** Wind speed measured over Sagar Island station for the year 2010

Month	Wind speed (m/s)
January	3.45
February	2.75
March	4.44
April	7.70
May	6.20
June	7.50
July	7.40
August	7.00
September	5.40
October	3.40
November	3.80
December	3.80

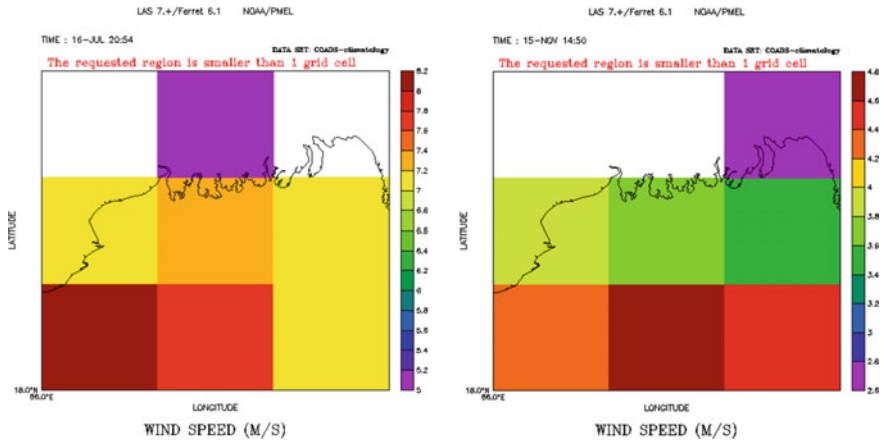


**Fig. 2** Wind speed for the months of July and November over Sundarbans

onset of monsoon over the region. The monsoon rains accompanied with strong wind have been the major cause of erosion in these islands. For easier interpretation, wind speed maps have been generated using Ferret software. The wind speed over the region becomes violent during cyclonic episodes (80–85 km/h). The graphical representation of wind speed over Sagar Island for 2010 (Fig. 2), and the overall wind speed for the entire Sundarbans is presented through Ferret software for the months of July and November. The wind speed results were tallied with the wind speed values available at Sagar Island by IMD, Pune. The National Data Centre at Indian Meteorology Department (IMD, Pune), which is the authorized clearing agency for the meteorological data, has made available all available data on wind speeds from 1966 to 2012 (Table 2). Strong winds with speeds above 22 m/s are generally associated with cyclonic storms. In summary, the wind velocity of the Sagar Island and its surrounding regions experiences maximum wind velocity of 45.26 m/s and minimum wind velocity of 2.44 m/s and a mean wind of 8.6 m/s. This shows that the region may experience a catastrophic situation during times of high wind speed. Wind speed thus is an important parameter that increases the vulnerability of the Indian Sundarbans as it accompanies cyclonic storms and also causes massive erosion and destruction of land.

**Table 2** Wind speed over Sagar Island (1966–2012)

Place	Total records	Number of years	Wind speed			
			Wind <sub>max</sub> (m/s)	Wind <sub>avg</sub> (m/s)	Wind <sub>min</sub> (m/s)	Extreme (m/s)
Sagar island	6783	46	45.26	8.608	2.44	21.938

Source IMD, Pune

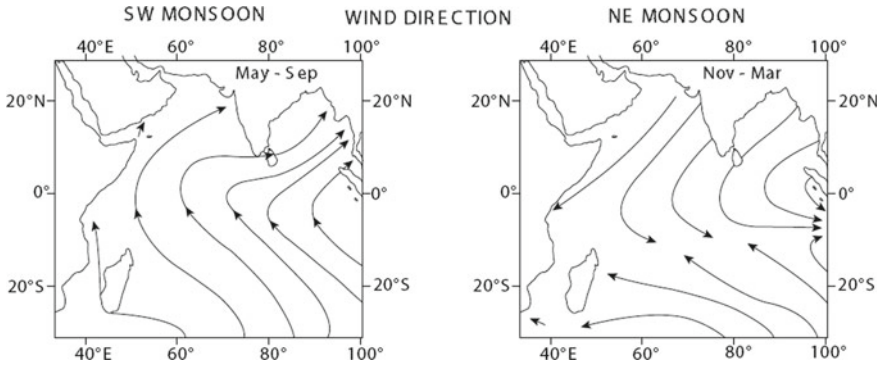


**Fig. 3** Mean surface wind direction in the tropical Indian Ocean, the Bay of Bengal and Arabian Sea during the southwest (left) and northeast (right) monsoons

### 4.2 Wind Direction

The wind direction in Sundarbans is south-western in summer and north-eastern during the winter. During the summer, the south-western winds are coupled with heating, precipitation and an increased freshwater run-off into the northern Bay [15]. During winter, the winds blow from the high-pressure region over the Asian continent into the Bay of Bengal. The wind speed is strongest in December with an average speed of 4.4 m/s attaining a maximum speed of 6 m/s over the central western Bay [16]. These winds become weak with variable magnitudes during March–April (NE-SW inter-monsoon). During this period, an anti-cyclonic wind field is developed over the Bay with westerly (eastward blowing winds) along the equator. The directional pattern intensifies by July and the maximum velocity attained is 7.4 m/s over the central Bay. Thus, the wind velocity and wind direction serve as an essential parameter in the context to assessing the vulnerabilities of Indian Sundarbans and can be stated as a primary parameter (Fig. 3).

### 4.3 Sea Surface Temperature (SST)

Sea surface Temperature is the temperature at the ocean surface. The exact meaning of ocean surface varies with the measurement methods. In this study, it has considered the SST at different depths of 0, 10 and 20 m. SST affects the air masses above it. Variations in SST are more on a calm day than on a breezy day. The sea surface temperature has shown change over the years. Mitra [12] suggested that SST has been rising at the rate of 0.005 °C/year. The analysis of cruise data from Sagar Kanya vessel of NIO shows slight variations in SST over different months (Table 3). The possible reason for less variation in SST could be small area of study. Warmer SST during the May to October favours the formation of tropical cyclones in Sundarbans. Increase

**Table 3** Sea surface temperature at various depths in the Sundarbans region

Month	0 m	10 m	10 m
January	23.32	24.87	25.86
February	26.06	25.01	26.08
March	26.91	26.56	26.75
April	28.16	27.90	27.66
May	29.86	29.84	29.58
June	29.57	29.53	29.39
July	28.93	28.86	28.77
August	29.38	28.81	28.71
September	29.30	29.05	28.88
October	29.22	29.16	29.19
November	27.07	27.30	28.24
December	25.70	26.44	26.69

in SST by thermal expansion is one of the major causes of sea level rise along with melting of polar ice sheets. Sea surface temperature has increased by 0.1 °C over a decade. Multispectral satellite imageries (Aqua MODIS) were used to study the yearly variations in SST between 2003 and 2012. The MODIS Aqua (day) images are of resolution (4 km × 4 km). Moderate resolution imaging spectral-radiometer (MODIS) was launched in December 1999 (Terra) and Aqua during May 2002. This MODIS data has 36 bands out of which 21 bands lie within 0.4–3.0 μm; 15 bands lie within 3–14.5 μm. The exact area of interest had a subset width of 10° and a subset height of 30°. The SST observed for the month of June near Sundarbans area in the Bay of Bengal has been shown in Fig. 4. The images also show the latitude and longitude for easier identification.

In the month of June shows one of the highest SST over this region and was thus the observations during this month were chosen for the purpose of this study. Observations for all the years were taken on a randomly chosen date (June 18th) and a particular time 8 am for easier and uniform interpretations. Figure 5 gives a graphical representation of SST increase over Bay of Bengal measured over 88.3° E to 89.08° E and 21.39° N to 22.14° N (Cruise data, Sagar Kanya Vessel, NIO, Goa).

The SST was calculated from the values observed over the region from the MODIS Aqua images for all the days the in June from 2003 to 2011. Table 4 shows the mean temperature calculated for the month of June from 2003 to 2011. It was observed that the mean SST calculated for the year 2003 was 29.25 °C for the month of June which increased to 30.33 in 2011, the highest during the time period of study. Thus, the rate of increase in SST from our studies shows an increase of 0.61 °C/decade. This result confirms the previous studies done by [17], which estimated a yearly increase in SST by 0.0453 °C.

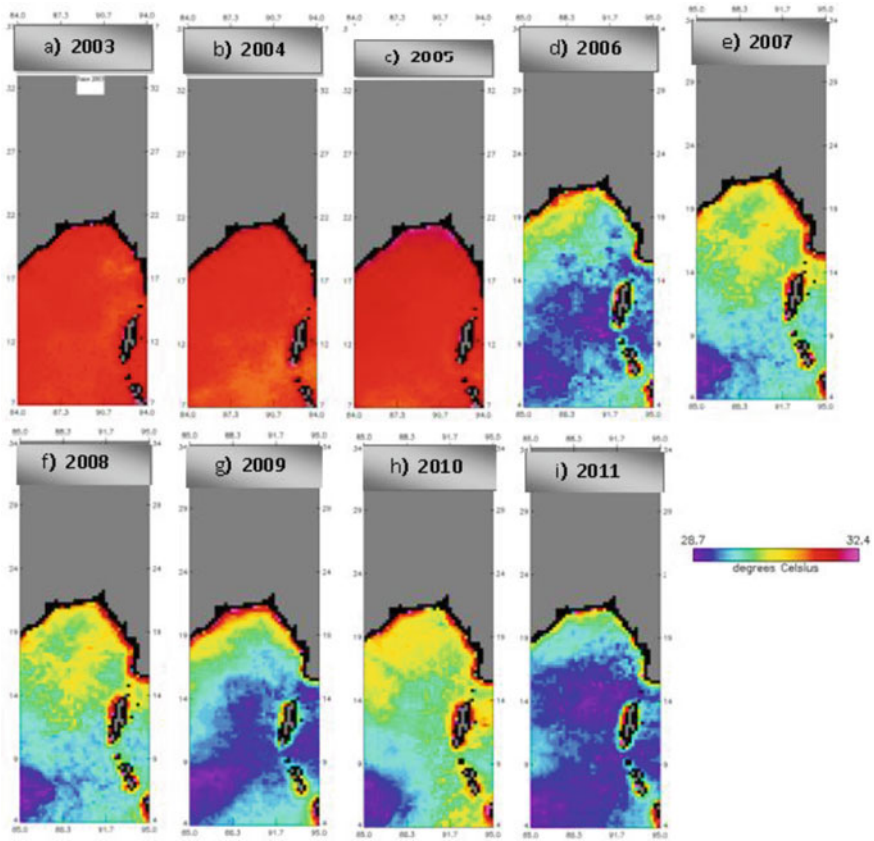
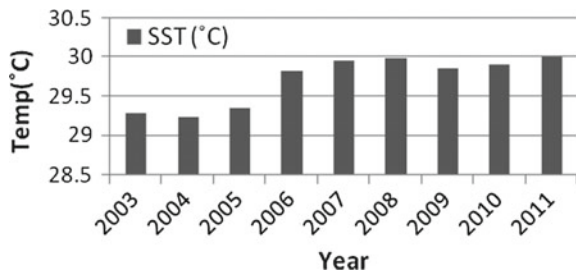


Fig. 4 a–i MODIS output of average monthly SST for the month of June (2003–2011)

Fig. 5 Graph representation of SST increase over the Bay of Bengal (2003–2011)



#### 4.4 Cyclones Over Bay of Bengal

The Sundarbans region is highly prone to cyclonic activities. Extreme weather conditions like cyclones and storms are becoming more frequent over Sundarbans. As

**Table 4** Average monthly SST (°C) for June (2003–2011)

Year	Mean SST
2003	29.28
2004	29.23
2005	29.35
2006	29.83
2007	29.95
2008	29.98
2009	29.86
2010	29.91
2011	30.01

**Table 5** Wind speed associate with low-pressure disturbance in the Bay of Bengal

Disturbances	Wind speed (kmph)
Low pressure	<31
Depression	31–49
Deep depression	40–51
Cyclonic	62–88
Severe cyclonic	89–118
Very severe cyclonic	119–221
Super cyclonic	222 and above

Source IMD, Pune

stated before, SST over Sundarbans is increasing which increases the chances of cyclone formations over Bay of Bengal. The direction of wind circulation is anti-clockwise in Northern Hemisphere and clockwise in Southern Hemisphere. The centre of cyclone has lowest pressure, where the pressure drop determines the intensity of cyclone. Indian Meteorological Department (IMD) has defined low-pressure area (Table 5).

Sunderbans are mostly affected due to pre- and post-monsoon cyclones which are stronger with high intensity. The increasing number of storms in the Bay of Bengal by 26% in the last century made Sunderbans most vulnerable [18]. As per the meteorological data, number of cyclones occurred in India has been increased like between 1921 and 1930, 56 cyclones and 1951–60, 32 cyclones were occurred [19]. The incidence of storms and cyclones has reduced in the past decade, although the intensity of storm has increased. Amongst the cyclonic activities over the Bay of Bengal that has affected Sundarbans (Table 6), cyclone Aila in 2009 claimed several lives and rendered a million homeless. In India, 149 people were killed and several people went missing. The impact of Aila was magnified due to the location of the Sundarbans with respect to approaching cyclone. Sundarbans lying perpendicular to the approaching storm faced severe damage as wind speed of 70–75 mph devastated this eco system. Thus, the cyclonic activities over this region are

**Table 6** Affected Cyclones in Sundarbans

Name of the cyclone	Date of occurrence	Speed (knots)	Category
	28th October, 1999	>140	Super cyclonic storm
	28th October, 2000	<40	Cyclonic storm
	19th May, 2003	<60	Severe cyclonic storm
	17th May, 2004	<60	Severe cyclonic storm
	2nd October, 2005	<40	Cyclonic storm
Mala	24th April, 2006	>120	Super cyclonic storm
Not given	13th May, 2007	<60	Severe cyclonic storm
Sidr	15th November, 2007	>120	Super cyclonic storm
Not given	28th June, 2007	>120	Super cyclonic storm
Rashmi	26th October, 2008	>40	Cyclonic storm
Nargis	27th April, 2008	<120	Very severe cyclonic storm
Bijji	16th April, 2009	<60	Severe cyclonic storm
Aila	24th May, 2009	<60	Severe cyclonic storm

Source School of Oceanographic Studies, Jadvapur University

one of the most important parameters that are making the ecosystem more vulnerable. If SST continues to rise in this location, then the cyclonic activities will also increase.

### 4.5 Local Sea Level Rise (L-SLR)

Local tide gauge records far exceed the nationally accepted average of 1.06–1.75 mm/year causing displacement of inhabitants of the islands. In the subsiding delta of Sundarban, both Diamond Harbour (5.22 mm/year) and Sagar (3.14 mm/year) exceed the national average [6]. It is suggested that the local sea level rise over Sundarbans is not just an outcome of global warming but also due to localized subsidence over Sundarbans. Figure 6 shows the tide increase over various tide stations in India and Gulf countries. Sagar station, located at Sagar Island, recorded the highest L-SLR. The local sea level rise over other Indian stations was much lesser than that of Sagar station on Sagar Island and Diamond Harbor station located very close to Sundarbans. The islands on the seaward side have got massively affected due to sea level rise and subsidence. Sea level rise and increased tide heights over the past three decades have inundated Lohachara, Bedford, Suparibhanga and

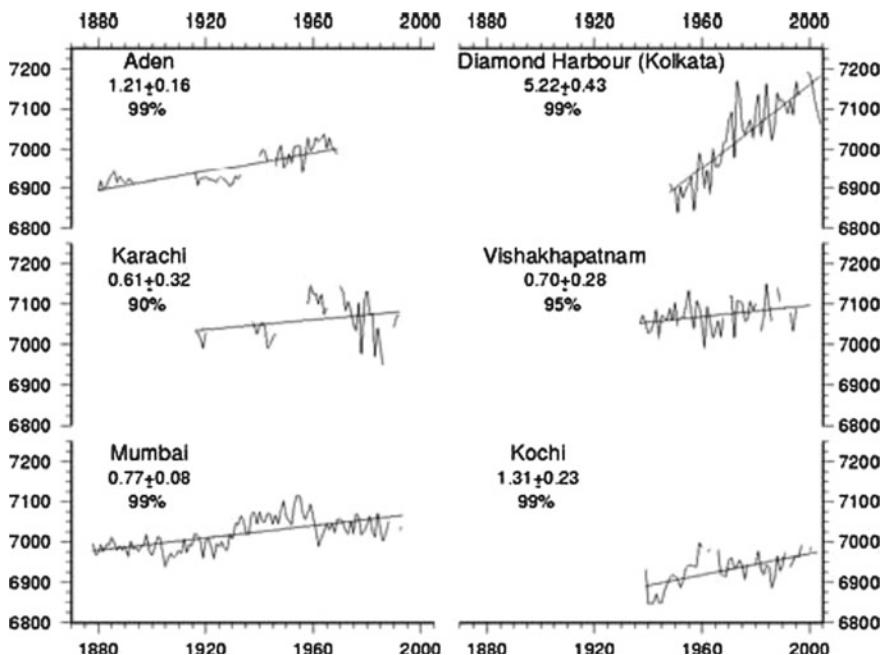


Fig. 6 Local sea level rise recorded at different tide stations.



Kabasgadi Islands. Other tide stations like Mumbai reported a local sea level rise (L-SLR) of 0.77 mm/year and Kochi reported an L-SLR of 1.31 mm/year. This clearly indicates that local sea level rise in Sundarbans region is making it highly vulnerable.

## 4.6 Salinity

Salinity over Sundarbans region varies drastically with respect to seasons. During summers, the salinity increases due to an increased rate of evaporation and lack of freshwater supply in the estuaries. The top soil salinity in 2010 was measured in different areas of Sundarbans (Table 7). Also, measured was the difference in seawater salinity values at 0, 10 and 20 m (Table 8). Salinity was measured from different depths, as the salinity value might not be accurate over the surface alone. The salinity of sea water is between 32 and 35 psu. Some regions in Sundarbans towards the east show an alarming increase in salinity. Increase in salinity has degraded forest vegetations and mangrove species. Salinity rise in sea has affected the top soil salinity as well. The tidewater inundates the island region during high tide thus intrusion of sea water into land leads to increase in top soil salinity and also affects the freshwater aquifers in this region. Increasing salinity has affected the crop production drastically. In some regions, the top soil has become almost unfit for agriculture, particularly paddy cultivation. Salt water inundates land and enters freshwater ponds, thus affecting freshwater fishes. Centre for Science and Environment, a Delhi-based NGO, in their recent study (2012), reported an increase in top soil salinity to 8 psu in northern areas and up to 20 psu in the southern Sundarbans. This is highly retarding factor for paddy cultivation in the region. The safe limit for growing rice is 4–6 psu. Increased salinity retards paddy seed germination. After cyclone, due to heavy rain and soil erosion, most often agriculture lands with paddy cultivation show salinity reaching up to 1.5 m below the soil for two years after the disaster occurred [20]. Increase in seawater salinity has also affected the mangrove growth tremendously. The mangroves are salt-tolerant species but excessive increase in salinity retards the mangrove growth. Satellite images show destroyed patches of mangroves in many islands. Mangroves have an optimum salt tolerance of 25 psu.

**Table 7** Top soil salinity during winter 2010 over Indian Subarbans

S. no.	Islands	Salinity (psu)
1	Kachuberia	1.67
2	Sagar	11.39
3	Fraserganj	12.19
4	Sajnekhali	13.33
5	Jhanrkhali	13.88

Source [12]

**Table 8** Salinity (psu) of seawater samples from different depth (m) collected from Sundarban area

Month	Depth (m)	Salinity	Month	Depth (m)	Salinity	Month	Depth (m)	Salinity
Jan	0	22.47	May	0	32.54	Sep	0	18.33
	10	30.12		10	32.88		10	21.36
	20	32.02		20	33.28		20	24.00
Feb	0	23.44	Jun	0	31.08	Oct	0	29.58
	10	31.67		10	31.57		10	30.23
	20	32.44		20	32.44		20	32.19
Mar	0	22.00	Jul	0	23.86	Nov	0	27.36
	10	32.24		10	30.61		10	28.02
	20	33.01		20	31.05		20	31.09
Apr	0	30.32	Aug	0	21.56	Dec	0	31.05
	10	32.64		10	26.6		10	31.49
	20	33.08		20	27.71		20	32.38

Source NIO database, 2010

#### 4.7 Rainfall

MODIS images for rainfall indicated a significant rise in precipitation rate over North Bay of Bengal. MODIS data were acquired for Sundarbans area using a subset angle of 30°. July was chosen as a standard month for all the years. Figure 7 shows MODIS images for precipitation rates over Sundarbans area from 2003 to 2009. In last ten years, precipitation shows gradual decrease at the rate of 0.005 mm/h. Decrease in precipitation rate has affected farmers as sufficient rain is required to dilute the salinity of soil and nearby water bodies. It can conclude that increase in SST beyond a certain limit actually reduces precipitation.

## 5 Conclusion

Sundarbans area is facing extreme threats due to global warming. SST has registered a decadal increase of 0.061 mm per decade. This shows that the chances of developing cyclone over the region have also increased. Cyclones like Aila and Sidr has devastated the region completely. An area is expected to become fertile post flood but post-Aila, and Sundarbans has become highly infertile. Studies also suggest that the Bengal basin is tilting eastward. Tilting of Bengal basin has increased salinity of the Indian Sundarbans. Increased salinity has reduced crop production and forced

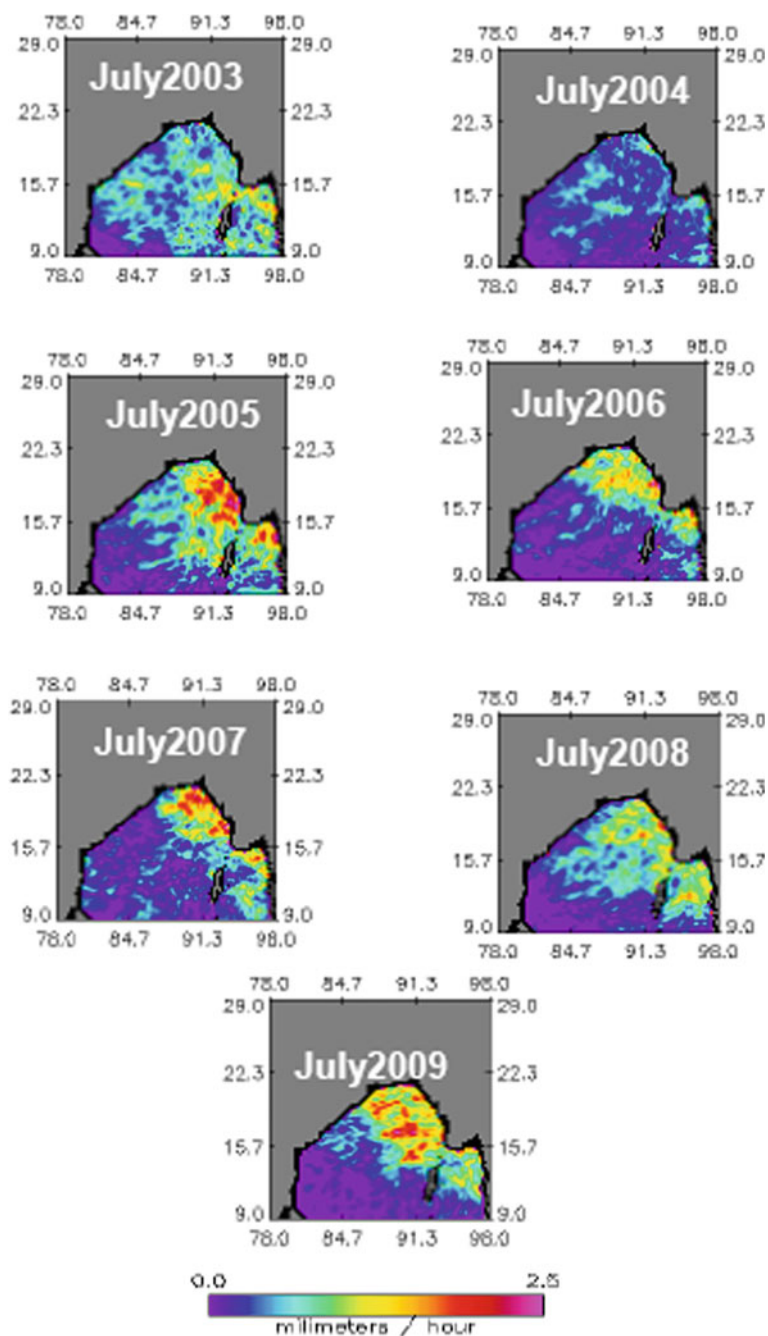


Fig. 7 MODIS image of rainfall rate over Sundarbans

people to look for an alternative livelihood. Sea level rise in this region is alarming as it is the highest recorded value of 5.22 mm/year. Localized subsidence and global warming are responsible for such high values. Increased tide height has led to increased inundation over this region. Several villages are facing problems due to seawater intrusions into their land. Embankments have failed to keep the sea water away from the islands. Many aqua culture farms are incurring losses due to this. Most importantly, the population pressure over the ecosystem is extremely high making this coastal area vulnerable. The government, NGOs and common people should join hands and put efforts in preserving this sensitive ecosystem.

**Acknowledgements** Authors would like to thank to Director, NIO and other team members for providing field data.





## References

1. Mirza, M. M. Q. (2003). Climate change and extreme weather events: can developing countries adapt?. *Climate policy*, 3(3), 233–248.
2. Clark, G. E., Moser, S. C., Ratick, S. J., Dow, K., Meyer, W. B., Emani, Y., Jin, W., Kasperon, J. X., Kasperon, R. E., & Schwarz, H. E. (1998). Assessing the vulnerability of coastal communities to extreme storms: the case of Revere, MA., USA. *Mitigation and adaptation strategies for global change*, 3(1), 59–82.
3. Smit, B., Burton, I., Klein, R. J., & Wandel, J. (2000). An anatomy of adaptation to climate change and variability. *Climate Change*, 45, 223–251.
4. Olmos, S. (2001). Vulnerabilities and adaptations to climate change concepts, issues, assessment method. *Climate Change Knowledge Network (CCKN)*, 1–16.
5. Wahid, S. M., Alam, M. J., Rahman, A. (2002). Mathematical river modelling to support ecological monitoring of the largest mangrove forest of the world—the Sundarbans. In *Proceedings of First Asia-Pacific DHI software conference*, Shanghai (17–18 June).
6. Unnikrishnan, A. S., & Shankar, D. (2007). Are sea-level-rise trends along the coasts of the north Indian Ocean consistent with global estimates?. *Global and Planetary Change*, 57, 301–307.
7. Purkait, B. (2009). Coastal erosion in response to wave dynamics operative in Sagar Island. *Frontiers of Earth Science*, 3, 21.
8. Coch, N. K. (1994) Geologic effects of hurricane. *Geomorphology*, 10, 37–63.
9. Kotal, S. D., Kundu, P. K., & Roy Bhowmik, S. K. (2009). An analysis of sea surface temperature and maximum potential intensity of tropical cyclones over the Bay of Bengal between 1981 and 2000. *Meteorological Applications*, 16, 169–177.
10. Mitra, A., Gangopadhyay, A., Dube, A., Schmidt, A. C., & Banerjee, K. (2009). Observed changes in water mass properties in the Indian Sundarbans (northwestern Bay of Bengal) during 1980–2007. *Current Science*, 97, 1445–1452.
11. Rahman, S. M. D. (2007). *Sundarbans A large biodiversity-rich unique Mangrove ecosystem*. Presentation: IDEC, Hiroshima University.
12. Mitra, A., Chowdhury, R., Sengupta, K., Banerjee, K. (2010). Impact of salinity on Mangrove of Indian Sunderbans. *Journal Coastal Environment*, 1, 41–47.
13. Gopal, B., Chauhan, M. (2006). Biodiversity and its conservation in the Sundarban Mangrove ecosystem. *Aquatic Sciences*, 68, 338–354.
14. Sen, H. S., & Oosterbaan, R. J. (1992). *Research on water management and control in the Sundarbans, West Bengal India*. Wageningen Netherlands: Annual report of International Institute for Land Reclamation and Improvement.

15. Varkey, M. J., Murty, V. S. N., Suryanarayana, A. (1996) Physical oceanography of the Bay of Bengal and Andaman Sea. *Oceanography and Marine Biology*, 34, 1–70.
16. Hasternath, S., & Lamb, P. J. (1979). *Climatic atlas of the Indian Ocean*. Madison: University of Wisc.
17. Hazra, S., Samanta, K., Mukhopadhyay, A., & Akhand, A. (2010). *Temporal change detection (2001–2008) study of Sundarban*. Kolkata: School of Oceanographic Studies, Jadavpur University.
18. Singh, O. P., Kumar, K. R., Mishra, P. K., Kumar, K. K., & Patwardhan, S. K. (2006). Simulation of characteristic features of Asian summer monsoon using a regional climate model. *Mausam*, 57, 221–230.
19. Gopinath, G., & Seralathan, P. (2005). Rapid erosion of the coast of Sagar island, West Bengal-India. *Environmental Geology*, 48, 1058–1067.
20. Roy Chowdhury, A. (2011) Post-Aila salinity defeats Sunderbans farmers.

# Development of Sustainable Community



B. G. Jagadeesha Kumar, M. G. Prajwala , V. Vishal , Mohan   
and M. M. Pavithra 

**Abstract** The increasing threat for environmental attributes has led to the onset of adopting sustainability concepts. In India, much importance is not given on systematic community development, rather we are still reigned on conventional methodology that leads to stress on environment and resource depletion caused by various types of pollution and giving no scope for community development on a larger scale. The prime focus is to look into water management, rainwater harvesting, vertical growth and vertical farming, zero waste management, green energy usage, water source management, etc., and integrating all these on a site-specific scenario. Through this project, a self-sufficient and future stable community is being achieved by self-production of energy through available solar, biomass and other energy sources, and water demand is trying to be sufficed by different water conservation methods using the available water and providing a green corridor for community health.

**Keywords** Community design · Water sustenance · Energy sufficiency · Green productivity · Vertical development

## 1 Introduction

### 1.1 Need and Justification for Sustainable Community

In India, from the past, where the revolutionary period rolled down there has been a rapid change in the field of automobile industry, IT, telecom industry, infrastructural development field, etc. Since all these industries stood up with a very fast pace so as people also thought upgradation and development in these fields are the signs of progress in one's life. On the later stages, when there was huge mass migration of people from rural to urban zone infrastructure field took a bloom then marked the beginning of township, municipalities, urban development projects, urban planning

---

B. G. J. Kumar · M. G. Prajwala · V. Vishal · Mohan (✉) · M. M. Pavithra  
Civil Engineering Department, RIT, Affiliated to VTU, Bengaluru, India  
e-mail: [mohankulkarnijalihal@gmail.com](mailto:mohankulkarnijalihal@gmail.com)

© Springer Nature Singapore Pte Ltd. 2020  
S. Saride et al. (eds.), *Advances in Geotechnical and Transportation Engineering*,  
Lecture Notes in Civil Engineering 71,  
[https://doi.org/10.1007/978-981-15-3662-5\\_12](https://doi.org/10.1007/978-981-15-3662-5_12)

and design, layout planning and housing, etc., where tapping of resources for basic human needs went on and led for huge dependency on non-renewable resources, coming up to this generation also the dependency is increasing with increase in population through technology. As a result of which all the parameters in nature have become critical and is on a verge of crisis, so in order to save our environment and maintain the ecological balance for future genre we gave to optimize the use of renewable energy resources, going for smart management of resources by adopting some balanced sustainable technologies, so achieving up all these can be done at the bottom-line level, i.e. at the “community level” by doing so we can try to stop imbalances in resource distribution, crisis of resources, curb out the saturation of local resource, improve the air quality, increase the green cover and precipitation and optimize the land usage at the urban level. As urban zones are the heart of a city/town achieving sustenance at this level with proper technologies that are adopted can be able to manage the resources and not lead that for depletion (Figs. 1, 2 and 3).

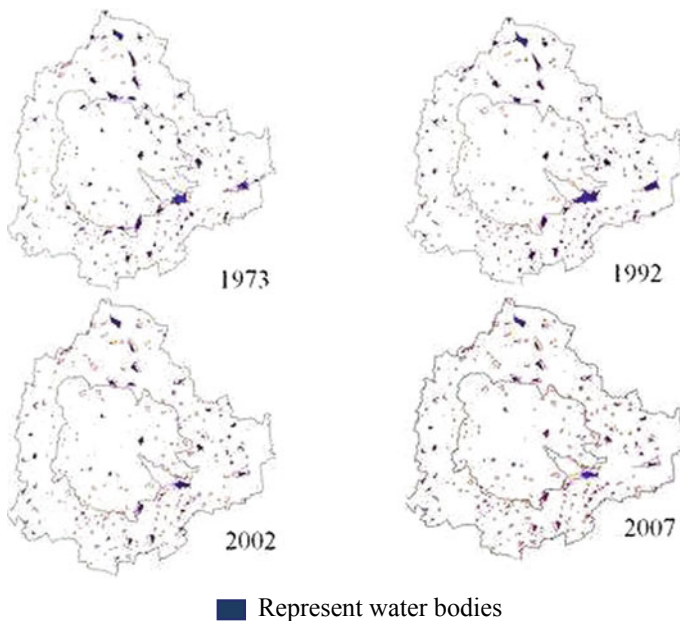


**Fig. 1** Temporal (1973–2007) changes in number of water bodies in Greater Bangalore. Urban floods: case study of bangalore; T. V. Ramachandra and Pradeep P. Mujumdar—Energy and Wetlands Research Group, Centre for Ecological Sciences, Department of Civil Engineering, Indian Institute of Science, Bangalore—560012, India

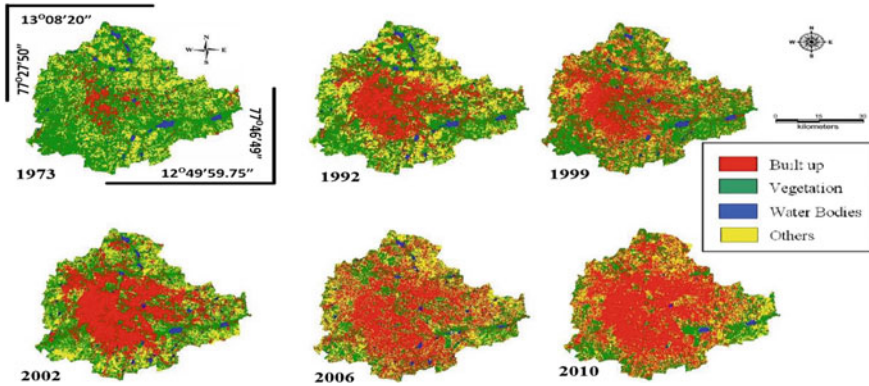


**Fig. 2** Temporal urban dynamics—Greater Bangalore since 1973. Greater Bangalore: emerging urban heat island; T. V. Ramachandra and Uttam Kumar—Energy and Wetland Research Group, Centre for Ecological Sciences, Indian Institute of Science

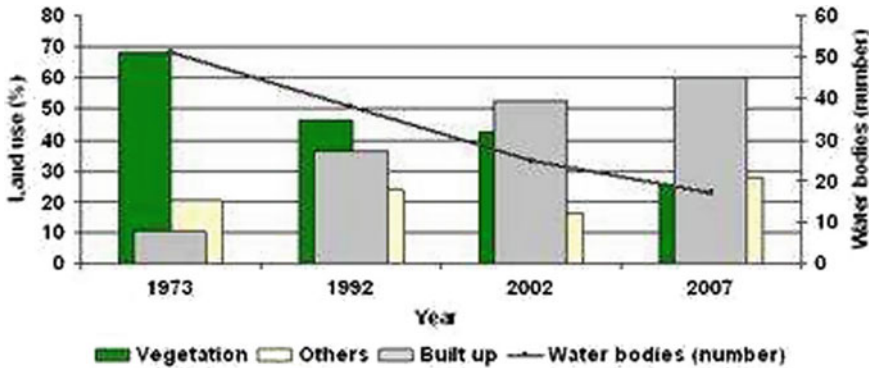


**Fig. 3** Change in land use in Bangalore between 1973 and 2001. Urban floods: case study of Bangalore; T. V. Ramachandra and Pradeep P. Mujumdar—Energy and Wetlands Research Group, Centre for Ecological Sciences, Department of Civil Engineering, Indian Institute of Science, Bangalore—560012, India

**1.2 Sustainability Domains and Possible Management**

- a. **Community area and other amenities**—As we can witness that all the layout or community are been plotted on a horizontal distribution basis where in having an intention for plotting more number of sites. Going for adopting vertical growth or development is the only choice left for optimizing the land usage effectively and giving space for inducting other basic amenities with vertical growth at the community level is a mere effective way of solving haphazard land usage.
- b. **Water usage and management**—Water has been a critical resource to handle the need for both primary and secondary purposes. The demand for it is been



extensively increasing where there is failure in supplying the same. So, as a result of it, there is to be smart resource technology to be adopted like rainwater harvesting, water treatment process, sewage treatment process, rainwater collection basins making it impervious, storage of water in closed reservoirs and delineating the dependency of groundwater and trying to suffice it with available sources of water.

- c. **Energy usage and management**—The next major parameter which is on a depletion verge is energy finding sustenance in this field is talk of the hour as there is huge dependency on coal, anthracite, etc., which is going in for electricity production. But that is not going to spare for long time as there depletion of non-renewable resource (coal) on large scale switching on for green energy supply like solar grid, windmills, etc., at the community level basically decentralizes the dependency on conventional supply.
- d. **Waste recycle and reuse**—Waste management has been an issue and also been a threat for environment and society managing it right away at its disposal seems to be challenging but managing them at the micro-level in a community like treating the grey water, black water and reusing them for secondary purposes using the organic waste as manure seems to be balanced at community level giving an approach for “zero waste” community and as well plastic free.
- e. **Green cover and productivity**—Major concern for finding imbalances in ecosystem is due to depletion of local plants and trees in urban zone and losing out fertility of soil, thereby losing scope for farming, decrease in groundwater level, very great extent of air getting polluted, high increase in temperature where land is getting converted as heat islands, thereby affecting the ambience. In order to tackle these issues going for vertical farming, dairy production, planting local plants and trees, etc., at the community level can to probable extent bring out positive changes to environment and the locality.

## 2 Case Study for Development of Sustainable Community

The development of sustainable community mainly depends on the community planning, achieving water sustenance, energy self-sufficiency, waste management and green landscaping along with the use of sustainable materials for construction. The same domains are further discussed in detail to complete the sustainable community along with a case study [1–11].

### 2.1 Background

See Figs. 4, 5 and 6.



**Fig. 4** Top view of an existing community layout. Topographical pictures from Google maps; Tavarekere, Bangalore—562130. Case study area

### 2.1.1 Land Details

See Figs. 7, 8 and Table 1.

### 2.1.2 Wind Direction

The surface winds in Bangalore have seasonal character with the easterly components predominating during one period followed by the westerly in the other. The high wind speed averages 17 kmph during the westerly winds in the month of July and a minimum of 8–9 kmph during the months of April and October (Table 2).

**Fig. 5** Conventional layout plan. Information collected from the layout planners during survey



## 2.2 Community Planning

### 2.2.1 Population Details

- Here, as we are giving sustainable approach at the community level for community development, conventionally the layout that is near Tavarekere, Doddaladamaru, SLN City have planned out for 600 sites with horizontal housing concept with an area of 3,148,800 sq. ft.
- As of our project focuses on vertical housing concept, we have turned out the number for 1200 sites.
- With the latest data and statistical info of having delineating joint family in urban zone and going out for nuclear or independent families, we have taken it has five persons per house.
- So mathematically convening,
  - Total of 1200 sites
  - Five persons per house/site

Totally that rounds up for = 6000 population.

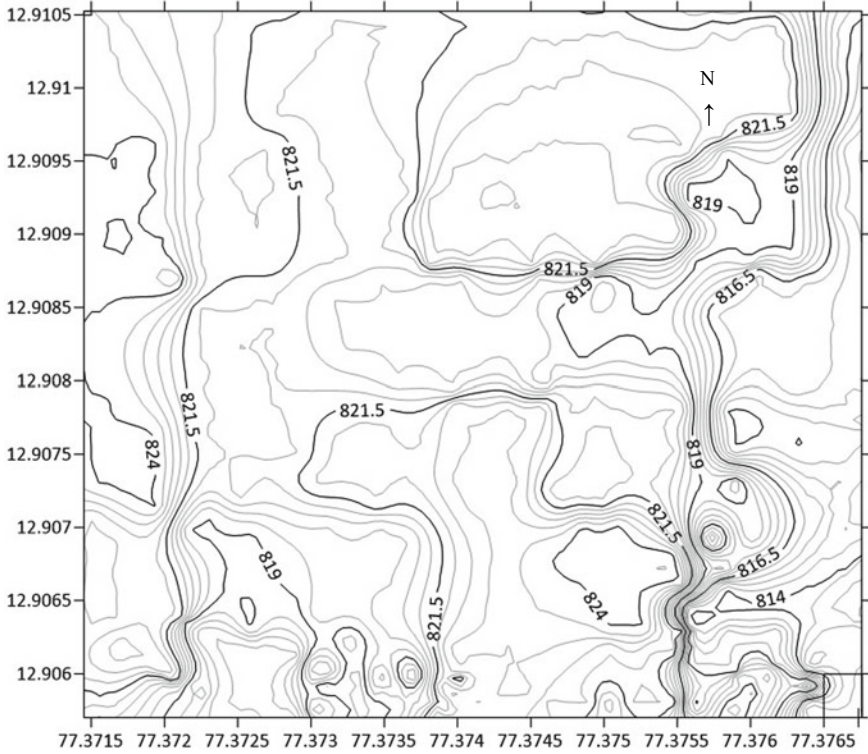


Fig. 6 Contours of the conventional selected area. Contours obtained using Google earth and physical survey done at the site

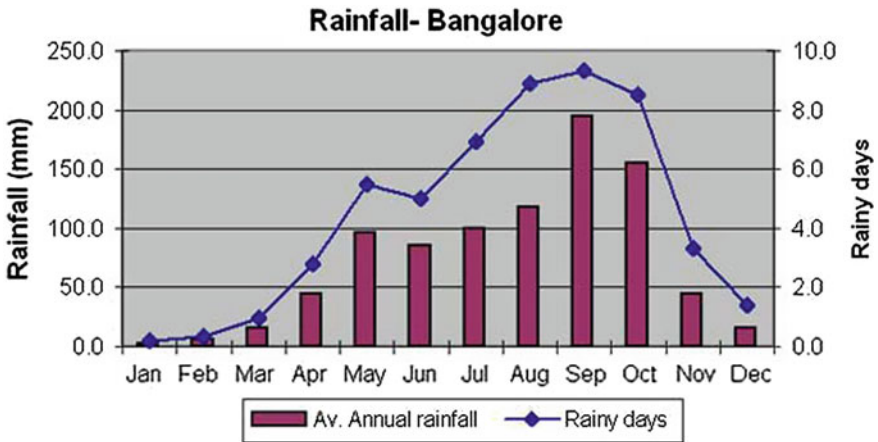
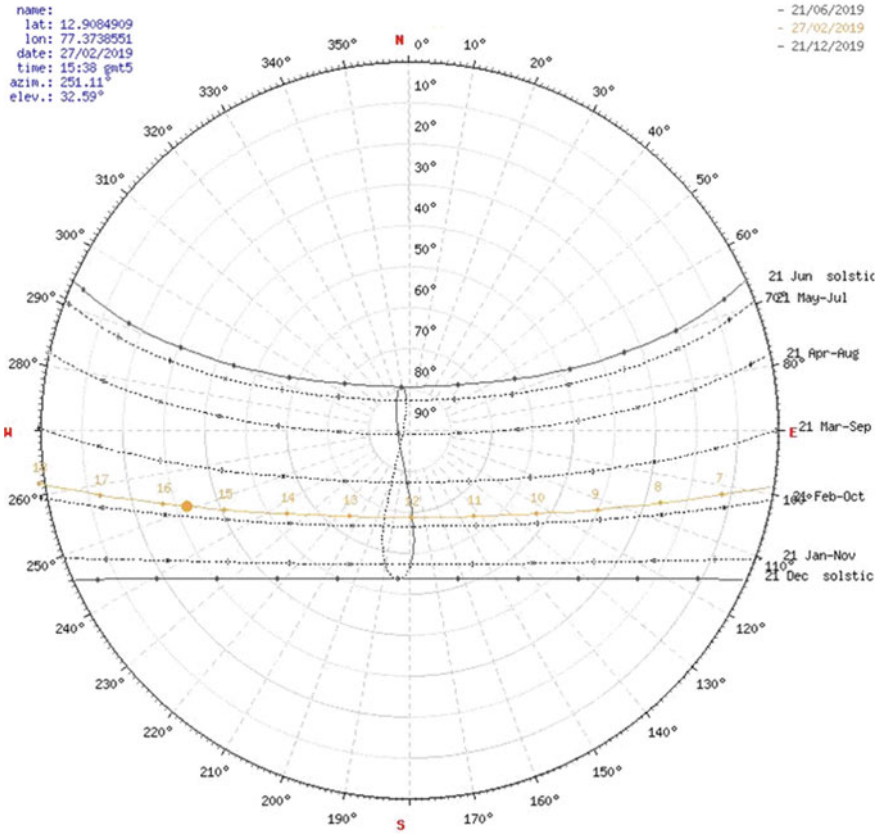


Fig. 7 Rainfall data for Bangalore. Data collected from Indian Meteorological Department, Bangalore



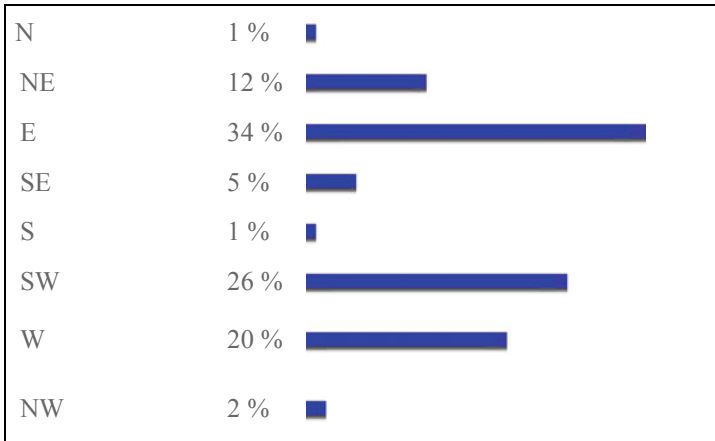
**Fig. 8** Sun path diagram at the location. Data collected from Indian Meteorological Department, Bangalore

**Table 1** Land details

Description	Data
Place	Ajjanhalli, Tavarekere Hobli, Bengaluru Rural—562130, near Dodda Alada Mara (big banyan tree)
Site area	3,148,800 sq. ft.
Sites distributed over this land	600 sites of (20 × 30, 30 × 40 and 40 × 60)
Geographical coordinates of the site	12°54'29" N; 77°22'26" E
Climatic/weather conditions	Tropical savanna climate 15–35 °C
Road network for project site	Site is connected with 40 ft. road
Nearby water sources	Pond of area 1.27 ha
Rainfall data	887 mm per annum

Data collected from survey at Indian Meteorological Department

**Table 2** Wind data



Data collected from Indian Meteorological Department, Bangalore

### 2.2.2 Amenities

The name indicates itself that these are the things that have to be given within the community for well-being. In this junior, the main emphasis is given on all domes well within community like residential plots, shopping complex, sports club, library, PHC (primary healthcare centre), garage, farming, dairy, etc., where in all these are subjected for “vertical growth” within community for smart land usage.

- The total layout area stretches out for 29.513 ha, i.e. 3,148,800 sq. ft.
- Basically, the total amenities consume upon 4.9 ha, i.e. 531,640 sq. ft.
- This renders out to a total percentage of 16.8% of total land use.
- The remaining space is best utilized for treatment units, parks, swimming pool, solar enabled jogging path, solar grid plant, green cover with locally available plant and tree species.

### 2.2.3 Summary

- The main shape of the residential plots comes out as an “oval” shape which appeals like that from the top view of the community plan.
- The backdrop of the shape is justified based on some local geographical, topographical and wind direction conditions.
- Usually, the wind direction and intensity are directed to be more in south–west and east direction for that layout and the prevailing conditions.
- By adopting to local wind directions conditions that shall give good cross ventilation and air movement within community.

- Helps out in maintaining the same temperature conditions inside the house and buildings.
- Totally there are 20 buildings in the community for residence with each building coming up in alternate manner.
- Each building having a dimension of 108' \* 108' ft. where in comes out to be 233,280 sq. ft. in total of occupancy.
- Just by going out in percentage turns out to be 7.4% of the total area for residential buildings.
- The buildings totally comprise of 1200 sites in all where in each building is of 16 floors, i.e. (G + 15) with the ground floor going for parking space completely.
- With going out for detailing of each house it figures out to be with two conditions:
  - Without setbacks—45' \* 45'.
  - With setbacks—60' \* 60'.
- The conditions given are in concerned with bylaw principles and its implications.
- On the peripheral of the resident slot is the jogging path mounted with the solar panels for green energy.
- Going with the ground aspect of it usually the layout is of varied elevations throughout with different R. L's based on it required amount of cutting and filling is done for convenience.
- To be specific the residential slot is on 819, 820, 821.5 R. L's on a bit of elevated portion of layout where in is having easy access for water, supply conduits to run along with the gravity for treatment units.
- The drainage system between the buildings usually carries the run-off water and is diverted to specially to underground conservation galleries.

The sump for drinking and secondary purpose use is been clustered for better usage and supply among the buildings (Fig. 9).

Thus, we have adopted vertical development which has 16 stories of 20 buildings provided with 1200 houses accommodating 6000 population (Fig. 10).

Vertical development is the only key for solving the problems of land usage and optimization. Thus, by adopting vertical development around 83.2%\* of the land will be for providing other amenities while only 16.8%\* of the land is used for construction. This results in providing all the commuters with their basic necessities of shelter and other amenities required along with which the 83.2% of the land can be utilized for the betterment of the society and achieving self-sufficiency and sustenance (\* as per design).

### ***2.3 Achieving Water Sustenance***

Water is one of the most critical aspects of today's world. Humans have depleted the existing 1% of available freshwater on earth and we see how fast the depletion is happening to an extent that in the next 20–50 years we are going to be left with



Fig. 9 Sustainable community plan. Designed data after analysis

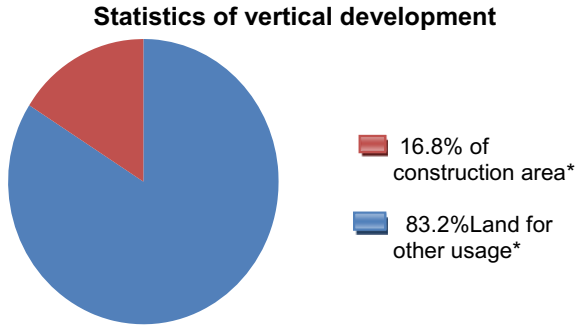


Fig. 10 Statistics of vertical development. Note \*As per designed data in 2

no freshwater but with increased saline waters. Thus, its everyone’s responsibility to protect the water resources and also consciously conserve it. Achieving water sustenance is the most important and critical part of a sustainable community which can be achieved by the following;

**Calculation of Water Requirement:**

See Table 3.

**Calculation of Water from Different Sources:**

See Table 4.

- Underground storage reservoirs are constructed to store the water.
- Closed storage reservoirs and pipe networks will be suggested so as to avoid evaporation losses.



**Table 3** Water requirement (Designed data after analysis)

Sl. No.	Purpose	Calculation	Quantity (litres/annum)
1	People	$6100 \times 135 \times 365$ (Population $\times$ lpcd $\times$ 365)	$300.58 \times 10^6$
2	Farming	$1600 \times 3 \times 365$ (No. of plants $\times$ litres per day $\times$ 365)	$1.75 \times 10^6$
3	Dairy	$250 \times 135 \times 365$ (No. of cows $\times$ litres per day $\times$ 365)	$12.32 \times 10^6$

Total water requirement =  $314.65 \times 10^6$  L/annum

**Table 4** Water from different sources (Designed data after analysis)

Sl. No.	Source	Quantity (million litres/annum)
1	<i>Rainwater</i>	
	• Rainwater harvesting (rooftop) (roof top area $\times$ 0.8 efficiency)	29.84
	• Surface run-off (total surface area other than roof top $\times$ 0.4 efficiency)	126.25
2	<i>Treated water</i>	
	{ $300.58 \times 10^6 \times 0.8 \times 0.8$ } (Water supplied $\times$ % of water that reaches TP $\times$ TP efficiency)	192.37

Total water getting from sources = 348.46 million litres/annum

- Base of collection basins will be made impervious to avoid percolation losses and water that will be collected in collection basins will be sent to the underground storage reservoirs through the underground piping system.

**Note** The whole community reaches self-sufficiency in water with one time supply of water for the population either from rain harvested water, or external intake or underground water table (Fig. 11).

### Critical Aspects of Water Sustenance:

Initially supplying water to the community is a challenging task, this can be achieved by initially taking water from other natural water bodies or from external supply just for once after which this water will be recycled and reused again and again.

Secondly, the rainwater harvesting is critical for a duration of two years after which the run-off water will be easily available for community usage.

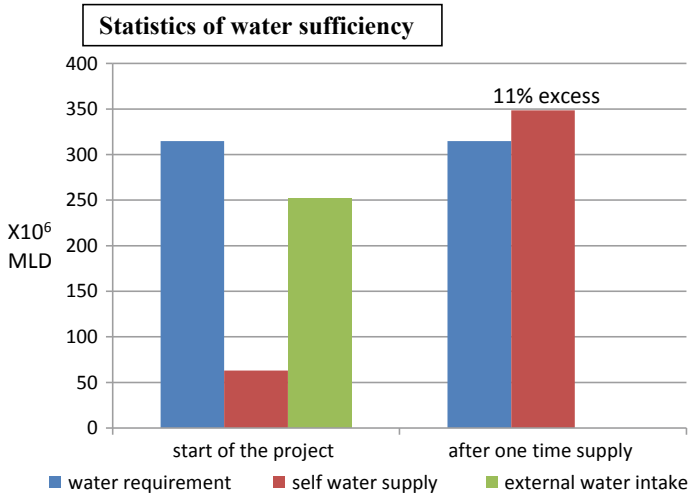


Fig. 11 Statistics of water sufficiency. Designed data after analysis

### 2.4 Energy Self-sufficiency

The second most important aspect of a sustainable community is energy which includes electrical energy as well as other energy such as biogas energy for cooking, etc. In this design, we are providing electrical energy sufficient for the community of 6000 population to sustain along with other amenities that are provided.

It is important to note that we are using renewable energy resources to generate electricity and secondly organic waste produced from the community as well as dairy in the community to generate biogas that will suffice the cooking and primary processes.

The following two criteria are considered is attaining energy self-sufficiency;

#### Calculation of Electricity Requirement

See Table 5.

##### 2.4.1 Electricity Production

From solar grid:

- Assuming 250 W solar panel with an efficiency of 60% and gives production output of 150 W per hour.
- Power produced from a solar panel unit = 150 × 5 (Assuming 5 h of production per day).
- 30,000 panels will be installed in the community which produces 22.5 mW of electricity per day.

**Table 5** Electricity requirement (Designed data after analysis)

Sl. No.	Purpose	Electricity needed	Total (Watts/day)
1.	Houses	$4720 \times 1200$ (Demand per house $\times$ no. of house)	$5.66 \times 10^6$
2.	Lift	$180 \times 10^3 \times 2 \times 20$ (Demand per unit $\times$ no. of lifts)	$7.2 \times 10^6$
3.	Parking	–	$53.76 \times 10^3$
4.	Library	–	$10.25 \times 10^3$
5.	Sports club	–	$2.4 \times 10^3$
6.	Primary health centre	–	$4.27 \times 10^3$
7.	Dairy	–	$55.7 \times 10^3$
8.	Treatment plant	–	$49.7 \times 10^3$
9.	Vertical farming	$36 \times 10^3 \times 30$ (Power needed for single floor $\times$ no. of floors)	$1.08 \times 10^6$
10.	OHT	$1492 \times 4 \times 8$ (Power needed for single pump $\times$ no. of pumps $\times$ hours of working)	$47.7 \times 10^3$
11.	Commercial complex	–	$1.2 \times 10^6$
12.	Biogas plant	–	$3.73 \times 10^3$
13.	Other misc.	–	$121 \times 10^3$

Total electricity requirement =  $20.516 \times 10^6$  Watts/day

- 1 panel covers 18.82 sq. ft. area and 22,600 panels can be installed and the boundary of community as solar belt/grid.
- Power produced from solar grid at boundary stretch:

$$22,600 \times 150 \times 5 = 16.95 \times 10^6 \text{ Watts/day} - 16.95 \text{ mW/day}$$

- Remaining 7400 panels will be installed on the top of jogging path and commercial buildings.

From windmills:

Windmills are the parallel source for electricity production that will be utilized in critical conditions and are kept as backup source. Eighty no. (4 no. of windmills on each building) of mini windmills will be installed on the top of residential complex which will be producing electricity around 2 mW/day and this power can be utilized for various purposes.

### 2.4.2 Biogas

- Around 1500 kg of waste that is produced from dairy, kitchen and other organic waste in the community will be used as raw material for the production of biogas.
- Six no. of digester will be kept for the production of biogas with detention quantity of 10 cumec each.
- Biogas produced in each unit will be supplied to the kitchen use.
- Waste output from biogas plant can be reused as manure.

## 2.5 Waste Management

Waste is a critical aspect today. Generation of waste is always there while approaching a zero waste community through different ways is a major and challenging task. The sustainable community is the one in which zero waste is achieved. The different types of waste and its recycle and reuse are being discussed and shown in Table 6.

Thus, all the waste that will be produced in the community is taken care of leading to zero waste community.

### 2.5.1 Treatment Plants

It is well-known fact to all that 80% of the water that is used per person will be wastewater. By treating these waters through initial separation water can be reused for further purposes. There will be two treatment plants provided (Table 7).

**Table 6** Waste management

Sl. No.	Type of waste	Type of treatment	Reused for
1.	Grey water and run-off water	Water treatment plant	Drinking purposes
2.	Black water	Waste water treatment plant	Secondary purposes
3.	Night soil and organic waste	Biogas plant	Domestic burning—cooking
4.	Organic sludge	–	Natural fertilizer for agricultural fields
5.	Primary medical waste	Local incineration	–
6.	E-waste	Exported after segregation	–
7.	Plastic waste	Segregation <i>n</i> further recycle	–

**Table 7** Treatment plants

Sl. No.	Type of wastewater	Treatment plant	Reused for
1.	Grey water and run-off water	Water treatment plant	Drinking purposes
2.	Black water	Waste water treatment plant	Secondary purposes <sup>a</sup>

<sup>a</sup>Secondary purposes include activities like washing vessels, washing machines, sinks, flushing and gardening

## 2.6 Green Cover and Productivity

Earth does not belong to us, we belong to the earth. As the quote says, it is our responsibility to use the resources judiciously. Due to rapid urbanization and development, afforestation has met a new line depleting the green cover affecting the climate, species and drastic changes in the biosphere. To overcome these issues, the key to the solution is vertical development which leads to decreased land usage while using the other land reforestation.

A sustainable community is where we maintain ecological balance, maintain improved air quality and have productivity. Therefore, the community has been provided with vertical farming, dairy and tree-planting of different productivity.

### 2.6.1 Vertical Farming

Producing food to a community level for only few essentials like leafy vegetables and vegetables is provided so that the outreach of commuters for markets reduces and also at low cost, generating revenue to the community.

Tomato, onion, coriander, brinjal, chilly, etc., and such crops are grown in the vertical farm.

### 2.6.2 Dairy

Dairy is being provided for a community of 6000 people consisting of 250 cows in a vertical building which helps in producing milk and milk products also generating employment and revenue for the community. The dairy waste mostly consists of organic waste with which we can produce biogas and reach sufficiency in producing biogas for the community and its purposes.

## Design

The dairy is being done on a vertical basis. The dairy consists of a building of dimensions  $108 \times 108$  in three stories accommodating 200 cows and 50 buffaloes.

The ground floor is provided with processing units, storage and shops for marketing the milk and its products.

Dairy farming generated employment as well as revenue for the community to sustain towards cost-free community.

The building is well ventilated and provided with lifts to move the animals for any purpose. Enough water is being supplied to make sure the cows are healthy and happy.

The food that is required by the cows is being grown around the dairy to meet the demands without any outreach for the food.

All the waste that is produced in the dairy is being utilized for producing biogas and also as fertilizers for the growing crops.

Through this, a community which can produce its own milk products and also biogas sufficient to all residents is being achieved through this.

### 2.6.3 Green Cover

The land that is left after the vertical development accounts to about 80% on which tree-planting is being achieved. Different trees that are locally present and have an affinity to the soil is being chosen and planted which are of different importance. Around 70% of the 31 lakh sq. ft. of the area is provided for tree-planting. The trees which are planted are;

- Trees that provide oxygen throughout the day and night—areca palm, neem tree, papal tree, mulberry trees.
- Trees that improve groundwater table—Thesperia Popular [*tulip tree*], Margosa tree [*neem tree*], banyan tree.
- Trees that improve soil fertility—Leguminous plants.
- Trees that produce fruits—Mango tree, custard apples, apple trees, avocado tree, jackfruit trees, papaya trees, banana plants, guava plants and coconut trees.
- Bio-augmentation plants that help in reduce BOD and COD of wastewater.
- Plants and trees that produce leafy and other vegetables.

Thus, by providing all the five important aspects into the community and achieving self-sufficiency in water, energy, improving air quality both indoor and outdoor, producing biogas for the community, planting trees to maintain ecological balance, and thereby achieving sustenance for future so that all the resources that are renewable and not harmful to the environment by any means and also protecting our Earth for future is all about sustainable community.

### 3 Conclusion

Thus, concluding this community is going to become water sufficient, energy sufficient and biogas sufficient in a span of maximum two years. The vertical development is produced only for few leafy vegetables and vegetables not sufficient for the community but reducing the outreach of community. The dairy is going to produce sufficient milk for the community and thus generating revenue. Through this community, underground water table is also improved. The community will become a cost-free community within a span of 2 years. The design of sustainable community is also economically feasible when what we have costed is all the natural resources from the earth (Table 8).

The main motto of the socio-technical project that we come up with this is to not only ink that on paper but to bring on to reality which is in the way to help the society and to protect the nature and give back to “Mother Earth”. As we have portrayed in the above space regarding the conventional practices drawbacks and the only choice that is left out for us to recline on sustainable technologies for future well-being and also highlighting the critical parameters that are crucial to achieve sustenance at the community level. So, as a result of this, there is a high need for adopting sustainable methodologies in the field of water, energy, waste, community housing and green cover where in balance in ecology can be brought about to major extent like around 80% which is of satisfactory level. Conventional modes are having great drawbacks like land congestion, dependency on non-renewable sources, lack of resource management, bulldozing green cover, these are major setbacks that have created room for going for sustainable resources management technology.

**Table 8** Conclusion (Data after analysis)

Sl. No.	Domain	Features	Conclusion
1.	Community planning	<ol style="list-style-type: none"> <li>Vertical development leading to land optimum usage and space for green development</li> <li>Amenities provided help in improving social living and well-being</li> <li>Community design is done according to the wind and sun data collected</li> </ol>	<ol style="list-style-type: none"> <li>16.8% of the land is used for construction while 83.2% of land can be used for green cover</li> <li>Around 6100 population which is more than population that can be accommodated in conventional ways. Such communities result in more civilized societies and reduce environmental impacts</li> <li>As the design is done technically accounting the temperature, weather, wind and sun path futuristic communities that achieve sustenance is developed</li> </ol>
2.	Water sustenance	<ol style="list-style-type: none"> <li>Rainwater harvesting from the roof top with 80% considered efficiency and the surface run-off with 40% efficiency is collected in the collection basins and underground water reservoirs</li> <li>Water treatment plants with 80% efficiency both water and wastewater plants are installed in the community</li> <li>Two large underground water reservoirs are constructed to store the rainwater for the year for further use</li> </ol>	<ol style="list-style-type: none"> <li>Rainwater accounts to 20% of the water demand that will be supplied for the commuters. It is the main source of water reliance</li> <li>The treatment plants supply 80% of the community water requirement. Thus, reaching the demand of the community. While initially either storage of water, underground water or external water intake for one time is inevitable</li> <li>The underground water reservoirs act as suppliers of water for dairy, farming and for the green cover provided. Thus, achieving water sustenance</li> </ol>
3.	Energy sufficiency	<ol style="list-style-type: none"> <li>Solar grid is the primary source of energy for the community</li> <li>Windmills (shaftless, lightweight) are installed on the top corners of the high rise buildings</li> </ol>	<ol style="list-style-type: none"> <li>The solar grid alone supplies the community with the necessary energy requirement. This can be stored for the further usage during other than summer seasons</li> <li>Wind energy is the secondary source which can be used during off-season or other purposes</li> </ol>

(continued)



Table 8 (continued)

Sl. No.	Domain	Features	Conclusion
		3. Biogas plant is provided that is self sufficed to the community is provided	3. The organic waste that is produced in the community along with the farm waste and diary waste is used for the production of biogas which can be used for cooking purposes within the community
4.	Waste management	Waste, as mentioned and described, is well managed by fundamental segregation, reuse and reuse	With this type of management, the contribution of waste from the community is going to be useful and productive rather than deteriorating the nature
5.	Green cover and dairy	1. Green cover which includes mostly different and locally productive types of trees inside the community 2. Vertical farming of local and favourable crops inside community 3. Dairy farming	1. This green cover helps in reducing the carbon production and also helps in providing a healthy atmosphere for the commuters and for future 2. This vertical farming helps in inculcating farming in the community and also generates revenue 3. This dairy farming produces milk and products for the community with sufficiency and also provides manure for biogas as well as generating revenue for a mutual well-being of the community

**Acknowledgements** This is to summon that for any thought or idea regarding the project to come up and to work on it there has to be some strength or support. We in the way to express our gratitude would like to thank our guide/Professor Dr. Jagadeesha Kumar and our institute RIT, Bengaluru for getting us an opportunity to making this happen and supporting us in this regard.

## References

1. Dale, A., & Newman, L. L. (2009). Sustainable development for some: Green urban development and affordability.
2. Schlebusch, S., & Cilliers, E. J. (2013). *Planning for sustainable communities: Layout and design approaches*. Potchefstroom, South Africa: North-West University.
3. Rusko, M., & Procházková, D. (2011). Solution to the problems of the sustainable development management.
4. Irvine, G., Lamont, E. R., & Antizar-Ladislao, B. (2010). Energy from waste: Reuse of compost heat as a source of renewable energy.
5. School of Engineering, Institute for Infrastructure and Environment, University of Edinburgh.
6. Adelekan, B. A. (2012). Recent advances in renewable energy: Research, applications and policy initiatives—IAR.
7. Elnimeiri, M., Susorova, I., & Kim, H.-I. *Sustainable structures and architectural forms of tall buildings*. Chicago, USA: CDCI.
8. Mekala, G. D., & Davidson, B. (2007). *Waste water reuse and recycling systems*.
9. Chance, T. (2009). Towards sustainable residential communities; the Beddington zero energy development (Bedzed) and beyond.
10. Suridechakul, W. (2015). Factors affecting sustainable community development: A case study of Dusit district community.
11. Zhivov, A. M., Case, M., & Liesen, R. (2014). *Energy master planning towards net-zero communities/campuses*.

# Cinder Coal-Aggregate Quality Index (AQI) Appraisal Based on Weighted Arithmetic Index Method and Fuzzy Logic



Penki Ramu , J. Y. V. Shiva Bhushan , B. Shravani and I. Nagarani

**Abstract** Strength is a major criterion for aggregates which are used in the design of a flexible pavement structure. So, an engineer assumes a certain degree of responsibility for each material to be used, so it is the duty of the engineers in the field to validate the materials by regular tests. The quality of the materials used plays a key role in determining the strength and durability of the infrastructure projects. As flexible pavement contains number of layers among them the surface course being the highest load-bearing layer in the flexible pavement, material like cinder coal is tested for the same. The representation of all the quality indicators added in a single form is called ‘quality index’ which makes it easy to obtain the composite influence of all the quality parameters in that system and also helps to compare the general quality of the aggregate with a unit value. The quality of aggregates was determined by using weighted arithmetic index method and fuzzy approach to judge its potentiality for the surface course. Crushed stone aggregate and cinder coal materials were been used to compare the feasibility for the desired application. Cinder coal is an industrial by-product which is obtained from combustion of coal. Tests were conducted to determine the physical properties of aggregates and cinder coal, and the obtained results were used for calculating the quality index. From this study, it was observed that cinder coal has a net fuzzy value of ‘86%’, which indicates ‘unfit’, whereas for conventional aggregate (crushed stone), it is ‘30.75%’, which indicates ‘good’ for the surface course. Fuzzy value is used to characterize and disseminate uncertainties and inaccuracies in data and functional relationships.

**Keywords** Cinder coal · Fuzzy logic · Quality index · Weighted arithmetic average method

---

P. Ramu (✉)  
GMRIT, Srikakulam, Andhra Pradesh, India  
e-mail: [ramu.p@gmrit.edu.in](mailto:ramu.p@gmrit.edu.in)

J. Y. V. Shiva Bhushan · B. Shravani · I. Nagarani  
VNR VJIET, Hyderabad, India  
e-mail: [shivabhushan\\_jyv@vnrvjiет.in](mailto:shivabhushan_jyv@vnrvjiет.in)

© Springer Nature Singapore Pte Ltd. 2020  
S. Saride et al. (eds.), *Advances in Geotechnical and Transportation Engineering*,  
Lecture Notes in Civil Engineering 71,  
[https://doi.org/10.1007/978-981-15-3662-5\\_13](https://doi.org/10.1007/978-981-15-3662-5_13)

## 1 Introduction

Industrialization and globalization have led to massive growth in mega construction projects such as the construction of the roads which led to the demand in transportation. Rapid economic development and population growth have led to the depletion of natural resources making it a major concern in our society. Improper resource usage leads to economic, social and political issues. Improper utilization of resources and discarding them is leading to environmental problems like ecosystem degradation. Cost of construction for infrastructure projects has also posed a severe problem, which alarmed the international scientific communities to find out new alternative solutions so as to have sustainable development. Due to the recent development in the construction of roads with new design methods and materials, the Indian Road Congress has revised the guidelines for flexible pavement design, wherein the use of alternate materials and stabilized layer has been incorporated by suggesting more research for Indian conditions. Industrial by-products can be investigated in economic and environmental aspects for the suitability of the flexible pavement layers as a full or partial replacement.

Inorganic waste produced by burning black coal in the boiler house is cinder coal (CC) [1]. This product can become an important resource and a substitute for aggregates. An important characteristic of CC is its high silica content [2] and its related mechanical and durability properties.

Murali Krishna and Sualatha defined this as, 'In response to the need for a uniform understandable yardstick of aggregate quality, scientists worked out to compile all the aggregate quality parameters into some convenient approach to representing an 'INDEX', a procedure generally described as 'aggregate quality index' (AQI)'. Horton defined aggregate quality index as reflecting the composite influence on the overall quality of individual quality characteristics and proposed two basic steps to develop AQI namely: Selection of quality characteristics on which the index is to be based and establishing of a rating scale for each characteristic giving weight to each parameter [3]. The simple AQI model and weighted arithmetic index method expressed by Brown et al. (1972) are applied in this study [4]. With the help of overall aggregate quality index, one can arrive at a rightful conclusion about the quality of aggregate. In this study, the permissible AQI for construction purpose is 100, i.e. any value above 100 indicates aggregate inherence/weakness, i.e. unfit for construction.

Lotfi A. Zadeh developed fuzzy logic in the 1960s in order to provide mathematical rules and functions that allow natural language queries. Fuzzy logic provides a way to calculate the value between absolute true and absolute false with the resulting value ranging between 0 and 1. With fuzzy logic, it is possible to calculate the degree of membership. Fuzzy sets introduce vagueness by removing sharp boundaries that divide class members from non-members [5]. A fuzzy set is characterized by a unique and distinct function called as the membership function, which is the most common, but not required to express the degree of membership in fuzzy sets by numbers within the closed interval [0, 1]. A fuzzy set is denoted in practice as  $A: X \rightarrow [0, 1]$ , where  $A$  = fuzzy set;  $X$  = universal set;  $X = [0, 1]$  membership function. A fuzzy

set can be represented graphically also. A graph can be plotted. The most common form of membership functions is triangular, although trapezoidal and bell-shaped curves are also used, but the shape is usually less important than the number of curves and their location. Three to seven curves are generally appropriate to cover the required range of input value or the 'universe of discourse' in fuzzy jargon. The fuzzy weighted average (FWA) is a function of fuzzy numbers and is useful as an aggregation method in engineering or management science based on fuzzy set theory. It provides an approximate and discrete solution by means of representation at the level of cuts  $\alpha$  of fuzzy sets and interval analysis.

## 2 Literature Review

Soncim et al. have developed fuzzy models for IRI and FPCI by using different variables which were considered in the questionnaire survey, for the analysis of pavement construction and maintenance [6]. Guo et al. proposed an effective and feasible vibration-based ASAC method by using piezoelectric materials (ceramic) and fuzzy control algorithms for controlling the interior noise of the vehicle [7]. Zehtabchi et al. have developed the fuzzy logic model to analyse the effect of changing the OBC, by changing the percentage of fractured particles (or) by adding granular polymer-modified bitumen on the compressive strength of bituminous mixes [8]. Turki had used an adaptive neuro-fuzzy inference system (ANIFS) for modelling the compressive strength of cementitious mixtures like mortar and roller compacted concrete mixed with shredded worn tyres and filler [9]. Sadrossadat et al. have investigated the efficiency of a powerful hybrid artificial intelligence (AI) paradigm, i.e. adaptive neuro-fuzzy inference system (ANFIS), for predicting the resilient modulus (MR) of subgrade soils [10]. Jeong et al. have presented a method for developing a climate impact assessment system using fuzzy inference to predict the alteration of infrastructure service of the flexible pavement. Brown et al. have observed that the parameter selection is considered as important in calculating the WQI, and consideration of too many parameters might give erroneous results. pH, dissolved oxygen, biochemical oxygen demand, colour, fluoride, chloride, hardness, nitrates, alkalinity, turbidity, sulphates, phenols are the preliminary indicators in determining the quality index of public water supply. The objective of an arbitrary rating scale (32 items) is to assign a value from zero to one to indicate the importance of individual quality parameter considering in a comparative way. Horton has found another approach for rating the scale by giving weightage for various parameters by assigning a value which is inversely proportional to the recommended standard ( $S$ ) for that corresponding parameter [11]. Many researchers studied water quality using fuzzy logic. Notable contributors being Dr. S. Mohan et al., and Dr. C. S. V. Subrahmanya.

### 3 Methodology

In this study, Cinder aggregate samples (as shown in Fig.1) and Crushed aggregates are collected from Coal-Linde India Gas Company and Hyderabad regions respectively, and have been tested.

Methodology in Calculating AQI Using WAAQI Method and Fuzzy: The aggregate quality index (AQI) of both the materials was calculated using weighted arithmetic average index method (WAAQI) and the quality rating ( $Q$ ) corresponding to an indicator, which is a number reflecting the relative value of this parameter.

**Step 1:** Collection of data of various aggregate properties or quality parameters.

**Step 2:** Calculation of proportionality constant 'K' value using formula

$$K = \left(1 / \left(1 / \sum_{i=1}^n S_i\right)\right) \quad (1)$$

where ' $S_i$ ' is standard value for  $n$ th parameter.

**Step 3:** Calculation of  $Q_i$  for  $n$ th parameter. The quality rating is calculated by using following expression  $Q_i = \{(M_i - I_i) / (S_i - I_i)\} * 100$ , where  $M_i$  = estimated values of the  $i$ th parameter in the laboratory,  $I_i$  = ideal values of the  $i$ th parameter  $I_i = 0$  for all the parameters except for angularity number as 7.0,  $S_i$  = standard values of the  $i$ th parameter. The sign (-) indicates the numerical difference between the two values ignoring the algebraic sign. All the ideal values ( $I_i$ ) are taken as zero except AN = 7.

**Step 4:** Calculate unit weight for the  $n$ th parameters. Unit weight ( $W_i$ ) value inversely proportional to the recommended standards ( $s_i$ ) of the corresponding parameter.  $W_i = (k/s_i)$ , where,  $s_1, s_2, s_3 \dots s_i$  are standard values of various parameters from 1, 2, 3,  $i$ .

**Step 5:** Calculate aggregate quality index (AQI) using formula

$$AQI = \left\{ \sum_{i=1}^n (W_i * Q_i) / \sum_{i=1}^n (W_i) \right\} \quad (2)$$

Fig. 1 Cinder coal aggregate



**Table 1** Aggregate quality rating by fuzzy value method

Fuzzy value	Aggregate quality rating
0–25	Excellent
26–50	Good
51–75	Poor
76–100	Unfit

The overall aggregate quality index (AQI) was calculated by aggregating the quality rating ( $Q$ ) with unit weight ( $W_i$ ) linearly.

**Step 6:** To find out the net fuzzy value, it is necessary to combine all the fuzzy values for various aggregates parameters. The major advantage with the fuzzy logic approach is that the final result of this method gives a single unique value for aggregates that can precisely confirm the extent of inherence or weakness properties. This unique distinct value is called as the net fuzzy value. The net fuzzy value can be calculated using the weightage and the fuzzy values for each aggregate parameters. This calculation is done by using the formula.

$$F_i = \left\{ \frac{\sum_{i=1}^n (W_i * C_i)}{\sum_{i=1}^n (W_i)} \right\} \quad (3)$$

where  $W_i$  = weightage factor,  $C_i$  = fuzzy value. The rating of aggregate by fuzzy value method is shown in Table 1.

The fuzzy value-based aggregate quality index above 75 indicates that aggregate has inherence or weak properties and is unsuitable for surface layer in road construction because of stress distribution in flexible pavement, i.e. grain to grain granular structure.

## 4 Results and Discussion

Cinder coal material and crushed stone aggregate have been taken, and all the aggregate tests were performed, and their properties are mentioned in Table 2. For each aggregate property, the fuzzy value ranges were defined by taking into considering the values mentioned in IRC for surface, base and sub-base courses of flexible pavement. The minimum aggregate crushing and abrasion value to be suitable for the surface course was 35% and hence any value which is equal to 35% or above 35%, the fuzzy value is taken as '1', and the lesser value was taken as '0'. The values for both the materials alongside the fuzzy curves are shown in Figs. 2 and 3.

The combined value for flakiness and elongation index should be less than 30% for material to be used for surface course, hence any value equal and higher than 30%, the fuzzy value is taken as '1', and a lesser value is taken as '0'. The values for these materials are shown in Fig. 4. Angularity number of aggregates should be in between '0' and '11', and the ideal value for this property is '7' which is a transition

**Table 2** Test results for cinder coal and crushed aggregate samples

Variables	Standards-surface	Cinder coal test results	Crushed stone test results
Aggregate crushing value	<35%	53.05%	22.75%
Abrasion	<35%	52.9%	22.4%
Elongation and flakiness	<30%	6.3%	41.47%
Angularity number	0–11	4%	7.802
Specific gravity	2.5–2.9	2.492	2.653
Water absorption	0.1–2%	4.25%	0.75%
Aggregate impact test	<30%	39%	18.97%

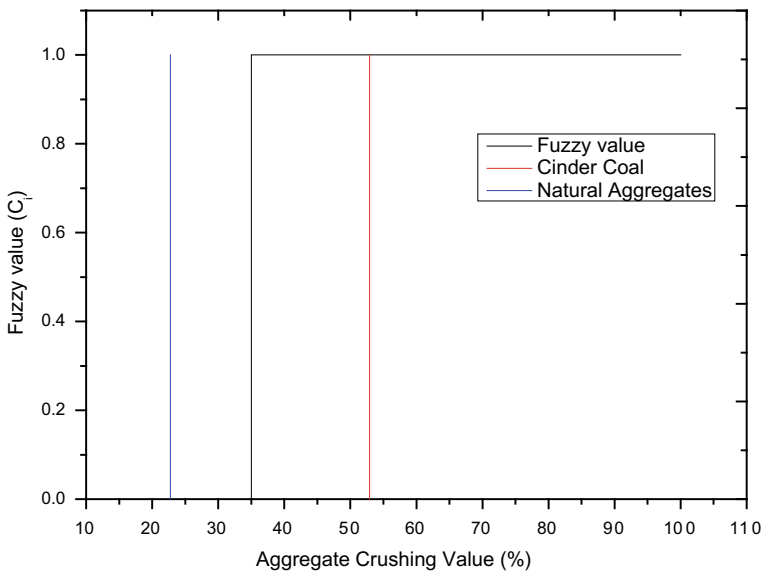


**Fig. 2** Fuzzy membership function graph for aggregate crushing value

zone for a rounded shape to angular shape. Hence, the fuzzy value is taken as a linear curve with a positive slope as shown in Fig. 5, and the fuzzy values obtained for CC and crushed stone aggregate were mentioned in Table 3. The specific gravity range is taken from 2.5 to 2.9, and the fuzzy graph is linear in between those values, and fuzzy value is ‘1’ for materials having less than 2.5 and greater than 2.9 were taken as ‘0’, which is shown in Fig. 6.

Water absorption values for the materials must be as small as possible for pavement applications, hence the fuzzy set was taken from 0 to 2% which varies linearly, and the value greater than 2% was taken as ‘1’. The water absorption of CC and crushed



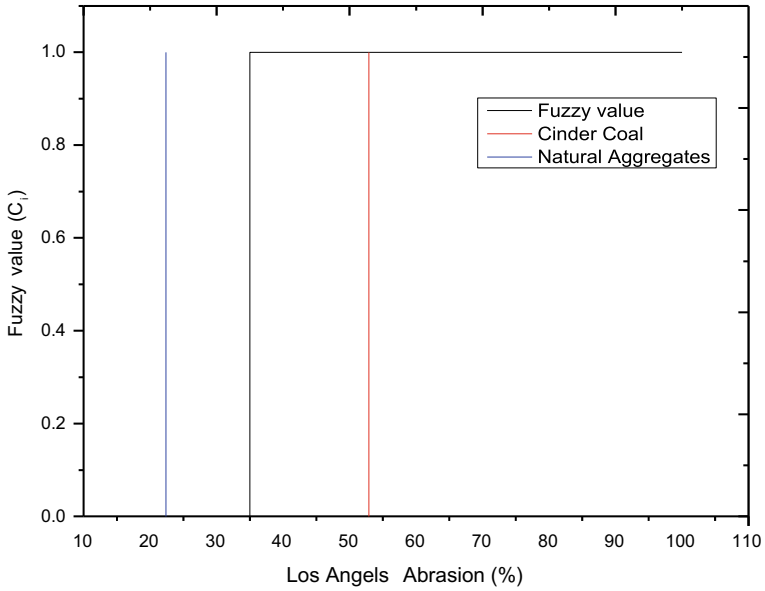


Fig. 3 Fuzzy membership function graph for abrasion value

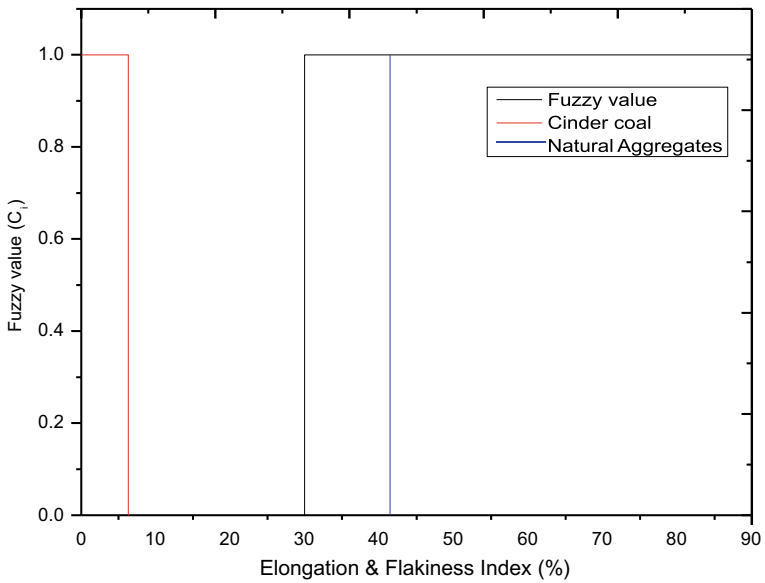


Fig. 4 Fuzzy membership function graph for elongation and flakiness indices

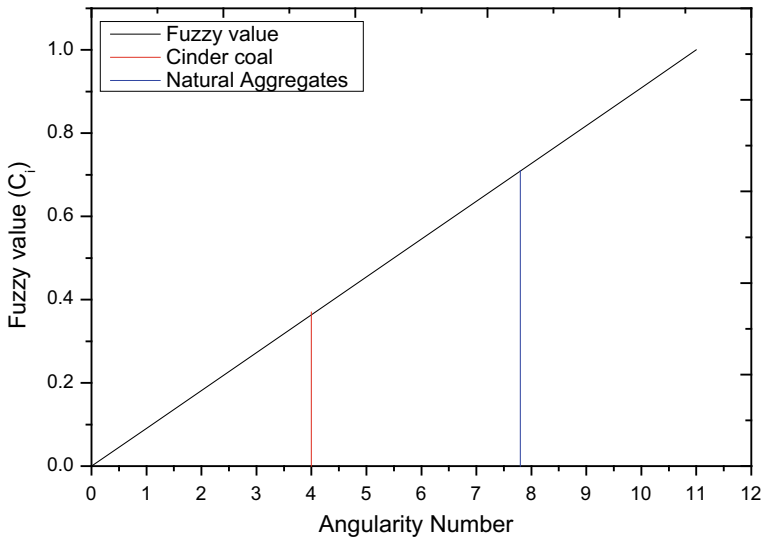


Fig. 5 Fuzzy membership function graph for angularity number

Table 3 Fuzzy value results for cinder coal and crushed stone aggregate

Variables	Standards-surface	Cinder coal ( $C_i$ )	Crushed stone ( $C_i$ )
Aggregate crushing value	<35%	1	0
Abrasion	<35%	1	0
Elongation and flakiness	<30%	0	1
Angularity number	0–11	0.36	0.71
Specific gravity	2.5–2.9	1	0.29
Water absorption	0.1–2%	1	0.34
Aggregate impact test	<30%	1	0

stone aggregates and their fuzzy values are shown in Fig. 7. Aggregate impact value for toughness property must be less than 30% for the surface course of flexible pavement, hence the fuzzy value equal to and greater than 30% is taken as ‘1’, and lesser than 30% indicates ‘0’. The aggregate impact value of CC and crushed stone aggregates and their fuzzy values are shown in Fig. 8.

Table 4 results were obtained by using Eqs. (1), (2) and (3) show the net fuzzy value for cinder coal as 86.78%, which indicates the inherence property is high. Table 5 shows the net fuzzy value for crushed stone aggregate as 30.75% that indicates the inherence property is low and engineer can, therefore, suggest the material for the surface course.

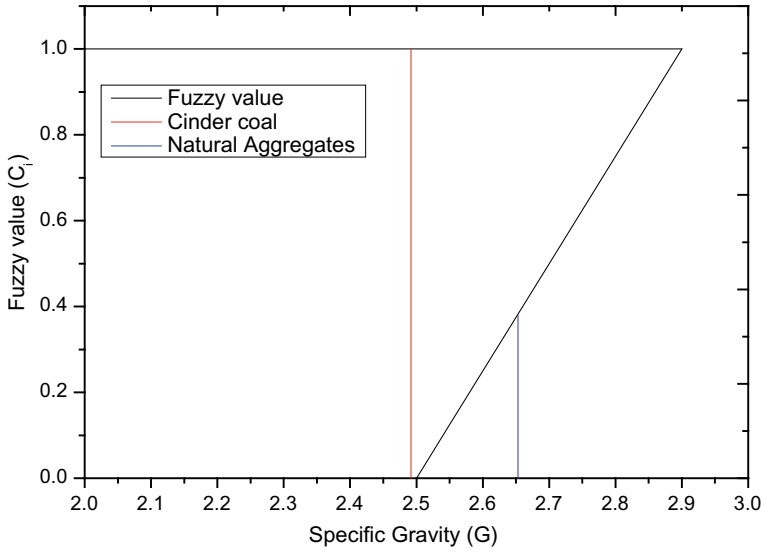


Fig. 6 Fuzzy membership function graph for specific gravity

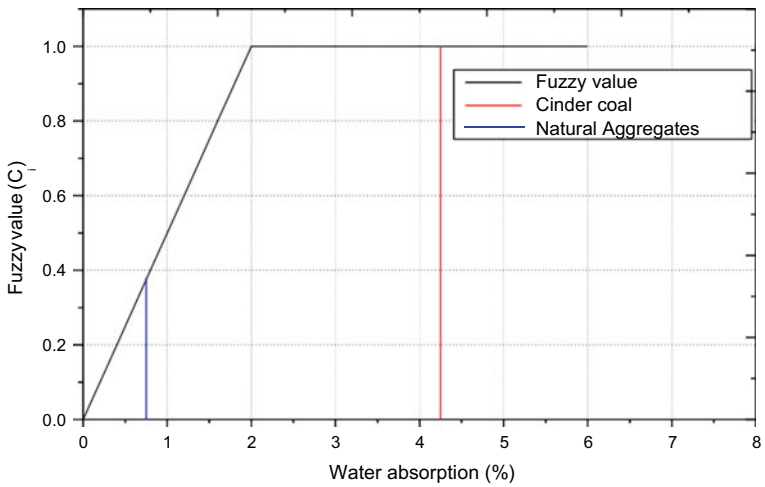


Fig. 7 Fuzzy membership function graph for water absorption

## 5 Conclusions

On the basis of observations and analysis of various tests of aggregates, the following conclusions were drawn.

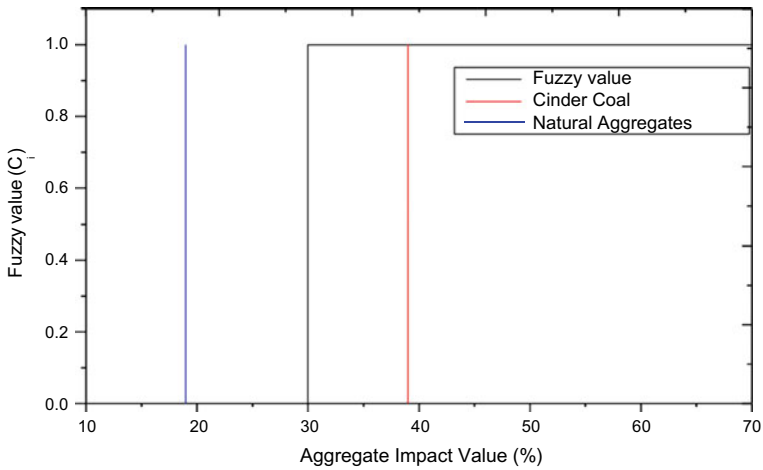


Fig. 8 Fuzzy membership function graph for aggregate impact value

Table 4 Quality index results for cinder coal

Variables	Test result	Standards	$Q_i$	$W_i$	$K$	AQI	NFV (%)
Aggregate crushing value	53.05%	<35%	151.571	0.0175		274.25	86.78
Abrasion	52.9%	<35%	151.143	0.0175			
Elongation and flakiness	6.3%	<30%	21	0.02046			
Angularity number	4	0–11	72.73	0.11164	0.614		
Specific gravity	2.492	2.5–2.9	92.296	0.2274			
Water absorption	4.25%	0.1–2%	404.76	0.5847			
Aggregate impact test	39%	<30%	130	0.02046			

- The net fuzzy value for cinder coal and crushed stone aggregate are found to be 0.8678 and 0.3075, respectively.
- The quality rating using fuzzy value revealed that the quality of aggregates is ‘unfit’ for cinder coal and ‘good’ for crushed stone aggregate.
- Based on above study, the cinder coal is not suitable for surface course, but it is suitable for base/sub-base courses because the stress intensity is less in base/sub-base courses when compared with surface course.
- Based on net fuzzy value for crushed stone aggregate, it is revealed that it is best suitable for surface construction and which is also suitable for other layers.

**Table 5** Quality index results for crushed stone aggregate

Variables	Test result	Standards	$Q_i$	$W_i$	$K$	AQI	NFV (%)
Aggregate crushing value	22.75%	<35%	65	0.0175		86.2	30.7532
Abrasion	22.4%	<35%	64	0.0175			
Elongation and flakiness	41.47%	<30%	138	0.02046			
Angularity number	7.802	0–11	141	0.11164	0.614		
Specific gravity	2.653	2.5–2.9	98.2	0.2274			
Water absorption	0.75%	0.1–2%	71.4	0.5847			
Aggregate impact test	18.97%	<30%	63.2	0.02046			

## References

1. Yang, J., Wang, S., Lu, Z., & Lou, S. (2009). Converter slag–coal cinder columns for the removal of phosphorous and other pollutants. *Journal of Hazardous Materials*, 168.
2. Smarzewski, P., & Barnat-Hunek, D. (2016). Mechanical and durability related properties of high-performance concrete made with coal cinder and waste foundry sand. *Construction and Building Materials*.
3. Khanna, D. R., Singh, S., Saxena, N., Bhutiani, R., Matta, G., & Kulkarni, D. B. (2011). Physico-chemical and microbiological characterization of the groundwater across the city Bareilly (U.P.), India. *Journal of Applied and Natural Sciences*.
4. Haque, E., Reza, S., & Ahmed, R. (2018). Assessing the vulnerability of groundwater due to open pit coal mining using DRASTIC model: A case study of Phulbari Coal Mine, Bangladesh. *Geosciences Journal*.
5. Zhang, J. C., & Styblinski, M. A. (1995). *Yield and variability optimization of integrated circuits*. Springer Nature.
6. Soncim, S. P., De Oliveira, I. C. S., & Santos, F. B. (2019). Development of fuzzy models for asphalt pavement performance. *Acta Scientiarum. Technology*.
7. Guo, H., Wang, Y. S., Yang, C., Wang, X. L., Liu, N. N., & Xu, Z. J. (2019). Vehicle interior noise active control based on piezoelectric ceramic materials and improved fuzzy control algorithm. *Applied Acoustics*.
8. Zehtabchi, A., Hashemi, S. A. H., & Asadi, S. (2018). Predicting the strength of polymer-modified thin-layer asphalt with fuzzy logic. *Construction and Building Materials*.
9. Turki, M., Zarrad, I., Quéneudec, M., & Bouaziz, J. (2017). Prediction performance of compressive strength of cementitious materials containing rubber aggregates and filler using fuzzy logic method. *Multidiscipline Modeling in Materials and Structures*.
10. Sadrossadat, E., Heidaripناه, A., & Osouli, S. (2016). Prediction of the resilient modulus of flexible pavement subgrade soils using adaptive neuro-fuzzy inference systems. *Construction and Building Materials*.
11. Bhutiani, R., Khanna, D. R., Kulkarni, D. B., & Ruhela, M. (2016). Assessment of Ganga river ecosystem at Haridwar, Uttarakhand, India with reference to water quality indices. *Applied Water Science*.

# Effect of Relief Shelves on Cantilever Retaining Walls



Preethi Sekar , Satya Kiran Raju Alluri and S. Suganya

**Abstract** Retaining walls are a part of everyday infrastructure, from retaining soil in mountain slopes to harbor structures. With the expectation to retain higher backfills, new and improved design methodologies, such as reinforced retaining wall, lightweight backfilling, are being implemented. A new method of construction consisting of relief shelves attached to the backfill side of the stem provides relief to the lateral pressure acting on the wall, thus reducing the overturning moment of the wall during stability analysis. Available literature suggests the use of retaining wall with shelf/shelves with experimental and theoretical computations based on provision of one or two shelves. The effect of using more than two shelves has not been studied extensively. This paper studies the effect of multiple shelves have on the lateral earth pressure acting on the stem. A parametric study was carried out to understand the variation of lateral earth pressure with the change in length and number of shelves at the back of the retaining wall. It is observed that the increase in number of shelves corresponds to reduction in total thrust and moment of the lateral earth pressure in comparison with that of single shelved retaining walls. It is also observed that short multi-shelved walls are much more efficient compared to long single shelved retaining walls of the same shelf length.

**Keywords** Special retaining structures · Lateral earth pressure · Relief shelves · FEM

---

P. Sekar (✉) · S. K. R. Alluri · S. Suganya  
National Institute of Ocean Technology, Chennai, India  
e-mail: [preethi.seera.sekar@gmail.com](mailto:preethi.seera.sekar@gmail.com)

S. K. R. Alluri  
e-mail: [raju@niot.res.in](mailto:raju@niot.res.in)

S. Suganya  
e-mail: [suganyas@niot.res.in](mailto:suganyas@niot.res.in)

© Springer Nature Singapore Pte Ltd. 2020  
S. Saride et al. (eds.), *Advances in Geotechnical and Transportation Engineering*,  
Lecture Notes in Civil Engineering 71,  
[https://doi.org/10.1007/978-981-15-3662-5\\_14](https://doi.org/10.1007/978-981-15-3662-5_14)

## 1 Introduction

Retaining walls are an integral part of retaining any vertical column of soil. For retaining walls less than 6 m, generally cantilever retaining walls are utilized while, for retaining walls greater than 6 m, counterfort retaining walls are used. However, with the development of infrastructure and space constraints, higher retaining structures are desired with less access to backfill area. Reduction in the lateral earth pressure can lead to an economical design. Reinforced retaining walls, geo-inclusion, lightweight backfilling and relief shelves are some of the methods adopted to relieve some of the lateral pressure on the stem of the retaining wall.

Relief shelves are horizontal cantilever beams constructed monolithically with the stem of the retaining wall along the length of the wall. However, limited theoretical knowledge of this methodology leads to failure of the retaining wall in many cases. The failure may include localized passive pressure on the stem leading to tension failure just below the shelf as seen in a location in Hyderabad [1–3]. They may also face other problems like wedge formation away from the relief shelves leading to a further complication of the design of retaining wall [4].

Though few structures have been constructed, the mechanism behind stress reduction has not been well documented due to its complexity and variability based on the uncertainties that develop due to the introduction of relief shelves. Few literature also demerits the use of shelves in retaining wall. The present study aims at understanding the theory of the relief shelves, their positioning and the desired number of shelves to be provided.

## 2 Literature Review

One of the earliest studies on retaining walls with relief shelves was carried out by Jumikis [5] where a study was carried out to assess the effect of introduction of relief shelves on the stability of the retaining structure. He theoretically established the lateral earth pressure for a counterfort retaining wall with two relief shelves. His study also concluded that there is a reduction in the lateral earth pressure of the soil on the wall if the shelf is extended to the rupture plane of the soil. Yakovlev [6–10] has extensively studied the effect of a single and two shelves on various factors. He concluded that if the wall is allowed to displace, an internal sliding surface is created from the backfill zone above the shelf. By introducing a shelf intercepting this sliding surface, a new surface is created originating from shelf above, thus reducing the lateral pressure on the wall.

Raychaudhuri [11] determined the reduction factors for the decrease in lateral earth pressure, due to the introduction of a shelf, on the backfill using Coulomb's theory and provided charts for the same. Phatak and Patil [12] derived the theoretical concept for computing earth pressure using Rankine's theory. They calculated the earth pressure distribution based on the shift of center of gravity of the backfill

material above the shelf and summarized that shelves reduce the active earth pressure. Shehata [13] summarized that using Mohr–Coulomb model may actually increase the lateral earth's pressure in cases of staged construction during the loading–unloading activity and suggested that hardening soil model best represents the behavior of soil in retaining wall with shelves. He has also studied the effect of shelves on the earth pressure and concluded that shelves significantly decrease the lateral earth pressure. He also studied the effect of shelf rigidity and concluded that effective stiffness is desired for the shelves. He also concluded the previous assumptions from literature that for a significant effect of shelves, the shelves should extend into the rupture plane. Padhye and Ullagaddi [14] proposed reduction factors for retaining wall with two relief shelves theoretically using Coulomb's method for computation of lateral earth pressure.

Chauhan [1–3] conducted a numerical analysis using FLAC-3D on the effectiveness of relief shelf/shelves and concluded that the thrust on a rigid retaining wall significantly reduces in the presence of shelves for a single and double relief shelved retaining wall. They extended the study and analyzed the length of shelves on the lateral earth pressure for both cohesive and cohesionless backfills. A parametric study on the length of the relief shelves was carried out against the lateral earth pressure for equally spaced multiple shelves. They concluded that using larger lengths of the shelf might lead to unanticipated stresses on the stem instigating distress. They identified that the relief shelves are suitable and effective for even cohesive backfills. They also conducted experimental studies to determine the influence of width for rigid retaining wall with a surcharge and observed that the deflection in the relief shelf is proportional to the width of the shelf.

Klein [15] derived the theory for the earth pressure under and over the shelf/shelves and corrected the slope transition of earth pressure between shelves to be defined by the angle of internal friction,  $\phi$ , which is more compatible with advanced soil models for finite element solutions as shown in Fig. 1.

### 3 Analytical Solution for Retaining Wall

Apart from the primitive solutions first derived based on Coulomb and Rankine's theory, a lot of modifications have been further introduced for the distribution of lateral earth pressure when relief shelf/shelves are considered. The shelved retaining wall works in the assumption that the shelf rests on a fully compacted soil and that the rigid connection between the shelf and stem. Of the theoretical models proposed for the distribution of lateral earth pressure on the stem, this paper utilizes Klein [15] model to analyze retaining wall with relief shelves if more than two relief shelves exist. It has already been established that extending the shelf into the rupture plane yields the maximum efficiency.

Therefore, this paper deals with shelves extruding into the rupture plane. Klein [15] model for a shelf intruding into the plane of rupture is as shown in Fig. 1. It can be seen that the lateral earth pressure near the base slab of the retaining wall remains



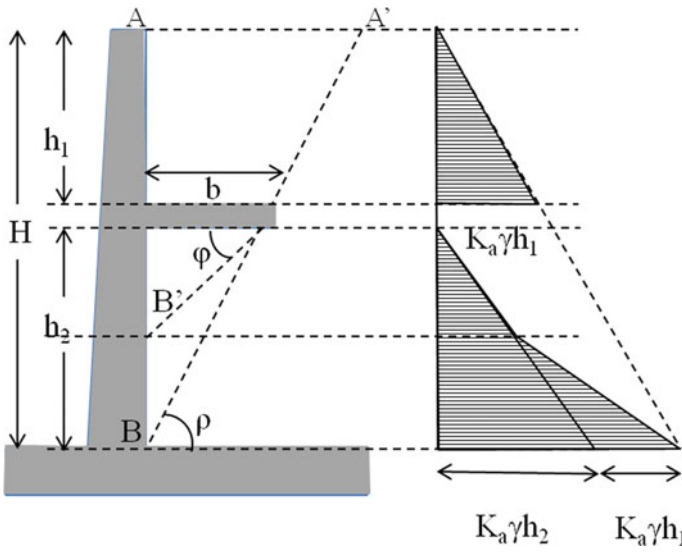


Fig. 1 Lateral earth pressure distribution. Adapted from Klein [15]

the same as that of a retaining wall without shelf. The same behavior is replicated for multi-shelved retaining wall as shown in Fig. 2. The shelf 'D' will have a rupture plane *D-D'* extending to the surface by an angle ' $\rho$ ' to the horizontal which is

$$\rho = 45^\circ + \frac{\varphi}{2} \tag{1}$$

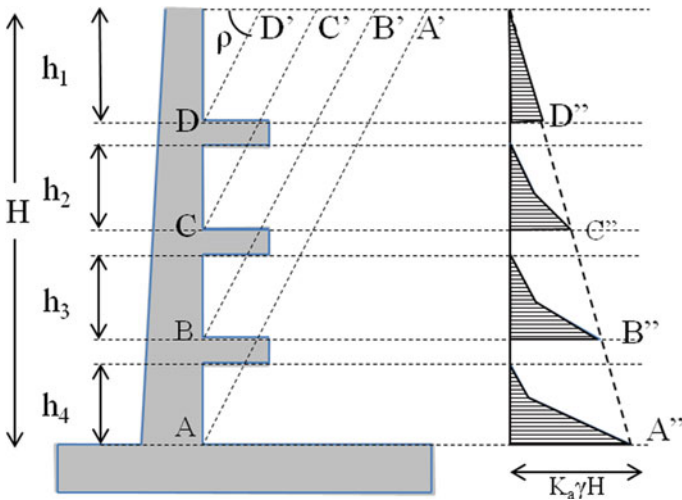


Fig. 2 Lateral earth pressure for multi-shelved retaining wall

The weight of soil just above the shelf ‘*D*’ produces a lateral earth pressure acting along height  $h_1$ . This weight gets transferred to the shelf, leading to zero lateral pressure just below the shelf. However, due to the change in center of gravity of the weight, an additional component of stress due to soil in  $h_1$  acts in the section  $h_2$ . This additional component acts from a height where a plane made by ‘ $\varphi$ ’ intersects the stem height from the bottom edge of the slab. Based on the above concept, the length of shelf needed for interfering with the rupture plane has been derived from

$$b = h \tan\left(45 - \frac{\varphi}{2}\right) \quad (2)$$

where  $b$  is the length of the shelf and  $h$  is the height of the shelf from the base.

## 4 Numerical Modeling of Shelved Retaining Wall

Various researches have been pursued in terms of shelved retaining wall as mentioned in the above literature. From the literature, it has been inferred that the Mohr–Coulomb model in a FEM tool allows for the lateral earth pressure distribution but is seen to increase considerably due to the loading–unloading in staged construction. Therefore, an advanced soil model is preferred in this study. A 14 m high retaining wall with cohesionless backfill has been chosen for the study. A finite element numerical package (PLAXIS 3D) has been used to understand the pressure distribution on the stem and the relief shelves. The sectional dimensions are as shown in Fig. 3. The basic model consists of a 14 m high stem resting on a base slab of length 7 m and a thickness of 1 m. Six models, namely R\_0, R\_2, R\_4, R\_7, R\_10, R\_3n and R\_4n, have been constituted in this paper and the details are as shown in Fig. 4. ‘R\_0’ is for a simple cantilever retaining wall, series ‘R\_2, R\_4, R\_7 and R\_10’ are for single shelved walls and series ‘R\_3n and R\_4n’ are for multi-shelved walls. Literature has already established that as the thickness of the shelves increase, there is a reduction in lateral earth pressure. Therefore, a study on thickness of the shelves is not incorporated in this study. A constant shelf thickness of 0.5 m is maintained in all models.

The meshing of the model is divided into 26,367 10-noded tetrahedral elements with local refinement around the stem of the retaining wall for better results. This results in the element size ranging from 0.2137 to 2.554 m. The dimensions are designed taking into consideration that the model should be a plain strain problem and the boundary does not affect the results obtained. Default boundary conditions as defined in PLAXIS 3D have been found sufficient for the model. Sample mesh models for a cantilever retaining wall and a shelved retaining wall are as shown in Fig. 5. The retaining wall is designed using linear elastic model (LE). The backfill soil and the soil below retaining wall are assumed to be the same and are modeled using Hardening Soil model (HS). The properties defined are as given in Table 1.

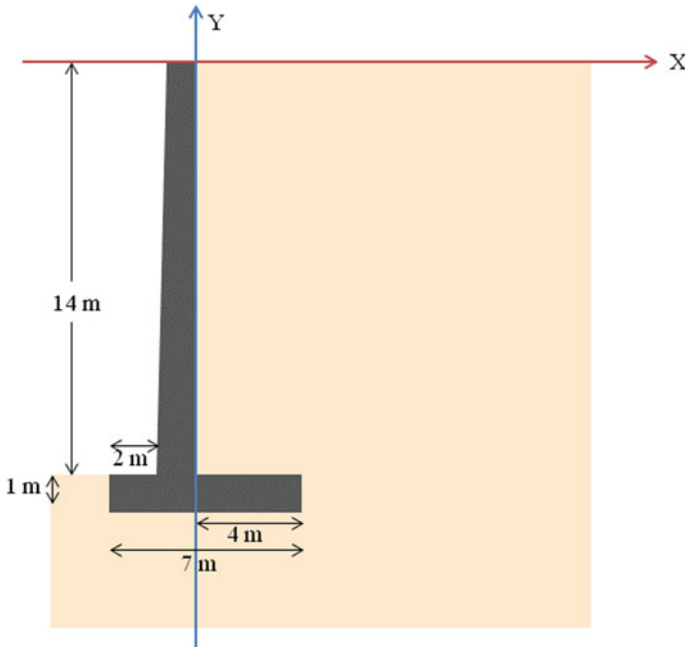


Fig. 3 Geometry of retaining wall

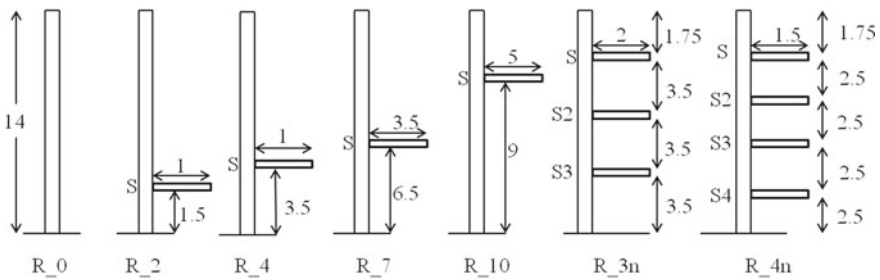
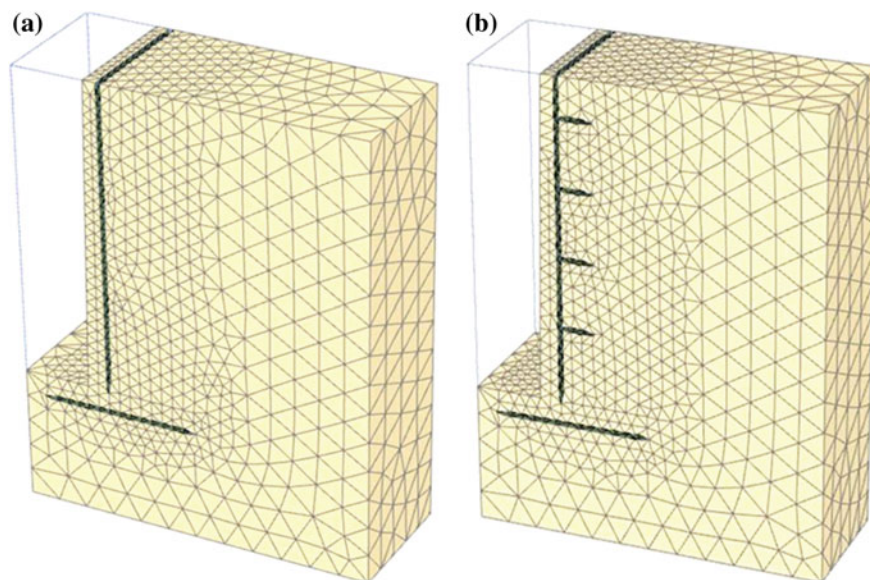


Fig. 4 Geometrical variation of various models

### 5 Cantilever Retaining Wall

The general assumption of theoretical design for a cantilever retaining wall is that the soil wedge gets fully mobilized and reaches the active earth pressure. However, in reality, the active pressure in the soil lies somewhere between that of an active pressure zone and that of at rest condition. To determine the effect of shelves, we need to first understand the actual mobilization. Figure 6 indicates the actual coefficient of earth pressure mobilized from a FEM model for a simple cantilever retaining wall for a particular soil and height of backfill. The stem top deflection is quite high when



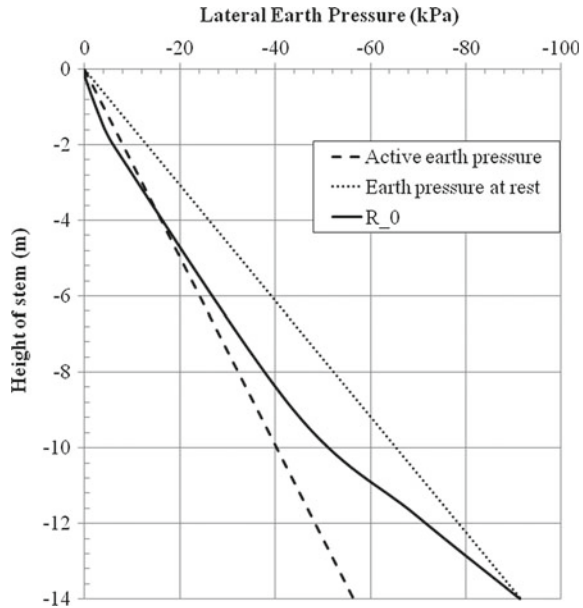
**Fig. 5** Meshing of retaining wall model in PLAXIS 3D **a** without shelves and **b** with shelves

**Table 1** Material properties used in the model

Parameters	Unit	Retaining wall	Backfill
Material model	–	Linear elastic	Hardening soil
Unit weight, $\gamma$	kN/m <sup>3</sup>	25	17
Young's modulus, $E$	kPa	31,622	–
Poisson's ratio, $\nu$	–	0.15	–
$E_{50}^{\text{ref}}$	kPa	–	10,000
$E_{\text{oed}}^{\text{ref}}$	kPa	–	10,000
$E_{\text{ur}}^{\text{ref}}$	kPa	–	30,000
Power, $m$	–	–	0.5
Cohesion, $C$	kPa	–	5
Friction angle, $\varphi$	°	–	38
Dilatancy angle	°	–	4

compared to the deflection at the base. This displacement mobilizes the soil wedge and the pressure moves from at rest to that of active pressure at the top. At the base of the retaining wall, no displacement is felt. Therefore, the condition remains in at rest position. It can be seen that the pressure remains close to that of active earth pressure in the case of the stem top while, at the bottom of the stem, the pressure

**Fig. 6** Comparison of lateral earth pressure in cantilever model with active pressure and pressure at rest



indicates that it is quite close to that of the retaining wall at rest condition. Klein [15] proposed the theoretical model with coefficient of active earth pressure ( $K_a$ ). However, in this paper, the coefficient of earth pressure at rest ( $K_0$ ) has been adopted due to this reason.

## 6 Effect of Shelf Position

From literature, it is understood that introduction of shelves in the stem of the cantilever retaining wall reduces the lateral earth pressure acting on to the stem. The shelf on itself is subjected to normal stresses from the soil weight in the backfill it retains. This normal stress is transferred to the stem as a moment on to the stem. The length and placement of shelf play a crucial role in both the normal stress on the shelf and the lateral earth pressure on the stem. In Fig. 7a, the shelf is placed at a height of 1.5 m as shown in Fig. 4 with the length of shelf as 1 m for it to intersect the rupture plane based on Eq. (2). The earth pressure obtained from the FE simulation of ‘R<sub>2</sub>’ is compared with the theoretical values obtained from Klein [15] and the FE model of a cantilevered retaining wall. Similar comparisons have been made for R<sub>4</sub>, R<sub>7</sub> and R<sub>10</sub>.

As seen from Fig. 7, the positioning of the shelf plays a major role in the reduction of the lateral earth pressure on the wall. In the case of R<sub>2</sub>, where the shelf is present 1.5 m from the base of the retaining wall, the pressure at the top of the stem is reduced when compared to that of a cantilevered retaining wall while there is an

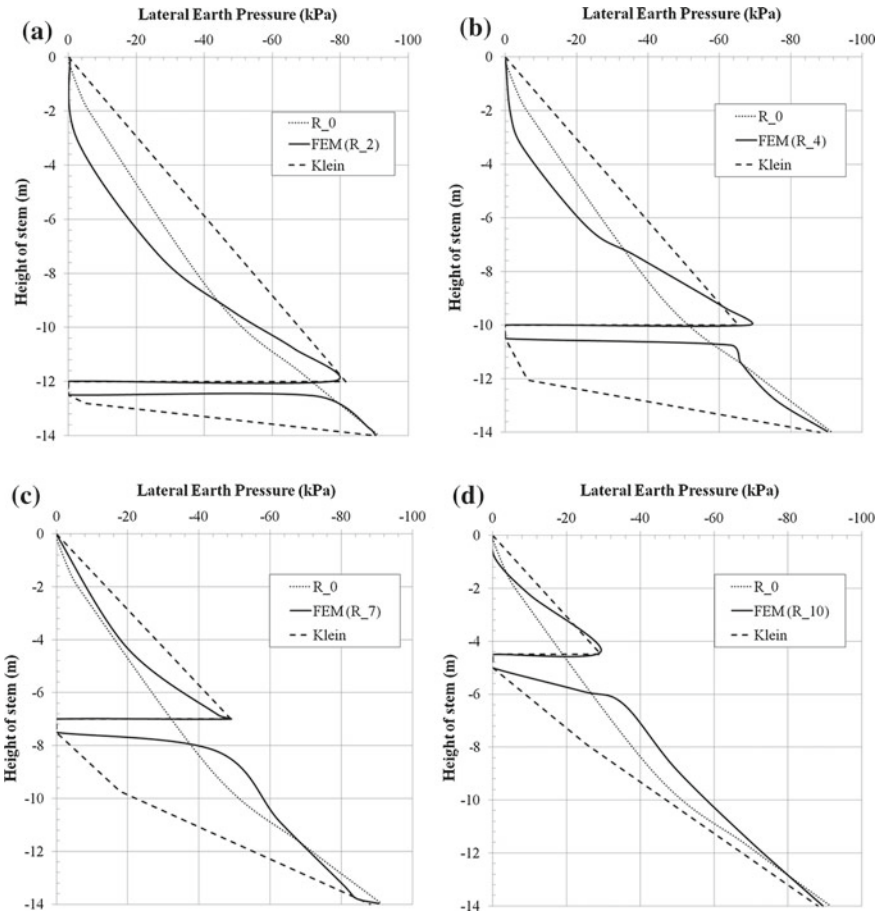


**Fig. 7** Comparison of lateral earth pressure for cantilever retaining wall and single shelved retaining wall at various positions. **a** Model R\_2, **b** model R\_4, **c** model R\_7 and **d** model R\_10

increase in the stress just on top of the stem. This increase is due to the resistance of the shelf for soil movement, leading to a slight increase in the lateral earth pressure. For overturning moment computation, the lever-arm for the zone where increase in pressure is observed, is quite low. However, for the reduction of stress at top, the lever-arm is quite high. The effective moment due to the product of pressure and lever-arm results in reduction of the overturning moment.

From Fig. 10, it can be seen that the lateral force on the stem in the cases of R\_2 and R\_4 is reduced by 40% and 37%, respectively, while the reduction in R\_7 and R\_10 yields a reduction of 28 and 25%. This reduction might be misleading as the moment computed in the cases of R\_2 and R\_4 has a moment reduction of 24 and 19% while there is an increase in moment by 6% in the case of R\_7 and 5% increase in the case of R\_10. Another observation is that even though the shelf at

**Table 2** Moment in kNm due to normal stress on the shelves

Sl. no.	Model	Moment due to pressure acting normal to the shelves (kNm)			
		Shelf S	Shelf S2	Shelf S3	Shelf S4
1	R_2	31.92	–	–	–
2	R_4	223.91	–	–	–
3	R_7	840.09	–	–	–
4	R_10	1366.62	–	–	–
5	R_3n	41.26	117.95	206.19	–
6	R_4n	17.76	41.44	69.56	98.97

R\_2 has around 12 m of backfill as surcharge, the end moment created due to this surcharge acting normal to the shelf is 31 kNm. This is because the length of the shelf is shorter when compared to all the other models. The moment developed due to pressure acting on shelf/shelves on all models is given in Table 2. It can be seen that the moment increases considerably due to the change in length even though the normal stress decreases as the shelf placement is moved toward the top of the stem.

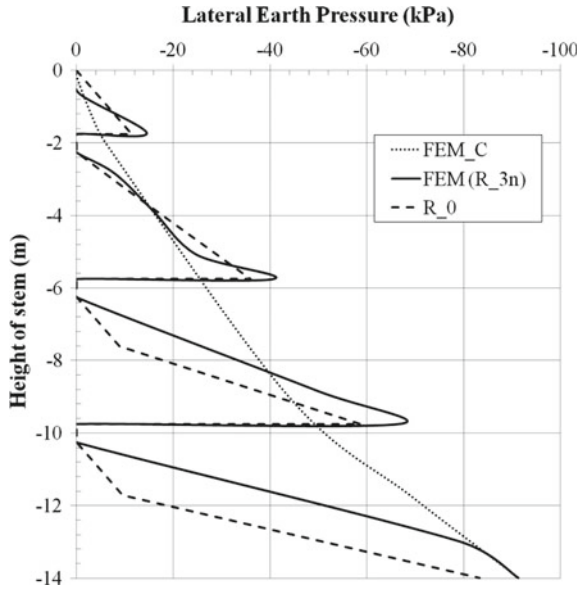
It is observed that there is a slight increase in the lateral earth pressure just above the shelves. This is due to introduction of ‘stiffer’ shelf which offers rigidity, which in turn increases the stress locally at that location. This is in concurrence with the inference by Shehata [13]. The theoretical observations, such as in the case of Klein [15], do not take the stiffness change into consideration and observe a linear pattern. It is also observed that the lateral earth pressure at the base remains constant irrespective of the height of provision of shelves and the length of the shelves. This is in concurrence with the theoretical solution proposed by Klein [15]. It can also be observed that the provision of a single shelf is effective in the cases of R\_2 and R\_4 which is below one-third of the height of stem when compared to R\_7 and R\_10 for stability of the retaining wall. This is in concurrence with the conclusion by Shehata [13] that for a single shelved system, the shelf should be placed from one-third from the base of the stem for effective reduction in lateral earth pressure.

## 7 Effect Due to Number of Shelves

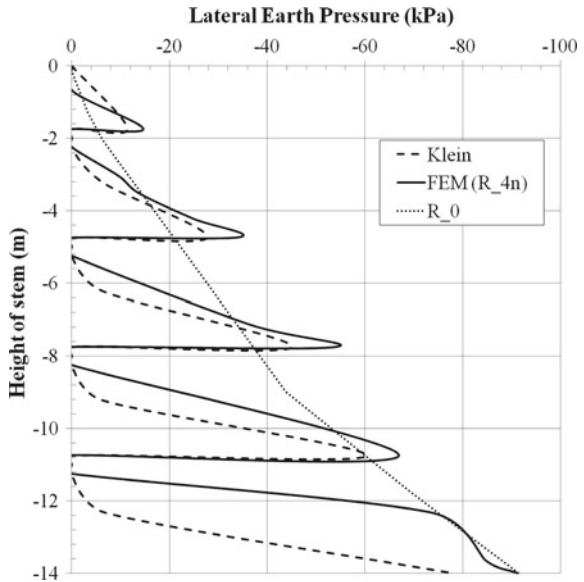
Considering the effectiveness of a single shelved retaining wall placed at one-third from the base, a wall with multiple shelves is being considered. Equally spaced, equally long, short shelves are placed and designed to intersect the rupture plane. Two models, namely R\_3n and R\_4n, are utilized in this study. ‘R\_3n’ consists of three shelves spaced at 3.5 m intervals from the base of the slab. For the shelves to intersect the rupture plane, created by the shelf below, a length of 2 m is adopted for the shelves based on Eq. (2). Similarly, ‘R\_4n’ consists of four numbers of shelves with lengths of 1.5 m and spaced 2.5 m apart. It is to be noted that the cumulative length of the shelves in both the models remains the same.

It can be observed from Fig. 8 that the pressure at shelf levels predicted by Klein [15] and that from FE model is a little high when compared to that of the cantilever retaining wall. Similarly, in Fig. 9, the cantilever retaining wall's pressure value is quite less in comparison with the other models at the position of shelves. Comparing

**Fig. 8** Lateral earth pressure for three shelved retaining pressure



**Fig. 9** Lateral earth pressure for four shelved retaining pressure





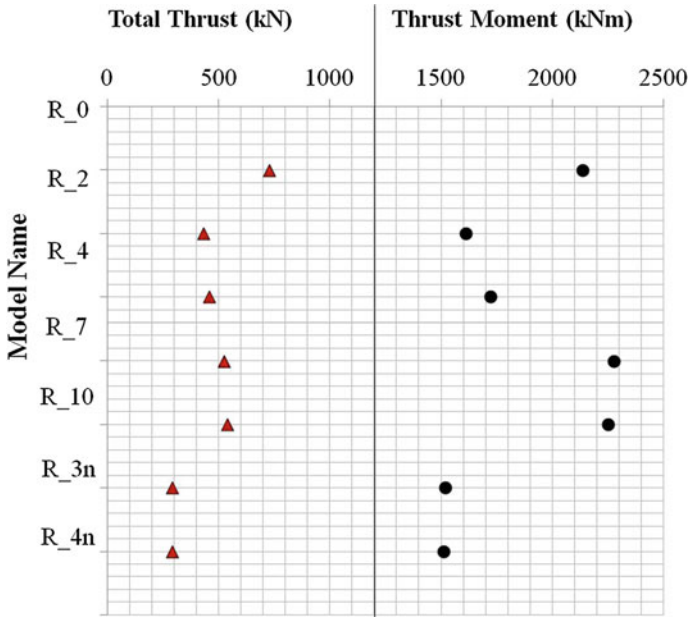


**Fig. 10** Comparison of force and moment on the stem for various FEM models

both Figs. 8 and 9, we can see a little decrease in pressure by the introduction of an additional shelf, resulting in little reduction of pressure acting on the stem. However, when compared to that of a cantilever retaining wall, a decrease in 59.81% in the thrust for R\_3n while a decrease of 59.9% is felt in the case of R\_4n. Similarly, the moment capacity is seen to reduce to about 28% while that of R\_4n is 29%. It is seen that introduction of additional shelves need not proportionally mean a decrease in lateral earth pressure on the stem. From Fig. 10, we can see that the moment and the thrust R\_3n and R\_4n remain almost constant. However, we also need to consider the normal pressure acting on the stem. From Table 2, we can see that a reduction of about 50% of moment is seen on almost all the shelves by the introduction of an additional shelf. It is to be understood that this moment on the shelves also gets transferred to the stem of the retaining wall, and therefore, the overall stability of the structure needs to be considered.

## 8 Conclusion

The paper studies the effect of position of the shelf and the length of the shelf on the retaining wall. It additionally studies the effect of using more than one shelf on the retaining wall by using a theoretical method proposed by Klein [15]. It had already been established through literature that provision of shelves to the retaining wall

proves beneficial for reducing the lateral earth pressure on the wall. This reduction in lateral earth pressure reduces the overturning moment in terms of stability, thus proving economical, especially in cases where the height of the soil to be retained is quite high. A lot of researchers have worked on this structure, both theoretically and experimentally to determine how efficient provision of shelves is to the structure. However, all the efforts have been toward a single shelved retaining wall or two shelved retaining wall. In some literature like the case study of retaining wall failure in Hyderabad, multi-shelved retaining walls were studied. However, the exact efficiency of the multi-shelved retaining walls has not been thoroughly studied. Under the assumption that the shelf rests on a fully compacted soil and that the rigid connection between the shelf and stem has been analyzed for fixed end moment, a study has been carried out for various models using a finite element package.

From the study, it is found that the lateral earth pressure on the stem of the retaining wall significantly reduces due to the introduction of shelves. It is also to be understood that provision of multi-shelved retaining wall is much more efficient than that of single or double shelved retaining wall. However, increase in number of shelves does not mean a significant decrease in the lateral earth pressure on the stem. It is also to be understood that provision of three 2 m shelf (R\_3n) is much more economical than one 5 m shelf at 10 m (R\_10) from the base. However, provision of too many shelves may shift the failure plane further away from the wall, which might create other stability issues. It is also possible that the shelf–stem connection is of importance and needs to be further studied. The structural stability and the stability of the shelves against the normal stress due to backfill soil have to also be studied.

## References

1. Chauhan, V. B., Dasaka, S. M., & Gade, V. K. (2016). Investigation of failure of a rigid retaining wall with relief shelves. *Japanese Geotechnical Society Special Publication*, 2(73), 2492–2497. <https://doi.org/10.3208/jgssp.TC302-02>.
2. Khan, R., Chauhan, V. B., & Dasaka, S. M. (2016). Reduction of lateral earth pressure on retaining wall using relief shelf: A numerical study. In *Proceedings of International Conference on Soil and Environment* (117 pp). Bangalore, India.
3. Chauhan, V. B., & Dasaka, S. M. (2016). Behavior of rigid retaining wall with relief shelves with cohesive backfill. In *Proceeding of 5th International Conference on Forensic Geotechnical Engineering* (pp. 350–357). Bangalore.
4. Bowles, J. E. (1996). *Foundation analysis and design*. McGraw-Hill.
5. Jumikis, A. R. (1964). *Mechanics of soils*. New Jersey: D. Van Nostrand Co., Inc.
6. Yakovlev, P. I. (1964). Experimental investigations of a new type of relieving device for retaining walls. In *Scientific Paper in 'Hydraulic Engineering' (in Russian)*, No. 3. Morskoi Transport.
7. Yakovlev, P. I. (1964). Investigation of the behavior of relieving platforms of retaining walls. In *Scientific Paper in Hydraulic Engineering, Russian*, No. 3. Morskoi Transport.
8. Yakovlev, P. I. (1965). Calculation of relieving beams. In *Scientific Papers 'Sea Ports' (in Russian)*, No. 1.
9. Yakovlev, P. I. (1966). Application of S. S. Golushkevich's method to calculation of retaining walls with relieving platforms. *Izvestiya VUZOV. Stroitel's tovo Arkhitektura* (9).

10. Yakovlev, P. I. (1974). *Experimental investigations of earth pressure on walls with two platforms in the case of breaking loads relieving on the backfill*. Translated from Osnovaniya, Fundamenty Mekhanika Gruntov, No. 3 (pp. 7–9). Odessa Institute of Naval Engineers.
11. Raychaudhuri, P. R. (1973). Design of retaining walls with relieving shelves. *Journal of the Indian Roads Congress*, 35(2), 289–325.
12. Phatak, D. R., & Patil, V. (1975). Effect of relief shelves on earth pressure. *Institute of Engineers (India) JournalCI*, 55, 156–159.
13. Shehata, H. F. (2016). Retaining walls with relief shelves. *Innovative Infrastructure Solutions*, 1(1), 4. <https://doi.org/10.1007/s41062-016-0007-x>.
14. Padhye, R. D., & Ullagaddi, P. B. (2011). Analysis of retaining wall with pressure relief shelf by Coulomb's method. In *Proceedings of Indian Geotechnical Conference* (pp. 671–673).
15. Klein, G. K. (1964). *Calculation of retaining walls*. Moscow: Vysshaya Shkola. (in Russian).

# Heave Studies on Expansive Clay Beds Reinforced with Granular Pile Anchors and Geogrid-Encased Granular Pile Anchors



Ammavajjala Sessa Sai Raghuram , B. R. Phanikumar, K. Purnanandam, Preethi Sekar and A. Sriramarao

**Abstract** This paper presents heave studies on expansive clay beds reinforced with granular pile anchors (GPAs) and GPAs encased with geogrid by conducting experiments on CBR (small) and fabricated (large moulds of size  $381 \times 381 \times 457$  mm) moulds. The technique of GPA was developed for reducing heave and improving load-carrying capacities of expansive clay beds. In the current study, GPAs were encased in geogrid cylinders in a separate series of tests to further decrease heave. Heave tests were conducted in small and large test moulds to study the heave of expansive clay beds reinforced with plain GPAs and GPAs encased with geogrid. Heave decreased by about 92.5% and 98.3%, respectively, when determined in small and large moulds in the case of geogrid-encased GPAs. In addition, time required for the development of equilibrium heave decreased significantly upon installation of GPAs. The unreinforced expansive clay bed required, respectively, 3600 and 10,080 min of continuous wetting to attain the equilibrium heave in small and large moulds. However, in the case of clay beds reinforced with GPAs, less time was required for equilibrium heave. Furthermore, as the length of the GPA increased, the time required for equilibrium heave further decreased.

**Keywords** Expansive clays · Granular pile anchors (GPAs) · Geogrid-encased GPAs · Rate of heave

---

A. S. Sai Raghuram (✉) · P. Sekar  
Department of Civil Engineering, Indian Institute of Technology Hyderabad, Kandi 502285, India  
e-mail: [raghuram.ammavajjala@gmail.com](mailto:raghuram.ammavajjala@gmail.com)

P. Sekar  
e-mail: [preethi.seera.sekar@gmail.com](mailto:preethi.seera.sekar@gmail.com)

B. R. Phanikumar  
Department of Civil Engineering, S. R. K. R. Engineering College, Bhimavaram 534204, India  
e-mail: [phanikumar\\_29@yahoo.com](mailto:phanikumar_29@yahoo.com)

K. Purnanandam · A. Sriramarao  
Department of Civil Engineering, UCEK (A), J. N. T. U. Kakinada, Kakinada 533003, India  
e-mail: [purnanandamk@yahoo.co.in](mailto:purnanandamk@yahoo.co.in)

A. Sriramarao  
e-mail: [sreeramaajjarapu@gmail.com](mailto:sreeramaajjarapu@gmail.com)

## 1 Introduction

Rise and fall of moisture content lead to the swell-shrink behaviour of expansive clays, as they are susceptible to volumetric changes triggered by changes in water content. This behaviour leads to distress in civil engineering infrastructure such as pavements, foundations, canals resting on these strata [1, 2, 6, 7]. Based on the suction and stress history, they may also exhibit collapse compression, which in turn leads to the settlement of the founded structure [3]. The distress caused by these expansive clays to the civil engineering infrastructure leads to huge financial loss as much as 1000 million dollars and several billions of pounds worldwide [4]. Various innovative techniques have been proposed to remedy the swell-shrink behaviour of expansive clay beds and to improve their overall engineering behaviour [1]. Some of these techniques include (1) physical and chemical alteration of the expansive soil; (2) cushion techniques like sand cushion method or cohesive non-swelling layer (CNS) method; (3) belled and drilled piers, under-reamed piles and granular pile anchors [1, 5, 8–11, 14–18]. In physical alteration methods, chemically non-reactive sand or gravel is mixed with expansive soil in different ratios to control swelling. In chemical stabilization methods, reagents (lime, cement, fly ash,  $\text{CaCl}_2$ ) are mixed with the expansive soils to modify the chemical composition of the expansive clay through various reactions such as cementation and flocculation. In cushion techniques, top few of the expansive soil would be replaced by sand or cohesive non-swelling soil to reduce the heave. Belled and drilled piers, under-reamed piles and granular pile anchors are classed as tension-resistant foundation techniques which directly address the problem of heave.

## 2 Mechanism Involved in GPA Foundation

In a GPA, which is a modification of the conventional granular pile, the foundation is fastened to a base plate at the bottom of the granular pile through a mild steel anchor rod. The mechanism of the GPA system and the forces acting on a GPA in detail are presented elsewhere [8, 12, 13, 15]. When the foundation experiences the uplift force ( $P_u$ ) by the swelling expansive soil, it is resisted by friction which is mobilized around the GPA–soil interface in the downward direction. The uplift force ( $P_u$ ) is caused by the swelling pressure of the expansive soil, and the resistance to uplift ( $P_R$ ) is developed due to

- (i) the weight of the GPA acting in the downward direction ( $W_{gp}$ ) and
- (ii) the frictional resistance which is mobilized around the GPA–soil interface because of the shear parameters of the interface ( $c'$  and  $\phi'$ ).

Geogrids are roughly textured and are highly resistant to tensile forces. Therefore, if GPAs are encased with geogrids, the resistance ( $P_R$ ) to uplift force ( $P_u$ ) would

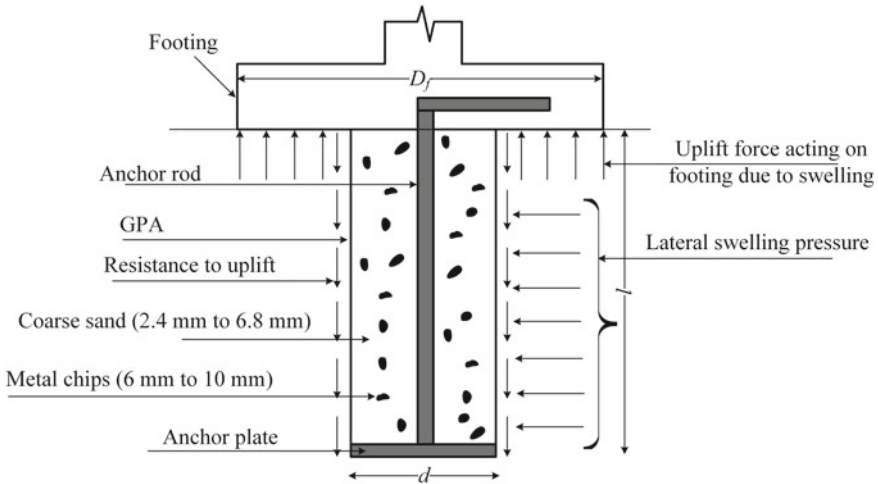


**Fig. 1** Forces acting on the GPA

increase due to the result of the friction mobilized around GPA–geogrid–soil interface. This could result in reduced heave. The forces acting on the GPA are shown in Fig. 1.

The main objective of the paper is to study the rate and amount of heave of expansive clay beds reinforced with GPAs and GPAs encased with geogrid in small and large moulds.

### 3 Experimental Study

Laboratory model tests were conducted to study the efficacy of GPAs and GPAs encased with geogrid embedded in expansive clay beds in arresting heave. The surface heave of the expansive clay beds reinforced with plain GPAs and GPAs encased with geogrid was measured by conducting 14 heave tests on unreinforced expansive clay beds and clay beds reinforced with GPAs and GPAs encased with geogrid. The expansive clay beds were compacted in laboratory-scale test moulds of two different sizes. In all, seven heave tests were performed in CBR moulds and seven more in larger fabricated tanks.

#### 3.1 Test Materials

The expansive clay was collected at a depth of 1.5 m below the ground surface in the town of Amalapuram, Andhra Pradesh, India. The index properties of the expansive

**Table 1** Index properties of expansive soil

Property	Value
Specific gravity, $G$	2.69
Sand (%)	13.33
Silt (%)	35.4
Clay (%)	51.27
Liquid limit (%)	90
Plastic limit (%)	35.2
Plasticity index (%)	54.8
USCS classification	CH
Free swell index (%)	140
Optimum moisture content, OMC (%)	27.7
Maximum dry density, MDD ( $\text{kN/m}^3$ )	14

soil are given in Table 1. The clay was classified as highly swelling clay based on its free swell index (FSI) of 140%. The granular material used for the installation of GPAs was a mixture of 20% stone chips whose particle size ranged from 6 to 10 mm and 80% coarse sand with its particle size between 2.4 and 4.8 mm. It was found from the previous pilot studies that the proportion of 20:80 of the stone chips and coarse sand gave a wide range of relative densities [8]. In the present study,  $D_R$  was fixed at 70% for compacting the granular piles. Polyvinyl chloride (PVC)-coated glass fibre geogrid, which has an aperture size of 10 mm  $\times$  10 mm, was overlapped to get an aperture size of 4 mm  $\times$  4 mm and used in the test programme. The geogrid has a tensile strength of 10 kN/m and was flexible to enwrap the GPA.

### 3.2 Variables Studied

Heave tests were carried out in small and large moulds with and without geogrid encasement.

1. In all the tests, the compaction of expansive clay beds is done at a dry unit weight of 14  $\text{kN/m}^3$  and a placement water content of 15%. These conditions were chosen for the convenience of compaction. Tests were performed in two moulds, namely
2. Small moulds: CBR moulds of size 150 mm in dia. and 175 mm in height without collar. The thickness of all the expansive clay beds was kept constant at 97 mm. The length of the GPAs ( $l$ ) was varied as 49, 73 and 97 mm. However, the diameter of the GPAs ( $d$ ) was kept constant at 30 mm. In other words, GPAs and GPAs encased with geogrid of  $l/d = 1.63, 2.43$  and  $3.23$ , respectively, are used.
3. Large moulds: prefabricated moulds of size 381 mm  $\times$  381 mm  $\times$  457 mm. The expansive clay beds were compacted to a thickness 381 mm in all the tests. The length of the GPAs ( $l$ ) was varied as 124.4, 185.4 and 246.4 mm, while the

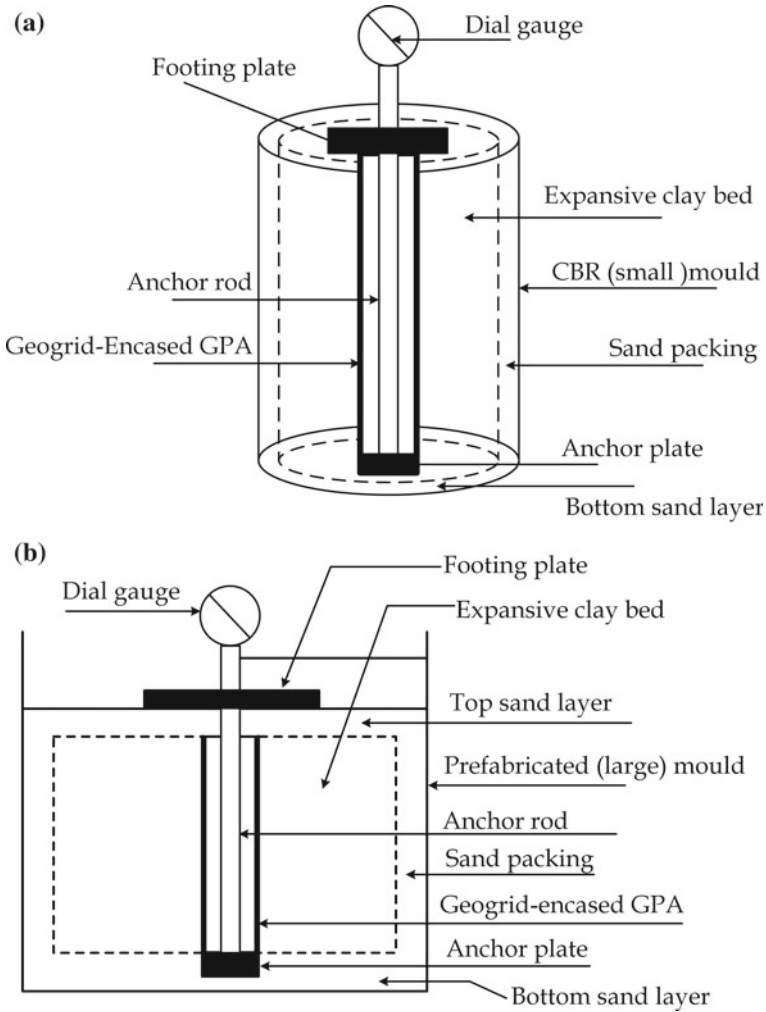


**Fig. 2** a Experimental set-up in CBR (small) mould, b experimental set-up in prefabricated (large) mould

diameter of the GPAs ( $d$ ) was kept constant at 76.2 mm to get GPAs and GPAs encased with geogrid of  $l/d = 1.63, 2.43$  and  $3.23$ , respectively.

### 3.3 Compaction of the Expansive Clay Bed and GPA

As illustrated in Fig. 2a, b (experimental set-up for small and large moulds), a sand layer of thickness 10 mm was laid at the bottom of the mould and levelled with a



rammer. In small moulds, a hollow cylindrical metal sheet of 130 mm diameter was pushed into the sand layer so as to form a circular box at a uniform distance of 10 mm from the sides of the tank. In large moulds, a square metal box of dimensions 361 mm  $\times$  361 mm  $\times$  437 mm was pushed into the sand layer at a distance of 10 mm from the sides of the tank and made to stand at a height on the bottom sand layer. This gap on the sides of 10 mm was filled with sand to form sand packing devised for a quick saturation of the expansive clay bed. The detailed description on the compaction procedure for the expansive clay beds and GPA can be found elsewhere [8, 13–15].

## 4 Tests Performed and Test Procedures

### 4.1 Heave Tests

In addition to the two unreinforced clay beds of expansive soils in small and large moulds, 12 heave tests were performed to assess and compare the heave of

1. plain GPAs of  $l/d = 1.63, 2.43$  and  $3.23$  in small moulds,
2. GPAs encased with geogrid of  $l/d = 1.63, 2.43$  and  $3.23$  in small moulds,
3. plain GPAs of  $l/d = 1.63, 2.43$  and  $3.23$  in large moulds and
4. GPAs encased with geogrid of  $l/d = 1.63, 2.43$  and  $3.23$  in large moulds.

The unreinforced expansive clay bed and the clay beds reinforced with GPAs and GPAs encased with geogrid were all wetted by continuously adding the water to the soil. Heave was monitored continuously with a dial gauge up to the point of saturation of the clay beds or equilibrium heave. After the equilibrium heave was reached, the water contents of samples collected from various depths of the expansive clay beds were determined to ensure complete saturation.

### 4.2 Measurement of Shear Parameters of Granular Pile-Clay Interface

Direct shear tests were conducted to find shear parameters  $c'$  and  $\phi'$  for the following cases:

1. of the granular material in the lower half of the shear box and the expansive clay in the upper half of the shear box and
2. of the granular material in the lower half of the shear box and the expansive clay in the upper half of the shear box with geogrid as interface between both.

Direct shear (shear box of size 60 mm  $\times$  60 mm  $\times$  20 mm) tests were conducted to evaluate the friction mobilized at the soil–granular material interface and at the soil–geogrid–granular material interface. The values of shear parameters  $c'$  and  $\phi'$

were 13 kPa and 30°, respectively, at the interface of soil–granular material and 13.3 kPa and 35° for the soil–geogrid–granular material interface.

## 5 Results and Discussion

Figure 3 shows the rate of heave for the unreinforced expansive clay bed in small and large moulds. Figure shows the variation of the amount of heave (mm) plotted on Y-axis to arithmetic scale with time (min) plotted on X-axis to logarithmic scale. It can be seen clearly that the amount of final equilibrium heave was 8 and 41 mm in small and large moulds, which was reached by the expansive clay bed in 3600 min in small moulds and 10,080 min in large moulds.

### 5.1 Effect of GPAs on Amount of Heave

When the clay bed was reinforced by GPAs and GPAs encased with geogrid, the amount of heave decreased drastically. Figures 4 and 5 show, by comparison, the heave profiles of the clay beds reinforced with GPAs of various *l/d* ratios (1.63, 2.43 and 3.23) in small and large moulds. As mentioned in the earlier sections, the final equilibrium heave of the unreinforced expansive clay bed was 8 mm in small moulds. The equilibrium heave decreased significantly to 0.75 mm, 0.86 mm and 0.9 mm,

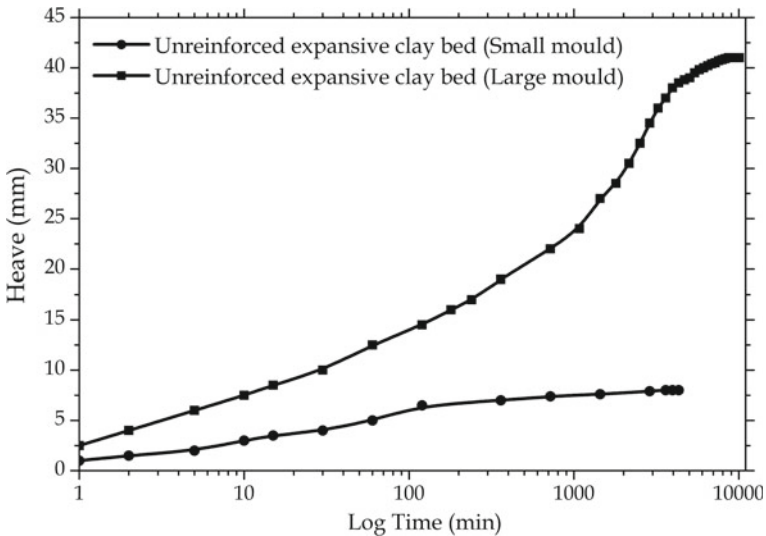


Fig. 3 Rate of heave of unreinforced expansive clay beds in small and large moulds

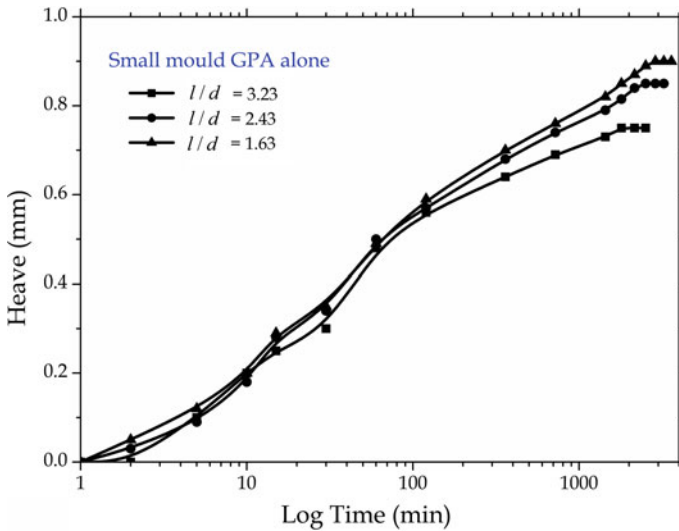


Fig. 4 Rate of heave of expansive clay beds reinforced with GPAs in small moulds

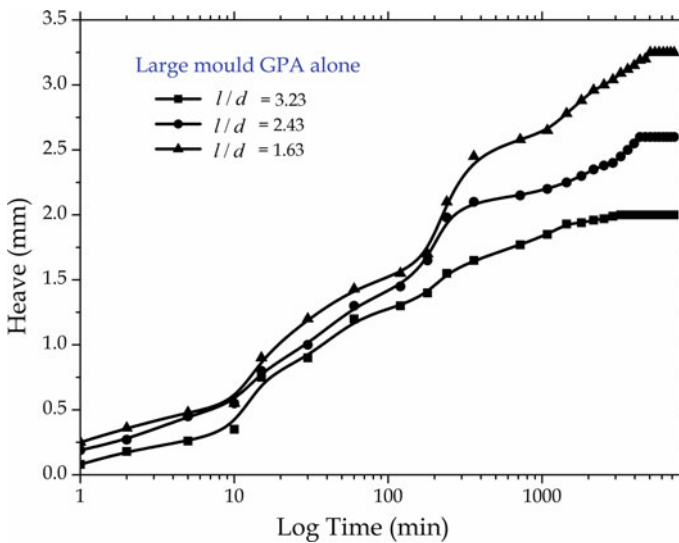


Fig. 5 Rate of heave of expansive clay beds reinforced with GPAs in large moulds

respectively, for GPAs with  $l/d = 3.23$ ,  $2.43$  and  $1.63$  in small moulds, whereas in large moulds, the final equilibrium heave of the unreinforced expansive clay bed was 41 mm. The equilibrium heave decreased significantly to 2 mm, 2.6 mm and 3.25 mm, respectively, for GPAs with  $l/d = 3.23$ ,  $2.43$  and  $1.63$  in large moulds. The

reduction in heave could be attributed to the uplift being resisted by the frictional force mobilized in the downward direction along the GPA–clay interface.

### 5.2 Effect of GPAs Encased with Geogrid on Amount of Heave

Heave further reduced upon the installation of GPAs encased with geogrid in the expansive clay beds. The final equilibrium heave recorded was 0.6 mm, 0.68 mm and 0.75 mm, respectively, for the GPAs encased with geogrid with  $l/d = 3.23, 2.43$  and  $1.63$  in small moulds. However, in large moulds, the amount of heave recorded was 0.7 mm, 0.8 mm and 0.97 mm, respectively, for the GPAs encased with geogrid having  $l/d = 3.23, 2.43$  and  $1.63$ . The heave profiles shown in Figs. 6 and 7 indicate this. In the case of GPAs encased with geogrid, the frictional resistance mobilized along the GPA–geogrid–clay interface would be higher, contributing to the higher reduction of heave. The increase in the shear parameters  $c'$  and  $\phi'$  presented in the earlier section shows this.

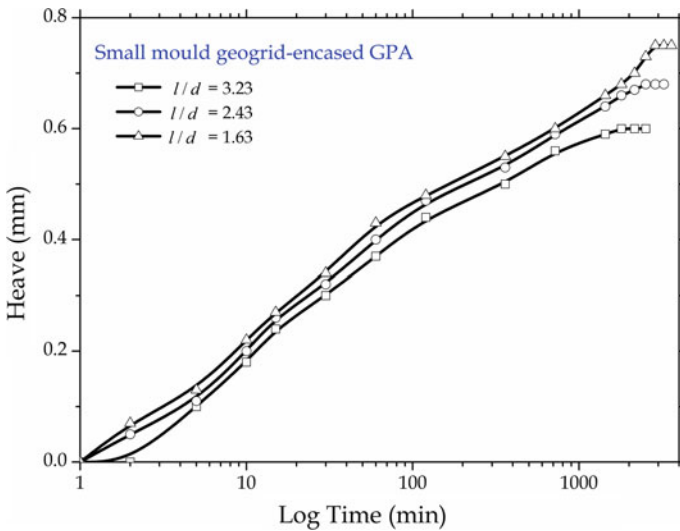


**Fig. 6** Rate of heave of expansive clay beds reinforced with GPAs encased with geogrid in small moulds

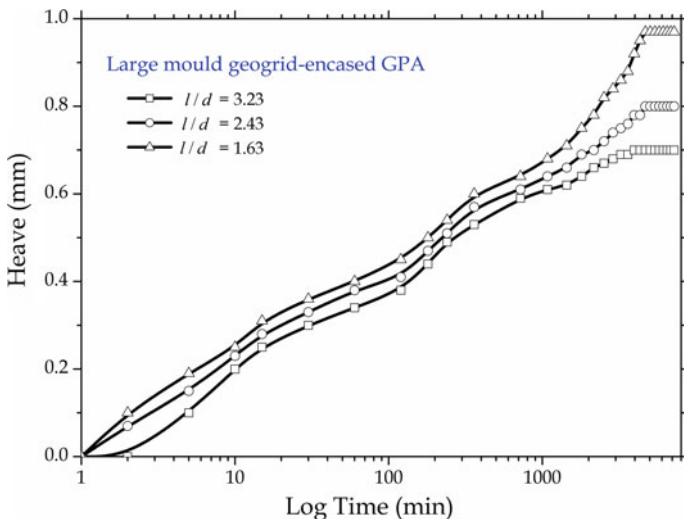


Fig. 7 Rate of heave of expansive clay beds reinforced with GPAs encased with geogrid in large moulds

### 5.3 Effect of GPAs and GPAs Encased with Geogrid on Rate of Development of Heave

The unreinforced expansive clay bed required about 3600 and 10,080 min of continuous wetting to attain the equilibrium heave in small and large moulds, while the clay beds reinforced with GPAs required much less time. As the GPA length increased, the time required for equilibrium reduced. For example, in small moulds, the time required for expansive clay beds to attain the final equilibrium heave was 1800 min, 2520 min, and 2880 min for the plain GPAs with  $l/d = 3.23, 2.43$  and  $1.63$ , respectively, whereas in case of large moulds, the time required by the clay beds to attain equilibrium heave was 3240 min, 4320 min and 5040 min for the plain GPAs with  $l/d = 3.23, 2.43$  and  $1.63$ , respectively. Granular pile material being highly permeable facilitating quicker saturation and the drastic reduction of heave through huge frictional resistance resulted in reduced heave and time durations for the final equilibrium heave. However, the time required to attain the final equilibrium heave did not change much in the case of the GPAs encased with geogrid (in both small and large moulds) though the amount of heave decreased.

The percentage reduction in heave ( $H_R$ ) is the ratio of the reduction in heave to the original heave of the unreinforced expansive clay bed and can be given as

$$H_R = \frac{H - H'}{H} \times 100 \tag{1}$$

**Table 2** Percentage reduction in heave of clay beds reinforced with GPAs

<i>l/d</i> ratio	Small mould ( $H_R$ %)	Large mould ( $H_R$ %)
1.63	88.75	92.0
2.43	89.3	93.6
3.23	90.6	95.1

**Table 3** Percentage reduction in heave of clay beds reinforced with GPAs encased with geogrid

<i>l/d</i> ratio	Small mould ( $H_R$ %)	Large mould ( $H_R$ %)
1.63	90.6	97.6
2.43	91.5	98.0
3.23	92.5	98.3

where  $H$  = amount of heave recorded,  $H'$  = reduced amount of heave obtained after reinforcing the expansive clay beds with GPAs and GPAs encased with geogrid.

Tables 2 and 3 show the percentage reduction in heave of expansive clay beds reinforced with plain GPAs and GPAs encased with geogrid. It can be seen that the percentage reduction in heave increased with increase in the length of the GPA. For an instance, the percentage reduction in heave are 92.0%, 93.6% and 95.1% with  $l/d = 1.63, 2.43$  and  $3.23$ , respectively, when the clay bed reinforced with GPAs in case of large mould. The clay bed reinforced with geogrid-encased GPA of  $l/d = 3.23$  resulted in the maximum percentage of heave reduction in both small and large moulds as shown in Tables 2 and 3. A maximum of 98.3% reduction in heave was observed for the geogrid-encased GPA of  $l/d = 3.23$ .

## 6 Conclusions

The following are the main conclusions that can be drawn from the experimental study:

1. Heave of the expansive clay beds decreased when they were reinforced by GPAs. Heave further decreased with increasing in  $l/d$  ratio of the GPAs. Reduction in heave was even more when the GPAs were encased with a geogrid.
2. Heave decreased by 92.5% and 98.3%, respectively, in the case of GPAs encased with geogrid in small and large moulds.
3. The time periods required for equilibrium heave also decreased when the clay beds were reinforced with GPAs. For example, the unreinforced expansive clay bed attained the equilibrium heave in 3600 and 10,080 min of continuous wetting, respectively, when the test was performed in small and large moulds. However, it requires much less time to attain equilibrium heave when the clay beds were reinforced with GPAs when compared to unreinforced expansive clay bed.
4. Further, it was found that as the GPA length increased, the time required to attain the final equilibrium further decreased.

5. It was noticed that the percentage reduction in heave increased with increase in the length of the GPA. For example, the percentage reduction in heave is 90.6%, 91.5% and 92.5% with  $l/d = 1.63, 2.43$  and  $3.23$ , respectively, when the clay bed reinforced with geogrid-encased GPAs in case of small mould.

## References

1. Chen, F. H. (1988). *Foundations on expansive soils*. Amsterdam: Elsevier Scientific Publishing Co.
2. Fredlund, D. G., & Rahardjo, H. (1993). *Soil mechanics for unsaturated soils*. New York: Wiley.
3. Gallipoli, D., Gens, A., Sharma, R., & Vaunat, J. (2003). An elasto-plastic model for unsaturated soil incorporating the effects of suction and degree of saturation on mechanical behaviour. *Geotechnique*, 53(1), 123–135.
4. Gourley, C. S., Newill, D., & Schreiner, H. D. (1993). Expansive soils: TRL's research strategy. In *Proceedings of 1st International Symposium on Engineering Characteristics of Arid Soils*. London.
5. Katti, R. K. (1978). Search for solutions to problems in black cotton soils. In *First IGS Annual Lecture*. Indian Institute of Technology, Delhi.
6. Lu, N., & Likos, W. (2004). *Unsaturated soil mechanics*. New York: Wiley.
7. Nelson, D. J., & Miller, J. D. (1992). *Expansive soils: Problems and practice in foundation and pavement engineering*. New York: Wiley.
8. Phanikumar, B. R. (1997). *A study of swelling characteristics of expansive soils and granular pile-anchor foundation system in expansive soils* (Doctoral thesis). JNTU Hyderabad, India.
9. Phanikumar, B. R., & Sharma, R. S. (2007). Volume change behaviour of fly ash-stabilized clays. *ASCE Journal of Materials in Civil Engineering*, 19(1), 67–74.
10. Phanikumar, B. R., Sharma, R. S., Rao, A. S., & Madhav, M. R. (2004). Granular pile-anchor foundation system for improving the engineering behaviour of expansive clay beds. *Geotechnical Testing Journal, ASTM*, 27(3), 279–287. <https://doi.org/10.1520/GTJ11387>.
11. Phanikumar, B. R., Rao, A. S., & Suresh, K. (2008). Field behaviour of granular pile-anchors in expansive clays. *Ground Improvement Journal*, 161(4), 199–206. <https://doi.org/10.1680/grim.2008.161.4.199>.
12. Phanikumar, B. R., Raghuram, A. S. S., & Sriramarao, A. (2019). Improving the expansive clay beds through granular pile anchors and geogrid-encased granular pile anchors. *Ground Improvement Journal*, 172(1). <https://doi.org/10.1680/jgrim.18.00086>.
13. Raghuram, A. S. S., Phanikumar, B. R., & Rao, A. S. (2018). Load carrying capacity of expansive clay beds reinforced with geogrid-encased granular pile-anchors. In M. Meguid, E. Guler, & J. Giroud (Eds.), *Advances in geosynthetic engineering. GeoMEast 2018. Sustainable Civil Infrastructures*. Cham: Springer.
14. Ranganatham, B. V., & Satyanarayana, B. (1965). A rational method of predicting swelling potential for compacted expansive clays. In *Proceedings, 6th International Conference on Soil Mechanics and Foundation Engineering* (Vol. 1, pp. 92–96). Canada.
15. Rao, A. S., Phanikumar, B. R., Babu, R. D., & Suresh, K. (2007). Pullout behaviour of granular pile-anchors in expansive clay beds in situ. *Journal of Geotech and Geoenvironmental Engineering, ASCE*, 133(5), 531–538. [https://doi.org/10.1061/\(asce\)1090-0241\(2007\)133:5\(531\)](https://doi.org/10.1061/(asce)1090-0241(2007)133:5(531)).
16. Rao, A. S., Phanikumar, B. R., & Suresh, K. (2008). Response of granular pile anchors under compression. *Ground Improvement Journal*, 161(3), 121–129. <https://doi.org/10.1680/grim.2008.161.3.121>.

17. Satyanarayana, B. (1966). *Swelling pressure and related mechanical properties of black cotton soils* (PhD thesis). Indian Institute of Science, Bangalore.
18. Sharma, D., Jain, M. P., & Prakash, C. (1978). *Handbook on under-reamed and bored compaction pile foundations*. Roorkee, India: Central Building Research Institute.



# Mathematical Modeling of Displacements in Building Frame Founded on Pile Groups Embedded in Sand



C. Ravi Kumar Reddy, K. Ramesh, G. Srinivasulu and N. V. Mohan Krishna

**Abstract** Conventional analysis of building frames will be made by assuming the bases to be rigid or hinged, whereas buildings rest on soil which allows the bases to displace and rotate. This paper presents the results of static vertical load tests carried out on model building frame supported on pile groups embedded in sand. The experimental results of displacements due to the applied loads on the experimental model have been modeled mathematically, and relevant equations have been developed. The developed equations show very good correlation coefficient which implies that the equations developed can be used to get output obtained from the experiment with fairly well with that of experiments. The present research is an attempt to model the experimental results of various displacements, viz. lateral, vertical, and rotational displacements in case of a building frame resting on group of piles embedded in sand. The developed equations can be utilized as a means to replace the experiment conducted in the laboratory with that of mathematical equations within the limitation of experimental inputs.

**Keywords** Modeling · Building frame · Pile groups · Sand · Displacements

## 1 Introduction

The design of any building frame by structural engineers is a challenging task due to loads and also soil interaction. The soil interaction is a difficult parameter to estimate. An attempt has been made in the present study, to determine the displacements by an experiment and also to model it mathematically for various loads applied experimentally. Soil settlement is a function of the flexural rigidity of the superstructure. The structural stiffness can have a significant influence on the distribution of the column

---

C. Ravi Kumar Reddy (✉) · G. Srinivasulu · N. V. Mohan Krishna  
Civil Engineering Department, Kallam Haranadhareddy Institute of Technology, Guntur 522019,  
India  
e-mail: [ravibecnitw@gmail.com](mailto:ravibecnitw@gmail.com)

K. Ramesh  
Civil Engineering Department, PVP Siddhartha Institute of Technology, Vijayawada 520007, India

© Springer Nature Singapore Pte Ltd. 2020  
S. Saride et al. (eds.), *Advances in Geotechnical and Transportation Engineering*,  
Lecture Notes in Civil Engineering 71,  
[https://doi.org/10.1007/978-981-15-3662-5\\_16](https://doi.org/10.1007/978-981-15-3662-5_16)

193

loads and moments transmitted to the foundation of the structure. Previous studies have, however, indicated that the effect of interaction between soil and structure can be quite significant.

In this regard, much of analytical work has been reported on the building frames founded on pile groups by Ingle and Chore [1] and Chore et al. [2, 3]. But no significant study has been made in the direction of experimental investigation of the effect of soil interaction on building frames founded on pile groups except by Reddy and Rao [4–6]. The aim of this paper is to present the experimental investigation as well as mathematical modeling. An attempt is made to model the experimental results of various displacements, viz. lateral, vertical, and rotational displacements in case of a building frame resting on group of piles embedded in sand. The experimentally obtained results were modeled to determine the relationship between load applied and the displacements at the base of the columns in the building frame.

## 2 Experimental Program

### 2.1 Frame and Pile Groups

Using the scaling law given by Eq. (1) proposed by Wood et al. [7], the material and dimensions of model were selected. An aluminum tube with outer diameter 16 mm and inner diameter 12 mm is selected as the model pile with a length scaling factor of 1/10. This is used to simulate the prototype pile of 350 mm diameter solid section made of reinforced concrete with a compressive strength of 30 MPa. Columns of height 3.2 m and beam of span 5 m of the plane frame were scaled in the same manner. Aluminum plates of 13 mm thickness were used as pile caps. In the pile group setup, pile spacing of eight diameter ( $8D$ ) is adopted, and the length of the piles is so selected to maintain length to diameter ( $L/D$ ) ratio of 20 [8]. The sufficient free-standing length was maintained from the bottom of the pile cap to top of the soil bed. Beam column junctions are made by welding for the fixed condition. Screwing of piles and columns in the threads provided in the pile cap leads to partial fixed condition. The scaling factors used in the study are presented in Table 1.

**Table 1** Scaling factors

Variable	Scaling factors
Length	1/10
Density	1
Stiffness	1/10
Stress	1/10
Strain	1
Force	1/10 <sup>3</sup>

$$\frac{E_m I_m}{E_p I_p} = \frac{1}{n^5} \quad (1)$$

where  $E_m$  is modulus of elasticity of model,  $E_p$  is modulus of elasticity of prototype,  $I_m$  is moment of inertia of model,  $I_p$  is moment of inertia of prototype, and  $1/n$  is scale factor for length.

## 2.2 Experimental Setup and Instrumentation

The photograph of the test setup is shown in Fig. 1. Different tests were conducted on model pile groups with frame embedded in sand bed in a concrete testing chamber which is well instrumented with the dial gauges of sensitivity 0.002 to study the lateral, vertical displacements and rotations at the base of the column. Loads on the frame are applied through the hooks provided to the beam at required locations according to the type of load on the beam. The model frame was placed at the center of the testing chamber using templates. The sand is poured in the testing chamber gently through the pores of a steel tray in layers to attain the loose state and uniformity for the sand bed. The installation procedure simulates the bored pile condition.



Fig. 1 Experimental setup

### 2.3 Test Procedure

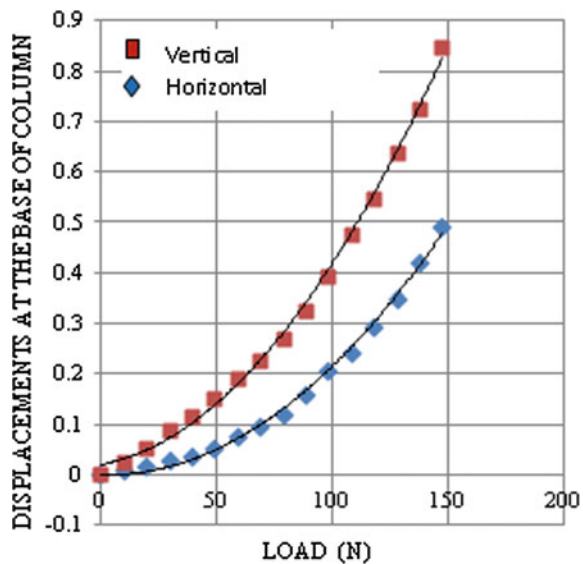
Static vertical loads were applied on the model frame by placing weights on hangers. The loads were applied in increments and were maintained for a minimum period to allow the deflection to stabilize. During the application of static loads, the lateral, vertical displacements at the base of the column and rotation of pile cap were measured using the instrumentation setup as described earlier.

## 3 Mathematical Modeling of Experiment

Figure 2 shows the relationship between the loads applied in the experimental setup and the vertical displacements at the base of the column measured from the experiment. The horizontal displacement is also shown in Fig. 2. From the figure, it can be seen that there is nonlinear relationship and is following a polynomial variation of order two. The developed relationship between load and vertical displacement is given in Eq. (2). The developed equation shows very good correlation of 0.9977. The developed relationship between load and horizontal displacements is given in Eq. (3). The developed equation shows very good correlation of 0.9972. Hence, the developed equations can be used to compute the displacements when a particular load is applied on the frame within the limits of experimental input.

$$y = 3 \times 10^{-5}x^2 + 0.0009x + 0.0196 \quad (2)$$

**Fig. 2** Displacements at the base of the column



where  $y$  is vertical displacement at the base of the column;  $x$  is load applied on the frame.

$$y = 2 \times 10^{-5}x^2 - 0.0001x \tag{3}$$

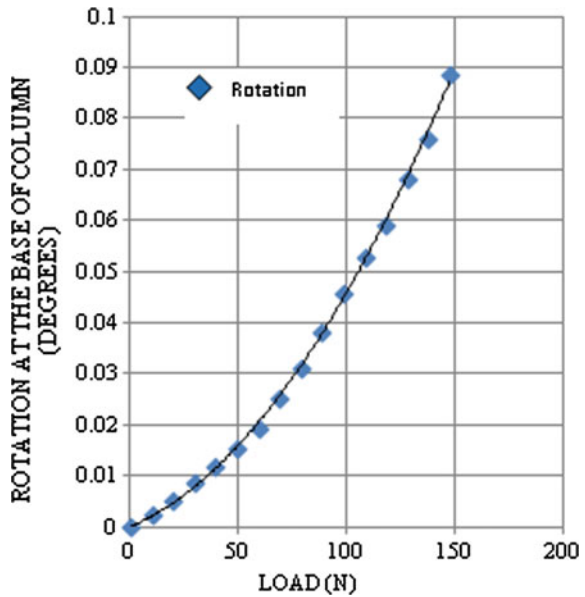
where  $y$  is horizontal displacement at the base of the column;  $x$  is load applied on the frame.

Figure 3 shows the relationship between the loads applied in the experimental setup and the rotation at the base of the column obtained from the experiment. The relationship between the load and rotation at the base of the column is following polynomial variation of order two. The developed relationship between load and rotation at the base of the column is given in Eq. (4). The developed equation shows very good correlation of 0.9991. Hence, the developed equation can be used to compute the rotation at the base of the column when a particular load is applied within the limits of experimental input.

$$y = 3 \times 10^{-6}x^2 + 0.0002x \tag{4}$$

where  $y$  is rotation at the base of the column;  $x$  is load applied on the frame.

**Fig. 3** Rotation at the base of the column



## 4 Conclusions

Based on the experimental results obtained from building frame supported on pile groups embedded in cohesion-less soil, the following conclusions have been drawn:

- An experimental study was successfully conducted in laboratory to model the building frame resting on pile groups embedded in sand based on Wood et al.'s scaling factors.
- The lateral displacement, settlement, and rotation at the base of the column were obtained from the experiment by direct measurement.
- The relationship between load and vertical displacement at the base of the column modeled indicates nonlinear relation with correlation of 0.9977. Similarly, the relation between load and horizontal displacement at the base of the column indicates a nonlinear relation with a correlation of 0.9972.
- The relation between load and rotation at the base of the column indicates a nonlinear relation with a correlation of 0.9991.
- The present research will be useful as a tool to simulate the laboratory experiment within the limits of experimental input, i.e., load to compute horizontal displacement, vertical displacement, and rotation at the base of the column from the experiment.

## References

1. Ingle, R. K., & Chore, H. S. (2007). Soil-structure interaction analysis of building frames—An overview. *Journal of Structural Engineering SERC*, 34(5), 201–209.
2. Chore, H. S., Ingle, R. K., & Sawant, V. A. (2009). Building frame-pile foundation-soil interactive analysis. *Interaction and Multiscale Mechanics*, 2(4), 397–411.
3. Chore, H. S., Ingle, R. K., & Sawant, V. A. (2010). Building frame—Pile foundation—Soil interaction analysis: A parametric study. *Interaction and Multiscale Mechanics*, 3(1), 55–79.
4. Reddy, C. R. K., & Rao, T. D. G. (2011). Experimental study of a modeled building frame supported by pile groups embedded in cohesionless soil. *Interaction and Multiscale Mechanics*, 4(4), 321–336.
5. Reddy, C. R. K., & Rao, T. D. G. (2012). Study of soil interaction in a model building frame with plinth beam supported by pile group. *International Journal of Advanced Structural Engineering*, 4(11).
6. Reddy, C. R. K., & Rao, T. D. G. (2014). Effect of rigidity of plinth beam on soil interaction of modeled building frame supported on pile groups. *Civil Engineering Dimension*, 16(1), 8–17.
7. Wood, D. M., Crew, A., & Taylor, C. (2002). Shaking table testing of geotechnical models. *International Journal of Physical Modelling in Geotechnics*, 1, 1–13.
8. Chandrasekaran, S. S., & Boominadhan, A. (2010). Group interaction effects on laterally loaded piles in clay. *Journal of Geotechnical and Geoenvironmental Engineering ASCE*, 136, 573–582.

# Capacity and Level of Service of Roundabouts Using Indo-HCM



Sadguna Nuli, Nagamani Gade and Kavya Beeravolu

**Abstract** A roundabout or traffic rotary is an enlarged road intersection where all converging vehicles are forced to move around a large central island in one direction before they can weave out of traffic flow into their respective direction radiating from the central island. In India and other countries which follow “keep to the left” regulations, vehicles move in clockwise direction around the central island. The objective of providing a rotary intersection is to eliminate the necessity of stopping even for crossing streams of vehicles and to reduce the area of conflict. The crossing of vehicles is avoided by allowing all vehicles to merge into the streams around the rotary and then to diverge out to the desired radiating road. Thus, the crossing conflict is eliminated and converted into “weaving maneuver,” i.e., merging from the left and diverging out to the right or merging from the right and a diverging out to the left. In this study, two circular roundabout intersections in Hyderabad city are chosen to analyze their operational performance under prevailing traffic composition, flow movements, and geometric conditions by conducting traffic volume and gap-acceptance studies. Both intersections are analyzed and their capacity and level of services (LOS) are estimated as per recently published Indian Highway Capacity Manual (Indo-HCM).

## 1 Introduction

At-grade intersections are the critical points of a road network where delay normally occurs due to sharing of space and time between conflicting streams of vehicles. Depending upon the type of control employed, intersections can be termed as uncontrolled intersections, stop-controlled intersections, rotaries, signalized intersections, and grade-separated intersections or interchanges. A rotary is a specialized form of

---

S. Nuli (✉)

Vardhaman College of Engineering, Kacharam, Shamshabad, Hyderabad 501218, India  
e-mail: [findguna@gmail.com](mailto:findguna@gmail.com)

N. Gade · K. Beeravolu

CVR College of Engineering, Vastunagar, Mangalpalli, Ibrahimpatan, Hyderabad 501510, India

© Springer Nature Singapore Pte Ltd. 2020

S. Saride et al. (eds.), *Advances in Geotechnical and Transportation Engineering*,

Lecture Notes in Civil Engineering 71,

[https://doi.org/10.1007/978-981-15-3662-5\\_17](https://doi.org/10.1007/978-981-15-3662-5_17)

at-grade intersection where vehicles from the converging arms are forced to move round a central island in one direction in an orderly and regimented manner and weave out of the roundabout into their desired direction.

Typically, roundabouts are classified according to their size and environment to solve design and evaluation of operational performance issues. They are classified based on the number of lanes and size as mini-roundabouts, single-lane roundabouts, double-lane roundabouts, and multilane roundabouts with more than two approach lanes. Mini-roundabouts are small roundabouts of about 4–12 m diameter and are generally provided when there is enough roadway width is not available. Finally, multilane roundabouts with more than two or more lanes are provided to accommodate more than one vehicle traveling side by side. The speeds at the entry on the circulatory roadway and at the exit are similar or may be slightly higher than those for the single-lane roundabouts. These roundabouts can be further subdivided based on their environment such as rural or urban roundabouts. In case of urban areas, consideration should be given for pedestrians, bicyclists, and large vehicles with low design speed. On the other hand, high design speed and large vehicles are considered in rural or non-urban areas.

In any of the above conventional roundabout, traffic at entry seek a suitable gap in the circulating stream to negotiate at the roundabout. Since these intersections are characterized by complex vehicular movements such as merging and diverging and to ensure safety of these vehicles, it is necessary to study them to arrive at capacity and level of service (LOS) under different operating conditions. Capacity of a roadway facility is defined as the maximum hourly rate at which vehicles can reasonably be expected to traverse a point or uniform section of a lane or roadway during a given time under the prevailing roadway, traffic, and control conditions. Under mixed traffic conditions, it is necessary to bring all the vehicles to a common type, usually the passenger car. The capacity is then expressed in passenger car units (PCUs) per hour.

On the other hand, level of service is used to refer congestion level. When a road is carrying a traffic volume equal to its capacity under ideal roadway and traffic conditions, the operating conditions become poor. Speed drops down, and the delay and frequency of stops mount up. Thus, the concept of level of service is defined as a qualitative measure describing the operational conditions within a traffic stream and their perception by motorists. Typically, in case of roundabouts, delay caused by queueing of vehicles at entry and by geometry is used as a standard parameter to measure the operational performance of a roundabout. The objective of the present study is to determine the capacity and level of services of chosen roundabouts under various geometric and traffic flow conditions. Having been introduced about roundabouts capacity and their operational performance, a comprehensive literature review on roundabouts with respect to the stated objective is presented below.

Macioszek and Akçelik [1] compared two roundabout capacities models such as Macioszek model and SIDRA model in their study. Both models were based on gap-acceptance theory with an exponential distribution of circulating road headways, but



their headways and capacity distributions are calibrated for two different traffic conditions prevailing in Poland and Australia. Vasantha Kumar et al. [2] studied a five approach multi-leg roundabout by conducting a traffic volume survey using video data collection. They found that the proportion of weaving traffic as 0.81 and then estimated required weaving width and lengths. They also estimated the capacity of the roundabout as 3020 PCU/h using TRL equation. Giuffrè et al. [3] analyzed modeling issues at multilane roundabout specifically, minor drivers' failure to obey stop or yield control. They found that existing operational models do not incorporate interdependencies between entering and circulating vehicles at multilane roundabouts. To account for this, an analytical capacity model is derived from field observations. Giuffrè et al. [4] reviewed measurement of two gap-acceptance parameters such as critical gap and follow-up times for various roundabouts across the world. They found that size of the roundabout such as single-lane/turbo influenced the gap-acceptance parameters. Finally, they have developed a single meta-analytic estimate to represent various roundabouts. Manage et al. [5] reviewed various capacity and delay models of various intersections and modified to suit Japanese traffic conditions. Finally, a roundabout was proposed as an alternative to signalized control, and they found it is promising under low traffic conditions. Mathew et al. [6] studied Indian roundabout capacity under heterogeneous traffic conditions. They found that relationship between entry flow and circulatory flow follows a negative exponential behavior, i.e., the entry capacity reduces exponentially with the increase in circulating flow. Finally, authors estimated stream equivalency factors for critical gap and follow-up times under mixed traffic conditions and a multiplicative adjustment factor for HCM 2010 equation to estimate entry capacity under mixed traffic conditions. Vasconcelos et al. [7] used several methods such as maximum likelihood, and logit to estimate gap-acceptance parameters at roundabout. The comparison of estimates with reference values from several countries indicates the existence of relevant driving style differences, which implies that locally calibrated, country-specific, parameters are required for capacity estimations.

## 2 Analysis of Roundabout

Generally, the roundabout is analyzed by its geometry, traffic flow, and driving behavior characteristics. The geometry of a typical roundabout can be described by its central island diameter, entry radius, entry width, exit radius, exit width, weaving length and width, and splitter island as shown in Fig. 1.

The traffic flow through the roundabout intersection can be broadly divided into entry flow through multiple approaches and circulating flow moving around the central island. The driving behavior of vehicles can be described by analyzing various headways such as gap, and headways are shown in Fig. 2. Gap is defined as the time span between two consecutive circulating vehicles that create conflict with an entering vehicle. Similarly, a headway can be defined as the time span between

**Fig. 1** Geometric elements of a typical roundabout.  
Source [8], pp. 7–4

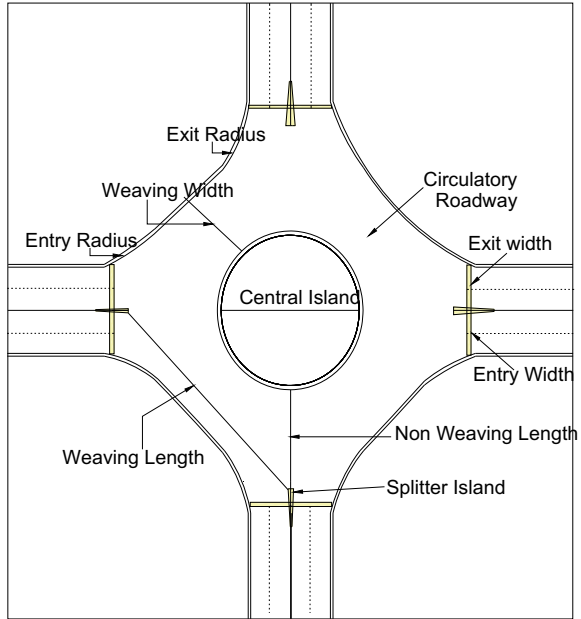
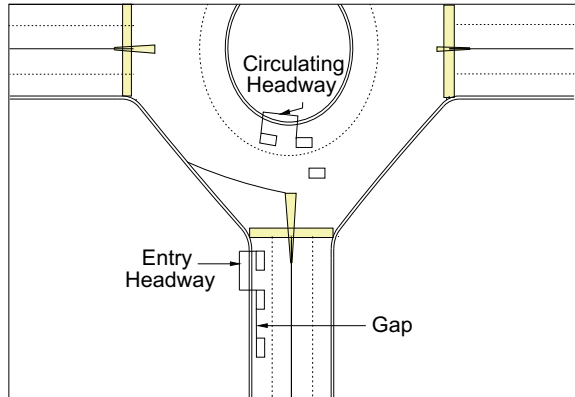


**Fig. 2** Measuring gap and headways between vehicles.  
Source [8], pp. 7–6



two following vehicles and is measured from the first vehicle’s front bumper to the following vehicle’s front bumper.

### 3 Methodology

The methodology for estimation of capacity and level of service of a given roundabout involves collection of geometric, traffic, and driving behavior parameters. The

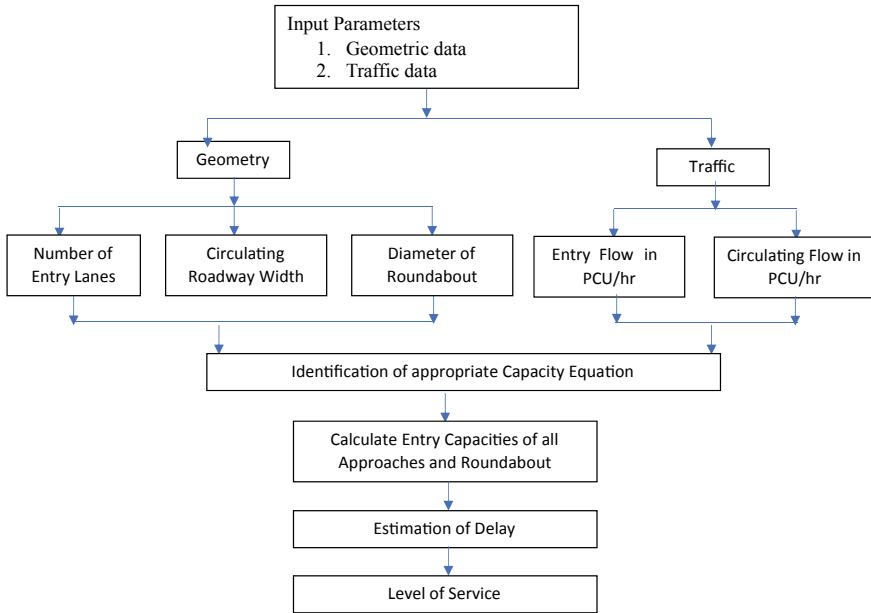


Fig. 3 Methodology flow chart. Source [8], pp. 7–8

geometric data includes details such as diameter of roundabout, number of approach lanes, approach width, number of circulating lanes, and circulating roadway width. And, traffic data includes details such as entry flow, circulating flow, and their conversion to passenger car units (PCU). Finally, the driving behavior data includes estimation of critical gap and follow-up time. Based on the above-collected data, suitable capacity equation must be chosen as per Indo-HCM manual [8]. Thereafter, the entry capacity of all approaches and the whole roundabout can be estimated by substituting estimated critical gap, follow-up time, and circulating flow details. The level of service of the roundabout can be estimated by substituting total entry flow from all the approaches and by estimating average delay experienced per vehicle. The above steps are outlined in Fig. 3. The same methodology can be applied for a planning and design of new roundabout by supplying traffic information and the desired level of service (LOS).

#### 4 Data Collection and Extraction

The study area is chosen as KBR park and NTR Marg roundabouts in Hyderabad city. The KBR park roundabout is a three-way intersection with 40 m diameter central island and 9 m each for entry and exit width for every approach. Similarly, the NTR Marg roundabout is a four-way intersection with 60 m diameter central

island and 10 m each for entry and exit width for every approach. The layouts of the study intersections are shown in Figs. 4 and 5. Apart from collecting geometric data, classified traffic volume surveys are carried out to get the various turning volumes such as entry flows and exit flows for all the approaches. Simultaneously, a separate team of members collected data for circulating flow at all the entries. Since the traffic is characterized by mix of multiple vehicle types, all these vehicles are converted to passenger cars by multiplying with appropriate PCU values as given in Indo-HCM [8]. The PCU values used in the study are given in Table 1. Finally, a gap-acceptance study is carried out by placing video cameras at vantage locations so that it covers entire weaving section, entry, circulating, and exit flows at each approach. Further, cameras are also focussed in such a way that they cover the part of non-weaving section so that available gap in the circulating traffic is visible before being accepted or rejected by the entry vehicle. Similarly, expected queue length at entry is also covered in the recording.

Data extraction was carried out with respect to gap-acceptance parameters such as accepted gap, rejected gaps, and follow-up time for different classes of vehicles and corresponding classified entry and exit flows.

To estimate capacity and level of service of the intersection, various parameters such as critical gap, follow-up time, and average delay of the vehicle must be estimated. Critical gap represents the minimum time gap in the circulating flow of vehicles when an entering vehicle from approach can safely enter a roundabout, whereas follow-up time is the headway corresponding to saturation flow rate for the approach if there were no conflicting vehicles from circulating flow. In addition, the delay can be defined as the additional time experienced by the vehicle from the

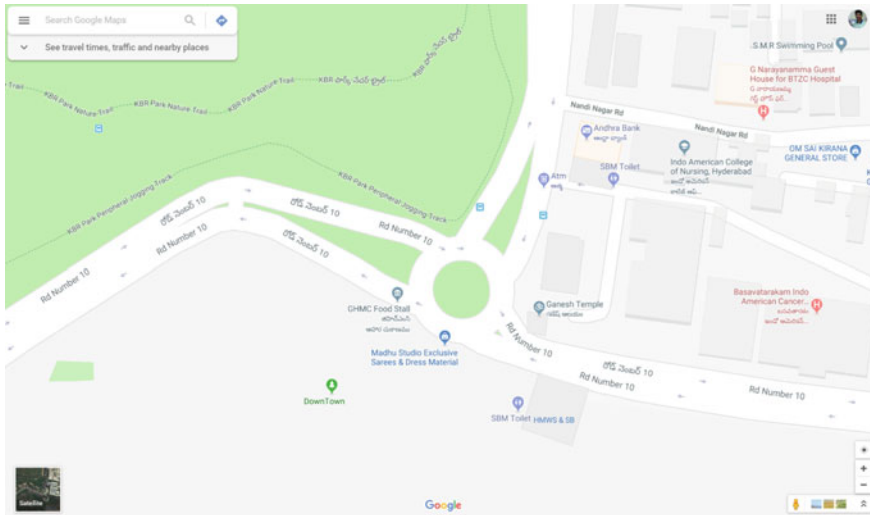


Fig. 4 Layout of the KBR park roundabout. Source Google Map

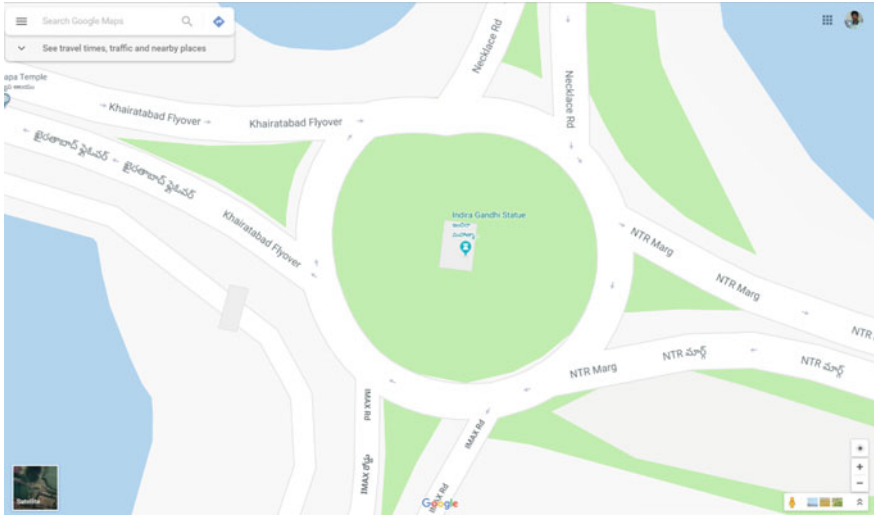


Fig. 5 Layout of the NTR Marg roundabout. Source Google Map

Table 1 Passenger car units

Dia (m)	TW	Auto	Small car	Big car	LCV	Heavy vehicle	Cycle
KBR (40)	0.32	0.83	1.0	1.4	1.53	3.2	0.25
NTR Marg (60)	0.32	0.83	1.0	1.4	1.46	3.05	0.28

Source [8], pp. 7–10

entry point to reach the exit point of the intersection. These parameters are further discussed in the subsequent sections.

### 4.1 Calculation of Critical Gap ( $T_c$ )

Critical gap is a parameter that depends on local conditions such as geometric layout, driver behavior, vehicle characteristics, and traffic conditions. However, critical gap cannot be measured directly in the field or from recorded events. The critical gaps are estimated based on the technique related to the accepted and maximum rejected gaps using root mean square method. Root mean square (RMS) is an analytical model where the minimization of square root of the mean squared deviation of predicted value from a given baseline or fit gives the absolute measure fit. Critical gap estimation requires information about the accepted gap and the maximum rejected gap for each driver. RMS model minimizes the square root of the mean squared deviation of rejected gap value  $R_i$  and accepted gap value  $A_i$  from expected critical gap value  $T_c$  to give the average critical gap value. The function depicting the estimation of

critical gap is given in Eq. (1) (Indo-HCM) [8].

$$\text{RMS} = \text{Min} \left[ \sum_{i=1}^n \sqrt{\frac{(A_i - T_c)^2 + (T_c - R_i)^2}{2}} \right] \quad (1)$$

where

$A_i$  Accepted gap of the  $i$ th entering vehicle (*seconds*)

$R_i$  Highest rejected gap of the  $i$ th entering vehicle (*seconds*) and

$T_c$  Critical gap value (*seconds*)

Using solver option in Microsoft EXCEL, function minimization can be carried out which is basically an iterative process and the first value for iteration must be logical. It would be good to use average of all the highest rejected gaps and all accepted gaps as a first value or starting point so that it can converge fast and reduce the number of iterations. Critical gap estimation is enumerated within the Excel worksheet as presented in Table 2. The values in column 2 and column 3 are the maximum rejected gaps ( $R_i$ ) and accepted gaps ( $A_i$ ), respectively. The initial value of  $T_c = 3.23$  s is given as input to start the iteration in solver, which is an average of all accepted and rejected gaps. This is used to calculate the value of RMS function as given in the last column. The sum of the function is given in the last row. The iteration process is started using the solver function in MS EXCEL to get the minimum value of sum of root mean squared values. The iterative process utilized helped in converging the function value from 17.31 to 17.20, the convergence was achieved at  $T_c = 3.01$  s, which is the estimated critical gap.

## 4.2 Calculation of Follow-up Time ( $T_f$ )

Follow-up time is measured at the stop line of the entry between the vehicles using the same gap in circulating flow. The vehicles on entry leg should be in a queuing position following each other while accepting the same gap in circulating flow. Follow-up time is the time between two entering vehicles, front to front, which can be calculated by the average difference between the passage times of two entering vehicles accepting the same mainstream gap under a queued condition. It is to be noted that follow-up time is considered as 0.75 times the critical gap as given in Indo-HCM [8].

## 5 Estimation of Capacity and Level of Service

The capacity of a roundabout depends on entry angle, lane width, and the number of entry and circulating lanes. Like other types of intersections, operational performance

**Table 2** Gap analysis and critical gap estimation

Rejected gap	Max. rejected gap (S)	Accepted gap (S)	RMS error
1, 2.32, 1.47, 2.95, 3.17, 2.37, 2.54, 2.89	3.17	3.24	0.20
0.75, 0.57, 1.24, 1.04, 0.68, 1.83, 1.89, 0.48	1.89	3.89	1.01
1.72, 1.62, 1.38, 0.92	1.72	3.56	0.99
0.38, 1.13, 0.16	1.13	2	6.44
1.02, 0.98, 1.35, 1.31	1.35	1.71	1.49
1.77, 0.89, 2.03, 1.63, 2.84, 3.37, 1.80, 1.76, 1.82	3.37	3.96	0.72
1.71, 3.83, 1.80	3.83	4.13	0.98
0.91, 0.97, 1.25	1.25	1.87	1.48
1.16, 1.28, 0.71, 0.97, 0.98	1.28	4.86	1.79
2.43, 1.31	2.43	2.9	0.42
1.58, 1.14, 1.48, 1.66, 1.76, 2.06, 2.90, 1.76, 1.57, 1.59, 2.31, 2.42, 1.60	2.9	3.07	0.09
1.58, 1.24, 1.54, 0.95, 1.07, 1.62	1.62	4.78	1.59
Average	2.16	4.16	Sum 17.20
Critical gap $T_c$		3.01	
Follow-up time $T_f$		2.3	

depends heavily on the volume of vehicles entering from all approaches. Many studies on roundabout capacity have been carried out in multiple countries. Most widely used Transportation Research Laboratory (TRL) models were developed based on the geometric parameters of the roundabout and driving behavior of the road users. Australian Road Research Board (ARRB) models differ from the TRL model significantly, following a lane-based gap-acceptance theory including geometric parameters. Sidra Intersection software includes roundabout capacity models developed in Australia and the USA. The highway capacity model (HCM 2010) developed by Transportation Research Board (TRB) combines a gap-acceptance model along with exponential regression and can be calibrated by estimating the critical headway and

follow-up headway. According to Indo-HCM [8], the capacity of a roundabout is a function of entry flow, circulating flow, critical gap, and follow-up time as given below:

$$C = A \times \text{Exp}(-B \times Q_c) \tag{2}$$

$$A = 3600/T_f \tag{3}$$

$$B = (T_c - 0.5 \times T_f)/3600 \tag{4}$$

where

$T_f$  Follow-up time in *seconds*

$T_c$  Critical gap in *seconds*

$Q_c$  Circulating flow in PCU/h

Therefore, capacities of study intersections KBR Park and NTR Marg are estimated as 3024 PCU/h and 7744 PCU/h using above model. Typically, a roundabout operates with less delay than signalized intersections. Roundabouts do not stop all entering vehicles, reducing both individual and queuing delays. However, they can increase delays in locations where high-volume road intersects with low-volume road. The level of service (LOS) of the above study intersections is determined by estimating the average delay experienced by each vehicle using Indo-HCM [8] model as follows:

$$\text{The average vehicle delay } y = 0.8 \times e^{0.001 \times x} \tag{5}$$

where

$y$  Vehicular delay in *seconds*

$x$  Total approach traffic flow in Veh/h

Based on the estimated delay, level of service is classified as per Indo-HCM [8] guidelines given in Table 3.

**Table 3** Level of service

LOS	Average delay “d” per vehicle (s)
A	$\leq 5$
B	$6 \leq d \leq 15$
C	$16 \leq d \leq 20$
D	$21 \leq d \leq 35$
E	$36 \leq d \leq 65$
F	$>65$

Source [8], pp. 7–13



**Table 4** Summary of KBR park roundabout level of service

	Ent 1	Ent 2	Ent 3	QC 1	QC 2	QC 3	Delay (s/veh)	LOS
<i>Morning</i>								
7:00–8:00	820	685	429	282	633	584	6	B
8:00–9:00	1342	832	614	464	1063	728	13	B
9:00–10:00	1509	804	1165	968	1287	746	26	D
10:00–11:00	1210	853	1149	794	1082	811	20	C
<i>Evening</i>								
4:00–5:00	1428	904	1111	890	1297	871	25	D
5:00–6:00	1298	1041	942	738	1265	951	21	D
6:00–7:00	1387	759	1137	862	967	695	21	D
7:00–8:00	1230	1017	1147	778	523	953	24	D
<i>Peak hour</i>								
8:45–9:45	1387	759	1137	862	967	695	21	D
4:30–5:30	1536	995	999	799	1361	924	27	D

The summary of the results such as entry flow, circulating flows, delay, and level of service during morning and evening periods at KBR Park and NTR Marg roundabouts are presented in Tables 4 and 5.

## 6 Conclusion

Roundabouts improve safety by converting crossing conflicts into weaving operations. The geometry of roundabouts such as diameter, width of circulatory flow, and width of entry and exit flows depends on the total traffic volume and share of turning movements passing through the intersection. In the present study, the capacities of KBR Park and NTR Marg roundabouts are estimated as 3024 PCU/h and 7744 PCU/h, respectively. Similarly, level of services of KBR Park and NTR Marg roundabouts during morning and evening peak hours are estimated as D and F, respectively. Furthermore, it may be noticed that the average delay of the vehicle is estimated as 896 s/veh during evening peak at NTR Marg roundabout, such a huge value seems to be unreasonable because there were no stopping and queuing of vehicles during the study period. Therefore, it may be concluded that the exponential model given by Indo-HCM for estimating average delay may not work under such high-volume and geometric conditions.

In general, level of service (LOS) of roundabouts can be improved by diversion of traffic or by increasing widths of entry approaches and circulatory roadways around Central Island. The study identified that the following are the contributing issues to the poor level of service at the above locations: mixed traffic conditions, no lane discipline, lack of enforcement measures, and inefficient and inadequate public

**Table 5** Summary of NTR Marg roundabout level of service

	Ent 1	Ent 2	Ent 3	Ent 4	QC 1	QC 2	QC 3	QC 4	Delay (s/veh)	LOS
<i>Morning</i>										
7:00-8:00	224	576	1022	886	778	1462	113	403	12	B
8:00-9:00	336	732	1592	1164	1149	1946	179	522	37	E
9:00-10:00	565	831	1897	1707	1815	2129	232	617	119	F
10:00-11:00	699	573	2304	1028	2533	1801	289	1082	80	F
<i>Evening</i>										
4:00-5:00	356	802	2781	1348	1903	1715	349	674	158	F
5:00-6:00	574	934	4794	1903	3647	2128	451	846	753	F
6:00-7:00	468	1128	1277	2161	3874	2490	635	1336	123	F
7:00-8:00	509	1231	4296	2371	3228	2711	560	1227	896	F
<i>Peak hour</i>										
9:30-10:30	720	744	2138	1412	2307	2217	271	787	120	F
6:00-7:00	468	1128	1277	2161	3874	2490	635	1336	123	F

transport system. Therefore, broad recommendations emerged out of the study can be written as:

1. Planning should focus on reduction of the traffic load on existing road network through various travel demand management measures.
2. Emphasis should be placed improving public transportation system.
3. Concerted efforts are needed in removing encroachments, bottlenecks, improving traffic signal, road condition, and geometrics at intersections.

## References

1. Macioszek, E., & Akçelik, R. (2017). A comparison of two roundabout capacity models. In *5th International Roundabout Conference, Transportation Research Board, Green Bay, Wisconsin, USA*, 8–10 May.
2. Vasantha Kumar, S. Gulati, H., & Arora, S. (2017). Design of a rotary for an uncontrolled multi-leg intersection in Chennai, India. In *Materials Science and Engineering Conference Series* (Vol. 263, pp. 30–32). <https://doi.org/10.1088/1757-899x/263/3/032030>.
3. Giuffrè, O., Grana, A., Giuffrè, T., & Marino, R. (2014). Estimating traffic operations at multi-lane roundabouts: A case study. *ARP Journal of Engineering and Applied Sciences*, 9(2).
4. Giuffrè, O., Granà, A., & Tumminello, M. L. (2016). Gap-acceptance parameters for roundabouts: a systematic review. *European Transport Research Review*, 8(2). doi: <https://doi.org/10.1007/s12544-015-0190-4>.
5. Manage, S., Hideki, N., & Koji, S. (2003). Performance analysis of roundabouts as an alternative for intersection control in Japan. *Journal of the Eastern Asia Society for Transportation Studies*, 5, 871–883.
6. Mathew, S., Dhamaniya, A., Arkatkar, S. S., & Joshi, G. (2017). Roundabout capacity in heterogeneous traffic condition: Modification of HCM equation and calibration. *Transportation Research Procedia*, 27, 985–992.
7. Vasconcelos, A. L. P., Seco, Á. J. M., & Silva, A. M. C. B. (2013). Comparison of procedures to estimate critical headways at roundabouts. *Promet-Traffic and Transportation*, 25(1), 43–53.
8. Indian Highway Capacity Manual (Indo-HCM). (2017). CSIR-Central Road Research Institute, New Delhi.

# Estimation of Arrival Time of Shear Waves in Fine-Grained Soils Using Bender Element Test



Kannekanti Prithvi Chandra and Kadali Srinivas

**Abstract** Application of piezoceramic elements for the evaluation of properties of geomaterials is a novel technique that uses wave propagation theory of shear and compression waves. Based on the travel time of shear wave, small-strain stiffness and other elastic properties can be determined which are helpful in predicting the displacements around the structures when subjected to dynamic loading such as earthquake and machine induced vibrations. To study this wave propagation, bender elements can be used to characterise the soil and rock samples along with the conventional triaxial set-up under static and dynamic conditions depending upon the frequency of excitation. Understanding the wave behaviour would be quite useful in predicting the engineering properties of soils, and keeping this in mind, an effort has been made to determine the response of wave. In the present study, fine-grained soils are subjected to different intensities of frequencies and the intensity of wave propagation is analysed with respect to the density of the sample and its travel time duration using bender elements. From the obtained results, variations in travel time were observed with compaction effort. It is believed that such a study would be quite helpful in predicting the velocity of the shear wave for estimating the small-strain stiffness.

**Keywords** Bender elements · Density · Piezoelectric effect · Shear wave velocity · Small-strain stiffness

## Nomenclature

BE Bender element  
 $G$  Specific gravity

---

K. P. Chandra · K. Srinivas (✉)  
VNR Vignana Jyothi Institute of Engineering and Technology, Hyderabad 500090, India  
e-mail: [srinivasciv@gmail.com](mailto:srinivasciv@gmail.com)

K. P. Chandra  
e-mail: [kannekantiprithvichandra@gmail.com](mailto:kannekantiprithvichandra@gmail.com)

© Springer Nature Singapore Pte Ltd. 2020  
S. Saride et al. (eds.), *Advances in Geotechnical and Transportation Engineering*,  
Lecture Notes in Civil Engineering 71,  
[https://doi.org/10.1007/978-981-15-3662-5\\_18](https://doi.org/10.1007/978-981-15-3662-5_18)

$G_{\max}$	Maximum shear modulus
ISC	Indian soil classification
$L_{tt}$	Tip-to-tip distance between the bender elements
LL	Liquid limit
ms	Milliseconds
mv	Millivolts
MDD	Maximum dry density
OMC	Optimum moisture content
PL	Plastic limit
PI	Plasticity index
SI	Swelling index
SSA	Specific surface area
$t$	Travel time of the wave (seconds)
$v_s$	Shear wave velocity
$\rho$	Density of soil

## 1 Introduction

Soil is an elasto-plastic material which behaves differently at various strain levels, but at lower strain levels, it behaves as an elastic material [1]. Practically, the soil at foundation level may experience lower strain levels which could be helpful in determining the soil structure interaction behaviour of soil [2, 3]. The deformation characteristics of soil when subjected to dynamic loading are regulated by the dynamic properties of the soil, such as the small-strain stiffness  $G_{\max}$ , which is a typical parameter giving the important information required for dealing various geotechnical problems, such as the foundation vibrations, seismic response of structures subjected to earthquake and ground improvement control. [2–6]. Bender elements are thin cantilever beams mostly made up of lead zirconate titanate (PZT), which function as electromechanical transducers and are capable of transmitting and receiving the signals. BEs work on the principle of piezoelectric effect, i.e. the element experiences a change in physical dimension either by extension or bending when an electric voltage is applied and reverse phenomena is observed when it experiences mechanical stress [7]. With this advantage, it is used in the geotechnical laboratory to generate shear (S) waves and compression (P) waves and is used for characterisation of the soil and rock samples, and the wave velocities can be obtained by estimating the travel time  $t$  and distance travelled by the wave; basically, the travel distance of the wave is assumed to be the tip-to-tip distance between the elements  $L_{tt}$  [2, 8–14]. By using bender elements, the small-strain stiffness can be obtained in terms of shear wave velocity which is calculated as the product of the density of soil sample and square of shear wave velocity, and the shear wave velocity can be obtained by distance travelled  $L_{tt}$  by the shear wave to the travel time  $t$ . The shear wave velocity depends on the response of the waveform, i.e. shape of the waveform gives an assessment of stiffness property

of soil which depends on the frequency under which sample is tested, and for this reason, a suitable frequency range has to be selected for the experiment, which can be decided by  $R_d$ , the ratio of the shear wave travel length to the wavelength, to eliminate the near field effect [13, 15–20].

This paper presents the results obtained from BE tests conducted on the black cotton and bentonite soil samples under unconfined test conditions at different densities and at five different frequencies, and the time lag between the input and output waves was considered and used for estimating the travel time of the shear wave. Due to the increase in the frequency, the shifting of peak values was noticed and this is due to the faster arrival of the shear waves at higher frequencies.

## **2 Experimental Investigations**

The soils used in the present study are Bentonite, designated as BT respectively, which was available commercially and naturally occurring soil, from Sanga Reddy of Telangana state, India, designated as BC, were selected for this study. These two soils were dried and used for the experimental study.

### **2.1 Specific Gravity**

The specific gravity,  $G$ , of the soil sample was determined with the help of density bottle and pycnometer as per [21] Results are presented in Table 1.

### **2.2 Specific Surface Area**

The specific surface area of different soils can be obtained using ethylene glycol monomethyl ether (EGME) method which has been most suitable for determining SSA [22–25].

### **2.3 Gradational and Consistency Characteristics**

The gradational and consistency characteristics such as liquid limit, plastic limit and plasticity index were determined as per [26, 27], and the results are represented in Table 1.

**Table 1** Properties of soils used for study

Soil	G	Fine content (<75 $\mu$ ) %	LL (%)	PL (%)	PI (%)	SI (%)	OMC (%)	MDD (g/cc)	ISC	SSA (m <sup>2</sup> /g)	pH
BC	2.8	93	68	32	36	70	26.6	1.558	CH	188	7.5
BT	2.7	100	226	50	176	429	38.5	1.270	CH	393	7.8

## **2.4 Swelling Index**

The swelling was determined with the help of graduated glass cylinder as per [28], and the obtained result of the experiment is shown in Table 1.

## **2.5 pH**

The pH value was determined as per [29], and the results are presented in Table 1.

## **2.6 Water Content and Dry Density Relation**

The water content and dry density relation using light compaction was determined as per [30], and the results obtained were presented in Table 1.

## **2.7 Sample Preparation**

Soil samples are prepared in a mould of 50 mm diameter and 170 mm height with the help of compacting tools, a sample of 50 mm diameter and 100 mm height is extracted from the mould and then the sample is mounted on to BE test set-up. In this study, the bender elements were fixed to the bottom pedestal and top cap was used to measure the shear wave velocity. The BEs were connected to the external source through which power to transducer is supplied. Signal amplification and conditioning of source wave are done and the signal conversions are done by the high-speed data acquisition system (16-bit resolution and 200 kHz sampling rate). The BEs were manufactured by GDS Instruments Ltd, which were about 11 mm wide, 1 mm thick and extended about 2 mm into the soil sample, and then the sample was made to stand in between the triaxial base pedestal element (P-wave transmitter/S-wave receiver) and top cap element (S-wave transmitter/P-wave receiver) comprising cylindrical titanium insert with flying leads connected to signal conditioning and data interface unit (supplied by GDS Instruments, UK) [31].

Then the samples were tested at frequencies in the range of about 1–5 kHz at different densities. The waveforms were obtained from the software named GDS bender element software (GDSBES) which was used for signal generation provided by the GDS Instruments, UK. After obtaining the results, the travel time was calculated using the software provided by GDS Instruments named GDS Bender Element Analysis Tool (GDSBEAT) which can be downloaded from the GDS website.



### 3 Methodology

Preparation of soil sample of 50 mm diameter and 100 mm height at different densities obtain the results from the experiments and analyse the data obtained from experiments. For sample preparation, a mould as shown in Fig. 1 was used. A sample of dimensions of 50 mm  $\times$  100 mm was then prepared, and the sample was tested. The sample preparation conditions play a crucial role based on which the response of the soil matters, i.e. environmental factors and compositional factors [32]. The BC and BT soil samples were prepared at a water content of 26.6% and 38.5%. Peak-to-peak approach which is the simplest and fastest method considers the time lag between the peaks of both input and output signals to estimate the travel time is adopted. The bender elements used in the present study are shown in Figs. 3 and 4, and the brass plates are arranged so that it holds the sample in good condition while performing the test (Fig. 2).

#### 3.1 Testing of the Soil Sample

After preparing the soil sample, it was mounted on to the bender elements test set-up manufactured by GDS Instruments Ltd. The BEs were inserted in the soil sample, with the help of grooving tool on top and bottom faces of the soil as shown in Fig. 2, and then bender elements were installed and signal was triggered at transmitter end and recorded at receiver end. Based on the type of wave generated, the behaviour of transmitter and receiver was interchanged. The soil specimens were arranged as shown in Figs. 5 and 6.

**Fig. 1** Mould used for preparing soil sample

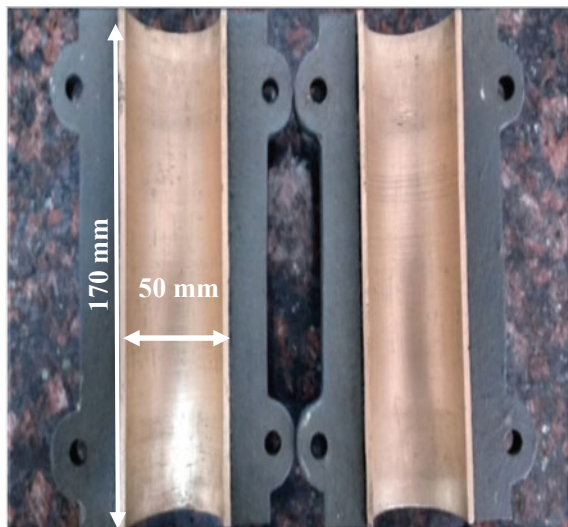
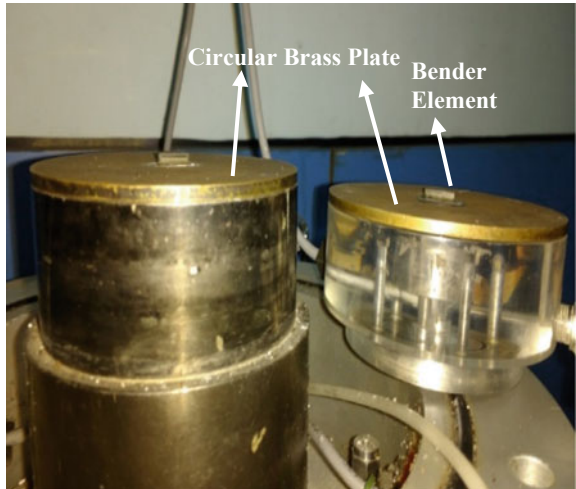


**Fig. 2** Tools used for making groove in the soil



**Fig. 3** Bender elements used for study



## 4 Results and Discussion

As stated above, the two soils were subjected to different frequencies and results obtained from various tests are presented and discussed in the following section.

Care should be taken while preparing the sample and during testing conditions, so that sample disturbances can be avoided. The waveforms of higher frequency were sharp in nature when compared to waveforms at a lower frequency. The waveforms obtained are of similar pattern when compared to each other just indicate a shift in the peak value intensity as shown in Figs. 7 and 8 for the soils used for the study.

**Fig. 4** Bender elements used for study

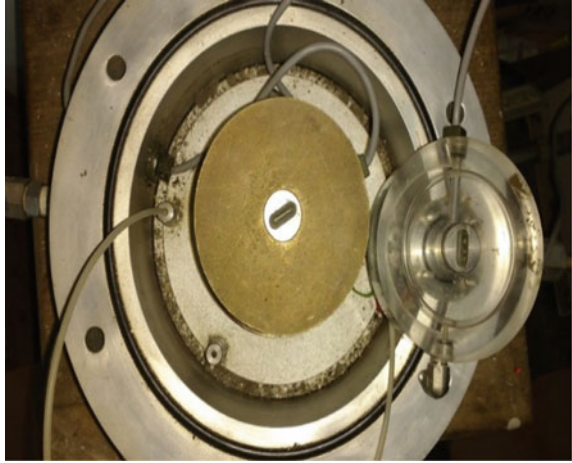
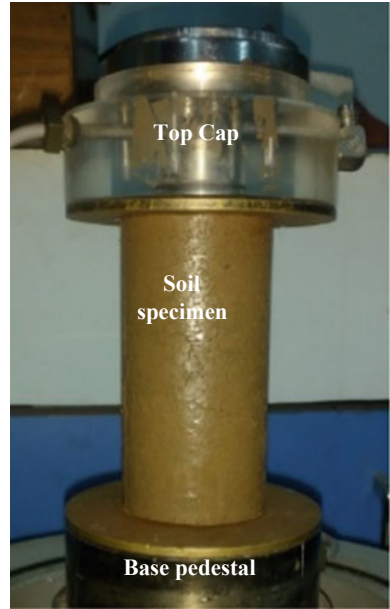
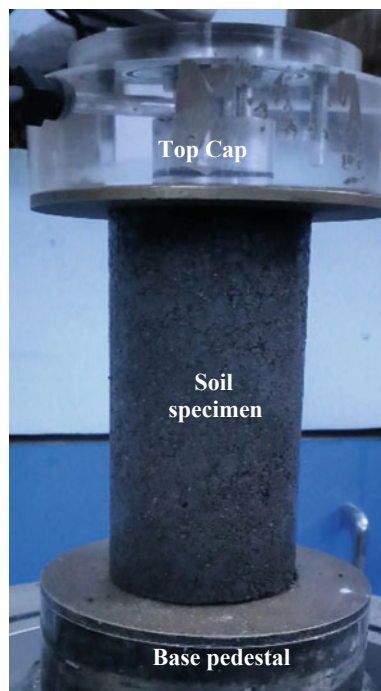


**Fig. 5** BT soil specimen mounted for testing



From Figs. 7 and 8 we can notice that travel time of the waveform is getting reduced as the first peak for different frequencies is narrowing down as the frequency is increasing the shift in the peak values for the same sample under different frequencies showed a decreasing trend, with a reduction of about 22% when frequency is increased from 1 to 2 kHz and at higher frequencies i.e. 3–5 kHz the amount of reduction in time was lower which is about 2–3%, this is due to the excitation of the bender element which varies with the applied input frequency and corresponding

**Fig. 6** BC soil specimen mounted for testing



input voltage, the travel time values for BC and BT soils at different frequencies are represented in Table 2, which indicates that the wave is travelling faster (Tables 3 and 4).

Significantly, the dynamic behaviour of the soil specimen depends upon the compositional characteristics and testing conditions [32]. From Figs. 9 and 10, we can infer that the soil at higher density has a shorter duration of time travel when compared to the soils at other densities at different frequencies. For BT soil in Fig. 9, the reduction in time duration was about 60% at lower frequencies and the variation was lower at higher frequencies which is about 3–5%. For BC soil in Fig. 10 the reduction in time was about 20% at lower frequencies (1–2 kHz) and at higher frequencies (3–5 kHz) the variation was about 5%, which is due to the rapid excitation of the element due to applied input voltage and compaction state of the soil specimen. From Figs. 11, 12, 13, 14 and 15 we can notice that the output wave patterns for BC soil are similar just a different peak is observed for the waveforms. The results are presented in Tables 5 and 6, but for the BT soil a regular trend in shift of peak is observed with respect to peak intensity value at lower frequency (1 kHz) which can be seen from Figs. 16, 17, 18, 19 and 20.

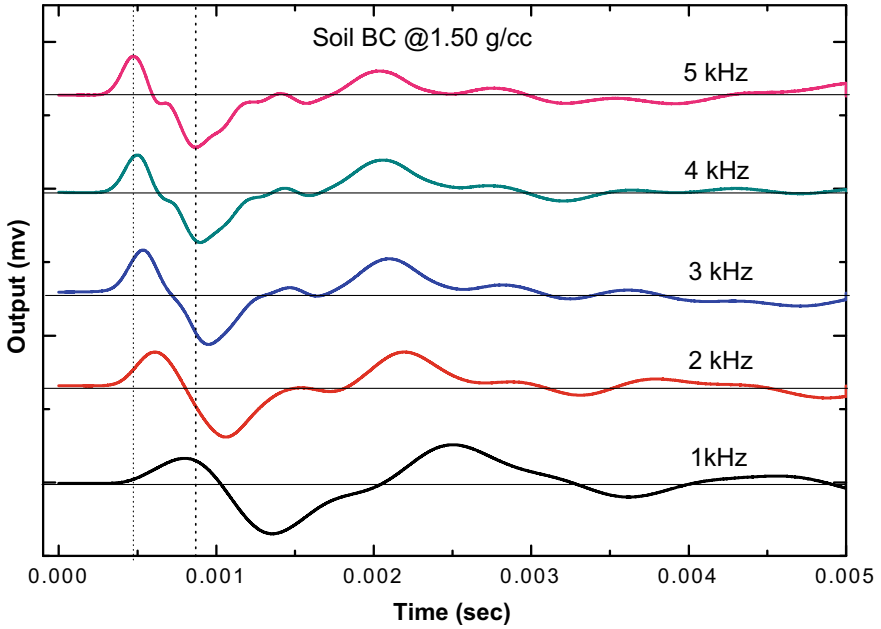


**Fig. 7** Output of BC soil specimen of density 1.50 g/cc tested at different frequencies (1, 2, 3, 4, 5 kHz)

## 5 Conclusions

Based on the analysis of the results, following can be concluded:

- The density of soil plays a key role in the travel time of the shear waves.
- The response of soil samples is not unique for all the frequencies; it is subjected as the frequency changes and its behaviour can be noticed in terms of change in time peak value in the output waveforms which makes an important point to be considered when soil is subjected to loading of higher frequencies.
- The value of small strain of soil depends on the time travel of the wave which can be used in the design of foundations of structures subjected to dynamic loading.

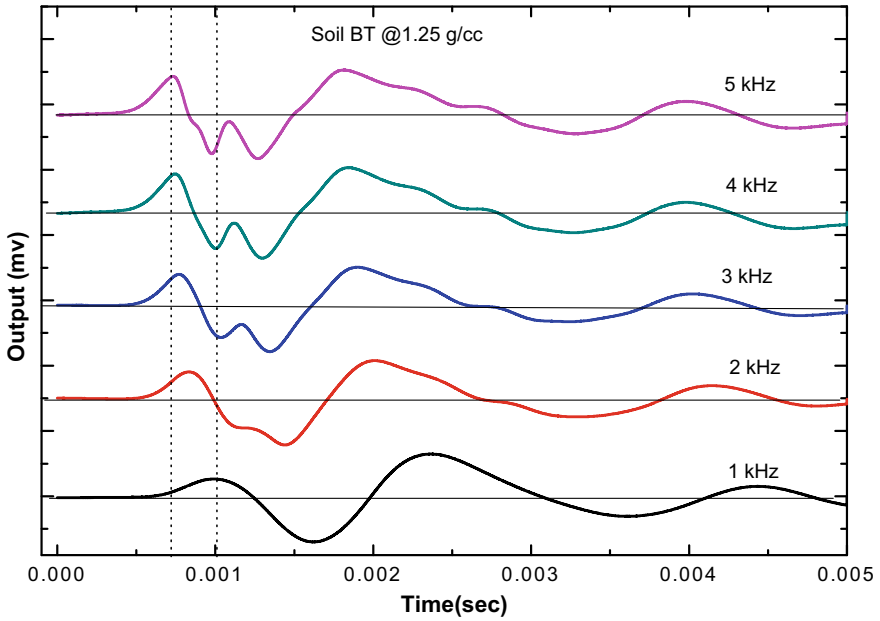


**Fig. 8** Output of BT soil specimen of density 1.25 g/cc tested at different frequencies (1, 2, 3, 4, 5 kHz)

**Table 2** Showing the peak values of waveforms for soil BC and BT soil (refer Figs. 7 and 8)

Frequency (kHz)	Travel time (milliseconds)	
	Soil BC	Soil BT
1	0.805	1.00
2	0.626	0.834
3	0.535	0.763
4	0.489	0.750
5	0.478	0.731

**Table 3** Showing travel time values for BT soil (refer Fig. 9)

Frequency (kHz)	Travel time at different densities (milliseconds)			
	1.20 (g/cc)	1.25 (g/cc)	1.30 (g/cc)	1.35 (g/cc)
1	2.487	2.367	2.302	2.194
2	2.191	2.012	0.807	0.771
3	2.164	1.899	0.736	0.697
4	2.080	1.847	0.702	0.666
5	2.047	1.819	0.688	0.644

**Table 4** Showing travel time values for BC soil (refer Fig. 10)

Frequency (kHz)	Travel time at different densities (milliseconds)			
	1.50 (g/cc)	1.55 (g/cc)	1.60 (g/cc)	1.65 (g/cc)
1	2.506	2.316	2.146	2.290
2	2.196	2.022	1.857	2.082
3	0.536	0.604	0.631	0.550
4	0.498	0.568	0.618	0.516
5	0.470	0.544	0.585	0.492

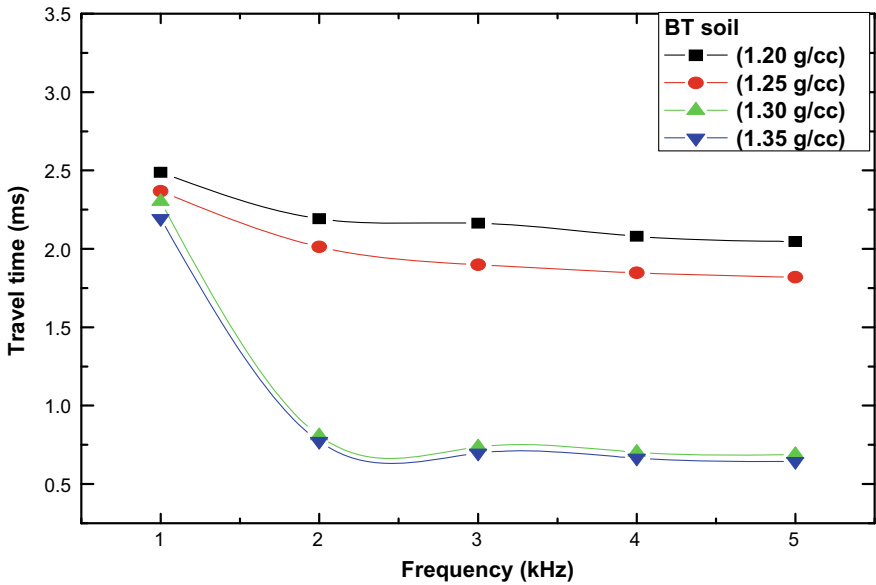


**Fig. 9** Variation of travel time of BT soil at different densities tested over a frequency range of 1–5 kHz

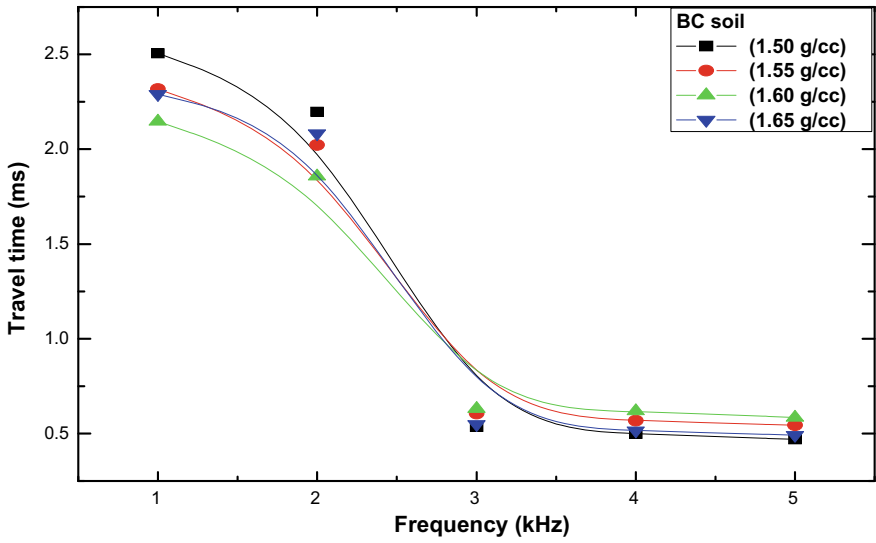


Fig. 10 Variation of travel time of BC soil at different densities tested over a frequency range of 1–5 kHz

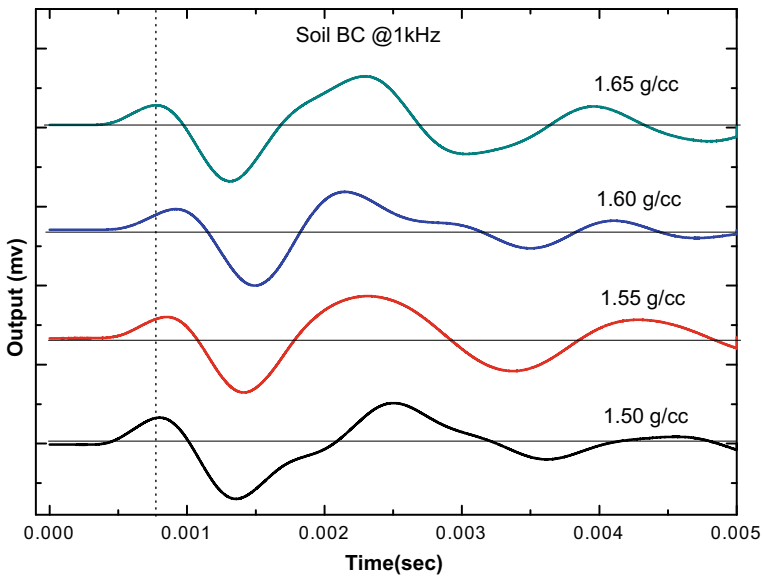


Fig. 11 Wave patterns of BC soil at different densities tested at 1 kHz frequency



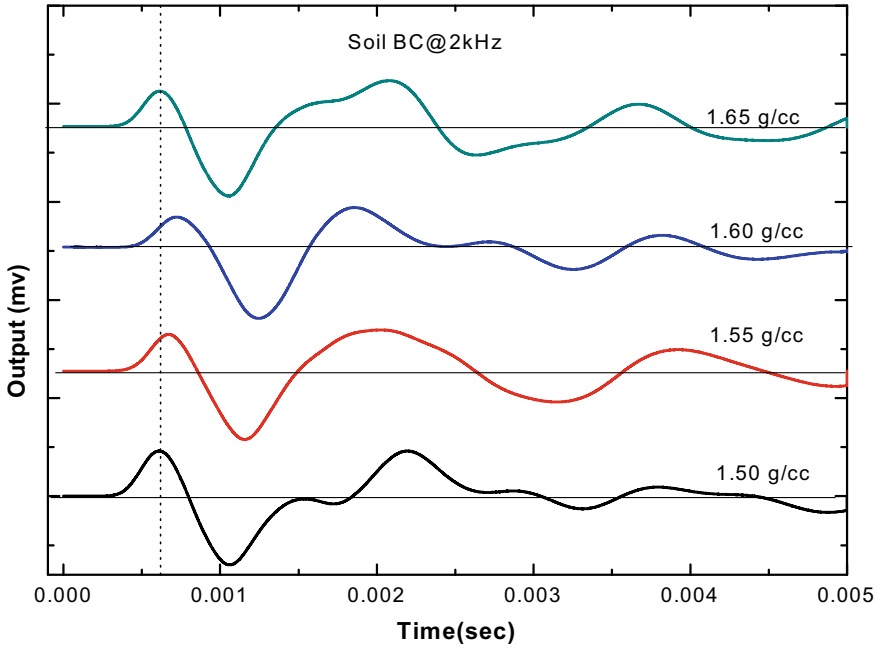


Fig. 12 Wave patterns of BC soil at different densities tested at 2 kHz frequency

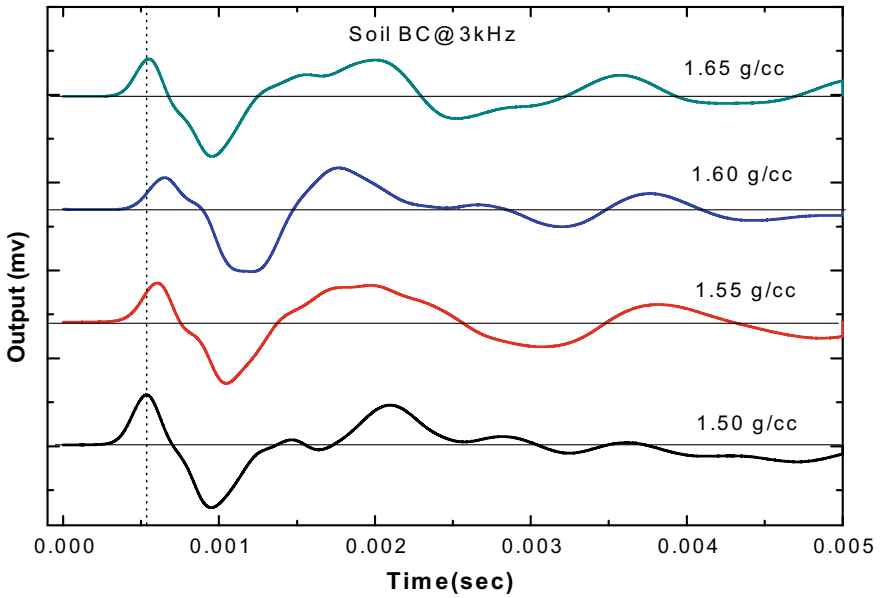


Fig. 13 Wave patterns of BC soil at different densities tested at 3 kHz frequency

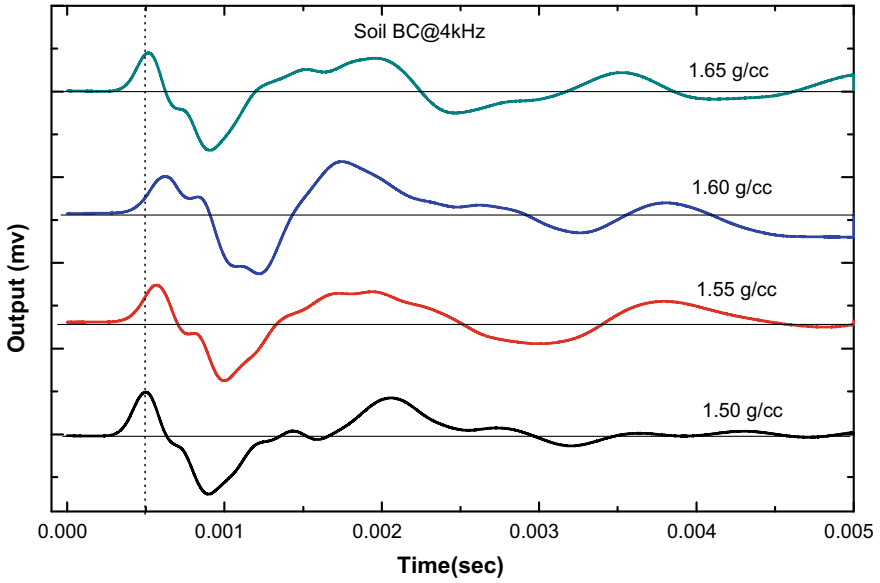


Fig. 14 Wave patterns of BC soil at different densities tested at 4 kHz frequency

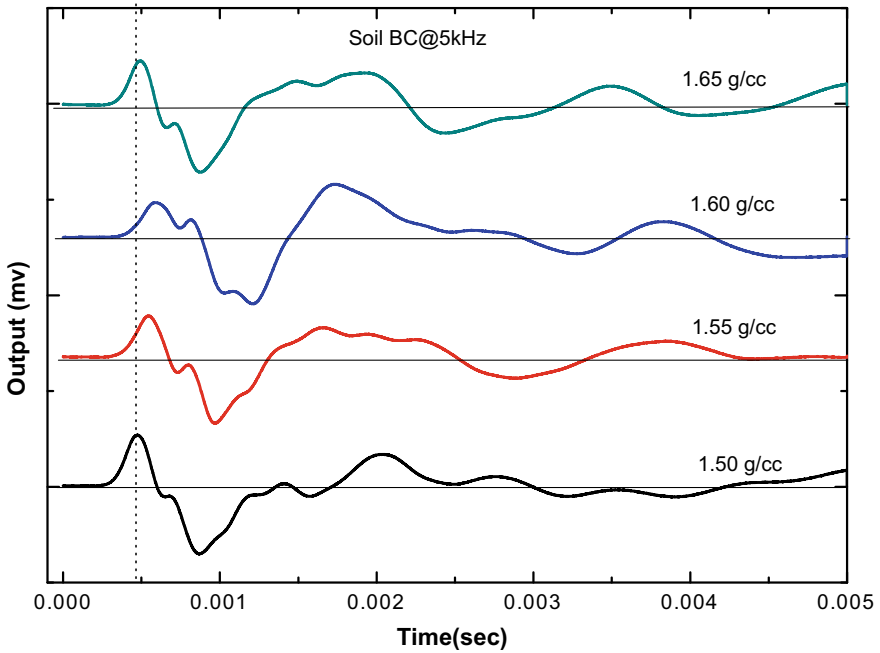


Fig. 15 Wave patterns of BC soil at different densities tested at 5 kHz frequency

**Table 5** Travel time values for BC soil at different densities and frequencies (refer Figs. 11, 12, 13, 14 and 15)

Density (g/cc)	Travel time in (milliseconds) at different frequencies				
	1 kHz	2 kHz	3 kHz	4 kHz	5 kHz
1.50	0.804	0.618	0.535	0.494	0.472
1.55	0.845	0.679	0.598	0.566	0.546
1.60	0.926	0.742	0.648	0.609	0.587
1.65	0.778	0.618	0.546	0.516	0.495

**Table 6** Travel time values for BT soil at different densities and frequencies (refer Figs. 16, 17, 18, 19 and 20)

Density (g/cc)	Travel time in (milliseconds) at different frequencies				
	1 kHz	2 kHz	3 kHz	4 kHz	5 kHz
1.20	1.102	0.926	0.862	0.824	0.813
1.25	0.988	0.845	0.772	0.747	0.728
1.30	0.985	0.815	0.731	0.699	0.679
1.35	0.978	0.762	0.700	0.659	0.642

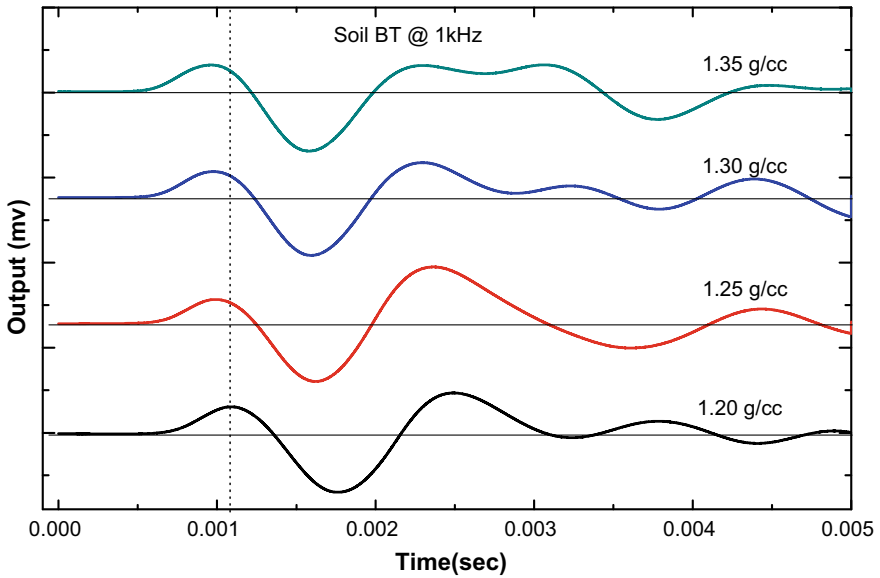


**Fig. 16** Wave patterns of BT soil at different densities tested at 1 kHz frequency

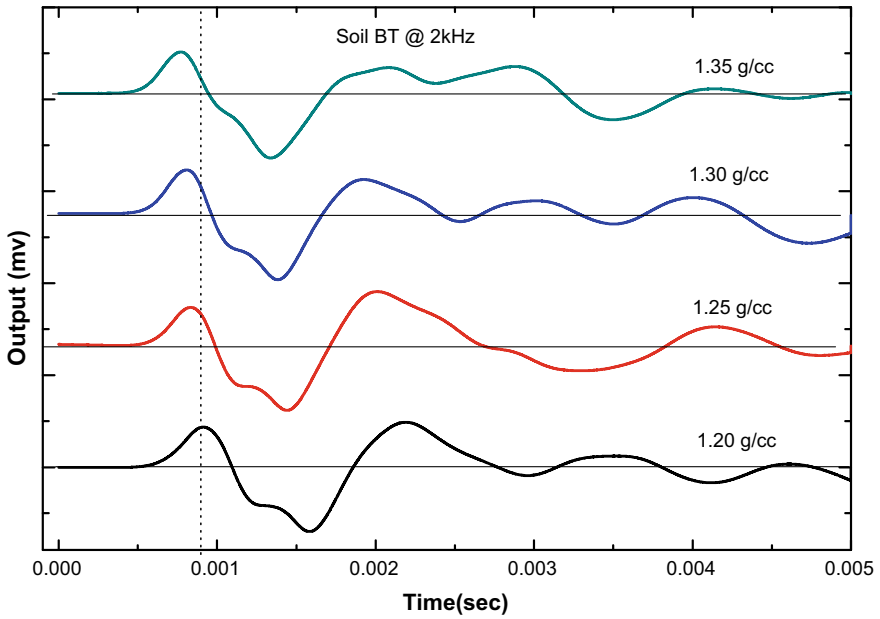


Fig. 17 Wave patterns of BT soil at different densities tested at 2 kHz frequency

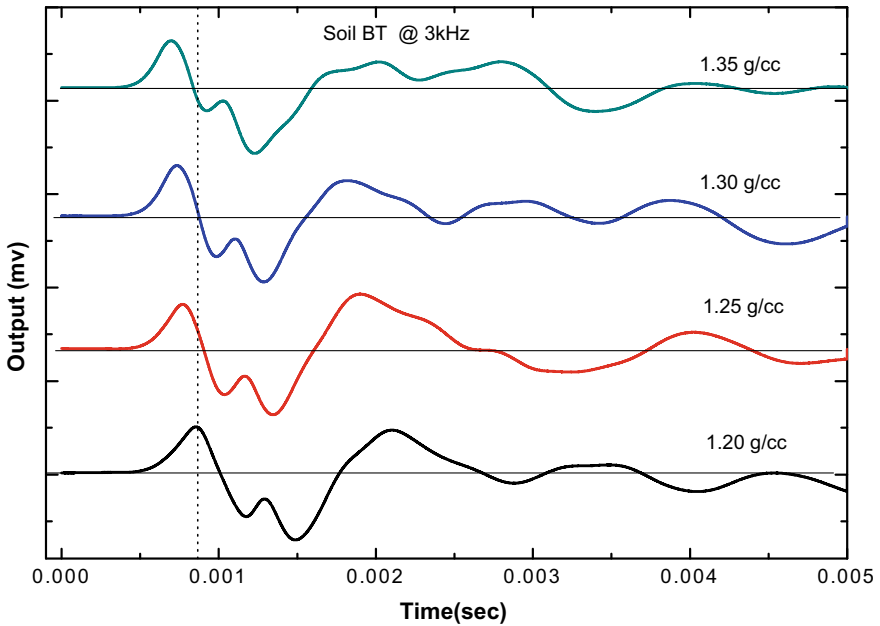


Fig. 18 Wave patterns of BT soil at different densities tested at 3 kHz frequency

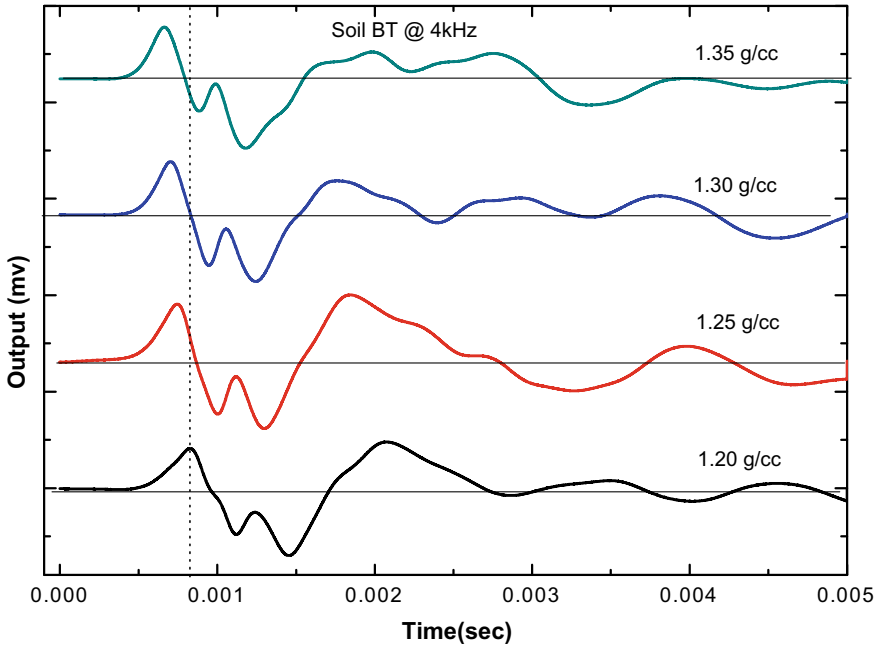


Fig. 19 Wave patterns of BT soil at different densities tested at 4 kHz frequency

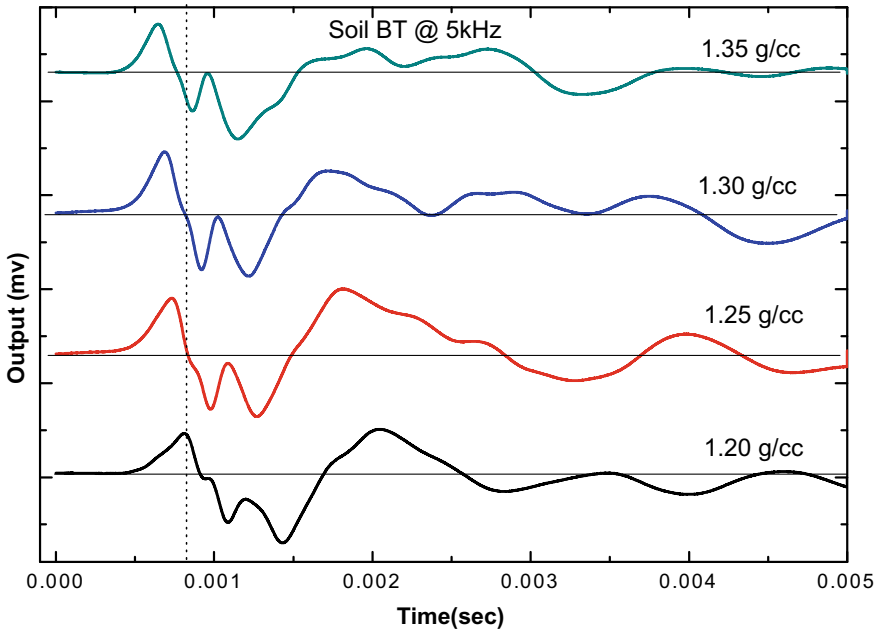


Fig. 20 Wave patterns of BT soil at different densities tested at 5 kHz frequency

**Acknowledgements** The Authors would like to take an opportunity to thank Dr. Anjan Patel for providing the facilities to carry out the presented research work at Geotechnical Engineering Laboratory at VNIT Nagpur.

## References

1. Taesik, K., David, G. Z. M., & Carlos, A. V. P. (2015). Analysis of bender element signals during triaxial testing. *Revista Facultad de Ingenieria*, 76, 107–113.
2. Bartake, P. P., Patel, A., & Singh, D. N. (2008). Instrumentation for bender element testing of soils. *International Journal of Geotechnical Engineering*, 4, 395–405.
3. Simpson, B. (1992). Thirty second rankine lecture: Retaining structures: Displacement and design. *Geotechnique*, 42(4), 539–577.
4. Andrus, R. D., & Stokoe, K. H., II. (2000). Liquefaction resistance of soils from shear-wave velocity. *Journal of Geotechnical and Geoenvironmental Engineering*, 126(11), 1015–1025.
5. Lee, J. S., & Santamarina, J. C. (2005). Bender elements: Performance and signal interpretation. *Journal of Geotechnical and Geoenvironmental Engineering*, ASCE, 131(9), 1063–1070.
6. Ku, T., Mayne, P. W., & Cargill, E. (2013). Continuous-interval shear wave velocity profiling by auto-source and seismic piezocone tests. *Canadian Geotechnical Journal*, 50(4), 382–390.
7. Viggiani, G., & Atkinson, J. H. (1995). Interpretation of bender element tests. *Geotechnique*, 45(1), 149–154.
8. Viggiani, G., & Atkinson, J. H. (1995). Stiffness of fine-grained soil at very small strains. *Geotechnique*, 45(2), 249–266.
9. Shirley, D. J., & Hampton, L. D. (1978). Shear-wave measurements in laboratory sediments. *Journal of the Acoustical Society of America*, 63(2), 607–613.
10. Leong, E. C., Yeo, S. H., & Rahardjo, H. (2005). Measuring shear wave velocity using bender elements. *Geotechnical Testing Journal*, ASTM, 28(5), 488–498.
11. Lings, M. L., & Greenings, P. D. (2001). A novel Bender/Extender element for soil testing. *Geotechnique*, 51(8), 713–717.
12. Arroyo, M., Pineda, J. A., & Romero, E. (2010). Shear wave measurements using bender elements in argillaceous rocks. *Geotechnical Testing Journal*, ASTM, 33(6), 1–12.
13. Patel, A., Singh, D. N., & Singh, K. K. (2010). Performance analysis of piezo-ceramic elements in soils. *Geotechnical and Geological Engineering*, 28, 681–694.
14. Prashant, S. S., & Singh, D. N. (2015). Implementation of a system for measuring velocity of primary and secondary waves in rocks and soils. In *Proceedings of the IEEE SoutheastCon, April 9–12*, Fort Lauderdale, Florida.
15. Sanches-Salinerio, I., Roesset, J. M., & Stokoe, K. H. (1986). *Analytical studies of body wave propagation and attenuation*. Report GR 86-15, University of Texas, Austin.
16. Brignoli, E. G. M., Gotti, M., & Stokoe, K. H. (1996). Measurement of shear waves in laboratory specimens by means of piezoelectric transducers. *Geotechnical Testing Journal*, ASTM, 19(4), 384–397.
17. Jovicic, V., Coop, M. R., & Simic, M. (1996). Objective criteria for determining  $G_{max}$  from bender element tests. *Geotechnique*, 46(2), 357–362.
18. Arulnathan, R., Boulanger, R. W., & Riemer, M. F. (1998). Analysis of bender element tests. *Geotechnical Testing Journal*, ASTM, 21(2), 120–131.
19. Patel, A., Singh, D. N., & Singh, K. K. (2011). Application of piezoceramic elements for determining elastic properties of soils. *Geotechnical and Geological Engineering*, 30, 407–417.
20. Ingale, R., Patel, A., & Mandal, A. (2017). Performance analysis of piezoceramic elements: A review. *Sensors and Actuators*, A, 262, 47–63.
21. IS 2720 Part III Section I. (1980). *Methods of test for soils determination of specific gravity for fine grained soils*. Bureau of Indian Standards, New Delhi, India.

22. Arnepalli, D. N., Shanthakumar, S., Rao, B. H., & Singh, D. N. (2008). Comparison of methods for determining specific-surface area of fine-grained soils. *Geotechnical and Geological Engineering*, 26, 121–132.
23. Carter, D. L., Mortland, M. M., & Kemper, W. D. (1986). *Specific surface-methods of soil analysis* (pp. 412–423). USA: American Society of Agronomy.
24. Cerato, A. B., & Lutenegeger, A. J. (2002). Determination of surface area of fine-grained soils by the ethylene glycol mono-ethyl ether (EGME) method. *Geotechnical Testing Journal, ASTM*, 25(3), 1–7.
25. Srinivas, K., Susha Lekshmi, S. U., Susmita, S., & Singh, D. N. (2013). Investigations to establish the influence of the thermal energy field on soil properties. *Acta Geotechnica Slovenica*, 2, 59–77.
26. IS 2720 Part IV. (1985). *Methods of test for soils grain size analysis bureau of indian standards*, New Delhi, India.
27. IS 2720 Part V. (1985). *Methods of test for soils determination of liquid limit and plastic limit*. Bureau of Indian Standards, New Delhi, India.
28. IS 2720 Part XL. (1978). *Methods of test for soils determination of free swell index of soils*. Bureau of Indian Standards, New Delhi, India.
29. IS 2720 Part XXIV. (1976). *Methods of test for soils determination of cation exchange capacity*. Bureau of Indian Standards, New Delhi, India.
30. IS 2720 Part XXVI. (1987). *Methods of test for soils determination of ph value*. Bureau of Indian Standards, New Delhi, India.
31. Patel, A., Ingale, R., & Kamlesh, B. B. (2017). Effect of compaction states and the confining pressure on Poisson's ratio of stratified and non-stratified soils. *Arabian Journal of Science and Engineering*, 43, 1983–1999.
32. Gokhan, I., Nazli, Y., & Takaaki, K. (2003). Experimental investigation of dynamic response of compacted clayey soils. *Geotechnical Testing Journal, ASTM*, 26(2), 1–17.

# Numerical Modelling of Lateral Deformation of the Cantilever Retaining Wall in Expansive Clays



Santosh Sharma, N. Vinod Prabhu, Y. Naveen and S. Bhuvaneshwari

**Abstract** Retaining walls are relatively rigid walls used for supporting the soil mass laterally. The soil properties of the retained material exert lateral pressure on the wall. Thus, the important consideration in the design of retaining wall is to counter the lateral pressure generated by the backfill. The present study focuses on theoretical study on the retaining wall parameters such as the heel width, stem height, inclined backfill, with cohesive and expansive soil backfill. The lateral earth pressure is evaluated in each of these cases using the Rankine's lateral earth pressure theory. The numerical modelling of the cantilever retaining wall in cohesive backfill (expansive in nature) is carried out using the finite element software (PLAXIS 2D). Two soil models, Mohr–Coulomb model and the Hardening Soil model, are used for modelling the backfill. The expansive nature of the backfill is incorporated in terms of the positive volumetric strain of the backfill. To cater to the large lateral pressure induced by the expansive backfill, geofoam layer is introduced in between the backfill layer and the retaining wall and modelled using Mohr–Coulomb model. A comparative evaluation is made for the behaviour of the retaining wall in terms of the lateral deformation. The expansive soil with 12% volumetric strain caused nearly 900 mm lateral deformation, compared to 600 mm on inclusion of the 2 m thick geofoam layers. The hardening soil model used for modelling of the expansive soil depicts an reduction in deformation compared to the elasto-plastic, Mohr–Coulomb model.

---

S. Sharma · N. V. Prabhu · Y. Naveen · S. Bhuvaneshwari (✉)  
Department of Civil Engineering, SRM Institute of Science and Technology, Kattankulathur,  
Chennai 603203, India  
e-mail: [bhuvaneshwari.su@ktr.srmuniv.ac.in](mailto:bhuvaneshwari.su@ktr.srmuniv.ac.in)

S. Sharma  
e-mail: [santosh\\_lakhi@srmuniv.edu.in](mailto:santosh_lakhi@srmuniv.edu.in)

N. V. Prabhu  
e-mail: [nandhigam\\_nandhigam@srmuniv.edu.in](mailto:nandhigam_nandhigam@srmuniv.edu.in)

Y. Naveen  
e-mail: [umanagavenkat\\_y@srmuniv.edu.in](mailto:umanagavenkat_y@srmuniv.edu.in)

© Springer Nature Singapore Pte Ltd. 2020  
S. Saride et al. (eds.), *Advances in Geotechnical and Transportation Engineering*,  
Lecture Notes in Civil Engineering 71,  
[https://doi.org/10.1007/978-981-15-3662-5\\_19](https://doi.org/10.1007/978-981-15-3662-5_19)



**Keywords** Expansive soil · Retaining wall · Mohr–Coulomb model · Hardening soil model · Geofam

## 1 Introduction

Retaining walls are structures specifically constructed for retaining large amount of soil, intended for bridge abutments, embankments, elevated roadways, etc. They are designed to withstand high lateral earth pressures due to vertical backfills [1]. The properties of the retained material, angle of internal friction ( $\phi$ ) and the cohesive strength ( $c$ ) create lateral pressure on the wall. Thus, the important consideration in the design of retaining wall is to counter the lateral earth pressure generated by the backfill [1]. Active lateral earth pressure is generated due to the movement of the soil towards the wall. Additional groundwater variation also causes a huge lateral earth pressure. If these factors are taken into account, there is a great possibility of overturning of the wall. The total thrust acts at one-third of the retaining wall from the lowest depth due to the triangular pressure variation. The lateral earth pressure on a retaining wall is determined using the Rankine's method or the Coulomb's method. The pressures acting on the wall cause movement of the wall due to the three differential pressures acting, at rest condition, active state and the passive state [2, 3].

In many of the practical situations, it becomes necessary to use the in situ soil present in the site for backfilling of the retaining wall. In many of the occasions, the in situ soil is cohesive in nature and could lead to excessive settlement or heaving of the backfill. Further, when the clay soil is expansive in nature, they induce additional pressure on the retaining wall. Expansive soils are typically clay soil that has a tendency to expand when it comes in contact with water and further shrinks when dries out. This volume change behaviour can cause adverse effects on the residential building, retaining walls and roads and pavements [4]. During expansion, these soils exert large uplift force against the concrete slabs and foundation footings which in turn causes a wide range of damage to buildings and surrounding areas. The costs associated with expansive soil damage, total to several billion rupees annually, more than all other natural calamities combined [4]. The damage of structures on expansive soil has been studied in various parts of the world specifically in Australia and United Nation (U.S) by various searches. Some of the problems have been studied by [4–6]. Retaining walls, buried structure like buried conduits, foundation piles are some of the structures subjected to large uplift pressures [4] and lateral swelling pressures. Hence, structures like retaining walls are subjected to additional lateral earth pressures if the backfill is expansive in nature causing further wall deformation and bending. The replacement of the expansive soil by non-expansive layer cannot be a viable option as it consumes large amount of resources and is usually expensive.

Few studies have been carried out to study the behaviour of the retaining walls in expansive soil. Tan [3] studied the behaviour of retaining walls in expansive soils. Experimental studies were carried out to determine the swell pressure on the retaining

wall. Based on the laboratory tests, equations for the prediction of swell pressure due to expansive soils were developed. Limited studies have been carried out to understand the behaviour of retaining wall in expansive soil through numerical modelling in 2D as well as 3D. Goh [7] carried out theoretical and numerical studies to investigate the behaviour of concrete cantilever retaining walls. Al-Busoda et al. [8] carried out numerical studies on retaining wall resting on expansive soil. A 3-D model of the cantilever retaining wall was created in PLAXIS 3D with expansive foundation soil. The expansive soil was modelled as hardening soil model and the retaining wall as elastic plate elements. The additional lateral pressure due to the expansive soil was modelled as the positive volumetric strain. Helical piles were also introduced to counter the swelling behaviour of the soil.

The behaviour of the retaining wall depends on many geometric influencing parameters such as the wall friction, sloping backfills and fluctuating water table and also the backfill soil properties. The present study focuses on the evaluation of the critical influencing parameter of the retaining wall and the theoretical evaluation of the swell pressure on the retaining wall. Further, based on the literature review, numerical analysis is also carried out to understand the deformation behaviour of the retaining wall with expansive backfill. Finally, remedial solutions are recommended for the retaining wall to control the excessive lateral deformation.

## 2 Methodology

### 2.1 *Proportioning of Retaining Wall*

The cantilever retaining wall is designed based on proportions prescribed by Bowles [9]. The stem height is taken as 5.8 m, and the heel width is taken as 3 m. Figure 1 shows the details of the retaining wall proportions.

### 2.2 *Theoretical Analysis Using Rankine's Theory*

The theoretical analysis is carried out for the cantilever retaining wall based on the Rankine's theory. The various parameters considered for the analysis are given in Fig. 2. The lateral earth pressure is calculated for the various factors influencing the behaviour of the retaining wall with the cohesive backfill. The effect of inclined backfill and the water table on lateral earth pressure is evaluated. Finally, the effect of the swelling soil as backfill material, on the lateral earth pressure, is calculated based on the method suggested by Thomas [10]. The lateral earth pressure is compared in all these cases, and the most critical parameter is evaluated. The analysis is carried out for stem height of 5.8, 6.8, 7.8, 8.8 and 9.8 m and heel width of 3, 4, 5 and 6 m.

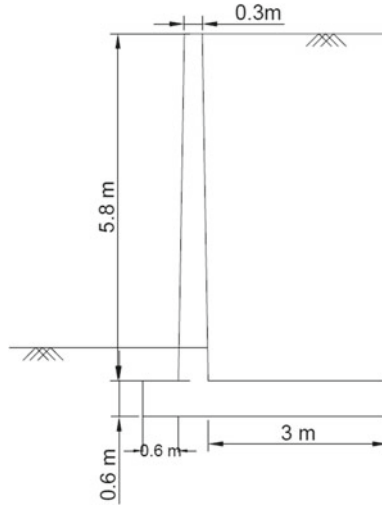


Fig. 1 Geometry of the cantilever retaining wall

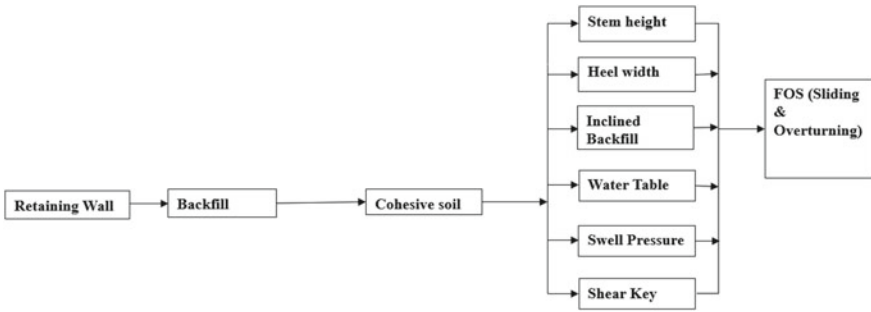


Fig. 2 Schematic of the theoretical analysis

### 2.3 Numerical Modelling Using PLAXIS 2D

The behaviour of the retaining wall with expansive backfill is studied through numerical modelling in PLAXIS 2D. The finite element software is adopted to understand the deformation of the retaining wall with cohesive backfill and also the effect due to the expansive backfill. PLAXIS 2D is a finite element software used for analysing practical geotechnical problems. The practical problems are modelled either as plane strain or axis symmetric depending on the geometry of the problem.

The behaviour of soil is highly nonlinear and time dependent, and advance models are required to predict the realistic behaviour. PLAXIS 2D provides many models for modelling of the real soil behaviour. For the present study, the backfill is modelled as

the Mohr–Coulomb model and hardening soil model, and the elasto-plastic Mohr–Coulomb model involves five input parameters such as the Young’s modulus ( $E$ ), Poisson’s ratio ( $\nu$ ), angle of internal friction ( $\phi$ ), undrained cohesion ( $C$ ) and angle of dilatancy ( $\psi$ ). Hardening soil model requires ten parameters.  $E_{50}^{ref}$ —triaxial compression,  $E_{ur}^{ref}$ —triaxial unloading and  $E_{oed}^{ref}$ —oedometer loading,  $P^{ref}$ —power,  $m_1$ —the stress-dependent stiffness formulation, Poisson’s ratio for unloading and unloading. In the present study, both Mohr–Coulomb model and hardening soil model are adopted.

### 2.3.1 Geometric Modelling of the Retaining Wall in PLAXIS 2D

In the present study, the cantilever retaining wall adopted for the theoretical analysis is modelled as a plane strain model. The discretised geometric model of the retaining wall is created and depicted as shown in Fig. 3. The retaining wall is modelled as elastic material with concrete properties. The backfill is modelled using both Mohr–Coulomb model and hardening soil model. The details of the parameters adopted are given in Tables 1 and 2. The properties are based on the analysis by Al-Busoda et al. [8]. Table 3 gives the details of the parametric study carried out using PLAXIS 2D. The expansive backfill is modelled using the volumetric strain. The volumetric strain percentage is based on the swell potential of the expansive soil. The volumetric strain is varied from 2 to 12% with 12% indicating highly expansive soil. In order to counter the effect of the lateral earth pressure due to expansive backfill, geofoam, a synthetic polystyrene material, is proceeded at the interface between the soil and retaining wall. Table 4 gives the properties of the geofoam material adopted for the parametric study. The values are based on the study by Mandal [11]. The remedial measures

**Fig. 3** Discretised geometric model in PLAXIS 2D

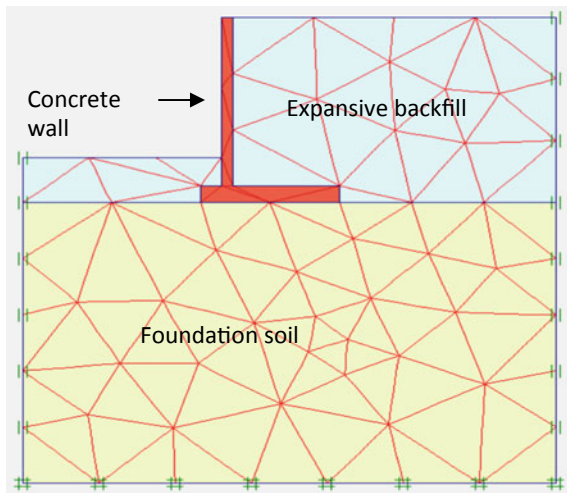


**Table 1** Input parameters of Mohr–Coulomb model (based on Al-Busoda et al. [8])

Model parameters	Expansive soil	Sandy soil	Concrete
$\gamma_{\text{unsat}}$ (kN/m <sup>3</sup> )	16	16	24
$\gamma_{\text{sat}}$ (kN/m <sup>3</sup> )	18	19	–
$E_{\text{ref}}$ (kPa)	20,000	180,000	30,000,000
$\nu$	0.3	0.25	0.3
$c_{\text{ref}}$ (kPa)	20	0.1	–
$\varphi$ (° deg)	24	37	–
$R_{\text{inter}}$	0.5	0.65	1.0

**Table 2** Input parameters of hardening soil model Al-Busoda et al. [8]

Model parameters	Expansive soil	Sandy soil	Concrete
$\gamma_{\text{unsat}}$ (kN/m <sup>3</sup> )	16	16	24
$\gamma_{\text{sat}}$ (kN/m <sup>3</sup> )	18	19	–
$E_{50}^{\text{ref}}$ (kPa)	5000	60,000	–
$E_{\text{oed}}^{\text{ref}}$ (kPa)	5000	60,000	–
$E_{\text{ur}}^{\text{ref}}$ (kPa)	30,000	180,000	30,000,000
Power (m)	1.0	–	1.0
$c_{\text{ref}}$ (kPa)	20	0.1	–
$\varphi$ (° deg)	24	37	–
$R_{\text{inter}}$	0.5	0.65	1.0
$V_{\text{ur}}$	0.5	0.2	–
$K_o$	0.4	0.6	–

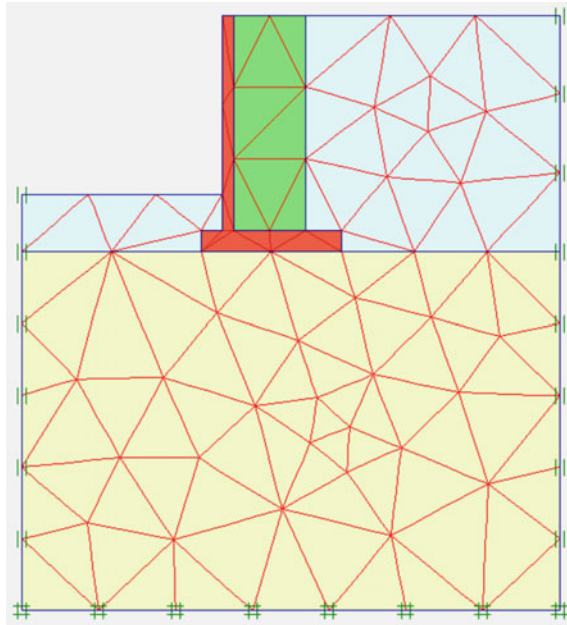
**Table 3** Details of the parametric study carried out

Sl. No	Parameter	Model used
1	Cantilever retaining wall	Mohr–Coulomb
2	Cantilever retaining wall	Hardening soil
3	Cantilever retaining wall + swelling backfill	Hardening soil
3 (i)	2% (volumetric strain)	Mohr–Coulomb, hardening Soil
3b (ii)	4%	Mohr–Coulomb, hardening soil
3 (iii)	6%	Mohr–Coulomb, hardening soil
3 (iv)	8%	Mohr–Coulomb, hardening soil
3 (v)	9%	Mohr–Coulomb, hardening soil
3 (vi)	12%	Mohr–Coulomb, hardening soil
4	Cantilever retaining wall + swelling backfill + geofoam	Mohr–Coulomb

**Table 4** Properties of geofoam Mandal [11]

Density ( $\rho$ ) ( $\text{kg/m}^3$ )	Cohesion $c$ (kPa)	Angle of internal friction $\varphi$ ( $^\circ$ deg)	Young's modulus $E$ (kPa)	Dry density $\gamma$ ( $\text{kN/m}^3$ )
15	33.75	1.5	2400	0.10
20	38.75	2	4000	0.12
22	41.88	2	5500	0.125
30	62.00	2.5	7800	0.17

**Fig. 4** Cantilever retaining wall with geofoam



using geofoam are also modelled using PLAXIS 2D. The discretised geometry of the retaining wall with geofoam is given in Fig. 4.

### 3 Results and Discussion

#### 3.1 Discussion on Theoretical Analysis

Theoretical calculations based on Rankine’s theory were adopted for the evaluation of the lateral earth pressure for the various influencing parameters under study (inclined backfill, water table, swell pressure and shear key). Shear key is provided as the

remedial method to counter the lateral earth pressure and can increase the FoS. These geometrical variations increase the lateral earth pressure and thereby reduce the FoS. Table 5 gives the FoS for the various influencing factors considered for a stem height of 5.8 m and different heel width. The results indicate that water table and swell pressure highly reduce the FoS compared to the inclined backfill for the same geometrical condition. The FoS reduction is comparatively high for the swelling soil factor compared to non-swelling backfill. For the non-swelling backfill, FoS against overturning is round 8.0, for the stem height of 5.8 and 3 m heel width, whereas for the swelling backfill for the same geometry, the values reduce to 0.83 (Figs. 5 and 6). Provision of shear key increases the stability of the retaining wall by providing passive resistance. The FoS against sliding is increased to 1.12 for the same geometrical condition on the presence of shear key (Table 5).

Figure 7 depicts the effects of different factors on the lateral earth pressures of the retaining wall. The contribution by swelling soil to the magnitude of lateral earth pressure is higher compared to the other factors.

### ***3.2 Results of Numerical Analysis***

Numerical modelling of the cantilever retaining wall is carried out using PLAXIS 2D. Figure 3 depicts the plane strain model of the cantilever retaining wall, adopted for the study. The cantilever retaining wall is modelled using concrete properties and modelled as elastic model. The backfill is modelled using both Mohr–Coulomb model and hardening soil model. The Mohr–Coulomb is the basic elasto-plastic model, and hardening soil model is the advanced soil model which precisely describes the soil behaviour. In this study, the expansive soil is modelled using hardening soil model. The input properties for the backfill are given based on the studies by Al-Busoda et al. [8]. In this study, a preliminary analysis is carried out by comparing the deformation behaviour of the retaining wall with the backfill modelled as Mohr–Coulomb and hardening soil model. Figures 8 and 9 depict the deformed mesh of retaining wall for both the Mohr–Coulomb model and hardening soil model. Mohr–Coulomb model causes a lateral deformation of 785 mm compared to the hardening soil model depicting 697 mm.

### ***3.3 Deformation Behaviour of Retaining Wall with Expansive Backfill***

The expansive backfill is modelled as the positive volumetric strain of the backfill. The numerical analysis is carried out for different percentages of strain (2–12%). The volumetric strain indicates the swell potential of the swelling backfill. The deformation obtained for different percentages of volumetric strain for Mohr–Coulomb model

**Table 5** Variation of the FoS for inclined backfill/water table/swell pressure/shear key

Parameters		Inclined backfill		Water table		Swell pressure		Shear key	
Stem height (m)	Heel width (m)	FoS sliding	FoS OT	FoS sliding	FoS OT	FoS sliding	FoS OT	FoS sliding	FoS OT
5.8	3	1.36	3.83	0.45	0.86	0.38	0.83	0.86	1.12
	4	1.63	5.56	0.57	1.33	0.48	1.29	1.00	1.74
	5	2.05	8.24	0.70	1.91	0.59	1.85	1.14	2.50
	6	2.41	11.07	0.82	2.60	0.70	2.51	1.29	3.38



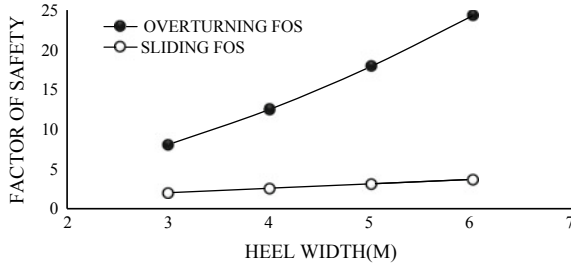


Fig. 5 Heel width versus FoS for 5.8 m stem height

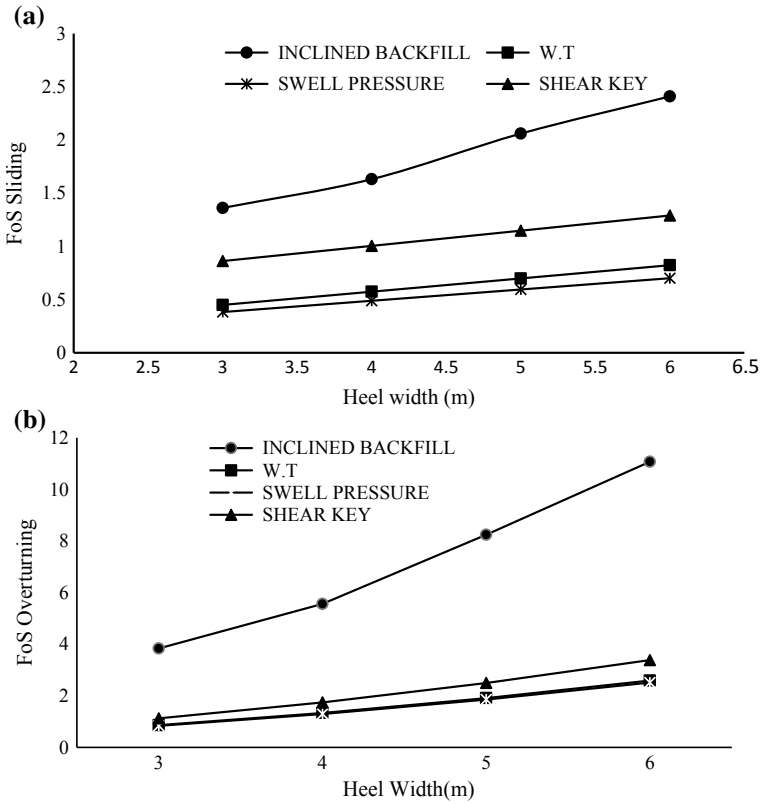


Fig. 6 a Variation of the FoS (sliding) for inclined backfill/water table/swell pressure/shear key. b Variation of the FoS (overturning) for inclined backfill/water table/swell pressure/shear key

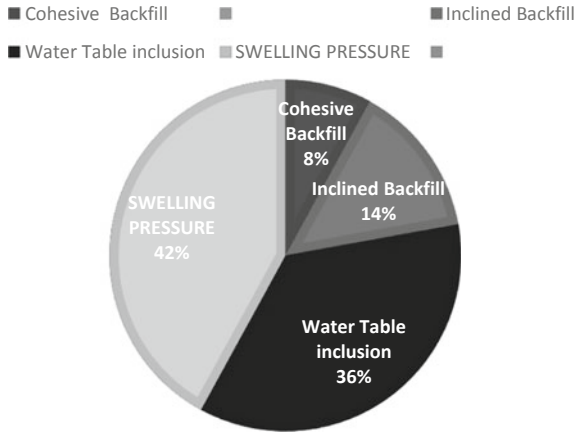


Fig. 7 Variation of lateral earth pressure for different factors

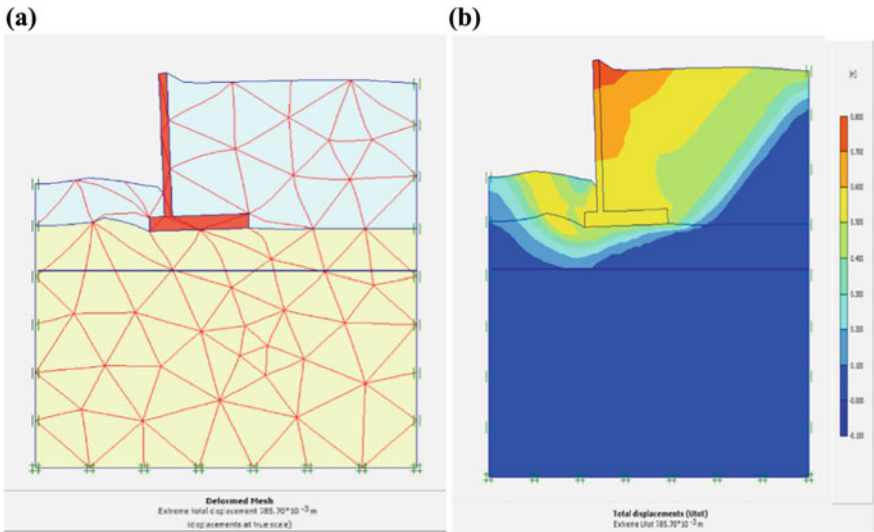
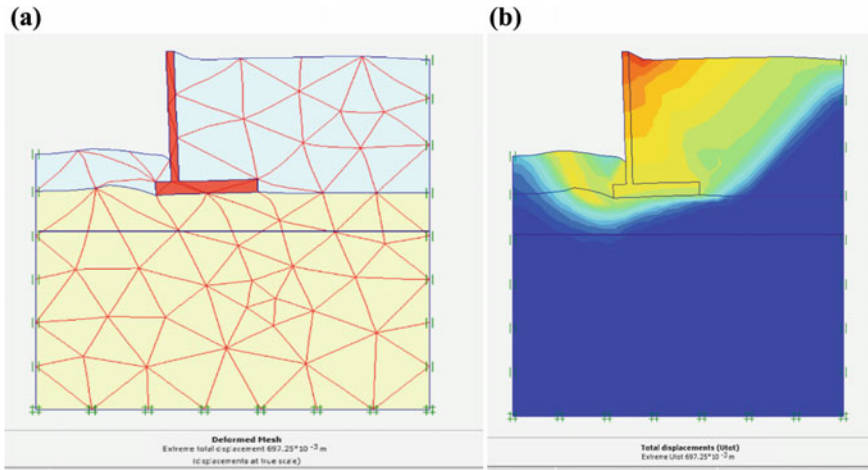


Fig. 8 a Deformed mesh of Mohr–Coulomb model with deformation of 785 mm b The deformation pattern for the retaining wall for the Mohr–Coulomb model

and hardening soil model is given in Table 6. As the expansive nature of the soil increases as indicated by the swell potential, the horizontal deformations increase 785 for (non-swelling soil) to 965 mm for 12% volumetric strain of the backfill. The hardening soil model also depicts a similar trend of increasing deformation with increase in volumetric strain; however, the deformation is lesser compared to Mohr–Coulomb model. For a volumetric strain of 12%, the deformation decreases



**Fig. 9** a Deformed mesh for hardening soil model with deformation of 697 mm. b The deformation pattern for the retaining wall for the hardening soil model

**Table 6** Mohr–Coulomb and hardening soil model results

Volumetric strain (%)	Deformation (mm) Mohr–Coulomb	Deformation (mm) hardening soil
0	785	697
2	610	542
4	551	648
6	738	733
8	762	799
12	965	901

from 965 mm for Mohr–Coulomb model to 901 mm for hardening soil model. The deformation pattern is depicted in Figs. 10 and 11 for 12% strain.

### 3.4 Numerical Model with Geofoam Layers

The geofoam layer is modelled as Mohr–Coulomb model. For the parametric study, geofoam thickness is varied as 0.5 m, 1.0 m and 2.0 m, respectively, and the corresponding change in the deformation is inferred. The deformation behaviour is observed for the various thickness of the geofoam material. As the thickness of the geofoam material increases, the lateral deformation is reduced. For a thickness of 2.0 m of the geofoam material, the deformation reduces to 636 mm from 965 mm. Figure 12 shows the deformation pattern of the retaining wall with the 2 m geofoam material. Table 7 depicts the variation of total deformation with different geofoam

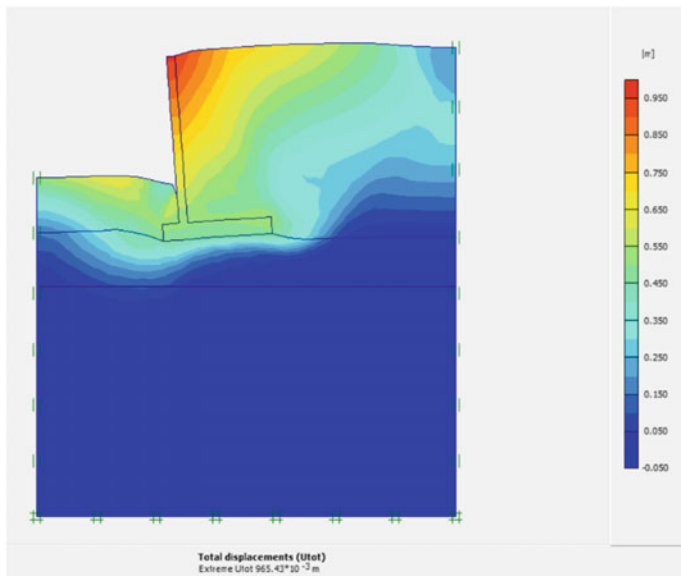


Fig. 10 Deformation of 965 mm for 12% volumetric strain (Mohr-Coulomb model)

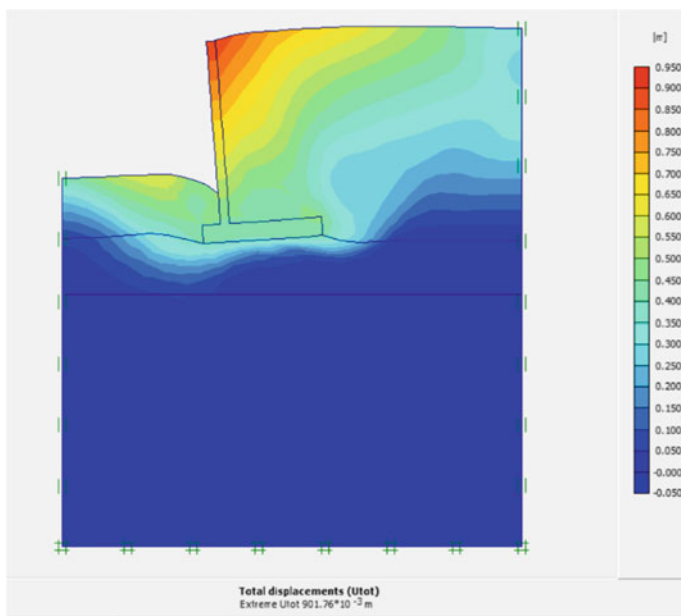
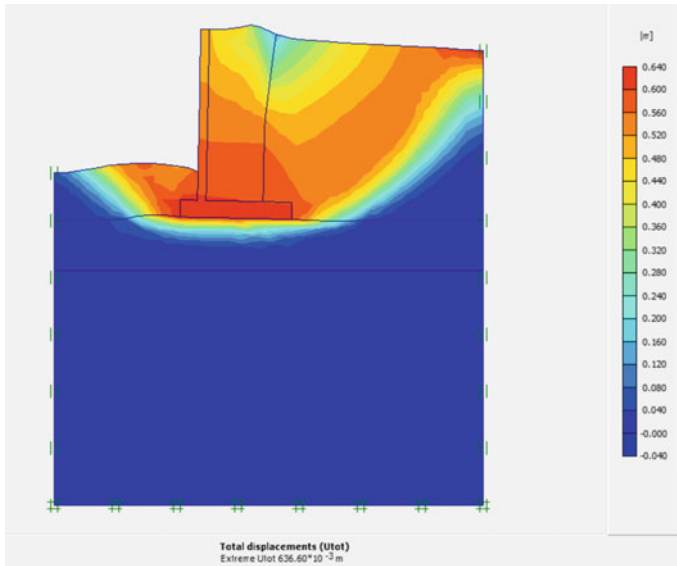


Fig. 11 Deformation of 901 mm for 12% volumetric strain (hardening soil model)



**Fig. 12** Deformations in retaining wall with geofoam layer

**Table 7** Comparison of lateral deformation with geofoam and without geofoam

Geofoam thickness (m)	Deformation (mm)	Deformation without geofoam (mm)
0.5	880	965
1.0	792	965
2.0	636	965

thickness. Limiting values of retaining wall displacements and impact to the adjacent structures the deformations of the retaining wall are within permissible limits (it can be greater than or less than 0.5% of total stem height), however not specific limit is applied as far the as the sufficient FoS is ensured [12].

## 4 Conclusion

The theoretical analysis is carried out for different influencing factors such as the inclined backfill, water table and swelling soil for the model cantilever retaining wall adopted in the study. Numerical analysis is carried out to predict the lateral deformation of the cantilever retaining wall under different soil conditions and different soil models in PLAXIS 2D. Based on the theoretical analysis, it is inferred that overall factor of safety (FOS) decreases with inclusion of cohesive inclined backfill, water table and swell pressure, respectively, with swell pressure parameter giving

high lateral earth pressure. Provision of shear key with a swelling backfill could counter the lateral earth pressure to a reasonable extent. The Mohr–Coulomb model and hardening soil model predict the lateral movement of the retaining wall more appropriately. The lateral deformation predicted by HSM (697 mm) is lesser than MC (785 mm) for cantilever retaining wall with non-swelling backfill. The HSM could be a more appropriate model for expansive soil modelling, the swelling soil is modelled as equivalent volumetric strain equal to the swell potential, and the lateral deformations are higher than the non-swelling backfills. The lateral deformation increases for increase in the swell potential of the soil. For 12% volumetric strain, the deformation predicted by hardening soil model (901 mm) is 1.3 times more than deformation predicted by normal backfill without swell pressure (697 mm).

## References

1. Chauhan, V. B., Dasaka, S. M., & Gade, V. K. (2016). Investigation of failure of a rigid retaining wall with relief shelves. *Japanese Geotechnical Society Special Publication*. <https://doi.org/10.3208/jgssp.tc302-02>.
2. Budhu, M. (2007). *Soil mechanics and foundations* (2nd edn).
3. Tan, Y. (2016). *Swelling pressure and retaining wall design in expansive soils* (Thesis submitted for Master of Engineering). RMIT University.
4. Chen, F. H. (1988). *Foundation on expansive soils* (2nd ed., p. 464). Amsterdam, The Netherlands: Elsevier Science Publishers.
5. Li, J., & Zhou, A. (2013). The Australian approach to residential footing design on expansive soils. *Applied Mechanics and Materials*, 438–439, 593–598.
6. Cameron, D. A. (2015). Management of foundations on expansive clay soils in Australia. In *SEC 2015 International Symposium* (pp. 15–36), IFSTTAR.
7. Goh, A. T. (1993). Behaviour of cantilever retaining wall. *Journal of Geotechnical Engineering*, 119(11), 1751–1770.
8. Al-Busoda, B. S., Awn, S. H. A., & Abbase, H. O. (2017). *Geotechnical Engineering Journal of the SEAGS & AGSSEA*. ISSN 0046-5828.
9. Bowles, J. E. (1997). *Foundation analysis and design* (5th ed.). Singapore: McGraw-Hill.
10. Thomas, M. G. (2017). *Impact of lateral swell pressure on retaining structure design using expansive cohesive backfill*, MS Theses., The University of Texas at Arlington.
11. Lal, B. R. R., Padade, A. H., & Mandal, J. N. (2014). Numerical simulation of EPS geo-foam as compressible inclusions in fly ash backfill retaining walls. In *Proceedings of ground improvement and geosynthetics* (pp. 526–535). Shanghai, China.
12. Fok, P., Neo, B. H., Veeresh, C., Wen, D., & Goh, K. H. (2012). Limiting values of retaining wall displacements and impact to the adjacent structures. *The IES Journal Part A: Civil & Structural Engineering*, 5(3), 134–139. <https://doi.org/10.1080/19373260.2012.696447>.

# MASW Survey for Mapping Soil Profiles at Investigation Site



Satya Sireesha, V. Padmavathi, V. Sai Venkata Harini and P. N. Rao

**Abstract** In geotechnical engineering projects, it is an essential task to map and identify the soil and rock profiles. Usually, these are done by conducting several standard penetration tests (SPTs). However, SPTs are time-consuming and expensive and require skilled workmanship for the execution. In recent days, development of various geophysical methods like multichannel analysis of surface waves (MASW) and ground-penetrating radar (GPR) are used and even very helpful to map and identify the soil and rock profiles. MASW is a seismic exploration technique that uses surface waves to measure the shear wave velocities ( $V_s$ ). The main aim of the present study is to evaluate the efficacy of MASW survey for determining the soil and rock layers. For this purpose, site investigations were carried out by conducting MASW and profiles of  $V_s$  at various depths depicted at construction site. The results of MASW survey are then cross-verified with SPT profiles. In addition, based on the obtained experimental data, an equation has been proposed to find the shear wave velocity. The validity of the proposed equation is presented by comparing the shear wave velocities obtained from experiments and predicted from the proposed equation.

**Keywords** MASW · SPT · Shear wave velocity · Geophones

---

S. Sireesha · V. Padmavathi · V. S. V. Harini (✉)  
Department of Civil Engineering, Jawaharlal Nehru Technological University Hyderabad,  
Hyderabad 500085, India  
e-mail: [harini.varahabhatla3@gmail.com](mailto:harini.varahabhatla3@gmail.com)

V. Padmavathi  
e-mail: [vpadma70@gmail.com](mailto:vpadma70@gmail.com)

P. N. Rao  
BITS-Pilani Hyderabad Campus, Shameerpet, India  
e-mail: [pnrao.bits@gmail.com](mailto:pnrao.bits@gmail.com)

© Springer Nature Singapore Pte Ltd. 2020  
S. Saride et al. (eds.), *Advances in Geotechnical and Transportation Engineering*,  
Lecture Notes in Civil Engineering 71,  
[https://doi.org/10.1007/978-981-15-3662-5\\_20](https://doi.org/10.1007/978-981-15-3662-5_20)

# 1 Introduction

Preliminary geotechnical investigation of a site is mandatory for engineers and contractors, well before the beginning of any construction project. These investigation reports enable one to have an idea about the soil profile in a given site. Estimation of dynamic properties of these soil and rock profiles present in a site as well as the mapping and identification of types of soils and rocks plays a major role during seismic hazard, site response as well as microzonation studies [1, 2]. Soil or rock profile can be obtained by conducting standard penetration test (SPT) at every 1.0 m depth intervals, until a hard rock is being encountered. It is very difficult to depend upon the SPT values provided by consultants due to lack of proper maintenance and poor handling of equipment or due to some unforeseen circumstances. However, in recent decades, the developments in geophysical testing like ground-penetrating radar (GPR) and multichannel analysis of surface waves (MASW) has proven to give reliable results, with less labour and within less time compared to conventional test like SPT. The most significant properties for modelling the seismic wave propagation are the shear modulus or shear wave velocity with density. These can be used to predict the site effects, source and path of earthquake types of loads. MASW is a seismic method that can be used for geotechnical characterization of near-surface materials [3–6].

In this paper, the details of field investigations carried out with MASW to find soil profiles are presented. In order to check the efficacy of MASW, the results of MASW surveys are then compared with four numbers of SPT profiles, which were conducted as a part of geotechnical investigation.

# 2 Study Area

The site was located at BHEL, R. C. Puram, Hyderabad. The study area comprises of 133 m in length and 90 m in breadth as shown in Fig. 1.

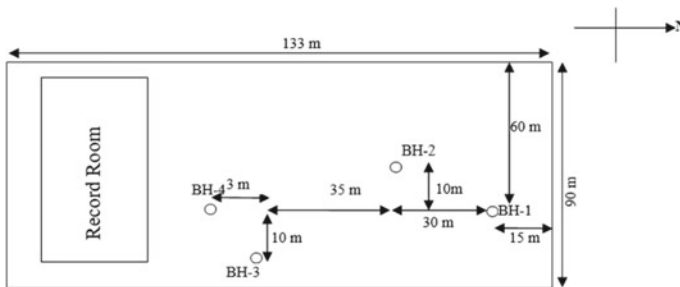


Fig. 1 Site location at BHEL



### 3 Experimental Program

#### 3.1 Geotechnical Investigations

The SPT testing was carried out at different locations in the aforementioned site (Fig. 1) in such a way that they are distributed throughout the construction site to represent site characteristics (see Fig. 1a). The standard penetration tests were carried out at four locations with 1.0 m depth of interval up to a depth of 5 m from ground level, even though the refusal was obtained within a depth of 5 m. Disturbed and undisturbed soil samples were collected at different depths from each borehole, and laboratory experiments were conducted to find the engineering properties of the soil. Table 1 shows the SPT test results with respect to depth in the construction site.

The collected soil samples were used to classify the soil and to determine the engineering properties. The classification details were presented in Table 2. Expansive soil is presented up to a depth of about 3.0 m from ground level followed by clayey sand. Undisturbed samples are collected in BH-1 and 4, and the properties are presented in Table 3.

#### 3.2 Geophysical Investigations

The MASW system which was used for the current investigation consists of 24 channels Geode seismograph with 16 geophones of 4.5 Hz capacity. By using the sledge hammer having an impulsive source of 10 lb and 30 cm × 30 cm hammer plate with ten shots, seismic waves are created and are captured by geophones.

Easy MASW was a commercial software available for characterization of the subsurface in terms of shear wave velocity profile. In this software, the wavenumber frequency and phase velocity–frequency spectra were produced. It determines the shear wave velocity profile only for the top 30 m of soil ( $V_s - 30$ ) (for both active and passive surveys) and provides the idea about soil type (based on certain specified category inbuilt in the software database), the velocity profile and geotechnical parameters such as shear modulus and elastic modulus of the soil. The traces which were obtained from field were imported into the software from the data acquisition system. The result obtained after the spectral analysis of the imported traces obtained using phase velocity–frequency spectra. It is known as dispersion spectrum. It shows the velocity profile of the soil site and the optimized velocity profile obtained through matching of the experimental and theoretical dispersion curve as well. It was obtained after the inversion process, and finally, it provides velocity profile of the soil site along with the thickness of the soil strata.

The site consists of four boreholes, and MASW tests were carried out in the region by spreading 16 geophones in a linear array spacing in such a way that covering all the bore holes. Once the test procedure was started, traces were obtained by generating waves at the source and the data was collected from field and recorded by the

**Table 1** SPT test results of site at four different boreholes

Location	Depth below GL (m)	SPT value (N)	Remarks
BH-1	1.0	23	
	2.0	27	
	3.0	37	
	4.0	55	7 cm penetration
	5.0	55	2 cm penetration
BH-2	1.0	24	
	2.0	24	
	3.0	55	5 cm penetration
	4.0	55	2 cm penetration
	5.0	55	2 cm penetration
BH-3	1.0	22	
	2.0	27	
	3.0	55	7 cm penetration
	4.0	55	5 cm penetration
	5.0	55	4 cm penetration
BH-4	1.0	15	
	2.0	25	
	3.0	50	
	4.0	55	9 cm penetration
	5.0	55	7 cm penetration

recording device (Laptop). Layout and arrangement of geophones at site and obtained seismograph (traces) were presented in Figs. 2a–d. The obtained seismogram was browsed into SYSMATRACK software and required parameters were given for further analysis. Figure 2d represents the predicted values of shear modulus ( $G$ ), Young’s Modulus ( $E$ ), edometric modulus ( $E_d$ ) and bearing capacity of the soil ( $Q$ ).

**Table 2** Atterberg limits and grain size analysis of soil at site

S. No.	Location	Depth (m) below ground level	Atterberg limits (%) (IS:2720 part V)			Particle size distribution (%) (IS:2720 part IV)					Classification
			Liquid limit (%)	Plastic limit (%)	Plasticity index (%)	Gravel > 4.75 mm (%)	Sand			Silt and clay < 0.075 mm	
							Coarse 2.0-4.75 mm	Medium 0.425-2.0 mm	Fine 0.075-0.425 mm		
	BH-1	0-3.0	Highly expansive clay								
1		3.0	48	23	25	13	12	33	16	26	SC
2		4.0	27	17	10	5	9	45	27	14	SC
	BH-2	0-3.0	Highly expansive clay								
3		3.0	54	25	29	17	15	22	23	23	SC
4		5.0	37	20	17	0	0	32	39	29	SC
	BH-3	0-3.0	Highly expansive clay								
5		3.0	51	24	27	13	12	32	18	25	SC
6		4.0	28	17	11	0	7	41	35	17	SC
	BH-4	0-3.0	Highly expansive clay								
7		5.0	38	20	18	5	17	32	14	32	SC

**Table 3** Engineering properties of the soil at site for boreholes 1 and 4

Location	Depth below GL (m)	Unit wt. (kN/m <sup>3</sup> )	Moisture content (%)	Cohesion <i>c</i> (kPa)	Phi (°)
BH-1	3.8	18.20	6.2	12	30
BH-4	4.3	19.05	5.3	20	29

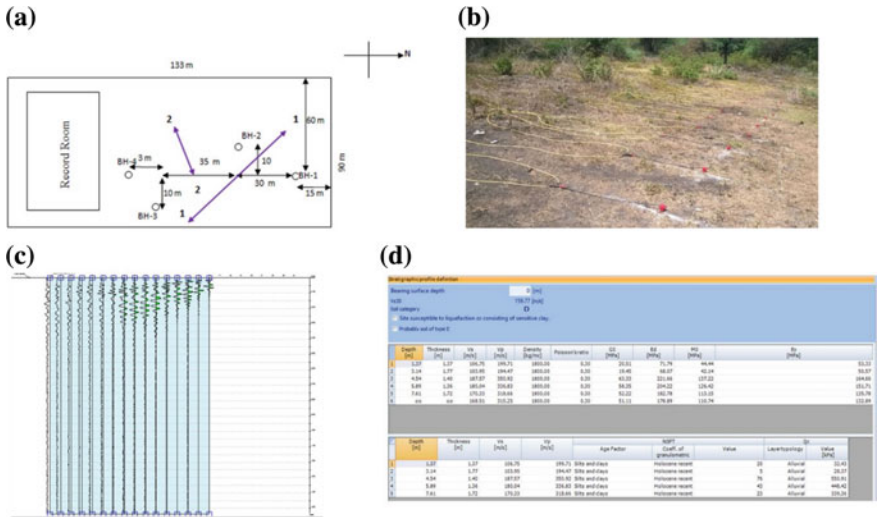


**Fig. 2** a Layout of geophones at the site, b arrangement of geophones in the site, c trace obtained from field and d results obtained from SYSMATRACK

### 4 Results and Discussions

Four boreholes were advanced from the existing ground level to a depth of 5 m. From Fig. 3a, it is clear that borehole (BH-1) consists of highly expansive clay up to

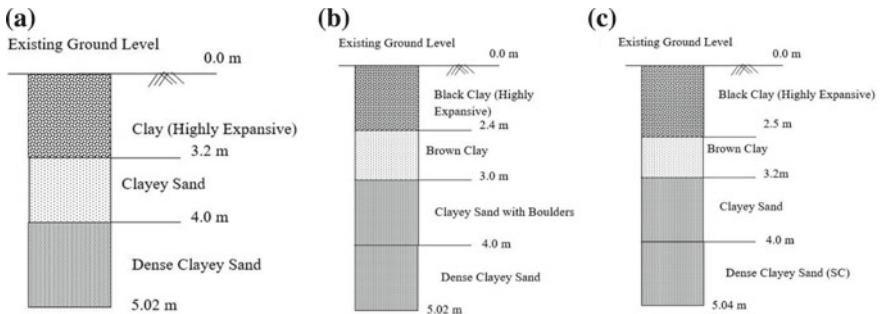


**Fig. 3** Soil profile at site, a BH-1, b BH-2, c BH-3 and d. BH-4

about 3.2 m followed by clayey sand also expansive in nature up to 4.0 m underlain by dense clayey sand up to 5.02 m. Figure 3b represents BH-2 soil profile, and it consists of highly expansive clay up to about 2.4 m followed by brown clay up to 3.0 m and clayey sand with boulders up to 4.0 m. This stratum was underlain by dense clayey sand up to 5.02 m. From Fig. 3c, we can notice that boreholes BH-3 and BH-4 consist of highly expansive clay up to about 2.5 m followed by brown clay up to 3.2 m underlain by clayey sand up to 4.0 m and then by dense clay sand up to 5.04 m.

Geophones were arranged in such a way that covering all the bore holes and tests are conducted, and seismograph obtained from field was analysed as a result shear wave velocity ( $V_s$ ); Young's modulus ( $E$ ), edometric modulus ( $E_d$ ), volumetric compressibility modulus ( $M_o$ ) and bearing capacity ( $Q$ ) of the soil are obtained.

SPT and MASW were conducted at the site. SPT  $N$  values were measured for every 1.0 m interval. Shear wave velocity profile was developed based on the layer formations observed from SPT and experimental dispersion curves from MASW testing. Shear wave velocity was measured using MASW testing, and the testing points were close to borehole locations where SPT was performed. A number of empirical relations were available for shear wave velocity ( $V_s$ ) and penetration resistance ( $N$ ) in the literature.

Among all, Eq. (2) proposed by Kanai was considered for estimating  $V_s$  from SPT  $N$  value for all soils.

$$V_s = 19N^{0.6} \text{ (m/s)} \quad (2)$$

Using the experimental data, Eq. (2) was slightly modified and a new equation is proposed to calculate the shear wave velocity and is presented as follows.

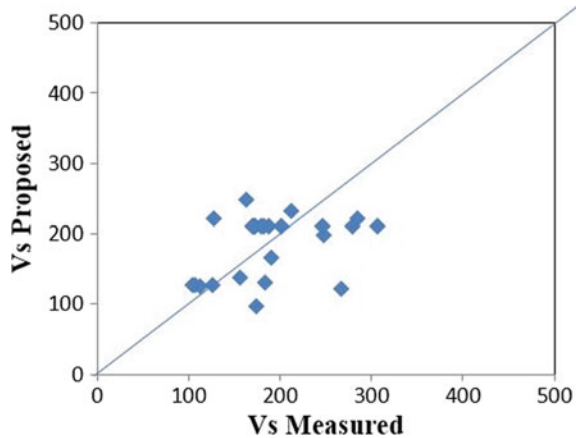
$$V_s = 16N^{0.6} \text{ (m/s)} \quad (3)$$

$N$  value was considered up to 50, and graph was plotted between  $V_s$  measured from MASW and  $V_s$  calculated from proposed Eq. (3). In order to validate the proposed equation to measure the shear wave velocity, the  $V_s$  values measured from MASW and  $V_s$  obtained from the proposed equation are presented in Fig. 4. It can be seen that there is a good comparison between proposed equation and measured data, showing the efficiency of the proposed equation.

## 5 Conclusions

This paper presents mapping of soil and rock layers below the ground level using MASW. MASW testing was conducted at BHEL site, Hyderabad. The soil profiles obtained from MASW surveys are cross-verified with the SPT data obtained from the fields. The following are the main conclusions that can be drawn from the present study.

**Fig. 4** Variation of measured and proposed shear wave velocity



1. The profiles of soil or rock layer identified using MASW data are in good agreement with the bore log data obtained from the field investigations.
2. A correlation between  $N$  values to shear wave velocity has been developed for  $N \leq 50$ .  $V_s$  measured and  $V_s$  from proposed expression are showing good validation.
3.  $V_s$  was evaluated up to 5 m depth for the selected investigation sites. For site-BHEL,  $V_s$  is less than 180 m/s, indicating the coarse grain/fine grain soils at shallow depth.

Hence, it can be concluded that MASW techniques can be suitably applied in construction sites to obtain soil and rock profiles. Therefore, it is highly recommended to use MASW techniques as they are economical and less time-consuming compared to other geotechnical explorations methods available.

## References

1. Anbazhagan, P., & Sitharam, T. G. (2006). Evaluation of dynamic properties and ground profiles using MASW: Correlation between  $V_s$  and  $N_{60}$ . In *Proceedings of 13th Symposium on Earthquake Engineering* (pp. 1–10), Roorkee, India.
2. Parhi, P. S., & Umashankar, B. (2018). MASW survey to map soil and rock profiles in a construction site. In *Proceedings of Indian Geotechnical Conference 2018*, Bengaluru, December 13–15, 2018.
3. Miller, R. D., Xia, J., Park, C. B., & Ivanov, J. (1999). Multichannel analysis of surface waves to map bedrock. *The Leading Edge*, 18(12), 1392–1396.
4. Park, C., Miller, R. D., & Xia, J. (1999). Multi-channel analysis of surface waves. *Geophysics*, 64(3), 800–808.
5. Xia, J., Miller, R. D., & Park, C. B. (1999). Estimation of near-surface shear-wave velocity by inversion of Rayleigh waves. *Geophysics*, 64(3), 691–700.
6. Xia, J., Miller, R. D., Park, C. B., & Tian, G. (2003). Inversion of high frequency surface waves with fundamental and higher modes. *Journal of Applied Geophysics*, 52, 45–57.

# Analysis of Rice Crop Phenology Using Sentinel-1 and Sentinel-2 Satellite Data



Radha Saradhi Inteti, Venkata Ravibabu Mandla,  
Jagadeeswara Rao Peddada and Nedun Ramesh

**Abstract** Present study explains the analysis of rice crop phenology using optical and SAR C-band of sentinel satellite data. Rice crop phenology is understood and analyzed based on various backscattered polarization. It will be useful to estimate crop acreage when the optical sensors data is not available or with cloud cover. The study also gives information of various stages of rice crop starting from sowing to the harvesting stage, along with NDVI and soil moisture data from SOMS.

**Keywords** Rice crop · Phenology · NDVI · Soil moisture · Sentinel

## 1 Introduction

Rice is the staple food for 60% of the world's population. India is the world's second largest producer, and on an average, it produces about 106.5 million tons yearly. Analysis of rice crop phenology through ground measurement is usually time taking process, and hence, it can be acquired through remote sensing. The rice crop is grown in three stages—vegetative, reproductive and ripening stages [1]. Figure 1 shows the transplantation of rice phenology stages.

Remote sensing analysis is the most suitable way for the estimation of rice crop yield, and it is low cost-effective to detect the large area crop classification, cropping pattern with temporal resolution. Change detection in the crops can be identified due to the growth in the physical characteristics of the plants. Different species of rice crop has its own changes in height, crop canopy cover, biomass, water intake, maturity stages and even in cropping pattern [2].

---

R. S. Inteti · J. R. Peddada

Department of Geo-Engineering, Andhra University, Vishakhapatnam, Andhra Pradesh, India

V. R. Mandla (✉) · N. Ramesh

CGARD, School of Science, Technology and Knowledge Systems, National Institute of Rural Development & Panchayati Raj (NIRDPR), Ministry of Rural Development, Government of India, Hyderabad, Telangana 500030, India

e-mail: [mvravibabu.nird@gov.in](mailto:mvravibabu.nird@gov.in)

© Springer Nature Singapore Pte Ltd. 2020

S. Saride et al. (eds.), *Advances in Geotechnical and Transportation Engineering*,  
Lecture Notes in Civil Engineering 71,

[https://doi.org/10.1007/978-981-15-3662-5\\_21](https://doi.org/10.1007/978-981-15-3662-5_21)

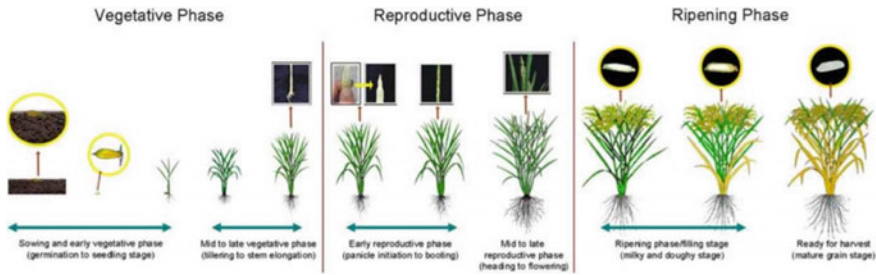


**Fig. 1** Transplanting of rice phenology stages

Monsoon season is the most crucial period for rice crop cultivation, but during the same time, cloud cover may occur. As the multispectral sensors cannot penetrate through the clouds, hence microwave sensors can be replaced. Microwave sensors can penetrate through the clouds and have the advantage of acquiring data during the day and night. Synthetic Aperture Radar (SAR) is one of the acquisition technique in microwave remote sensing, and the advances in SAR applications has the availability of data at different frequencies and polarizations which give good results in rice crop growth analysis [3, 4].

Timely estimation of soil moisture is necessary for monitoring the rice crop growth, and in the current study to measure it, Soil Moisture and Ocean Salinity (SMOS) satellite data is used [5]. The objectives of the current study are (1) rice crop phenology growth analysis through Sentinel-1 and Sentinel-2 satellite data and (2) analysis of soil moisture pattern changes in rice crop field.

## 2 Data

### 2.1 Study Area

In India, almost every state cultivates rice, from which Andhra Pradesh is the fifth largest producer. In this state, the rice crops have been cultivated on over 2.16 million hectares of land, with an average production of 7.49 million tons annually. Guntur district is the fifth largest district in Andhra Pradesh to produce rice in Kharif season. Toward the eastern part of the Kondaveedu hills, laterite red soil is found. The center of the city is surrounded by Black cotton and Alluvium soil.



## **2.2 Sentinel-1 Data**

Sentinel-1 satellite is a constellation of two satellite missions, Sentinel-1A and Sentinel-1B, and data is acquiring in four different special modes, which are Stripmap (SM), Wave (MV), Interferometry Wide Swath (IW) and Extra Wide Swath (EW). The IW is the default land operational mode. The IW mode products have a swath width of 250 km and with a polarization of vertical transmitting and horizontal receiving (VH) and vertical transmitting and vertical receiving (VV). Sentinel-1 SAR data with 12-day temporal resolution consists of C-band wavelength and different levels of data can get. In the current study, Level-1 Ground Range Detection (GRD) IW mode products were used in the duration of rice crop about July 11, 2018, to December 26, 2018.

## **2.3 Sentinel-2 Data**

Sentinel-2 satellite is a constellation of two satellite missions, Sentinel-2A and Sentinel-2B, and provides 5-day revisit time having the 10 m spatial resolution. In the current study, Sentinel-2 Level-1C (L1C) cloud-free products were used in the duration of rice crop presence in the field from July 13, 2018, to December 20, 2018. The top of atmosphere image was converted to the bottom of the atmosphere using atmospheric correction of Sen2Cor module where the spatial resolution is resampled to the 10 m.

## **2.4 Soil Moisture Data**

Soil Moisture and Ocean Salinity (SMOS) with L-band wavelength operational satellite, which is an interferometry radiometer technique to measure brightness temperature and to estimate the surface soil moisture (SSM) with the spatial resolution of 35–50 km, provides a 2-day revisit time data. Soil moisture is obtained by exchange of water and temperature availability between atmosphere and land. In the current study SMOS, satellite products were used in the duration of rice crop presence about July 13, 2018, to December 16, 2018.

## **3 Methodology**

The overall methodology in this study is depicted in Fig. 2. The processing has been done for Sentinel-1, Sentinel-2 satellite data and SMOS data. The temporal

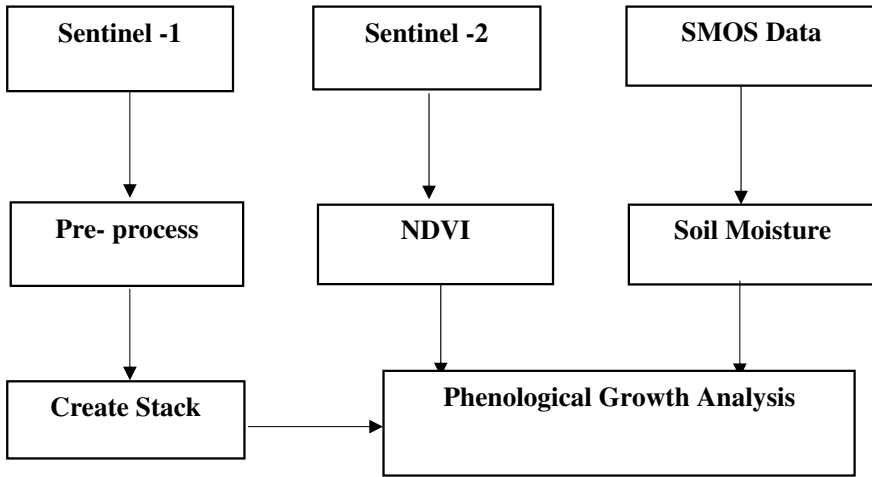


**Fig. 2** Overall methodology flowchart for phenological growth analysis

phenology changes of rice crop have been monitored through the backscatter intensity of Sentinel-1 data, NDVI of Sentinel-2 data and soil moisture changes in the field by SMOS data.

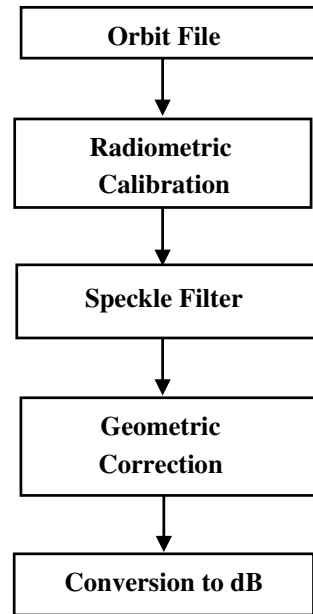
### ***3.1 Sentinel-1 Data Preprocessing and Postprocessing***

Sentinel-1 satellite data has been processed to analyze the products by the backscatter intensity of VH and VV polarization. In the process of SAR data, preprocess and postprocess are included. The preprocessing of Sentinel-1 has been done by the Sentinel Application Platform to represent the natural numbers into sigma nought backscatter intensity from the reflected surface, for that Radiometric Calibration was done. Due to the irregular, constructive and damaging interference brings salt-and-pepper noise in the image, to reduce the noise applied speckle filter to the radiometric calibrated product.

Usually, the active nature of the system acquires the SAR product in the slant looking range geometry, due to the ground elevations results geometric shifts in the image like foreshortening, layover and shadow. Range Doppler terrain correction was done where pixels were shifted in their exact locations by the given SRTM 3 s digital elevation model (DEM). For the better analysis, the results were converted to the logarithmic scale, which had conveniently represented in a specific scale [6, 7]. Figure 3 represents the preprocessing of the products.

In the postprocessing, the temporal images were co-registered to get the time series backscatter intensity results by maintaining the optimal master product [8, 9].

**Fig. 3** Preprocessing flow chart of Sentinel-1 SAR data



The time series backscatter intensity has been generated for both polarizations VH and VV by taking the mean of the field.

### 3.2 *Sentinel-2 Data Processing*

Sentinel-2 satellite data has been processed in the Sentinel Application Platform tool for Normalized Difference Vegetation Index (NDVI), which is the simple graphical representation that can be used to analyze the crop growth and the NDVI time series process has been done for the cloud-free images only, during the crop season. By NDVI health of the plants can monitor and NDVI process is based on the near-infrared band and red band, NDVI depends on the chlorophyll content in the plants, which represents in Eq. (1), [9, 10].

$$\text{NDVI} = (\text{NIR} - \text{Red}) / (\text{NIR} + \text{Red}) \quad (1)$$

### 3.3 *SMOS Data Processing*

SMOS satellite data with 35–50 km spatial resolution, a 2-day revisit time satellite. Temporal soil moisture data has been taken directly from the SMOS satellite data by taking the mean of the field in the Sentinel Application Platform [11, 12].

## 4 Results and Discussion

In the current study, the general rice crop was sown for about 110–130 days, and on an average, about 5700 kg per hectare yield was being produced. In the vegetative stage, initially, the seeds are grown in a nursery which are pulled out and transplanted using the random method all over the field. For potential tillering and rooting ability, within 20–30 days of seedlings the plants are transplanted into the field when 2–3 leaves are grown, which tends to provide maximum yield potential. After transplantation, it takes about 25–35 days from tillering to stem elongation stage. In the reproductive stage, it takes about 30–40 days from panicle initiation to the flowering stage, while in the ripening stage, it lasts for about 35–45 days from milky stage to mature grain stage and then harvest in the field.

### 4.1 *Sentinel-1 Temporal Backscatter Intensity Analysis*

As per the microwave backscatter time series analysis, the rice crop growth analysis is based on the VH and VV polarizations of the satellite. The mean backscatter intensity of VH polarization varies between  $-14.71$  and  $-19.65$  dB, and the backscatter intensity of VV polarization varies between  $-7.09$  and  $-13.97$  dB. The rice crop field at nursery stage's backscatter intensity of VH polarization range is  $-15.85$  dB, while the backscatter intensity of VV polarization is  $-10.13$  dB. On the main field, the transplantation requires more water for puddling. In the vegetative stage, stagnant water is present due to which it leads to low backscatter intensity. The backscatter intensity of the VH polarization varies from  $-19.65$  to  $-19.27$  dB, while VV polarization varies from  $-13.97$  to  $-12.16$  dB. In the reproductive stage due to the vegetation cover, the backscatter intensity is increased. The backscattering intensity of VH polarization ranges between  $-17.44$  and  $-14.71$  dB, while VV polarization varies from  $-10.56$  to  $-7.09$  dB. In the ripening stage due to color change from green to yellow, the backscatter intensity again decreases up to the harvesting stage. The backscatter intensity of VH polarization ranges between  $-14.75$  and  $-13.72$  dB, while VV polarization varies from  $-8.15$  to  $-8.56$  dB. Figure 4 represents the time series backscatter intensity of both VH and VV polarizations.

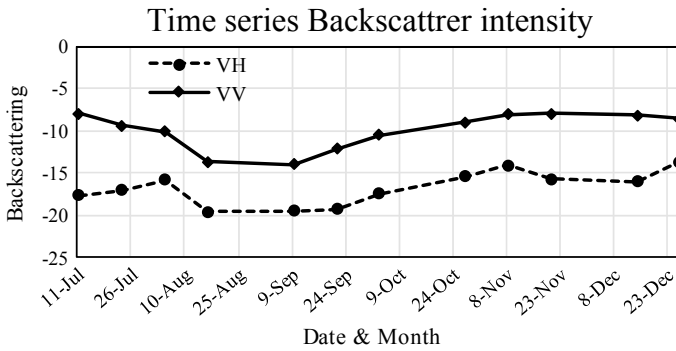


Fig. 4 Time series backscatter intensity of VV and VH polarizations

### 4.2 Soil Moisture Change Analysis

Rice is more sensitive to water, when water stress occurs at the reproductive stage, 50–60% of production will be reduced in the yield. Irrigation is done in the initial stage, and water is drained from the field prior to 15–20 days of harvesting. The minimum amount of water is maintained up to 5 cm in the vegetative and flowering stages. The highest amount of water is required in the panicle initiation stage, where soil moisture is 0.63 cm<sup>3</sup>. The crops have been transplanted during the initial stage where the water availability is high. Figure 5 represents the temporal changes of SMOS surface soil moisture.

SMOS estimated soil moisture is decreasing because of its reflection from the crop when the crop growth is high soil moisture value decreases. Table 1 represents the crop growth stages and its average soil moisture availability. SMOS is a microwave satellite, with L-band of longest wavelength, and it follows the same pattern as the following as C-band polarizations. The statistical regression analysis is carried out based on different crop growth stages of SMOS surface soil moisture with VV

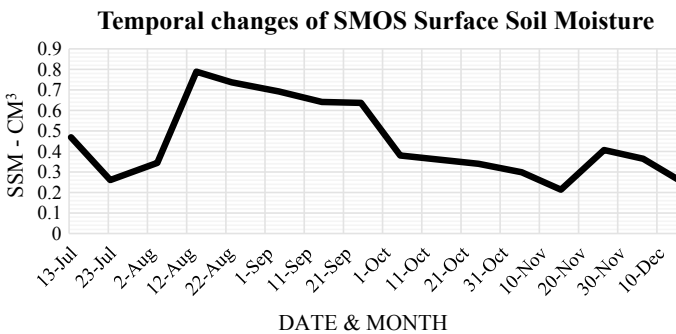


Fig. 5 Temporal changes in SMOS surface soil moisture

**Table 1** Crop growth stage and average SMOS soil moisture

Crop growth stages	Approximate water requirement (cm)	Days	Average SMOS soil moisture in cm <sup>3</sup>
Nursery	4	1–20	0.789
Main field preparation	20	20–25	0.760
Planting to panicle initiation	45	25–38	0.739
Panicle initiation to flowering	41	38–90	0.617
Flowering to maturity	12	90–120	0.314

backscattering and VH backscattering. From the analysis, SMOS is a dependent variable, and both VV and VH polarizations are two different independent variables. The  $R^2$  value of VV polarization is 0.4631 with significant value of 0.43, and  $R^2$  value of VH is 0.6229 with significant value of 0.26. The VV backscattering analysis is having lower  $R^2$  compare to VH backscattering.

### 4.3 Validating of Backscattering Intensity with NDVI

NDVI is the usually performed operation to validate the time series analysis. The Sentinel-2 images were preprocessed using Sen2Cor processing. The sensor has wavebands centered at wavelengths 650 nm (red) and 810 nm (NIR). The time series cloud-free Sentinel-2 images from July to December 2018 are acquired. The values are lower in the initial stage 0.053, where the water activity is more, and it maintains the range up to the reproduction stage, where the multi-tillering has occurred. When vegetation gets increased, the mean time NDVI value increases up to 0.546 in this phase, where panicle initiation, early maturity and heading occurred. After the final stage of maturity, chlorophyll content of the plants decreased, so it reduces the NDVI to 0.367 at the time of harvesting. Figure 6 represents the temporal changes of NDVI for rice crop field.

The correlation was carried out between the time series NDVI with time series backscatter intensity of VV and VH polarization, where VV polarization backscatter intensity behaves the same as NDVI but VH polarization backscatter intensity showed a significant difference in land preparation and crop establishment stage as well as represented the real rice growth cycle. VH polarization has been selected for the future analysis of the study as it gives better monitoring results compared to the VV polarization monitoring.

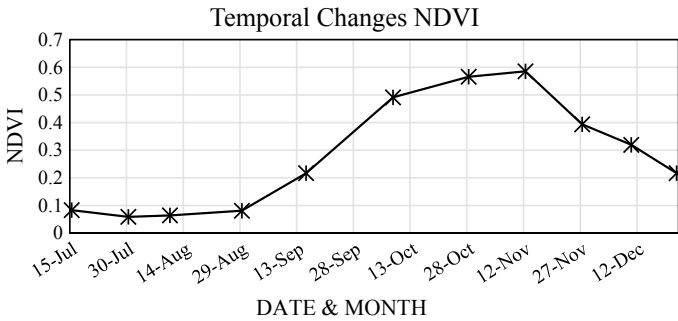


**Fig. 6** Temporal changes in NDVI analysis for rice crop

## 5 Conclusion

From the analysis, it can be concluded that microwave remote sensing analysis over passive remote sensing analysis gives better monitoring results for rice crops. It is due to the capacity of penetration through clouds and also day and nighttime images can be acquired. Sentinel-1 has both VV and VH polarizations. Both these polarizations give a better interpretation for rice crops to monitor at different growing stages, as there is different backscatter intensity. Based on the backscatter intensity of both VV and VH polarizations observed on each stage of rice crop growth, which can be monitored regularly. Timely monitoring of rice has an advantage in increasing the nation's economy and for predicting the yield. While comparing both these polarization, VH polarization gives better interpretation than VV polarization, as in VH polarization temporal changes can be interpreted magnificently. Soil moisture is needed to monitor large area fields. SMOS satellite data is one of a better way to analyze the soil moisture changes for the rice crop area. The soil moisture is derived from L-band of SMOS satellite data because it has the capability to penetrate up to a certain level into the soil. The SMOS soil moisture has a high regression value with VH polarization.

## References

1. Aghamolki, M. T. K., Yusop, M. K., Jaafar, H. Z., Kharidah, S., Musa, M. H., & Zandi, P. (2015). Preliminary analysis of growth and yield parameters in rice cultivars when exposed to different transplanting dates. *Electronic Journal of Biology*, 11(4), 147–153.
2. Kuenzer, C., & Knauer, K. (2013). Remote sensing of rice crop areas. *International Journal of Remote Sensing*, 34(6), 2101–2139.
3. Nelson, A., Setiyono, T., Rala, A., Quicho, E., Raviz, J., Abonete, P., et al. (2014). Towards an operational SAR-based rice monitoring system in Asia: Examples from 13 demonstration sites across Asia in the RIICE project. *Remote Sensing*, 6(11), 10773–10812.
4. Fontanelli, G., Crema, A., Azar, R., Stroppiana, D., Villa, P., & Boschetti, M. (2014). Agricultural crop mapping using optical and SAR multi-temporal seasonal data: A case study in Lombardy region, Italy. In *2014 IEEE Geoscience and Remote Sensing Symposium*, 1489–1492.

5. Zeng, J., Li, Z., Chen, Q., Bi, H., Qiu, J., & Zou, P. (2017). Evaluation of remotely sensed and reanalysis soil moisture products over the Tibetan Plateau using in-situ observations. *Remote Sensing of Environment*, 163, 91–110.
6. Nguyen, D. B., & Wagner, W. (2017). European rice cropland mapping with Sentinel-1 data: The Mediterranean region case study. *Water*, 9(6), 392.
7. Chen, C. F., Son, N. T., Chen, C. R., Chang, L. Y., & Chiang, S. H. (2016). Rice crop mapping using Sentinel-1A phenological metrics. *International Archives of the Photogrammetry, Remote Sensing and Spatial Information Sciences*, 41, 8.
8. Kurosu, T., Fujita, M., & Chiba, K. (1995). Monitoring of rice crop growth from space using the ERS-1 C-band SAR. *IEEE Transactions on Geoscience and Remote Sensing*, 33(4), 1092–1096.
9. Stendardi, L., Karlsen, S. R., Niedrist, G., Gerdol, R., Zebisch, M., Rossi, M., & Notarnicola, C. (2019). Exploiting time series of Sentinel-1 and Sentinel-2 imagery to detect meadow phenology in mountain regions. *Remote Sensing*, 11(5), 542.
10. Wu, M., Yang, C., Song, X., Hoffmann, W. C., Huang, W., Zheng, N., et al. (2016). Monitoring cotton root by synthetic Sentinel-2 NDVI time series using improved spatial and temporal data fusion. *Scientific Reports*, 8, 2045–2322.
11. Souza, A., Neto, A., Rossato, L., Alvala, R., & Souza, L. (2018). Use of SMOS L3 Soil moisture data: validation and drought assessment for Pernambuco state, northeast Brazil. *Remote Sensing*, 10, 1314.
12. Sánchez, N., González-Zamora, Á., Piles, M., & Martínez-Fernández, J. (2016). A new soil moisture agricultural drought index (smadi) integrating MODIS and SMOS products: A case of study over the Iberian Peninsula. *Remote Sensing*, 8(4), 287.



# Life-Cycle Assessment of Various Synthesis Routes of Silver Nanoparticles



Vantepaka Arundhathi, Sreeram Nagalakshmi Manasa,  
Suriseti Kalyani Lakshmi, Veeramaneni Varsha  
and Baranidharan Sundaram

**Abstract** The current study evaluated the environmental impacts caused due to different synthesis routes of Ag NPs using life cycle analysis. Silver nanoparticles (Ag NPs) have been studied extensively in the past due to their unique physical, chemical, antibacterial and anti-fungal properties. The study was aimed to identify the environmental hot spots due to system variables like Ag NPs synthesis route, its application (on socks) and its disposal into environment (water) from a life-cycle assessment (LCA) perspective. Presently, various synthesis methods of Ag NPs (physical, chemical and biological methods) are available for fabrication of different size distributions. A life cycle study on different synthesis routes (microwave-assisted, green synthesis and laser ablation method) of Ag NPs was carried out to assess the impacts on the environment due to fabrication of NPs. This was assessed with the help of LCA tool (SimaPro), and the assessment was performed at midpoint levels using ReCIPE method. When evaluating the results from the LCA study, we observed that the synthesis of NP is dominated by the environmental impacts associated with energy and chemical use, especially relevant for the type of synthesis method used. After coating a cotton sock with the synthesised Ag NPs, it can be seen that about 90% contribution towards FEU and MEU is due to the production of Ag NPs coated socks, and nearly 50% of the contribution towards TET is caused by transportation. In terms of various factors, Ag NPs synthesised using non-renewable energy (grid) have more impact compared to renewable source (solar).

**Keywords** Silver nanoparticles · Synthesis routes · Life cycle analysis · SimaPro · NP-coated socks

---

V. Arundhathi · S. Nagalakshmi Manasa · S. Kalyani Lakshmi · V. Varsha · B. Sundaram (✉)  
Department of Civil Engineering, National Institute of Technology Andhra Pradesh,  
Tadepalligudem, Andhra Pradesh, India  
e-mail: [baranis@nitandhra.ac.in](mailto:baranis@nitandhra.ac.in)

© Springer Nature Singapore Pte Ltd. 2020  
S. Saride et al. (eds.), *Advances in Geotechnical and Transportation Engineering*,  
Lecture Notes in Civil Engineering 71,  
[https://doi.org/10.1007/978-981-15-3662-5\\_22](https://doi.org/10.1007/978-981-15-3662-5_22)

## 1 Introduction

In recent years, nanotechnology, an interdisciplinary study, has become popular in various fields of life [1]. Nanoparticles (NPs) are addressed as atomic or molecular aggregates characterised by size of less than 100 nm [2]. NPs are used in wide range of applications which include, drugs, environment, electronics, energy harvesting, mechanical industries. Due to their high surface area and nanoscale size led to the immense research and large-scale production [1], Silver NPs (Ag NPs) have been studied for a long time due to their unique physical and chemical properties and their vast applications in various fields (anti-plasmodial, anti-microbial, targeted drug delivery, sensing and imaging, anti-fungal, anti-cancerous and wound healing) [3]. Physical and chemical properties of Ag NPs include surface chemistry, size, size distribution, shape, particle morphology, particle composition, coating/capping, agglomeration, dissolution rate, particle reactivity in solution, efficiency of ion release, cell type and finally type of reducing agents are crucial. Ag NPs have been shown potential applications in cancer diagnosis and therapy, degradation of environmental pollutants [4]. There are many types of socks materials available in market of which we have considered cotton sports socks. Ag NPs are coated on socks because of their antibacterial property. Life-cycle assessment (LCA) as a tool helps to determine the environmental impacts caused by a product or a process throughout its life span, i.e. from its raw material extraction to its final disposal and also helps the governing authorities to arrive at a decision regarding the environmental impacts [5, 6]. Researchers in the past have carried out LCA studies on different NPs such as copper, carbon nanostructures, silver, titanium oxide, MoS<sub>2</sub> and tungsten disulphide [7–18]. The major findings from these studies report that both energy and raw materials used during the synthesis contribute significantly towards the environmental impacts [11, 14, 19], and as more and more NPs find their place in variety of consumer products, more such studies are need of the hour.

## 2 Ag NPs

Ag NPs synthesis in simple terms can be defined as the method which deals with the production of Ag NPs. There are several methods which involve the Ag NP synthesis like physical, chemical and biological which differ in mechanisms, inputs, yield, reaction conditions and size distributions [20, 21]. In brief, physical methods include evaporation–condensation and laser ablation, while chemical methods include microwave-assisted and conductive heating, and biological methods include the use of microorganism, plant for the synthesis of Ag NPs. Due to the shorter reaction times, reduced energy consumption microwave-assisted method was chosen for the present study. Microwave-assisted involves chemical reduction of silver salt by a reducing agent in the presence of a stabilising agent. The reducing agents commonly

used are sodium borohydride, hydrazine, N, N-dimethylformamide. Biological methods have easy accessibility, safe and in most cases deploy non-toxic plants which can help to reduce silver ions. It involves mixing up of extract up with a solution of metal salt at room temperature, and the reaction gets carried out completely in a few minutes. The nature and concentration of the plant of extract, concentration of metal salt, pH, temperature and contact time can have a strong effect on the speed and amount of NP production. By varying important parameters such as substrate concentration, pH, light intensity, temperature, buffer strength, electron donor, biomass concentration, mixing speed, and exposure time both the sizes and morphologies of NPs can be controlled [18]. Increasing production volumes of Ag NPs generally had led to extensive research into potential environmental and health implications of their use, particularly given the projections for their widespread incorporation into consumer products because of their unique properties [22]. Ag NPs are widely used in drug encapsulation, cloth fabrics, cosmetics, etc. Ag NPs also find its way in *clothes such as socks* to kill the bacteria associated with smelly feet and can easily be found into wastewater due to washing process [23]. In the present study, an attempt was made to quantify and compare the environmental effects caused due to different synthesis routes/methods of Ag NPs. Also, an attempt was made to understand the impact of Ag NPs released from cotton socks to environment.

### 3 Synthesis of Ag NPs

**Microwave-Assisted Method** In this study, Ag NPs are synthesised from chemical reaction of silver nitrate solution and a reducing agent at temperature of 80–100 °C, and the synthesised NPs were reported in the range of 20–30 nm. Microwave heating is better than conventional heating as it yields nanostructures with smaller size distributions with a high degree of crystallisation [18]. Moreover, microwave heating has shorter reaction time, reduced energy consumption and better product yield where there has been less chance for particle agglomeration.

**Green Synthesis** Ag NPs are synthesised from chemical reaction of silver nitrate solution and a reducing agent. Commonly used reducing agents are different plant extracts like neem, turmeric, etc. In this study, Ag NPs were synthesised using onion plant extract (*Allium cepa* extract) as a reducing agent and silver nitrate solution [24]. The plants have various bioactive molecules with different biological activities and their extracts can be used for the NPs biosynthesis. Previously, studies have found that Ag NPs synthesis from plant extracts is advantageous because of its reduced biosafety issues and faster reduction rate [25, 26].

**Laser Ablation** By laser ablation, bulk metallic materials in solution Ag NPs can be synthesised. Parameters like wavelength of the laser impinging the metallic target, the duration of the laser pulses, the laser fluence, the ablation time duration and effective liquid medium, with or without the presence of surfactants have impact on the ablation efficiency and the characteristics of produced nano-silver particles. While

comparing with other synthesis methods, laser ablation has an advantage of absence of chemical reagents in solutions for the production of metal colloids. Therefore, by using this method, pure and uncontaminated metal colloid for further applications can be prepared.

**Socks** The amount of cotton and energy required for making a pair of socks was considered in this study. This coated socks were subjected to four washings with time lapse of 24 h to know the amount of Ag NPs released into water and effect of detergent on Ag NPs released was neglected [23].

**Methodology** Life-cycle assessment (LCA) is a technique to assess the potential environmental impacts related to all stages of a product life from its raw material extraction stage to its disposal stage [9]. According to environmental management standard ISO:14044—2006, LCA methodology consists of four steps: (i) goal and scope definition (ii) inventory analysis (iii) impact assessment and (iv) interpretation.

The aim of this LCA study was to assess the environmental impacts of Ag NPs synthesised by various methods. Gate-to-grave analysis of Ag NPs was done by considering processed materials collection to disposal of Ag NPs (Fig. 1). The synthesis routes of Ag NPs considered in this study comprise three ways: Physical method, chemical method and biological method. In this paper, the Ag NPs have been synthesised by the methods like green synthesis (biological), microwave synthesis (chemical) and laser ablation (physical). The functional unit chosen for this study was the release of 1 g of Ag ion from Ag NP-coated socks. The inventory data for all the unit processes has been collected in a quantitative aspect within the system boundary. The detailed information on LCI data of Ag NPs synthesis and its application on socks is shown in Table 1. The data for the Ag NP synthesis was obtained from the literature collected from science direct site. Following are the list of assumptions made for the present study,

- Raw materials extraction was not considered.
- Only processed materials were used for NP synthesis.

**Table 1** Inventory of Ag NPs synthesis

Synthesis route	AgNO <sub>3</sub> amount (g)	Reducing agent	Amount of reducing agent	Water (ml)	Power (kWh)	Amount of Ag NPs (g)	References
Green	0.107	<i>Allium cepa</i> extract	1 ml	100	0.033	1.26	[24]
Microwave	0.85	Citric acid NaOH Formaldehyde	0.96 g 0.6 g 2.25 g	100	0.011	5.184	[18]
Laser ablation	8.42	Sodium Hydrogen Diborane	0.056 g 0.004 g 0.03 g	4	0.0003	1.899	[27]

- Water required for washing (Glasswares) was taken from groundwater.
- For preparation of chemical solution, de-ionised water was used.
- Ag NP-coated socks were transported by means of truck which follows BS VI standards.
- Sources of energy was taken from Indian southern grid energy (non-renewable energy).
- 85% of water used in the process gets converted into wastewater.
- Effect of detergents was neglected.
- Socks material used were assumed to be purely cotton.
- Packaging of finished goods was not considered.
- Socks are washed twice a week, and the study is done for one year.
- Entire Ag NPs coated on socks were assumed to get disposed as silver ions (Fig. 1; Tables 2 and 3).

**LCI Assessment** The evaluation is as per the international standards ISO 14040 (ISO 14040, 2006) and ISO 14044 (ISO 14044, 2006). The life-cycle assessment is carried using SimaPro software and Ecoinvent V 1.03 database to calculate the overall life cycle impact using the ReCIPE2016 Midpoint (H) (world recipe) method. The potential impacts evaluated in the ReCIPE method were global warming (GW)

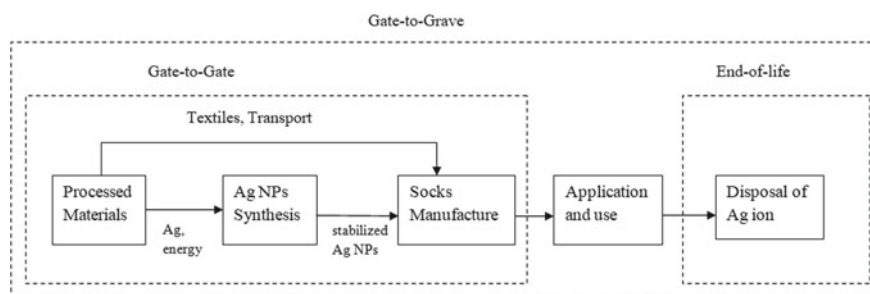


**Fig. 1** System boundary

**Table 2** Inventory of Ag NP-coated socks

Weight of a pair of socks (g)	Ag NPs(g) from different synthesis routes	Electricity (kWh)	Transport (tKm)
47	1.21	45	200

**Table 3** Inventory of silver ion release into technosphere

S. No.	Amount of Ag NP-coated socks (g)	Amount of silver ions (mg)	Transport (tKm)	Water (ml)	Nitric acid amount (kg)	Waste water (ml)
1	60.8	10.8	250	50,000	0.05	42,500

(kg CO<sub>2</sub> eq.), stratospheric ozone depletion (SOD) (kg of CFC-11 eq.), ionising radiation (IR) (kBq Co-60 eq.), ozone formation (OF) (kg NO<sub>x</sub> eq.), fine particulate matter formation (FPM) (kg PM<sub>2.5</sub> eq.), terrestrial acidification (TA) (kg SO<sub>2</sub> eq.), freshwater eutrophication (FE) (kg P eq.), marine eutrophication (ME) (kg N eq.), terrestrial ecotoxicity (TE) (kg 1,4 DCB), marine ecotoxicity (ME) (kg 1,4 DCB), human carcinogenic toxicity (HCT) (kg 1,4 DCB), human non-carcinogenic ecotoxicity (HNCT) (kg 1,4 DCB), land use (LU) (m<sup>2</sup>a crop eq.), mineral resource scarcity (MRS) (kg Cu eq.), fossil resource scarcity (FRS) (kg oil eq.), water consumption (WC) (m<sup>3</sup>).

## 4 Results and Discussion

### 4.1 Environmental Impacts

The environmental impacts of Ag NP synthesis using grid energy was analysed by means of the ReCiPe method and compared based on per g of NP, and the results are shown in Fig. 2. It is well understood that compared to other two synthesis routes, NP synthesised through laser ablation had greater impact on all the categories. This can be mainly due to the use of raw materials as well the power used from the national grid. The percentage share of Indian National Power Grid as on March 2019 is as

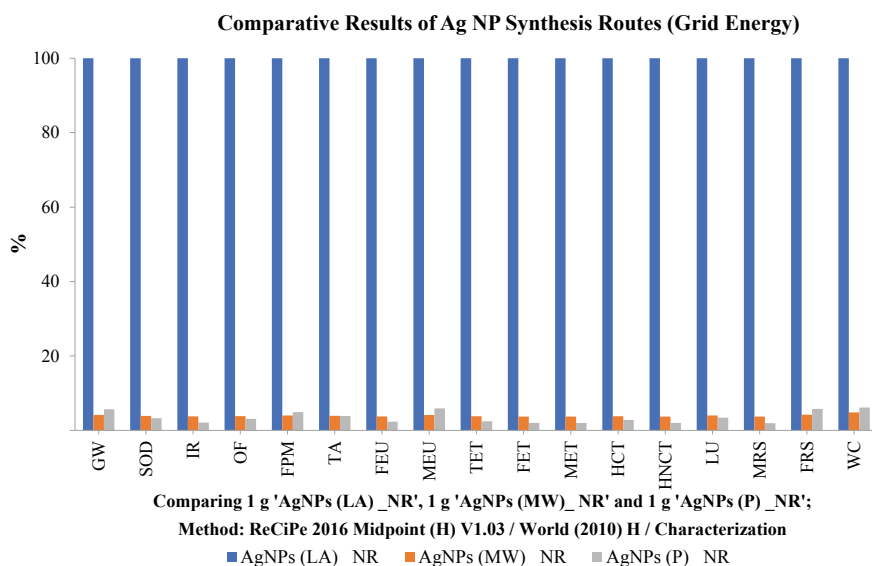


**Fig. 2** Comparative results of Ag NP synthesis routes (grid energy)

follows, total thermal (coal, lignite, gas and oil)—63.7%, hydro—13.0%, nuclear—1.9% and other renewable energy source (RES)—21.2%. From the analysis, it has been found that synthesis of NPs by using electricity from national grid itself has the most impact on all the environmental categories, and this was due to the fact that India depends largely on the fossil fuels. The difference in estimated GHG emission output is directly related to the usage of energy for heating purpose for the synthesis of NPs, which was similar to the previously published data [14, 16, 19, 28]. From Fig. 2, it can be seen that the green synthesis route has less impact than the other two routes. It can also be seen that about 25 times greater impact was found than chemical synthesis route when compared with physical method of NP synthesis. When compared between chemical and green synthesis, greater impact was observed for categories such as GW, FPM, MEU, FRS and WC. For all the other categories, impact was found to be greater due to chemical synthesis. In order to lower the footprint on the environment consequently, other alternate possibilities should be encouraged. The environmental analysis of alternative scenarios such as power from rooftop solar panel (renewable source) has been taken into consideration and the results are reported in Fig. 3.

In order to have the complete life cycle analysis of NPs, synthesised NPs were coated to a cotton sock, and its fate was studied while washing. The LCA results were found to be interesting when a pair of cotton socks was coated with Ag NPs. It was found, when compared to all three synthesis routes, laser ablation had greater impact and when normalised, higher effect was found on the following categories TET, FET, MET, HCT and HNCT (Fig. 4).

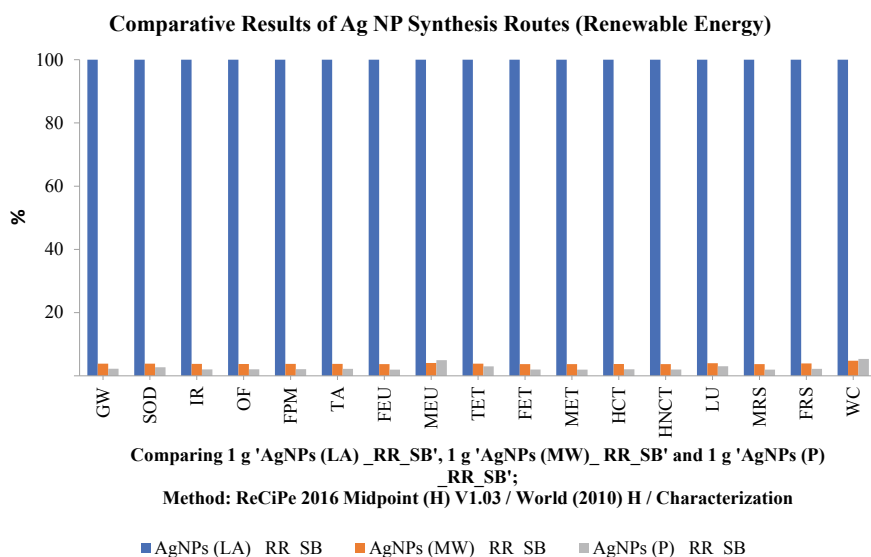


**Fig. 3** Comparative results of Ag NP synthesis routes (renewable energy)

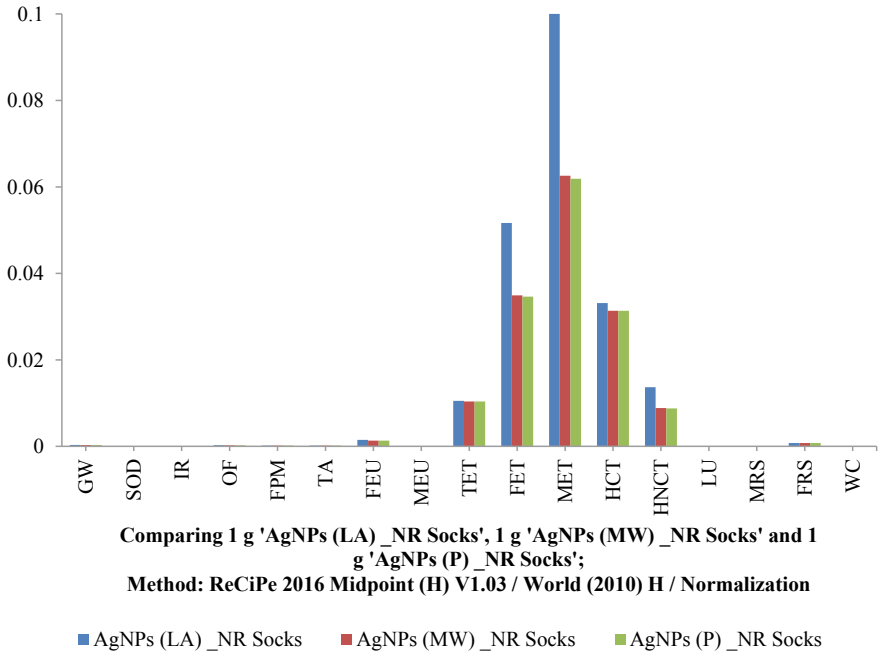


**Fig. 4** Comparative results of Ag NP-coated socks (grid energy)

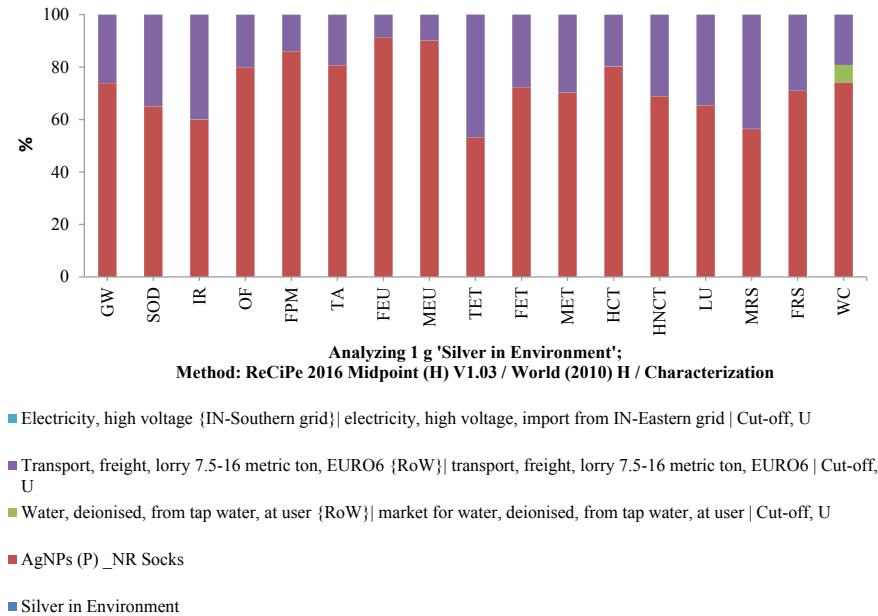


**Fig. 5** Silver presence in environment



From Fig. 5, it can be seen that about 90% contribution towards FEU and MEU is due to the production of Ag NP-coated socks, and nearly 50% of the contribution towards TET is caused by transport. From the Fig. 5, it can be well understood that the maximum impact was due to the production of Ag NP-coated socks compared to the energy and processed materials used.

## 5 Summary

In this study, synthesis of Ag NPs through different synthesis routes had impact in different ways during its different stages of life when their synthesis is carried out with three different routes. Here, physical synthesis method has shown major impact on environment compared to other two synthesis routes. This is due to the raw materials used for the NP synthesis and their production and transport. Pourzahedi and Eckelman [19] show comparative LCA of various synthesis routes, where synthesis of Ag NPs by flame spray pyrolysis has greater impact. This shows that impacts depend on the materials, methods, energy, etc. These results also show the sensitivity of the overall impacts of the method used for NP synthesis, again underlining the importance for product manufacturers and researchers of using synthesis-specific LCI data when conducting environmental assessments of nano-enabled products. The factors like energy, materials and transport used for synthesis coating, etc., are to be controlled or modified to reduce these impacts.

## 6 Conclusion

An attempt was made to understand the life-cycle assessment of Ag NPs and its associated products. When sufficient inventory data becomes available, the LCA study boundaries can still be stretched and can be extended to other NPs as well.

## References

1. Ashraf, A., Zafar, S., Zahid, K., Salahuddin Shah, M., Al-Ghanim, K. A., Al-Misned, F., et al. (2018). Synthesis, characterization, and antibacterial potential of silver nanoparticles synthesized from *Coriandrum sativum* L. *Journal of Infection and Public Health*. <https://doi.org/10.1016/j.jiph.2018.11.002>.
2. Fatimah, I. (2016). Green synthesis of silver nanoparticles using extract of *Parkia speciosa* Hassk Pods assisted by microwave irradiation. *Journal of Advanced Research*. <https://doi.org/10.1016/j.jare.2016.10.002>.
3. Keshari, A. K., Srivastava, R., Singh, P., Yadav, V. B., & Nath, G. (2018). Antioxidant and antibacterial activity of silver nanoparticles synthesized by *Cestrum nocturnum*. *Journal of Ayurveda and Integrative Medicine*, 1–8 (2018). <https://doi.org/10.1016/j.jaim.2017.11.003>.

4. Joseph, S., & Mathew, B. (2014). Microwave-assisted facile synthesis of silver nanoparticles in aqueous medium and investigation of their catalytic and antibacterial activities. *Journal of Molecular Liquids*, *197*, 346–352. <https://doi.org/10.1016/j.molliq.2014.06.008>.
5. Gnansounou, E., & Kenthorai Raman, J. (2016). Life cycle assessment of algae biodiesel and its co-products. *Applied Energy*, *161*, 300–308. <https://doi.org/10.1016/j.apenergy.2015.10.043>.
6. Bennion, E. P., Ginosar, D. M., Moses, J., Agblevor, F., & Quinn, J. C. (2015). Lifecycle assessment of microalgae to biofuel: Comparison of thermochemical processing pathways. *Applied Energy*, *154*, 1062–1071. <https://doi.org/10.1016/j.apenergy.2014.12.009>.
7. Babaizadeh, H., & Hassan, M. (2013). Life cycle assessment of nano-sized titanium dioxide coating on residential windows. *Construction and Building Materials*, *40*, 314–321. <https://doi.org/10.1016/j.conbuildmat.2012.09.083>.
8. Bobba, S., Deorsola, F. A., Blengini, G. A., & Fino, D. (2016). LCA of tungsten disulphide (WS<sub>2</sub>) nano-particles synthesis: State of art and from-cradle-to-gate LCA. *Journal of Cleaner Production*, *139*, 1478–1484. <https://doi.org/10.1016/j.jclepro.2016.07.091>.
9. Pourzahedi, L. (2016). Environmental impact assessment of nanoparticles and nano-enabled products using LCA frameworks. *ProQuest Dissertations & Theses*, *10105399*, 168.
10. Pourzahedi, L., & Eckelman, M. J. (2015). Environmental life cycle assessment of nanosilver-enabled bandages. *Environmental Science and Technology*, *49*, 361–368. <https://doi.org/10.1021/es504655y>.
11. Deorsola, F. A., Russo, N., Blengini, G. A., & Fino, D. (2012). Synthesis, characterization and environmental assessment of nanosized MoS<sub>2</sub> particles for lubricants applications. *Chemical Engineering Journal*, *195–196*, 1–6. <https://doi.org/10.1016/j.cej.2012.04.080>.
12. Manda, B. M. K., Worrell, E., & Patel, M. K. (2015). Prospective life cycle assessment of an antibacterial T-shirt and supporting business decisions to create value. *Resources, Conservation and Recycling*, *103*, 47–57. <https://doi.org/10.1016/j.resconrec.2015.07.010>.
13. Feijoo, S., González-García, S., Moldes-Diz, Y., Vazquez-Vazquez, C., Feijoo, G., & Moreira, M. T. (2017). Comparative life cycle assessment of different synthesis routes of magnetic nanoparticles. *Journal of Cleaner Production*, *143*, 528–538. <https://doi.org/10.1016/j.jclepro.2016.12.079>.
14. Slotte, M., & Zevenhoven, R. (2017). Energy requirements and life cycle assessment of production and product integration of silver, copper and zinc nanoparticles. *Journal of Cleaner Production*, *148*, 948–957. <https://doi.org/10.1016/j.jclepro.2017.01.083>.
15. Papadaki, D., Foteinis, S., Mhlongo, G. H., Nkosi, S. S., Motaung, D. E., Ray, S. S., et al. (2017). Life cycle assessment of facile microwave-assisted zinc oxide (ZnO) nanostructures. *Science of the Total Environment*, *586*, 566–575. <https://doi.org/10.1016/j.scitotenv.2017.02.019>.
16. Pini, M., Bondioli, F., Montecchi, R., Neri, P., & Ferrari, A. M. (2017). Environmental and human health assessment of life cycle of nano TiO<sub>2</sub> functionalized porcelain stoneware tile. *Science of the Total Environment*, *577*, 113–121. <https://doi.org/10.1016/j.scitotenv.2016.10.115>.
17. Sadhukhan, J., Joshi, N., Shemfe, M., & Lloyd, J. R. (2017). Life cycle assessment of sustainable raw material acquisition for functional magnetite bionanoparticle production. *Journal of Environmental Management*, *199*, 116–125. <https://doi.org/10.1016/j.jenvman.2017.05.048>.
18. Bafana, A., Kumar, S. V., Temizel-Sekeryan, S., Dahoumane, S. A., Haselbach, L., & Jeffries, C. S. (2018). Evaluating microwave-synthesized silver nanoparticles from silver nitrate with life cycle assessment techniques. *Science of the Total Environment*, *636*, 936–943. <https://doi.org/10.1016/j.scitotenv.2018.04.345>.
19. Pourzahedi, L., & Eckelman, M. J. (2015). Comparative life cycle assessment of silver nanoparticle synthesis routes. *Environmental Science: Nano*, *2*, 361–369. <https://doi.org/10.1039/c5en00075k>.

20. Anthony, K. J. P., Murugan, M., Jeyaraj, M., Rathinam, N. K., & Sangiliyandi, G. (2013). Synthesis of silver nanoparticles using pine mushroom extract: A potential antimicrobial agent against *E. coli* and *B. subtilis*. *Journal of Industrial and Engineering Chemistry*, 20, 2325–2331. <https://doi.org/10.1016/j.jiec.2013.10.008>.
21. Sreeram, K. J., Nidhin, M., & Nair, B. U. (2008). Microwave assisted template synthesis of silver nanoparticles. *Bulletin of Material Science*, 31, 937–942. <https://doi.org/10.1007/s12034-008-0149-3>.
22. Salieri, B., Turner, D. A., Nowack, B., & Hirschier, R. (2018). Life cycle assessment of manufactured nanomaterials: Where are we? *NanoImpact*, 10, 108–120. <https://doi.org/10.1016/j.impact.2017.12.003>.
23. Benn, T. M., & Westerhoff, P. (2008). Nanoparticle silver released into water from commercially available sock fabrics. *Environmental Science and Technology*, 42, 4133–4139. <https://doi.org/10.1021/es7032718>.
24. Gomaa, E. Z. (2017). Antimicrobial, antioxidant and antitumor activities of silver nanoparticles synthesized by *Allium cepa* extract: A green approach. *Journal of Genetic Engineering and Biotechnology*. <https://doi.org/10.1016/j.jgeb.2016.12.002>.
25. Govindarajan, M., AlQahtani, F. S., AlShebly, M. M., & Benelli, G. (2016). One-pot and eco-friendly synthesis of silver nanocrystals using *Adiantum raddianum*: Toxicity against mosquito vectors of medical and veterinary importance. *Journal of Applied Biomedicine*. <https://doi.org/10.1016/j.jab.2016.10.004>.
26. Mishra, A., Kaushik, N. K., Sardar, M., & Sahal, D. (2013). Evaluation of antiplasmodial activity of green synthesized silver nanoparticles. *Colloids Surfaces B Biointerfaces*, 111, 713–718. <https://doi.org/10.1016/j.colsurfb.2013.06.036>.
27. Muñetón, D., Santillán, J. M. J., Arce, V. B., Fernández, M. B., Raap, V., Muraca, D., et al. (2018). Materials characterization a simple and “green” technique to synthesize long-term stability colloidal Ag nanoparticles : Fs laser ablation in a biocompatible aqueous medium. *140*, 320–332 (2018). <https://doi.org/10.1016/j.matchar.2018.04.021>.
28. Wang, F., Deng, Y., & Yuan, C. (2019). Comparative life cycle assessment of silicon nanowire and silicon nanotube based lithium ion batteries for electric vehicles. *Procedia CIRP*, 80, 310–315. <https://doi.org/10.1016/J.PROCIR.2019.01.004>.

# Ground Response Analysis of Passighat Airport and Moga Bridge Sites



Pabba Vinod Kumar Goud, Boya Manikanta Reddy and Madhav Madhira

**Abstract** Ground response analysis plays a significant role in predicting the ground surface motions. The propagation of body waves from focus to ground surface traveling through various soil layers influences the input motions at the ground level. The present study focuses on ground response analysis for two sites—Passighat in Arunachal Pradesh and Shahkot–Moga bridge site in Punjab. Soil profile at the Passighat indicated the presence of silty clay to clay and sandy soil deposits, whereas the profile corresponding to the Shahkot–Moga site indicated the presence of only sandy soil. Shear wave velocities of soil profiles were evaluated from SPT  $N$  values based on available correlations. Peak bedrock accelerations of Bhuj, Chamoli, Kobe and Sikkim earthquake data were used for the analyses. One-dimensional equivalent linear analysis was performed for all the borelog data using DEEPSOIL software, and values of PGA, PSA and FAR as functions of frequency were derived. Amplification factors for Passighat and Shahkot–Moga sites vary from 1.5 to 2.5 and 1.9 to 4, respectively.

**Keywords** Ground response · DEEPSOIL · Peak ground acceleration · Peak spectral acceleration

## 1 Introduction

Structures at or below ground level exhibit cracks and distress due to their response during an earthquake. Study of lithology at the site plays a key role in understanding ground motions due to seismic wave travel across several soil layers among the focus

---

P. V. K. Goud (✉) · B. M. Reddy  
VNR Vignana Jyothi Institute of Engineering and Technology, Hyderabad, India  
e-mail: [vinodkumargoudp377@gmail.com](mailto:vinodkumargoudp377@gmail.com)

B. M. Reddy  
e-mail: [mani02.b@gmail.com](mailto:mani02.b@gmail.com)

M. Madhira  
AICTE-INAE, Hyderabad, India  
e-mail: [madhavmr@gmail.com](mailto:madhavmr@gmail.com)

© Springer Nature Singapore Pte Ltd. 2020  
S. Saride et al. (eds.), *Advances in Geotechnical and Transportation Engineering*,  
Lecture Notes in Civil Engineering 71,  
[https://doi.org/10.1007/978-981-15-3662-5\\_23](https://doi.org/10.1007/978-981-15-3662-5_23)

and the ground surface. The waves may get either amplified or de-amplified. In order to carry out ground response analysis, dynamic soil properties need to be evaluated for wave propagation. These dynamic properties of soil depend on the type, structure, density, stress condition and factors such as age, stress and strain history of the soils at the site. Evaluation of ground response also helps in predicting the hazards due to possible occurrence of liquefaction.

In the current study, DEEPSOIL v 7.0 [1] software was used for performing ground response analysis. DEEPSOIL is a one-dimensional equivalent linear analysis software advanced by the University of Illinois, Urbana, Champagne. The program has the capability to perform linear, equivalent linear (EQL) and nonlinear analyses depend on the input data, viz. thickness of soil strata, unit weight, shear wave velocity and shear strength of soils. The basic assumptions used for one-dimensional ground response analysis are

- (a) The soil strata is horizontal and spread out to infinity.
- (b) The ground surface is level.
- (c) The incident earthquake motions are spatially uniform, horizontally polarized shear waves and propagate vertically.

In the linear approach, transfer functions based on geotechnical conditions are used to evaluate ground response parameters (displacement, velocity, acceleration, shear stress and shear strain) for an input bedrock acceleration. The soil layers are assumed to have constant shear modulus and damping ratio.

The equivalent linear method is used to study the nonlinear response of soil with frequency domain analysis with the help of linear transform functions. The equivalent linear analysis approximates the nonlinear behavior of soil by using a flexible repetitive practice [2]. This repetitive practice is adopted to determine the well-matched shear modulus and damping ratio for a specific effective shear strain. In general, the effective shear strain is taken as 0.65 times the maximum shear strain acquired in a specific soil layer [2]. The strain time histories which are attained for each soil layer are used to estimate maximum shear strain which can be used in calculation of effective shear strain. The evaluated effective shear strain of soil layers is used for further estimation strain-compatible shear modulus and damping ratio based on the repetitive method. The method is repeated until a compatible shear modulus and damping ratio are obtained.

A set of shear modulus and damping ratio curves are available for different soils in DEEPSOIL software. In the absence of experimental data, these curves can be used. In case of sandy soils, based on the effective overburden stress curve, the proper modulus reduction curves can be attained. In case of clayey soils, the damping ratio and shear modulus curves can be attained based on the effective overburden stress and plasticity index of the soil.

Studies on ground response analysis are reported in the literature for India. Site-specific ground response analysis and seismic vulnerability assessment were carried out for Kolkata city [3]. It has been observed that maximum peak spectral acceleration varies from 0.78 to 0.95 g and the amplification factor 4.46–4.82. 1-D EQL ground response analysis was accomplished for Mumbai city [4] for four input motions

(0.103–0.834 g), for which the amplification factor ranges from 2.5 to 3.45. 1-D EQL ground response analysis for Guwahati city was accomplished using input motions of peak ground acceleration of 0.102–0.345 g, and the amplification factor obtained was in the range of 1.49–4.2 [5]. Earthquake responses of sites in the state of Haryana were accomplished using three input motions of PGA ranging from 0.117 to 0.360 g. The amplification factors were in the range of 0.702–2.331 [6]. Effect of local soil circumstances on ground response analysis for Kolkata city was performed using with SHAKE2000 software with five different input motions of PGA ranging from 0.106 to 0.834 g, and the amplification factors were in the range of 1.9–2.4 [7]. Ground response analysis and liquefaction vulnerability assessment were performed for Vishakhapatnam city using input motion of PGA 0.103 g, and the amplification factor ranged from 1.0 to 1.4 [8].

The objective of this study is to characterize the site with the help of large number of borehole data and to estimate the peak ground acceleration, amplification ratio, frequency and response spectra and amplification factors of different locations. The scope of the study is thus to carry out dynamic analysis for important structures in earthquake-prone areas. A performance-based design has to be adopted, which requires ground motion characteristics as well as local site response. Even to use the simplified approach to evaluate liquefaction, one requires the magnitude of earthquake, PGA, shear stresses and strains at site, which can be obtained by performing ground response analysis.

## 2 Methodology

The present study evaluates the ground responses for two sites. The data corresponding to 31 borelogs from Passighat in Arunachal Pradesh (Site A) and 14 borelogs from Shahkot–Moga bridge site in Punjab (Site B) were made available. As per IS-1893, Site A is situated in Seismic Zone V and Site B in Zone IV. Site A is located near the Brahmaputra River. The borelogs had profile data to a depth of 5 m, after which bedrock was encountered. Most of the soil layers at Site A correspond to sandy clay to silty soils and sandy deposits. Groundwater table existed at a depth of 1 m from the ground surface. Site B is located near Sutlej River. Borelogs extend to a depth of 30 m. Soils at this location are loose to medium dense sandy soil deposits up to a depth of 11 m below which are dense non-plastic sandy soil deposits. Groundwater table was observed at depths varying from 2 to 6 m from the ground surface.

Ground response analysis was accomplished using DEEPSOIL software for both the sites for which the data corresponding to shear wave velocities serve as a major input. In the nonexistence of shear wave velocity ( $V_s$ ) data, SPT  $N$  values were used to approximate shear wave velocity using the correlation given by Maheshwari et al. [9] as

$$V_s = 95.64N^{0.301} \quad (1)$$

In the present study, four strong motion earthquakes with PHA of 0.103 g, 0.248 g, 0.834 g and 0.18 g are used which correspond to the strong motions of 2001 Bhuj earthquake, 1999 Chamoli earthquake, 1995 Kobe earthquake and 2011 Sikkim earthquake, respectively. Kobe earthquake motion data were available in the built-in database of DEEPSOIL software [1], which were efficiently used by Phanikanth et al. [4] for EQL ground response analysis of Mumbai sites, while the data of Bhuj (2001), Sikkim (2011) and Chamoli (1999) were obtained from database available in [www.cosmos.org](http://www.cosmos.org) and [www.pesmos.org](http://www.pesmos.org), correspondingly. Passighat airport and Shahkot bridge sites are highly prone to earthquakes. Bhuj, Chamoli and Sikkim earthquake motions which happened in India are used as input motions for ground response analysis, with different peak ground accelerations as site-specific earthquake motions are unavailable for these sites. Kobe earthquake one of the largest earthquakes with a magnitude of  $M = 6.9$  and  $a_{max} = 0.8$  g that occurred recently is considered for the sake of comparison with the Indian earthquakes. Here, the bedrock was presumed to be elastic half space where shear wave velocity, density and damping ratio are given as input into software. The acceleration time histories of the four input motions are presented in Fig. 1 a–d. The soil profiles, SPT  $N$  and shear wave velocity with depth of one borelog from each site are shown in Figs. 2 (Passighat) and 3 (Shahkot-Moga) (Table 1).

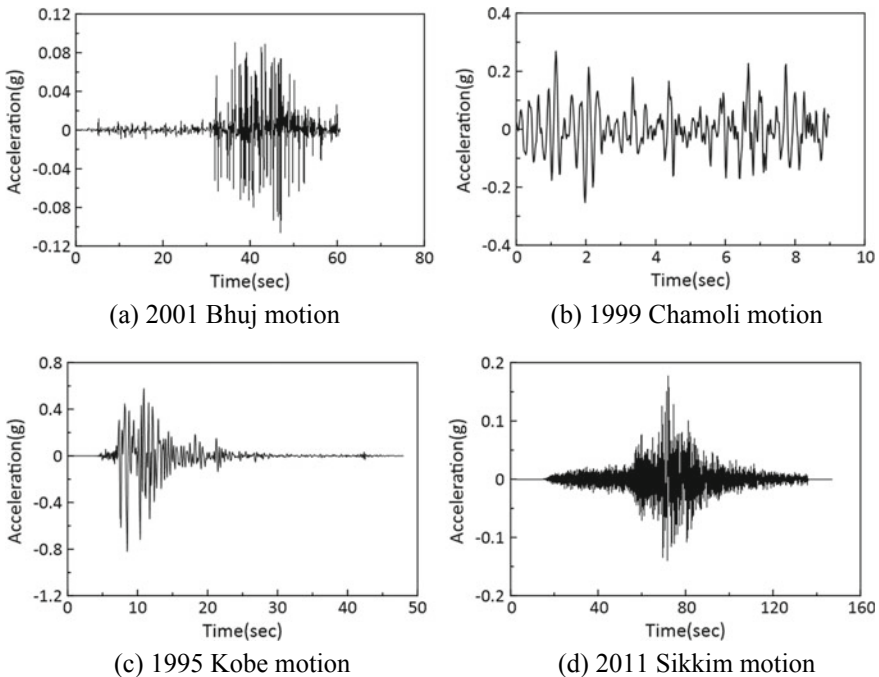


**Fig. 1** Acceleration time histories of four major earthquakes

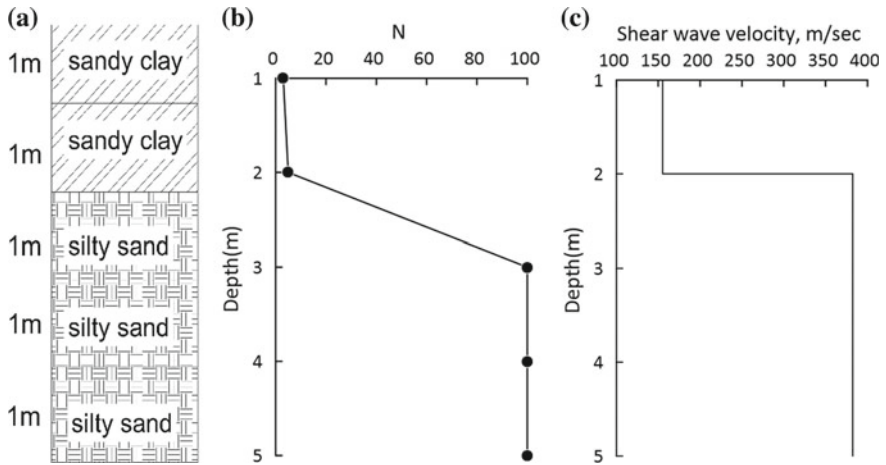


Fig. 2 a Soil profile at site PBH#1 Passigat, b SPT *N* with depth and c shear wave velocity

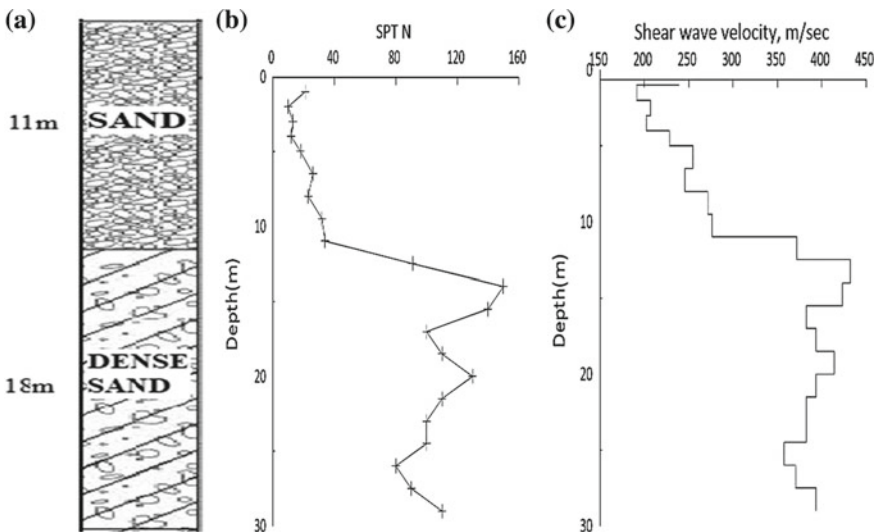


Fig. 3 a Soil profile site SBH#1 Shahkot–Moga, b SPT *N* with depth and c shear wave velocity with depth

### 3 Results

The soil layers at different sites are characterized by the dynamic properties with respective models. Modulus reduction curves based on Vucatic–Dobry model [10], for clayey soils and Seed–Idriss model [11] for sandy soils are used. Acceleration time histories at ground level for PBH#1 location for the four earthquakes are shown



**Table 1** Strong motion parameters for different earthquakes

Strong motion parameter	1995 Kobe	2001 Bhuj	1999 Chamoli	2011 Sikkim
Magnitude ( $M_w$ )	6.9	7.7	6.6	6.9
Station	KJMA	Ahmadabad	Almora	Gangtok
Site category	B	B	B	B
Distance from fault (km)	0.6	239	15	10
PGA (g)	0.834	0.103	0.272	0.18

Source: Strong motion parameters data collected from Centre for Engineering Strong Motion Data (CESMD). <https://strongmotioncenter.org/>, Accessed in the month March, 2019

in Fig. 4a–d. Figure 4a shows the maximum output surface acceleration for Bhuj earthquake motion (0.103 g) to be 0.178 g showing an amplification of 1.6. Figure 4b shows peak ground acceleration for PBH#1 site for Chamoli earthquake motion (0.248 g) as 0.316 g, and the amplification factor is 1.2. Figure 4c shows the PGA plot for PBH#1 site for Kobe motion (0.834 g) as 0.9 g, and the amplification factor is 1.0. Figure 4d shows the PGA plot for PBH#1 site for Sikkim earthquake motion (0.18 g) as 0.195 g, and the amplification factor is 1.0. The analysis is carried out for all the borelogs using these seismic input motions.

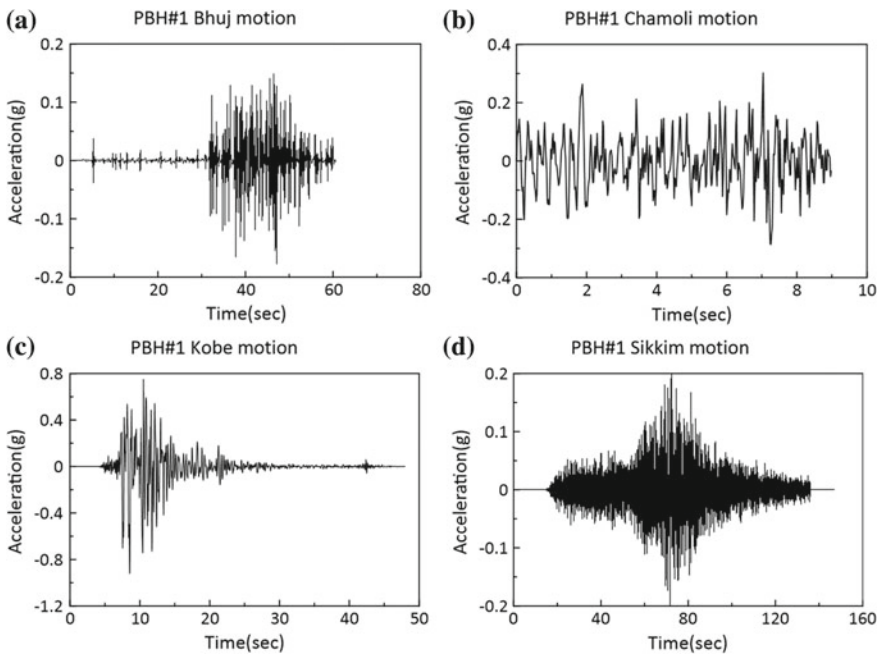


**Fig. 4** Acceleration time history at ground level for **a** Bhuj, **b** Chamoli, **c** Kobe and **d** Sikkim motions for PBH#1

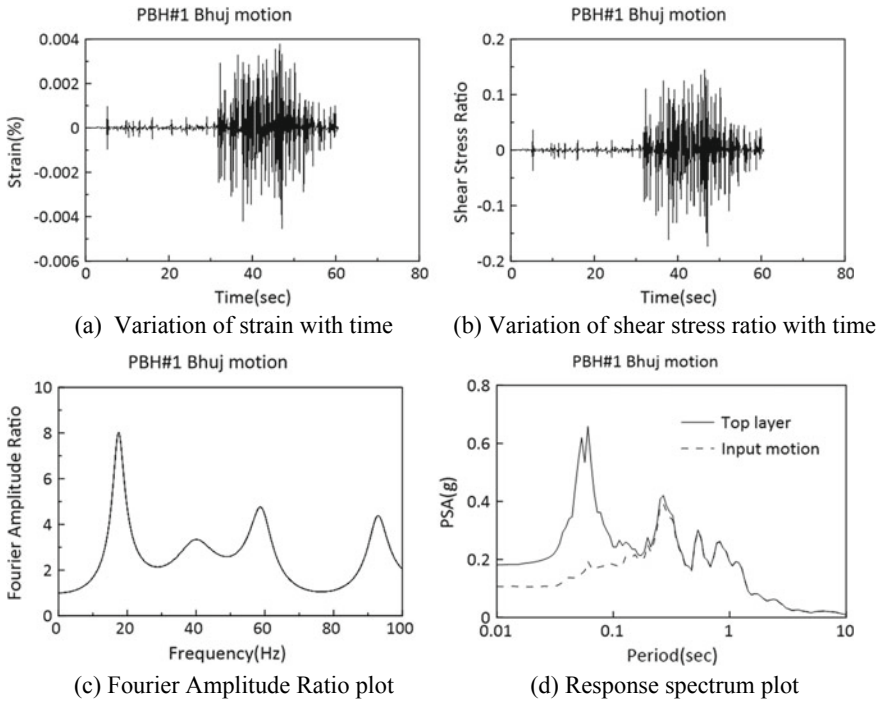


**Fig. 5** Variation of strain (%), shear stress ratio, Fourier amplitude ratio, response spectrum for 5% damping ratios for PBH#1 site

Figure 5a–d displays the fluctuation of % strain and shear stress ratio with time, frequency versus Fourier amplitude and 5% damped response spectral plots for PBH#1 site for the Bhuj input motion. It is observed that strain rate at this site is about 0.001% much smaller than 1%. Shear stress ratios are 0.145 for Bhuj input motion and 1.93 for Kobe motion. Fourier amplification ratio is 4.2 for Bhuj motion and 3.3 for Kobe motion. These results help in evaluating the natural frequencies of the subsoil. PSA is 0.658 g, which is 1.8 times more than the input motion.

Similarly, ground response analysis is accomplished for the Site B. Figure 6a–d shows the acceleration time history plots for SBH#1 for the four peak bedrock accelerations. The peak ground acceleration is 0.37 g for peak bedrock acceleration (PBRA) of 0.103 g (Bhuj motion, 2001), and the amplification factor is 3. For the PBRA of 0.248 g (Chamoli motion, 1999), the PGA is observed as 0.645 g, and the amplification factor is 2.5. For PBRA of 0.834 g (Kobe motion, 1995), the PGA is 0.73 g, and the amplification factor is 0.9. The PGA is observed as 0.40 g for the PBRA of 0.18 g, and the amplification factor is 2.2 for Sikkim earthquake motion.

Variation of % strain and shear stress ratio with time, frequency versus Fourier amplitude and response spectrum plots for SBH#1 site is shown in Fig. 7a–d for Bhuj input motion. It is observed that the strain is 0.002% which is less than 1%. The stress ratio (shear stress/effective stress) is observed as 0.26 for Bhuj motion (0.103 g) and

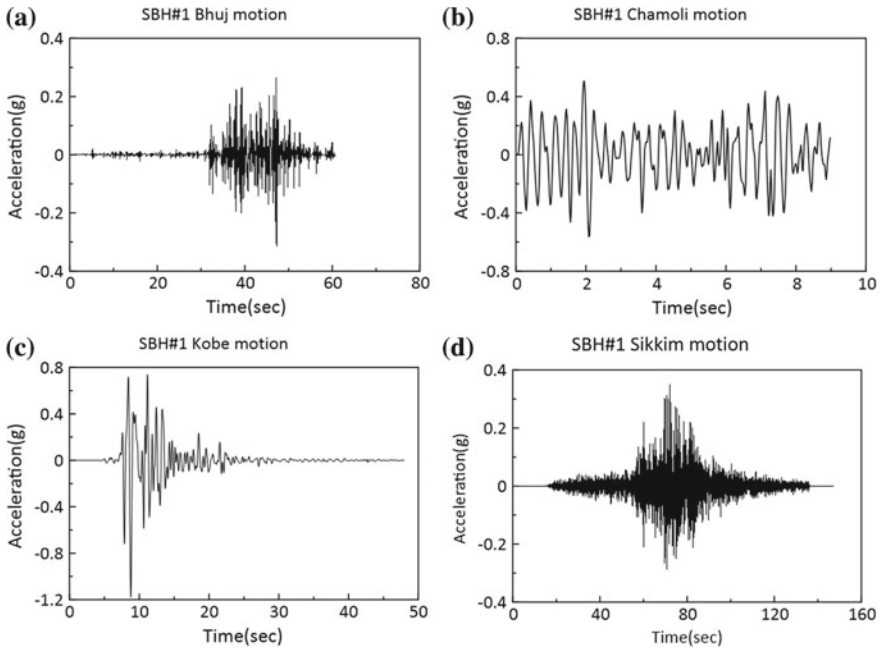


**Fig. 6** a Acceleration time history at ground level for a Bhuj, b Chamoli, c Kobe and d Sikkim motions for SBH#1

0.74 for Kobe motion (0.834 g). The Fourier amplitude ratio is observed as 4.1 for SBH#1 site, and the peak spectral acceleration is 1.33 g which is three times more than the input motion (0.103 g).

Amplification factors for the Passighat and Shahkot–Moga sites for the four input motions are presented in Fig. 8a, b, respectively. Figure 8a shows amplification factors for different borelogs for Passighat site for the four input motions. The minimum and maximum amplification factors of 1.12 and 1.96 are obtained at PBH#13 and PBH#11, respectively, for Bhuj motion. Similar values are 1.11 at PBH#2 and 2.29 at PBH#27 for Chamoli, 0.8 at PBH#9 and 1.53 at PBH#29 for Kobe and 1.0 at PBH#12 and 1.75 at PBH#24 for Sikkim motions. Chamoli motion gives the largest maximum amplification of 2.29.

Figure 8b shows similar amplification factors for different borelogs at Shahkot–Moga site for the four input motions. The minimum and maximum amplification factors of 1.76 at PBH#12 and 3.84 at PBH#5 for Bhuj, 1.8 at PBH#11 and 3.29 at PBH#7 for Chamoli, 1.41 at PBH#8 and 1.47 at PBH#11 for Kobe and 1.5 at PBH#11 and 2.15 at PBH#10 for Sikkim motions are obtained for Shahkot–Moga site. The largest maximum amplification for this site is as large as 3.84 because of the granular soils.

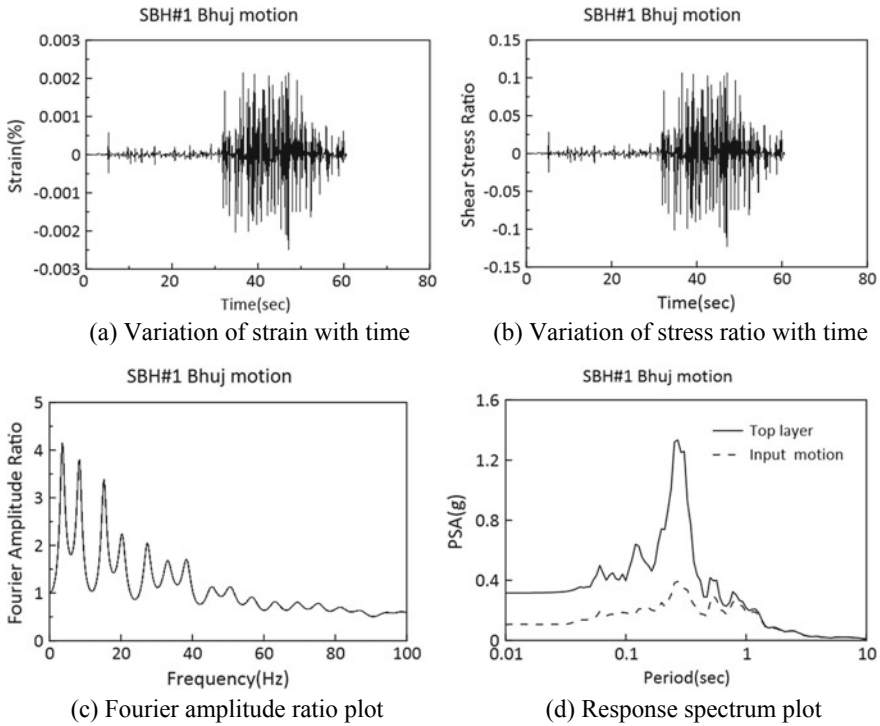
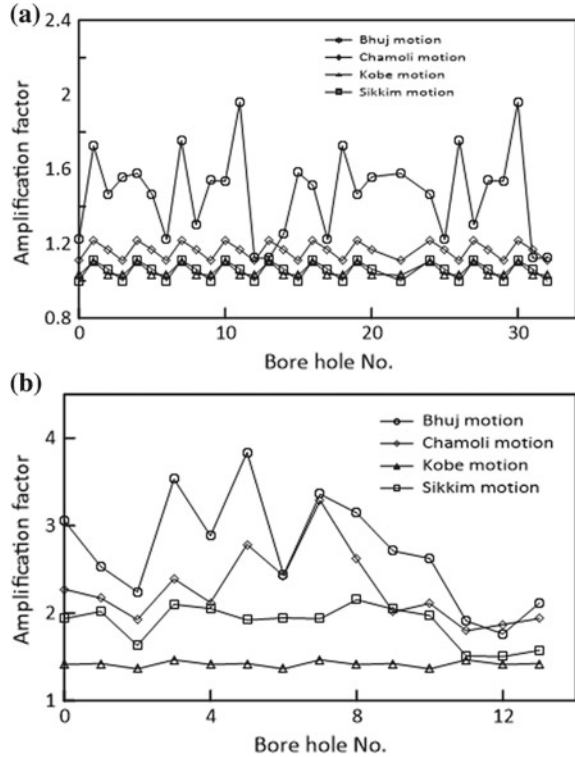


Fig. 7 Strain, stress ratio, Fourier amplitude ratio, response spectrum plots of SBH#1 site

### 4 Conclusions

One-dimensional equivalent linear ground response analysis is carried out using DEEPSOIL software for Passighat airport and Shahkot–Moga bridge sites. Based on the soil strata, Vucatic–Dobry and Seed–Idriss models are used to fit modulus reduction and damping curves. Amplification factors for Passighat site A are 0.8–2.5 and PGA values at the ground surface in the range of 0.2–1.2 g for different input earthquake motions. At Shahkot–Moga site, the peak ground acceleration (PGA) values are in the range of 0.2–1.3 g and the amplification factors 1.7–4 for the same input earthquake motions. The ground amplification is very high at the latter site compared to that at Passighat site. The acceleration and response spectra plots developed for these sites would be helpful in the design of structures.

**Fig. 8** Amplification factors for different borelogs at **a** site A and **b** site B



## References

1. Hashash, Y. M. A., Musgrove, M. I., Harmon, J. A., Ilhan, O., Groholski, D. R., Phillips, C. A., & Park, D. (2017). DEEPSOIL 7.0, user manual.
2. Kramer, S. (1996). *Geotechnical earthquake engineering*. New York: Prentice Hall.
3. Raju, G. L., Ramana, G. V., Rao, H. C., & Sitharam, T. G. (2004). Site specific ground response analysis. *Current Science*, 87(10), 1354–1362.
4. Phanikant, V. S., Choudhury, D., & Reddy, G. R. (2011). Equivalent-linear seismic ground response analysis of some typical sites in Mumbai. *Journal of Geotechnical and Geological Engineering*, 29(6), 1109–1126.
5. Kumar, S. S., Dey, A., & Krishna, A. M. (2018). Importance of site-specific dynamic soil properties -for seismic ground response studies: Ground response analysis. *International Journal of Geotechnical Earthquake Engineering*, 9(1), 78–96.
6. Puri, N., Jain, A., Mohanty, P., & Bhattacharya, S. (2018). Earthquake response analysis of sites in state of Haryana using DEEPSOIL software. *Procedia Computer Science*, 125(2018), 357–366.
7. Chatterjee, K., & Choudhury, D. (2018). Influence of local soil conditions for ground response in Kolkata city during earthquakes. *The National Academy of Sciences*, 88(4), 515–528.
8. Putti, S. P., & Satyam, N. (2018). Ground response analysis and liquefaction hazard assessment for Vishakhapatnam city. *Innovative Infrastructure Solutions*, 3(12), 1–14.
9. Maheswari, R. U., Boominathan, A., & Dodagoudar, G. R. (2010). Use of shear waves in statistical correlations of shear wave velocity and penetration resistance of Chennai soils. *Journal of Geotechnical and Geological Engineering*, 28(2), 119–137.

10. Vucatic, M., & Dobry, R. (1991). Effect of soil plasticity on cyclic response. *Journal of Geotechnical Engineering, ASCE, 117*(1), 89–107.
11. Seed, H. B., Wang, R. T., Idriss, I. M., & Tokimatsu, T. (1986). Moduli and damping factors for dynamic analysis of cohesionless soils. *Journal of Geotechnical Engineering, ASCE, 112*(11), 1016–1032.

# Use of Waste Polypropylene Plastic in Geotechnical Applications



Manisha Gajanan Ujankar and P. Hari Krishna

**Abstract** Presently, human mankind is facing the biggest problem in terms of saving the environment from solid waste disposal. The problem of pollution is becoming more critical because of the huge percentage of plastics in the municipal solid waste, especially one-time used plastics. Research is being carried out to explore the methods for the utilization of these plastic wastes for any of civil engineering applications. In geotechnical engineering, the well-established techniques of soil stabilization soil reinforcement are often used to improve the geotechnical materials through the addition of various binding and bonding agents. One of the most possible uses of these waste plastics is to use them in some of the geotechnical applications. In the present investigation, an effort is made to improve the strength of sandy soil by the inclusion of plastic to the sand and sandcrete. The plastic was added to sand in two forms such as fibers form and molten form. Fibers that used were of 12 mm length, whereas molten plastic was obtained by melting the plastic glasses obtained from NITW campus. Uniaxial compressive strength tests were conducted on the samples. In the present investigation, an effort is made to improve the strength of sandy soil. Experimental results have indicated that polypropylene plastic waste can be used in the stabilization of loose sandy soils.

**Keywords** Polypropylene · Sand–plastic · Sand–cement–plastic

## 1 Introduction

Over the last few years, solid waste disposal is increasing in a rapid manner especially in major cities. Due to the increased use of plastic for various applications, it has become a major threat to our environment especially with one-time used plastic products. The pollution caused due to these plastics especially in the dumping yards has reached alarming heights, and its adverse effects are increasing rapidly with time. Efforts have been made all over the world for the inclusion of this waste plastic

---

M. G. Ujankar (✉) · P. Hari Krishna  
NIT Warangal, Warangal, Telangana, India  
e-mail: [mgujankar1996@gmail.com](mailto:mgujankar1996@gmail.com)

© Springer Nature Singapore Pte Ltd. 2020  
S. Saride et al. (eds.), *Advances in Geotechnical and Transportation Engineering*,  
Lecture Notes in Civil Engineering 71,  
[https://doi.org/10.1007/978-981-15-3662-5\\_24](https://doi.org/10.1007/978-981-15-3662-5_24)

291

in civil engineering applications so as to resolve the problem of disposal of waste plastic. Possible areas of waste plastic utilization are pavement blocks or footpath blocks. The technique of casting pavement blocks is often used to make soil–cement blocks. Soil–cement blocks are generally used in the case of lightly loaded structural applications such as pavement or footpath blocks.

The compressive strength and tensile strength values of the cemented sand have been studied in the past by some investigators [1–3]. It has been observed both the compressive and tensile strengths increase with an increase in cement content and curing period.

In addition, studies on the engineering behavior of the sand reinforced with plastic waste have been carried out by some investigators [4]. The unconfined compressive strengths and the tensile strengths of cemented sand were significantly increased with the addition of fiber.

Nowadays, the use of waste plastic in bituminous road pavement is gaining a lot of research interest. Effect of waste plastic on the thermal stability of bitumen has been studied by a few researchers. Use of plastic as a modifier for bitumen serves the dual purpose of enhancing binder performance and providing a means for recycling the plastic and is a much better disposal solution compared to other options such as incineration and landfilling.

In this paper, an effort is made to study the utilization of waste polypropylene plastic in soil–cement. In this study, plastic was added to the samples in two different ways in molten form and in fibers form. Plastic in molten form was added to sand to make it work like binder, and plastic in fibers form was added to sand–cement to make it work like reinforcement.

Compressive strengths of the prepared soil–cement and soil–plastic samples were determined by uniaxial compressive strength test as per IS code of practice. Also, efforts were made to study the effects of adding plastic to soil–cement mix and to arrive at the optimum quantity of plastic to be used.

## 2 Methodology

In the present work, the compressive strength of soil samples of the sand–plastic mix, sand–cement mix, and sand–cement–plastic mix was determined using unconfined compressive strength test as per IS 2720.

The materials used are:

1. Sand
2. Cement
3. Plastic.

**Sand:** The sand used in the present study was obtained from the Godavari River near Eturnagaram, Warangal. The soil is classified as non-plastic uniform sand (SP) as per IS classification system. The properties of the sand are as follows:



Sr. No.	Property	Value
1	Specific gravity	2.57
2	Gravel Sand Fines	0 100% 0
3	Effective size	3.975 mm
4	Coefficient of uniformity	3.73
5	Coefficient of curvature	1.7
6	IS classification	SP
7	Cohesion value	0 kPa
8	Angle of internal friction	34°
9	Permeability	$2.429 \times 10^{-3}$ cm/s

Cement: The cement used in this ordinary Portland cement (43 grade) obtained from the structural engineering laboratory of NIT Warangal.

Plastic fibers: The plastic polypropylene was used in two forms such as fibers form and molten form. The fibers used were of 12 mm length, and the molten plastic was obtained by heating the shredded waste plastic glasses available in the NITW campus. Fibers of 12 mm length were chosen as per the literature. The specific gravity of the plastic used in this study is around 1.08. The properties of the plastic are as follows:

Sr. No.	Property	Value
1	Density	0.855 gm/cc
2	Melting point	160°
3	Chemical formula	C <sub>3</sub> H <sub>6</sub>

Soil samples of 38 mm diameter and 76 mm length were prepared for testing them in uniaxial compressive strength testing machine. To understand the influence of adding plastic to the sand, samples were prepared by mixing varying percentage of plastic (by weight of soil) to sand both in molten form and fibers form to the sand. For comparison purpose, soil–cement samples were also prepared by adding different percentages of cement (by weight of soil) to the sand. Further to investigate the influence of plastic on soil–cement mixes, samples were prepared by mixing varying percentages of plastic to the soil–cement mixes.

### Phase 1 Sand–plastic mix proportions

Sand–plastic mix samples were prepared by adding 10, 15, 20, 25, and 30% plastic by weight in molten form to the sand. The percentage of plastic to be added was decided based on trial and error method.

Initially, the sand was heated in a container on a gas stove until it gains a temperature of around 100 °C. Then the shredded polypropylene plastic waste was added to the heated sand. It was observed that plastic starts melting at 160 °C, and then the mixture was made homogenous by stirring continuously so as to get a uniform consistency of soil–plastic mix.

This mix was filled in uniaxial compressive strength test sampler and kept for cooling for a period of 4 h. Samples obtained were then tested in uniaxial compressive strength test to obtain the compressive strength value as per IS 2720 (Fig. 1).

### **Phase 2 Sand–cement mix proportions**

Soil–cement samples were prepared by adding 7.5, 10, 12.5, and 15% of cement by weight to the sand (Fig. 2). Samples were cured for a curing period of 7 days and then were tested in the uniaxial compressive strength testing machines as per IS code of practice.

### **Phase 3 Sand–cement–plastic mix proportions**

To investigate the effect of plastic in the soil–cement mix, different percentages of plastic waste were added to the soil–cement mix. Samples were prepared by adding 1, 2, 3, 4, 5, and 6% plastic by weight of sand in the form of polypropylene fibers to the sand–cement mix (Fig. 3). The percentage of plastic to be added was decided based on a literature review.

For this study, two percentages of 10 and 15% of cement by weight of sand were selected. Samples were compacted and kept open in the atmosphere for setting time of 10 h and then immersed in water for a period of 7 days. After 7 days, samples were removed and kept in sun drying for 1 day. Samples obtained were tested in uniaxial compressive strength test as per IS code of practice.

**Fig. 1** Sand–plastic sample



**Fig. 2** Soil–cement samples**Fig. 3** Plastic fibers in soil–cement sample

### 3 Results and Discussion

#### Phase-1

The unconfined compressive strength values of sand–plastic samples are furnished in Table 1.

**Table 1** Phase 1 sand–plastic mix proportions

Sr. No.	Plastic content (%)	Compressive strengths (MPa)
1	10	0.264
2	15	2.4
3	20	3.65
4	25	1.74
5	30	0.835

As can be seen from this table, the optimum percentage of plastic to be added to the sand is observed as 20% by weight of sand. At this mix proportion, compressive strength of 3.65 MPa could be achieved which is more than the required minimum compressive strength value of 3.5 MPa which is specified for use of bricks as per the code of building material testing. The brittle failure pattern observed is shown in Fig. 4.

### Phase-2

Table 2 provides the unconfined compressive strengths values of sand–cement mix proportions for 7 days curing periods.

As can be seen from the above table, the compressive strength of sand–cement mix samples is increasing with an increase in the cement content.

### Phase-3

Table 3 shows the unconfined compressive strength values of samples prepared by adding different percentages of plastics to the soil–cement mix for 7 days curing period.

**Fig. 4** Sand–plastic sample failure



**Table 2** Phase 2 soil–cement mix proportion

Sr. No.	Cement content (%)	Compressive strengths (MPa)
1	7.5	1.35
2	10	2.79
3	12.5	3.96
4	15	4.62

**Table 3** Phase 3 soil–cement and plastic mix proportions

Sr. No.	Curing period (days)	Cement content (%)	Plastic content (%)	Compressive strengths (MPa)
			1	3.18
			2	4.77
1	7	10	3	5.57
			4	5.96
			5	8.75
			6	4.77
			1	4.85
			2	5.29
2	7	15	3	5.73
			4	6.17
			5	9.26
			6	4.85

As can be observed from the above table, for both cement contents selected, the compressive strength of sand–cement–plastic mix is increasing with the increase in plastic content up to 5% by weight of sand. The maximum increase in the compressive strength value of sand–cement mix is found to be around 100–200% with the addition of plastics. This can be attributed to the reinforcing effect given by plastic fibers in the sand–cement mix before the failure of the sample. Even at the failure load, the samples could retain the shape of the sample without leading to shear failure. Only crushing of the particles at the outer periphery could be observed rather than complete shear or crushing failure as shown in Fig. 5.

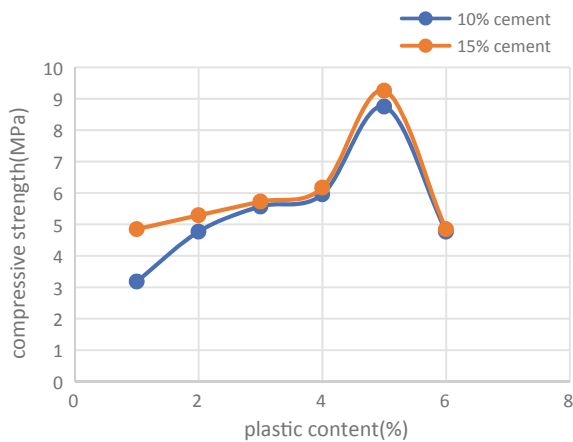
The variation of unconfined compressive strength values of sand–cement–plastic mix soil samples with plastic content is shown in Fig. 6.

As shown in the figure, the variation of UCS values with plastic content is almost similar for both percentages of cement used in the present investigation. As suggested by Bentur et al. [5], the increase in the strength because of the addition of fibers to sandcrete can be attributed to interfacial adhesion and mechanical anchoring as these are the two main factors affecting fiber–matrix interaction. According to Broda and Brachaczek [6], fibers of more length have relatively large contact surface to form a sufficient number of adhesive connections with the mortar components and to provide high friction forces during pulling out of the fibers from the matrix. For shorter fibers, the contact area is smaller leading to the lower number of adhesive connections and lower friction because of which only fibers of 12 mm length were used in this study. As presented by Jewell et al. [7], the cement–fiber interfacial bond results from the mechanical interlocking of cement hydration products with the fiber surface. Fractured specimens of fiber-reinforced concrete show that failure takes place primarily due to fiber pullout or debonding. Generally, fiber pullout, rather than rupture, confers a larger ductility to the FRC. Unlike plain concrete, a

**Fig. 5** Plastic in soil-cement sample failure



**Fig. 6** Comparison of compressive strength of plastic in soil-cement samples



fiber-reinforced concrete specimen does not break immediately after initiation of the first crack, thereby increasing the work of fracture or toughness.

#### 4 Conclusion

The following general conclusions may be drawn from the present study:

1. Usage of waste polypropylene plastic in sands could improve the strength and stability criterion of sand.

2. With the addition of plastics (in the molten form), cylindrical samples of sandy soil could be prepared for the unconfined compression tests.
3. The optimum percentage of plastics to be used for sandy soils is observed as 20% by weight of sandy soil.
4. With the addition of plastic to the sand, the maximum compressive strength of 3.65 MPa could be achieved which is more than the minimum required value of 3.5 MPa for the usage of bricks in building materials.
5. The compressive strength of sand–cement can be increased by 100–200% by adding an optimum plastic percentage of 5%.

Based on these experimental results obtained, it is observed that the polypropylene plastic waste could improve the unconfined compressive strength of sandy samples both with and without cement contents. Hence, this polypropylene plastic waste can be used in the stabilization of sandy soils used for some civil engineering applications like basement foundation, retaining walls, and pavement blocks further investigations on large scale are required before recommending this procedure in the actual field conditions.

## References

1. Fan, J., Wang, D., & Qian, D. (2018). Soil cement mixture properties and design considerations for reinforced excavation. *Journal of Rock Mechanics and Geotechnical Engineering*.
2. Ramana Murthy, V., Madhubala, K. V., & Raman Sastry, M. V. B. (1995). Soil cement mixes—A critical evaluation. *Indian Highways*.
3. Walker, P. J. (1995). *Strength, durability and shrinkage characteristics of cement stabilized soil blocks*. Elsevier Science Limited.
4. Consoli, N. C., Montardo, J. P., Prietto, P. D. M., & Savitri Pasa, G. (2002). Engineering behavior of sand reinforced with plastic waste. *Journal of Geotechnical and Geoenvironmental Engineering*, 128, No. 6, ©ASCE.
5. Bentur, A., Mindess, S., & Vondren, G. (1989). Bonding in polypropylene fibre reinforced concretes. *International Journal of Cement Composites and Lightweight Composites*, 11(3).
6. Broda, J., & Brachaczek, W. (2015). Influence of polypropylene fibre geometry on the mechanical properties of cement mortars. *Fibres and Textiles in Eastern Europe*, 23(2)(110), 123–129.
7. Jewell, R. B., Mahboub, K. C., Robl, T. L., & Bathke, A. C. (2015). Interfacial bond between reinforcing fibers and calcium sulfoaluminate cements: Fiber pullout characteristics. *ACI Materials Journal*.

# A Study on Influence of Organic Ligand on the Adsorption of Lead by Clayey Soil



Sudheerkumar Yantrapalli and P. Hari Krishna

**Abstract** This paper presents the feasibility study on utilization of locally available clayey soil as a compacted clay liner based on its contaminant adsorption capacity under the presence of organic chemical Ethylene Diamine Tetra-acetic Acid (EDTA) which is abundantly released into the environment. Lead ion was selected as a contaminant and its adsorption by the soil was assessed by conducting batch sorption experiments with lead solution, presence of organic chemical EDTA with varying pH and concentration of lead. From this study, it was observed that, with an increase in the concentration of lead (from 10 to 30 mg/L), percentage adsorption of lead by soil was observed to be decreased with increase in initial concentration and percentage of absorption was increased with increase in the pH of the solution. With the presence of EDTA at pH 7, the percentage adsorption of lead by the soil decreased due to the formation of  $PbEDTA^{2-}$  complex. This study shows that locally available clayey soil can be used as a compacted liner, where presence of EDTA is assured.

**Keywords** Clayey soil · Compacted clay liner · Lead · EDTA · Batch sorption · XRD

## 1 Introduction

Landfills play a significant role in waste management practices by accepting different types of wastes (i.e., hazardous and nonhazardous) and minimizing the contamination of surface and subsurface water bodies from the leachate generated by the wastes in it [9, 31, 43, 44]. Unplanned dumping of different types of wastes, like industrial, urban and agricultural, may cause extreme pollution to soil and ground water bodies due to the ingress of heavy metals into the environment (i.e., lead, nickel, cadmium, chromium) [1, 3, 14, 22]. To prevent such kind of ingress of pollutants into the

---

S. Yantrapalli (✉)

Civil Engineering Division, MITS Madanapalle, Madanapalle, India

e-mail: [sudheerkumary@mits.ac.in](mailto:sudheerkumary@mits.ac.in)

P. Hari Krishna

Civil Engineering Department, NIT Warangal, Warangal, India

© Springer Nature Singapore Pte Ltd. 2020

S. Saride et al. (eds.), *Advances in Geotechnical and Transportation Engineering*,

Lecture Notes in Civil Engineering 71,

[https://doi.org/10.1007/978-981-15-3662-5\\_25](https://doi.org/10.1007/978-981-15-3662-5_25)



**Table 1** Limiting values of soil to be used as a CCL [12]

Property	Limiting value
Gravel (%)	<30
Particle size (mm)	<25
Fines content (%)	>30
Liquid limit (%)	>20
Plasticity index (%)	>10 and $\leq 35$
Shrinkage limit (%)	>12
Cation exchange capacity (CEC) (meq/100 g)	10
Permeability (cm/s)	$\leq 1 \times 10^{-7}$

surrounding areas, it is necessary to construct a barrier (such as compacted clay liner) between the waste and the surrounding environment [2, 4, 43]. Construction of clay liners with commercially available clays (such as bentonite) may increase the overall cost of the landfill. In such circumstances, if the locally available soil meets the basic requirements to construct a hydraulic barrier as mentioned in Table 1, it can be used as a compacted clay liner [16].

Along with the abovementioned properties, attenuation or adsorption capacity (i.e., the ability of soil to adsorb the contaminant) also plays an important role in preventing the migration of contaminants into the surrounding environment [23, 30, 34]. Studies have shown that adsorption of heavy metals by the soil depends mainly on its physicochemical-mineralogical properties such as redox potential, surface charge, pH and moisture content [3, 19, 25, 28, 29].

However, the adsorption of heavy metals and their migration shows a markedly different behavior when organic contaminants (humic acid, citric acid, glutaric acid and phenolic compounds) are present in the soil. These organic substances form metal complexes by interacting with the heavy metals from the leachate which can get desorbed from the soil rather than getting adsorbed under changing pH conditions [2, 37]. Generally, the adsorption capacity of a soil is evaluated through sorption isotherm models such as linear, Freundlich and Langmuir [6, 13, 33, 34, 40, 41, 47].

A very common organic chemical that leads to heavy metal desorption from soil is Ethylene Diamine Tetra-acetic Acid (EDTA). More than half of the volume of EDTA is being discharged into the environment from detergents, soaps and textile industries [10, 32]. Though many studies are focused on the utilization of EDTA for the cleaning of heavy metals contaminated soils and sediments [38, 39]. On the other side, the presence of EDTA in excess causes severe health problems such as liver diseases, asthma, tuberculosis and kidney failure [32]. EDTA can also influence the mobility of heavy metals through the soil [8]. There is limited information available on the influence of EDTA on adsorption of heavy metals by the soil at different pH environment.

In this paper, studies were conducted to understand the adsorption of lead ions by the clayey soil in the presence of EDTA. Batch sorption tests were conducted for estimating the sorption parameters of clayey soil viz. distribution coefficient and

intensity of adsorption, by fitting the data into isotherm models. These parameters are used to predict the breakthrough time of heavy metals under the influence of organic chemicals.

## 2 Materials and Contaminant Solutions Used

Clayey soil (collected from Warangal city of Telangana state, India) was used for the present study. The physical properties, chemical composition and major minerals present in the selected soil are listed in Table 2.

The locally available soil is classified as SC soil and meets the basic requirements of being used as a compacted clay liner, as mentioned in Table 2. The major minerals present in the soil are montmorillonite, illite, quartz.

Notably, the CH soil was found to have a CEC value of 92 meq/100 g, which surpasses the recommended minimum CEC value of 10 meq/100 g for liner materials [27]. The mineralogical studies revealed that the clayey soil mainly consists of montmorillonite mineral which is a smectite group mineral. The presence of montmorillonite mineral results in the soil exhibiting high cation exchange capacity (CEC) [11] and low hydraulic conductivity. These favorable properties of smectite group minerals support the utilization of this soil as a compacted clay liner instead of bentonite.

**Table 2** Physical, chemical and mineralogical properties of clayey soil

Properties	Value
Sand (%)	30
Silt (%)	39
Clay (%)	31
Liquid limit (%)	61
Plastic limit (%)	21
Plasticity index (%)	40
Specific gravity	2.69
Classification	SC
Hydraulic conductivity $k$ (cm/s)	$5.05 \times 10^{-7}$
Maximum dry density (MDD) (g/cc)	1.75
Optimum moisture content (OMC) (%)	19.6
Free swell index (%)	90
CEC (meq/100 g)	92
pH	9.0

$k$ —Hydraulic conductivity;  $MDD$ —Maximum dry density;  $OMC$ —Optimum moisture content

## 2.1 Preparation of Contaminant Solution

Different concentrations of the contaminant solution containing lead were prepared by using analytical reagent grade lead nitrate salt ( $\text{Pb}(\text{NO}_3)_2$ ). Ethylene Diamine Tetra-acetic Acid (EDTA) was chosen as the organic chemical with a concentration of 50 mg/L. The volume of EDTA added was 5% v/v of that of the volume of lead solution to prepare Pb-EDTA mixture.

## 2.2 Experimental Investigation

A series of batch sorption tests were conducted on clayey soil (CH) to determine the adsorption efficiency of the soil for the lead metal ion. The cation exchange capacity tests were also conducted to know how the cation exchange capacity of clayey soil was influenced after getting contaminated with Pb and Pb-EDTA solution.

## 2.3 Batch Sorption Studies

Adsorption is the phenomenon by which ions in a solution move from liquid phase to the solid phase by means of surface attraction. In batch sorption studies, this phenomenon is initiated by allowing the soil particles to interact with the heavy metal solution. These heavy metal solutions were prepared with various initial concentrations such as 10, 15, 20, 25 and 30 mg/L from the nitrate salt of lead. Sample preparation involved mixing of selected quantity of clayey soil (5 g) with 100 mL of lead solution (liquid to solid ratio (L/S) 20) for different concentrations of contaminant solution in a conical flask [5]. Later, pH of the soil solution was adjusted with 0.1M NaOH or 0.1M  $\text{HNO}_3$ . In this experiment, a wide range of pH values (2, 4, 6 and 7) was used for each initial concentration because the general landfill leachate pH ranges from 4.5 to 9. Each Pb and Pb-EDTA mixture was prepared in triplet.

These prepared samples along with blank were placed in orbital shaker for 24 h. The samples were then removed and filtered immediately using a Whatman no. 42 filter paper. The filtered clear solution obtained was analyzed using ICP-OES (Inductively Coupled Plasma-Optical Emission Spectrophotometer for determining the concentration of heavy metal that persisted in the solution  $C_e$  (mg/L). Then  $Q_e$  (mg/g) corresponding to the lead ion adsorbed on the soil was found by using Eq. 1. Further, the distribution coefficient ( $k_d/k_f/k_L$ ) was computed by fitting the data into adsorption isotherm models such as linear (LR), Langmuir (LM) and Freundlich (FH) as represented by the Eqs. (2)–(4) [4, 34].

$$Q_e = (C_i - C_e) * \left( \frac{V}{M} \right) \quad (1)$$

$$Q_e = k_d * C_e \quad (2)$$

$$\frac{C_e}{Q_e} = \frac{1}{k_L Q_{\max}} + \frac{C_e}{Q_{\max}} \quad (3)$$

$$\log(Q_f) = \log(k_f) + \frac{1}{n} \log \quad (4)$$

$C_i$  = Initial concentration of heavy metals solution (mg/L);  $C_e$  = final equilibrium concentration;  $k_d$  = linear adsorption coefficient;  $k_f$  = Freundlich adsorption coefficient;  $M$  = mass of the soil;  $n$  = porosity of soil;  $1/n$  = Freundlich isotherm exponential;  $Q_e$  = amount of metal ions adsorption per unit weight of the adsorbents (mg/g);

$Q_{\max}$  = Maximum adsorption capacity (mg/g);

$V$  = Volume of the heavy metal Lig solution (L).

## 2.4 Cation Exchange Capacity (CEC) Studies

The CEC is the potential of a soil to exchange the cations present on its surface and it depends on the pH, the ionic strength of the pore solution and the presence of dissolved salts in the soil [17]. For determining the CEC of CH soil, the guidelines presented in Indian Standard [21] were followed. Approximately, 2 g of soil sample was mixed with 50 mL of 1N Sodium acetate solution ( $\text{CH}_3 \text{COONa}$ ) and incubated in a constant temperature water bath at 100 °C for 15 min with intermittent stirring. The sample was then centrifuged to separate the clear liquid from the soil. The clear liquid was discarded and the soil was collected to repeat the above procedure three times. The treated soil thus obtained at the end of the above procedure was then mixed with 50 mL of 1N calcium chloride solution ( $\text{CaCl}_2$ ) and then processed in the same manner as that of with sodium acetate ( $\text{CH}_3 \text{COONa}$ ). Finally,  $\text{CaCl}_2$  treated soil was again mixed with 50 mL of 1N ( $\text{CH}_3 \text{COONa}$ ) and the above procedure was repeated to obtain a clear supernatant liquid containing the exchanged  $\text{Ca}^{2+}$  ions. The unknown concentration of the  $\text{Ca}^{2+}$  ions in the clear liquid was found using ICP-OES, and subsequently, the CEC of soil was found by using Eq. 5. The CEC value is reported as meq/100 g of the soil. Each sample was tested three times and average value was reported.

$$\text{CEC (meq/100 g)} = \frac{\text{Cation Concentration} * 100 * \text{Vol. of Extract (mL)}}{\text{Equivalent weight of cation} \times 1000 \times \text{wt. of sample (g)}} \quad (5)$$

## 2.5 Mineralogical Characterization

The mineralogical characterization of CH soil contaminated with lead and lead-EDTA solution was carried out by using X-ray diffraction spectrometer (Philips, Eindhoven, the Netherlands), fitted with a graphite monochromatic and a Cu-K $\alpha$  radiation source. From the CH soil that interacted with lead and lead-EDTA solution, the clay fraction was separated and scanned from  $2\theta$  ( $\theta$  = Incidence angle of X-rays) ranging from  $8^\circ$  to  $70^\circ$ . The presence of minerals in the geomaterials was analyzed with the help of the International Center for Diffraction Data (ICDD) files.

## 3 Results and Discussions

### 3.1 Batch Sorption Studies

By adopting the experimental procedure described in experimental program, the observed variation of percentage adsorption of lead with varying pH and initial concentration of the solution is presented in Fig. 1.

It shows that for various initial concentrations of the lead solution, the lead adsorption efficiency of the soil is increasing with an increase in the pH of the soil solution. The lead adsorption efficiency variation pattern with the pH of the solution is similar for all the initial concentration values except for 10 mg/L. In the case of 10 mg/L concentration, there is a significant increase in the lead adsorption efficiency when

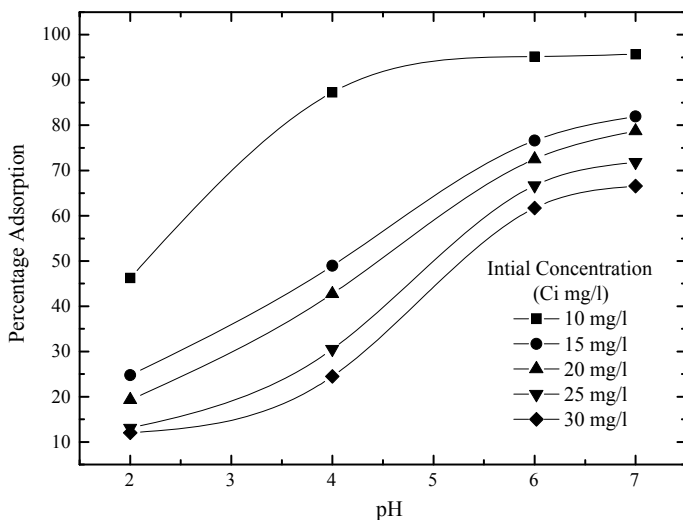


Fig. 1 Percentage adsorption of lead varying with pH

the pH is increased from 2 to 4, while this increase is insignificant from 4 to 7 [7]. For all other concentrations, the lead adsorption efficiency is constantly increasing from 2 to 7. For analyzing the results, the increase in the value of the lead adsorption efficiency for all the initial concentrations with an increase in pH of the solution from 2 to 7 is shown in Table 3.

It shows that the increase in the lead adsorption efficiency by the clay soil for all the initial concentration values at pH 2 and pH 7 of the solution is in the range of 52–60%. For any pH value, the lead adsorption efficiency is decreasing with an increase in the initial concentration of the lead in the solution. This can be attributed to the fact that there is a decrease in the number of sorption sites available on the soil with an increase in the number of metal ions in the heavy metal solution.

Figure 2 displays the variation of lead adsorption efficiency of the soil with increasing pH of the solution for various initial concentrations of lead solution mixed with EDTA. The adsorption efficiency pattern with the pH of the solution is similar for all

**Table 3** Increase in lead retention efficiency with change in pH 2–pH 7

Initial concentration ( $C_i$ ) mg/L	Lead adsorption (%) @ pH 2	Lead adsorption (%) @ pH 7	Increase in lead % adsorption
10	46.24	95.68	52.0
15	24.78	81.94	57.16
20	19.35	78.75	59.4
25	13.05	71.81	58.75
30	11	66.56	55.56

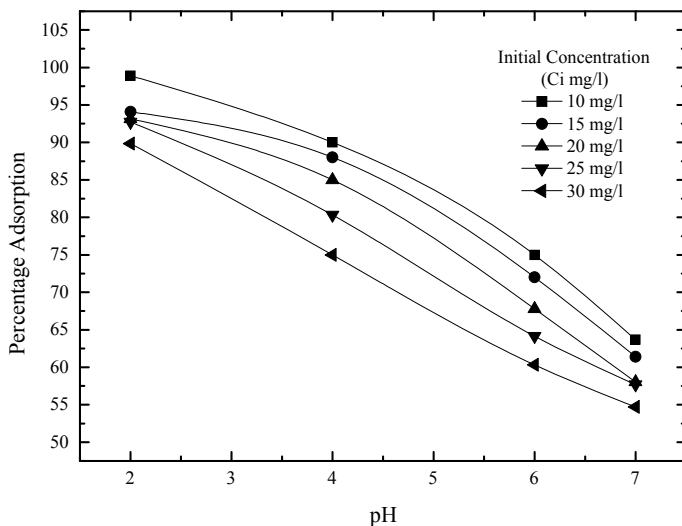


**Fig. 2** Influence of EDTA on lead adsorption efficiency with varying pH

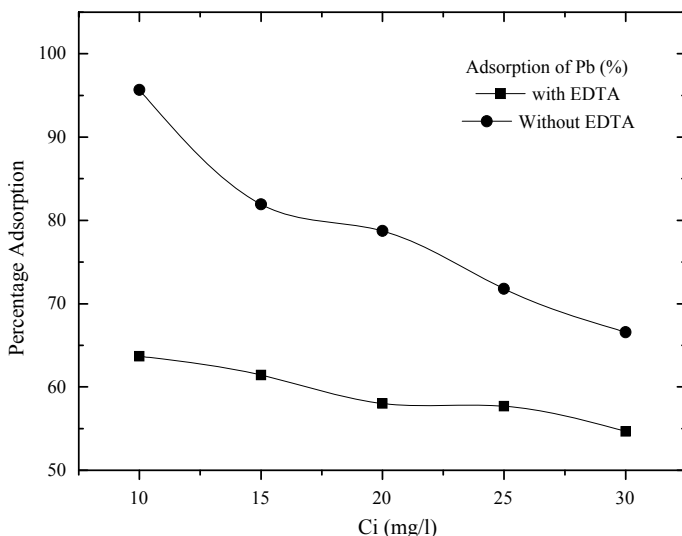


**Fig. 3** Influence of EDTA on lead adsorption efficiency by soil with varying concentration

the initial concentrations of the solution (Fig. 2). In contrast to the pattern observed without EDTA (as discussed in Fig. 1), there is a constant decrease in the adsorption efficiency with an increase in the pH of the solution. This can be attributed to the fact that, at higher pH values, the positive charge density due to  $H^+$  ions decreases and the negative charge on the soil surface accounts for increase in the adsorption of cationic contaminants like lead (Pb) [7, 18, 20, 24, 45]. However, when CH soil interacts with lead-EDTA solution, most of the lead ions form covalent bonds with EDTA [48] at higher pH values, thus leading to reduction in the metal uptake by the soil. At lower pH environment, the solubility of EDTA is very less. So, as the solubility of EDTA increases, the lead adsorption by soil gets decreased.

Figure 3 presents the variation of lead adsorption efficiency with different initial concentrations ( $C_i$  mg/L) of soil-lead solution with and without EDTA at a neutral pH environment (i.e., pH 7). The lead adsorption efficiency was observed to be smaller in the case of lead-EDTA solution when compared to without EDTA solution at all initial concentrations (Fig. 3). This is mainly because of the chelation effect of EDTA (i.e., EDTA forms bonds with the heavy metal ions by means of its six donor atoms, resulting in the formation of a heterogeneous ring structure). The stability of the resulting metal complex depends on the number of ring structures created with the central metal ion [35, 36], which prevents the precipitation of metal ions and hinders the adsorption of lead ions by clayey soils at high pH environment [15]. The average decrease in the lead adsorption by the clayey soil is 20% for all the concentrations of lead ions varying from 10 to 30 mg/L.

The adsorption characteristics of clayey soil can be understood by employing a parameter known as the distribution coefficient ( $k_d/k_f/k_L$ ) and this is computed by using isotherms which are modeled for both with and without EDTA conditions. The

**Table 4** Adsorption isotherm coefficient values for CH soil

Isotherm model	Parameters	Without EDTA	With EDTA
Linear	$k_d$ (L/kg)	19.70	9.1
	$Q_e$ (mg/kg)	90.70	10.9
	$R_2$	0.90	0.97
Freundlich	$k_f$ (L/g)	0.4707	0.2741
	$1/n$	2.75	1.374
	$R_2$	0.98	0.99
Langmuir	$Q_{max}$ (mg/g)	0.445	0.791
	$k_1$	0.7044	0.0525
	$R_2$	0.96	0.98

best-fit equations representing the variation of  $Q_e$  with respect to  $C_e$  are obtained are presented in Table 4.

The value of  $k_d$  obtained from the linear isotherm model without EDTA is more than two times of the value obtained with EDTA. Also, without EDTA, the  $Q_e$  value obtained is nearly ten times more than that of with EDTA condition and the value of  $k_f$  obtained from the Freundlich isotherm model for without EDTA condition is nearly twenty times greater than that of the value when EDTA is present in the solution. The value of exponent ( $1/n$ ) for without EDTA condition is nearly 40% lesser than that of the exponent value obtained with EDTA condition. Lower the value of the exponent, stronger is the affinity for adsorption. Hence, the presence of EDTA as a complexing agent decreases the potential of lead to get sorbed into the soil. The distribution coefficients of the contaminant are very less in the case of lead-EDTA solution as compared to that of lead solution alone as shown in Table 4. The diffusion of contaminant through compacted clay liner increases as distribution coefficient of contaminant decreases. This is because the diffusion of reactive solute is indirectly proportional to the distribution coefficient as shown in Eq. 6 [46].

$$D_s = \frac{D^*}{\left(1 + \frac{\gamma}{n}k_d\right)} \tag{6}$$

$D_s$  = Effective diffusion coefficient of reactive solute;  $D^*$  = effective diffusion coefficient;  $\gamma$  = density of soil (g/cc).

By considering the distribution coefficient of lead-EDTA solution, it is possible to design the most reliable barrier to prevent contamination of soil and groundwater bodies where there is a significant presence of EDTA.



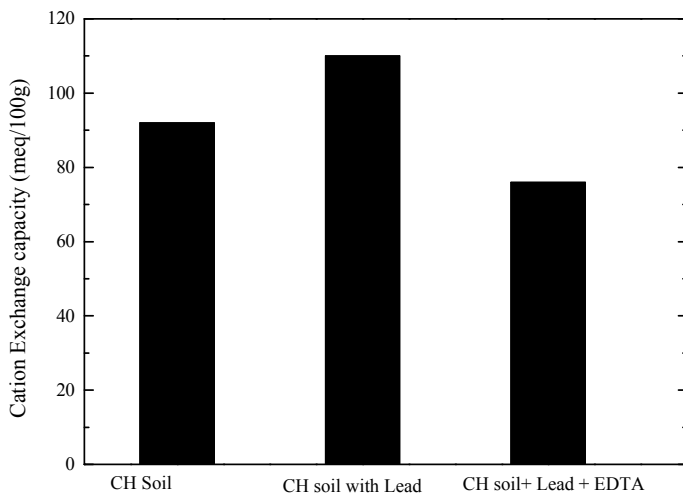


**Fig. 4** CEC of lead-contaminated CH soil with and without EDTA solution

### 3.2 CEC Studies

CEC tests were conducted on CH soil contaminated with and without EDTA mixed lead solution. The values obtained from CEC tests are shown in Fig. 4.

It can be observed from Fig. 4 that the CEC of contaminated CH soil is increasing by about 20% when compared to the uncontaminated CH soil. This is because most of the lead ions adsorbed on the surface of the CH soil are replaced with the sodium cation ions. The increase in the CEC of the soil when mixed with lead ions shows that most of the lead ions are attracted onto the surface of the soil. However, the CEC value of the soil when it interacts with EDTA solution is decreasing by about 30% as compared to the soil that interacted with lead solution alone. This is due to the organic chemical coatings which can drastically alter the surface charge, thus decreasing the CEC value of soil [26, 42]. Reduction in the value of CEC of soil contaminated with EDTA mixed lead solution signifies the reduction in the adsorption potential of CH soil. From these studies, the CEC of contaminated soil can be used as an index of contaminant adsorbed by the CH soil.

### 3.3 Mineralogical Studies

X-ray diffractogram (XRD) analysis is carried on soil interacted with lead ion, with and without organic chemical (EDTA) is presented in Fig. 5.

The intensity of reflections for a soil interacted with lead ion is higher when compared with uncontaminated soil. When soil interacted with lead ion under the

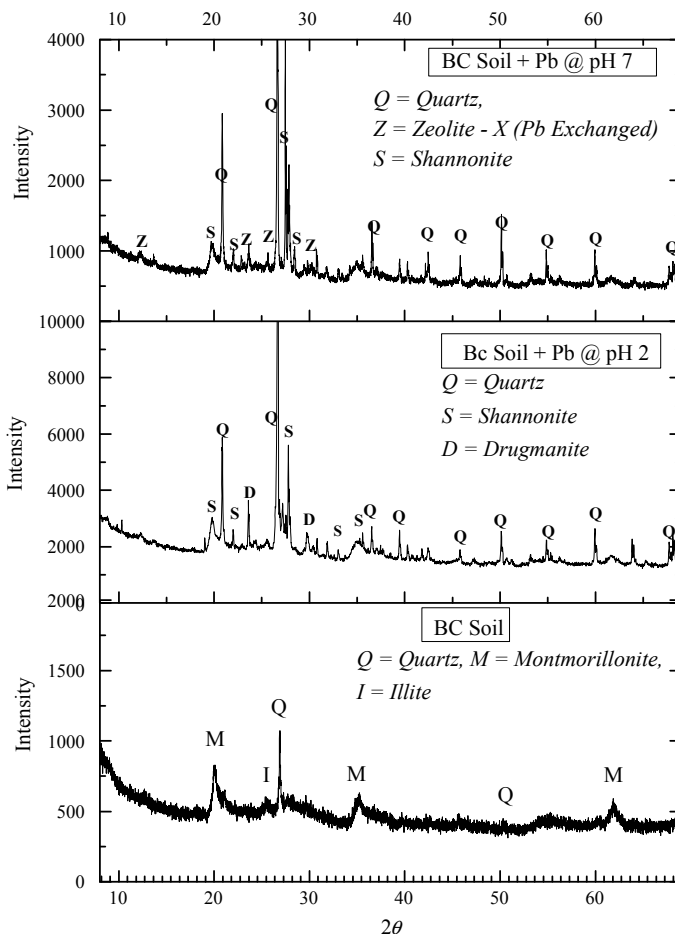


**Fig. 5** XRD analysis of soil contaminated with lead at pH 2, pH 7 and virgin soil

acidic environment (i.e., pH 2), the oxidized forms of lead ion (Shannonite and Drugmanite) were deposited on the surface of the soil, whereas at pH 7, the zeolite-X (Pb exchanged) was also deposited on the surface of the soil particle along with the oxidized form of lead ion. XRD patterns for CH soil contaminated with lead and lead-EDTA combined solution under acidic condition (pH 2) are shown in Fig. 6.

From this figure, it is observed that when the soil is contaminated with lead solution, under acidic condition (i.e., pH 2), the lead-based mineral zeolite-X (Pb exchanged) and Shannonite were deposited on the soil surface. Soil contaminated with lead and EDTA mixed lead solution at a neutral pH condition (i.e., pH 7) is presented in Fig. 7.

From this figure, it is also observed that when the soil interacted with lead-EDTA mixture under neutral condition (i.e., pH 7), lead-based minerals like Wickenburgite

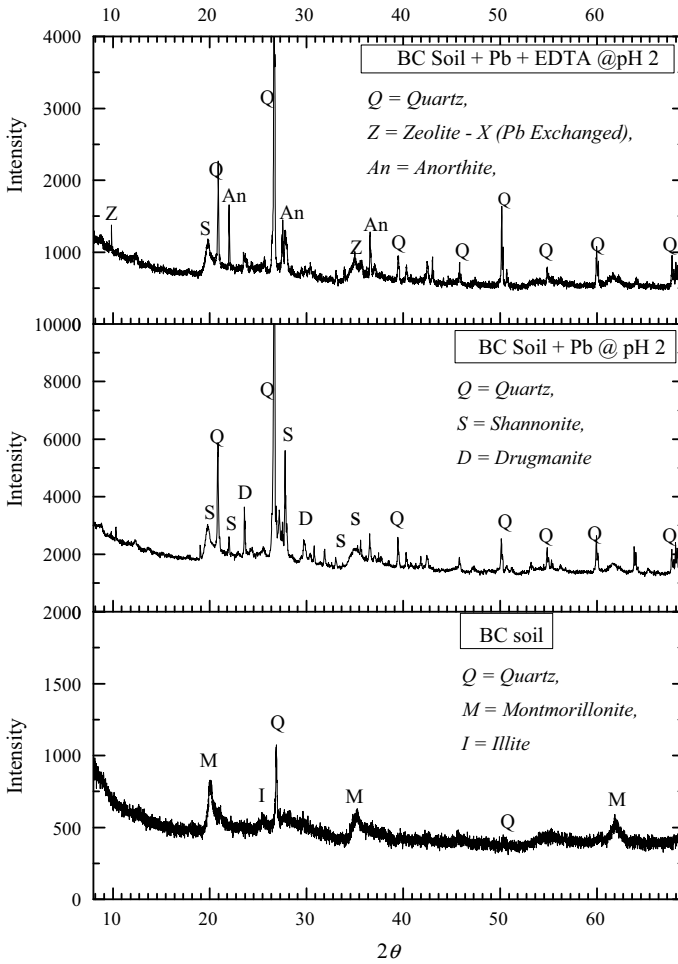


**Fig. 6** XRD analysis of soil contaminated with EDTA at pH 2

and Almosite were formed due to oxidation of the lead metal ion. On the whole, mineralogical studies show that lead metal ion is deposited on the surface of the earth in the form of oxides and it is confirmed that lead metal ions get adsorbed on the surface of the CH soil.

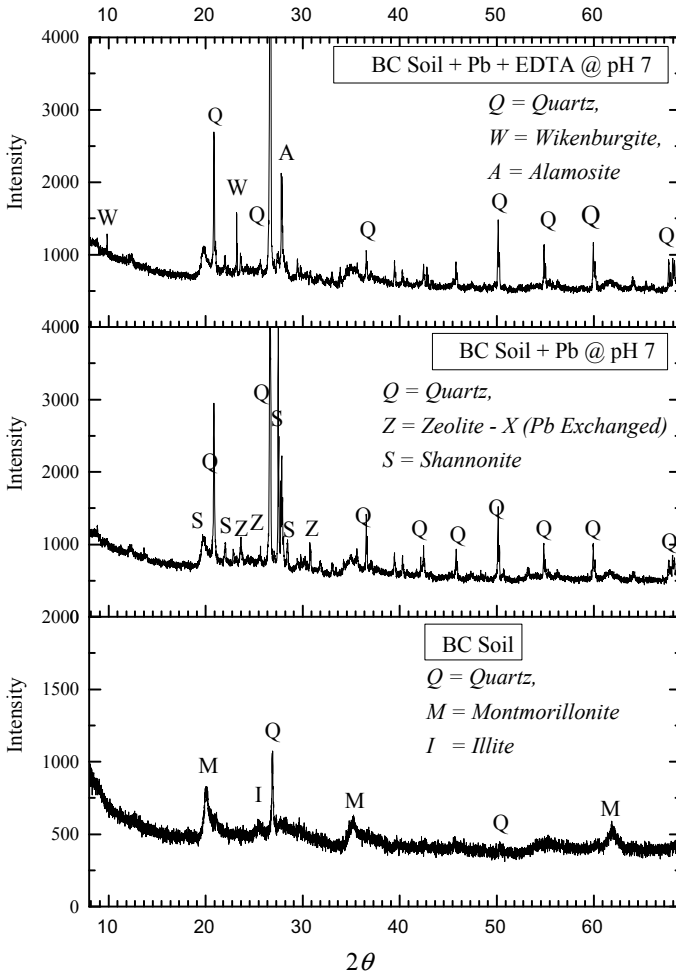


Fig. 7 XRD analysis lead-EDTA contaminated soil at pH 7

## 4 Conclusions

From the laboratory studies on the soil contaminated with a lead solution, with and without the presence of organic chemical (EDTA), the following conclusions are made:

1. The percentage adsorption of lead increases with increasing pH values. When EDTA is present in lead aqueous solution, the percentage of adsorption decreases with increase in pH.

2. The CEC of the contaminated soil confirmed that adsorption potential of soil increased after interaction with heavy metal solution, while the value decreased when the soil was mixed with EDTA—heavy metal solution.
3. When EDTA is present in the lead aqueous solution, the distribution coefficients were observed to decrease and it is an indication of the increase of heavy metal migration through the soil.
4. This study shows that CH soil adsorbed the heavy metal lead effectively, even in the presence of EDTA. Thus, it is suggested that the locally available CH soil is feasible as a compacted clay liner material where disposal of heavy metals along with EDTA is present.

## References

1. Abdel-Halim, S. H., Shehata, A. M. A., & El-Shahat, M. F. (2003). Removal of lead ions from industrial waste water by different types of natural materials. *Water Research*, 37(7), 1678–1683.
2. Abollino, O., Acceto, M., Malandrino, M., Sarzanini, C., & Mentasi, E. (2003). Adsorption of heavy metals on Na-montmorillonite. Effect of pH and organic substances. *Water Research*, 37(7), 1619–1627.
3. Appel, C., & Lena, M. (1997). Concentration, pH, and surface charge effects on cadmium and lead sorption in three tropical soils. *Journal of Environment*, 31, 581–589.
4. Arnepalli, D. N., Hanumantha Rao, B., & Shanthakumar, S. (2010). Determination of distribution coefficient of geomaterials and immobilizing agents. *Canadian Geotechnical Journal*, 47(10), 1139–1148.
5. ASTM D 4646. (2008). Standard test method for 24-h batch-type measurement of contaminant sorption by. Distribution, 3(Reapproved 2008): pp. 3–6.
6. Bellir, K., Bencheikh-Lehocine, M., Meniai, A., & Gherbi, N. (2005). Study of the adsorption of heavy metals by natural material used as liners in landfills. *Desalination*, 185(1–3), 111–119.
7. Bourliva, A., Michailidis, K., Sikalidis, C., Filippidis, A., & Betsiou, M. (2013). Lead removal from aqueous solutions by natural Greek bentonites. *Clay Minerals*, 48(5), 771–787.
8. Bowers, A. R., & Huang, C. P. (1986). Adsorption characteristics of metal-EDTA complexes onto hydrous oxides. *Journal of Colloid and Interface Science*, 110(2), 575–590.
9. Cerqueira, B., Covelo, E., Andrade, M., & Vega, F. A. (2011). Adsorption and mobility of copper and lead in soils as influenced by soil horizon properties. *Pedosphere*, 21(5), 603–614.
10. Chen, S. S., Hsu, H. D., Lin, Y. J., & Chin, P. Y. (2008). Removal of EDTA from low pH printed-circuit board wastewater in a fluidized zero valent Iron reactor. *Water Science and Technology*, 58(3), 661–667.
11. Cherian, C., & Arnepalli, D. N. (2015). A critical appraisal of the role of clay mineralogy in lime Stabilization. *International Journal of Geosynthetics and Ground Engineering*, 1, 8.
12. David, E. D. (1993). *Geotechnical practice for waste disposal* (p. 1993). London: Chapman and Hall.
13. Demirbas, A. (2008). Heavy metal adsorption onto agro-based waste materials: A review. *Journal of Hazardous Materials*, 157(2–3), 220–229.
14. Dube, A., Zbytniewski, R., Kowalkowski, T., Cukrowska, E., & Buszewski, B. (2001). Adsorption and migration of heavy metals in soil. *Polish Journal of Environmental Studies*, 10(1), 1–10.
15. Farrah, H., & Pickering, W. F. (1977). The sorption of lead and cadmium species by clay minerals. *Australian Journal of Chemistry*, 30(7), 1417–1422.

16. Ghosh, S., Mukherjee, S., Al-Hamdan, A. Z., & Reddy, K. R. (2013). Efficacy of fine-grained soil as landfill liner material for containment of chrome tannery sludge. *Geotechnical and Geological Engineering*, 31, 493–500.
17. Gillman, G. P. (1979). A proposed method for the measurement of exchange properties of highly weathered soils. *Australian Journal of Soil Research*, 17, 129–139.
18. Hamadneh, I., Abu-Zurayk, R., Abu-Irmaileh, B., Bozeya, A., & Al-Dujaili, A. H. (2015). Adsorption of Pb(II) on raw and organically modified Jordanian bentonite. *Clay Minerals*, 50(4), 485–496.
19. Hamdan, A. Z., & Reddy, K. R. (2006). Adsorption of heavy metals in glacial till soil. *Geotechnical and Geological Engineering*, 24, 1679–1693.
20. Ikhtiyarova, G. A., Ozcan, A. S., Gok, O., & Ozcan, A. (2012). Characterization of natural- and organo-bentonite by XRD, SEM, FTIR and thermal analysis techniques and its adsorption behaviour in aqueous solutions. *Clay Minerals*, 47, 31–44.
21. IS 2720-XXIV. (2010). Indian standard methods of test for soils (IS: 2720 (Part XXIV)—1976 (Reaffirmed 2010)). pp. 1–11.
22. Kumar, P. R., & Singh, D. N. (2005). A novel technique for monitoring contaminant transport through soils. *Environmental Monitoring and Assessment*, 109(1–3), 147–160.
23. dos Leticia, S. M., Fernanda, P. M., & Giulliana, M. (2014). Batch test methodology applied at a site contaminated with hexachlorocyclohexane. *Environmental Geotechnics*, 2(6), 371–381.
24. Mbaye, A., Diop, C. A. K., Miehé-Brendle, J., Senocg, F., & Maury, F. (2014). Characterization of natural and chemically modified kaolinite from Mako (Senegal) to remove lead from aqueous solutions. *Clay Minerals*, 49(4), 527–539.
25. Moghimi, A. H., Hamdan, J., Shamsuddin, J., Samsuri, A. W., & Abtahi, A. (2013). Physico-chemical properties and surface charge characteristics of arid soils in southeastern Iran. *Applied and Environmental Soil Science*.
26. Mohamed, A. M. O., & Antia, H. E. (1998). *Geoenvironmental engineering* (vol. 82). The Netherlands: Elsevier Science.
27. Mohamedzein, Y., Al-Rawas, A. A., Al-Aghbari Mohammad, Y., Ahmed, Q., & Abdul-Hamid, A.-R. (2005). Assessment of crushed shales for use as compacted landfill liners. *Engineering Geology*, 80(3–4), 271–281.
28. Naidu, R., Bolan, N. S., Kookana, R. S., & Tiller, K. G. (1994). Ionic-strength and pH effects on the adsorption of cadmium and the surface charge of soils. *European Journal of Soil Science*, 45, 419–429.
29. Naidu, R., Sumner, M., & Harter, R. (1998). Sorption of heavy metals in strongly weathered soils: An overview. *Environmental Geochemistry and Health*, 20, 5–9.
30. Nascentes, R., Christina, I., & Azevedo, D. D. (2011). Variation in hydraulic conductivity by the mobility of heavy metals in a compacted residual soil, hydraulic conductivity issues, determination and applications. In L. Enlango (Ed.). In Tech, ISBN: 978-953-307-288-3. Available from: <http://www.intechopen.com/books/hydraulic-conductivity-issues-determination-and-applications/variation-in-hydraulic-conductivity-by-the-mobility-of-heavy-metals-in-a-compacted-residual-soil>.
31. Nithya, K. M., Arnepalli, D. N., & Gandhi, S. R. (2016). Role of sorption characteristics of geomaterials on long term performance of landfill barrier role of sorption characteristics of geomaterials on long term performance of landfill barrier. *International Journal of Soft Computing and Engineering*, 2(5), 77–86.
32. Oviedo, C., & Rodríguez, J. (2003). EDTA: The chelating agent under environmental scrutiny. *Química Nova*, 26(6), 901–905.
33. Pandey, P. K., Sharma, S. K., & Sambi, S. S. (2010). Kinetics and equilibrium study of chromium adsorption on zeoliteNaX. 7(2), 395–404.
34. Pathak, P., Singh, D. N., Pandit, G. G., & Rakesh, R. R. (2016). Guidelines for quantification of geomaterial-contaminant interaction. *Journal of Hazardous, Toxic, and Radioactive Waste*, 20(1).
35. Peters, R. W. (1999). Chelant extraction of heavy metals from contaminated soils. *Journal of Hazardous Materials*, 66(1–2), 151–210.

36. Peters, R. W., & Shem, L. (1992). Adsorption/desorption characteristics of lead on various types of soil. *Environmental Progress and Sustainable Energy*, 11(3), 234–240.
37. Pickering, W. F. (1986). Metal ion speciation -soils and sediments. *Ore Geology Reviews*, 1, 83–146.
38. Reddy, K. R., Danda, S., Yukselen-Aksoy, Y., & Al-Hamdan, A. Z. (2010). Sequestration of heavy metals in soils from two polluted industrial sites: Implications for remediation. *Land Contamination and Reclamation*, 18(1), 13–23.
39. Reddy, K. R., Chaparro, C., & Saichek, R. E. (2003). Removal of mercury from clayey soils using electrokinetics. *Part A, Toxic/Hazardous Substances and Environmental Engineering, Journal of Environmental Science and Health*, 38(2), 307–338.
40. Reddy, K. R., Xie, T., & Dastgheibi, S. (2014). Nutrients removal from Urban stormwater by different filter materials. *Water, Air, and Soil Pollution* 225.
41. Robert, W. P., & Shem, L. (1992). Use of chelating agents for remediation of heavy metal contaminated soil. In *Environmental remediation, ACS symposium series* (vol. 509, pp. 70–84).
42. Robles, I., Serrano, T., Perez, J. J., Hernandez, G., Solis, S., Garcia, R., et al. (2014). Influence of EDTA on the electrochemical removal of mercury (II) in soil from san Joaquin, Queretaro, Mexico. *Journal of the Mexican Chemical Society*, 58(3), 332–338.
43. Rowe, R. K. (2012). Third Indian geotechnical society: Ferroco Terzaghi Oration design and construction of barrier systems to minimize environmental impacts due to municipal solid waste leachate and gas. *Indian Geotechnical Journal*, 42(4), 223–256.
44. Rowe, R. K. (2014). Performance of GCLS in liners for landfill and miming applications. *Environmental Geotechnics*, 1(1), 3–21.
45. Saada, A., Gaboriau, H., Cornu, S., Bardot, F., Villieras, F., & Croue, J. P. (2003). Adsorption of humic acid onto a kaolinitic clay studied by high-resolution argon adsorption volumetry. *Clay Minerals*, 38(4), 433–443.
46. Shackelford, C. D., & Daniel, D. E. (1991). Diffusion in saturated soil. I: Background. *Journal of Geotechnical Engineering*, 117(3), 467–484.
47. Viraraghavan, T., & Dronamraju, M. M. (1993). Removal of copper, nickel and zinc from wastewater by adsorption using peat. *Part A Environmental Science and Engineering, Journal of Environmental Science and Health*, 28(6), 1261–1276.
48. Vohra, M. S. (2010). Adsorption of lead, Ethylene Diamine Tetra acetic acid and Lead-Ethylene diamine tetra acetic acid complex onto granular activated carbon. *International Journal of Environmental Science and Technology*, 7(4), 687–696.

# Numerical Analysis of Single Track Railway Tunnel in a Stratified Soil Condition



Pallavi Badry, M. Venkateshwarlu, D. Sai Kiran Reddy, V. Prasad and M. Vishal Preetham

**Abstract** Tunnels are usually constructed in stratified geotechnical environments. However, most tunnel designers prefer to use a simplified model with the assumption of homogeneous soil conditions. This paper presents a numerical model of the semi-circular tunnel in a stratified soil condition. In this study, the tunnel displacement and stresses are studied at critical points say top and bottom of tunnel geometry for geostatic and induced load condition as the tunnel is considered to be served for the single railway track. The study extended for different stratified sequence. This infers that the stresses are more at the bottom of the tunnel and propagate higher towards the bottom of stratification. But the observation is not the same for the settlement, and the weak settlement zones are created in the soil and values vary for different stratified sequences.

**Keywords** Numerical model · Tunnel · Stratified soil · Tunnel in soil

## 1 Introduction and Literature Review

Tunnels are underground passages used for transportation, where the disturbances with surface life and traffic can be avoided economically than the bridges. Also, it is used to carry freights and passengers, water, sewage, etc. There are several types of tunnels depending upon usages and the material used for constructions including mine tunnel, public work tunnels and transport tunnels. The mine tunnels are used in the ore excavation while public work tunnels are used for sewage work, gas pipelines, etc. Transportation tunnel is used for subways, undisturbed footpaths and railways, etc. The tunnels are categorized as rock and soil tunnels depending upon the material in which the tunnel is constructed. The surrounding material undergoes a variety of stress conditions during phase constructional activities of the tunnel. The engineering properties and initial stress condition of surrounding soil/rock and tunnel material play an important role in numerical modelling. Several researchers

---

P. Badry (✉) · M. Venkateshwarlu · D. Sai Kiran Reddy · V. Prasad · M. Vishal Preetham  
Department of Civil Engineering, Vidya Jyothi Institute of Technology, Hyderabad, India  
e-mail: [pallavibadrim@vjit.ac.in](mailto:pallavibadrim@vjit.ac.in)

© Springer Nature Singapore Pte Ltd. 2020  
S. Saride et al. (eds.), *Advances in Geotechnical and Transportation Engineering*,  
Lecture Notes in Civil Engineering 71,  
[https://doi.org/10.1007/978-981-15-3662-5\\_26](https://doi.org/10.1007/978-981-15-3662-5_26)

317



tried to understand the stress–strain behaviour of the surrounding material and the construction material. The overview of the different studies carried out on tunnels is presented precisely in the following paragraph.

In the numerical analysis of the tunnel, the material behaviour needs to consider as a 3D nonlinear problem, and it exhibits the same behaviour right from the excavation phase. However, several studies reveal that the 2D behaviour also maps the actual scenario with considerable error [10, 13]; hence, the tunnels are still frequently analysed considering two-dimensional problem, simulating the excavation in sperate and considering those stresses as a prestress condition for the further analysis [14]. In some cases, the tunnel problem can also be modelled as an even one-dimensional approach with ground interaction, assuming the tunnel problem as axially symmetric, is still considered as an effective tool for preliminary support design, as shown by some recent research works [2]. Although, several attempts are made for different facets in the tunnel modelling system, the numerical models are increasingly being used to assess the stability of tunnels. Two-dimensional numerical approach is used by Zhang et al. and infers that the stability problem can be well addressed by this approach by addressing the case study on slurry shield tunnelling system [15]. Tunnels in sandy soil are analysed by Chen et al. using 3D discrete element method and instructed the detailed process for the phase stability of shallow shield tunnels in dry sand [4, 16]. Zhang et al. adopted 3D numerical simulations to analyse the effects of diameter to depth ratios and soil properties on tunnel face stability [15]. Deep long tunnel with single shield, double shield and universal double shield for excavation and several construction phases are analysed by several researchers to investigate the influence of different construction schemes on the tunnel heave [5, 6, 9]. The wedge limit equilibrium model has become very popular in calculating the stability of the tunnel face and [1, 8, 11] revealed the influence of steel pipe-reinforced multi-step grouting on tunnel face stability using the limit equilibrium method. Broere et al. carried out the analysis on the tunnel in saturated soil and worked out the magnitude of the support pressure using a time-dependent groundwater flow water model and the limit equilibrium wedge model [3]. Subsequently, considering the failure zone theory, the similar attempt was made to analyse the tunnel and studied that the magnitude of failure propagates as per the pressure line mentioned in the failure theory [10]. Several researchers [7, 12] derived the limit support pressure for tunnel face failure by assuming that the failure zone is a different shape.

In this study, the tunnel in the stratified soil is considered. The study is aimed at the realistic condition of the soil, i.e. heterogeneity in soil domain. The tunnel is considered to be constructed in the soil, which has four different stratifications, and stresses and displacement are studied at several points surrounding the tunnel.

## 2 Methodology

The finite element model of the tunnel with mentioned geometry (Fig. 1) is developed using the Tunnel GeoStudio programme. The different sequence of stratification is

**Fig. 1** Geometry of tunnel under consideration

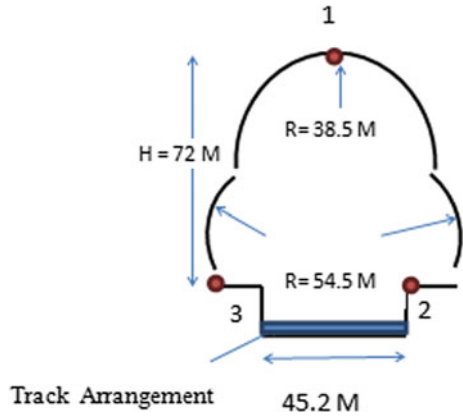


**Table 1** Engineering properties of soil for study

Soil/rock	Symbol	Profile (m)	$\gamma$ (kN/m <sup>3</sup> )	C (kPa)	PHI (°)	$\eta_c$	$E_{ode}$ (mPa)
Silty sand	<b>A</b>	0–3	19.5	10	29	0.3	10
Silty gravel	<b>B</b>	3–5	19.5	8	33	0.3	70
Weathered slate	<b>C</b>	5–10	24	30	29	0.33	45
Slate	<b>D</b>	Over 10	26	250	38	0.25	350
Bedrock	<b>E</b>	–	24	63	29	0.33	45

Bold signifies the layer name in a soil stratification

considered including the altering sequence of soil layers for each case (Table 2). The engineering properties of each layer are detailed in Table 1. The deviation of stresses and displacement at different points of the tunnel is studied for different cases, and the best stratification sequence is suggested for tunnel construction.

The numerical model is developed by assigning the soil and concrete properties to the system (Fig. 2).

In the following model, the stratification sequence is altered as per given in Table 2. And for each case, the stresses and the displacement of tunnel critical points are studied. In the following image, 1 stands for letter A followed accordingly till 4, i.e. D (Fig. 3).

### 3 Result and Discussion

The FEM model of the tunnel with the considered geometry model is analysed for static loading conditions, and the stresses and displacement are studied for the

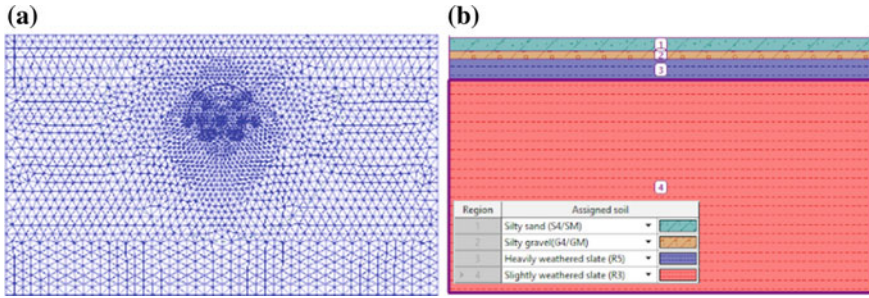


**Fig. 2** FEM model of the tunnel with soil stratification

**Table 2** Casewise sequence of stratification

Model cases	Sequence of stratification
Case-1 (C1)	A–B–C–D–E
Case-2 (C2)	D–A–B–C–E
Case-3 (C3)	C–E–A–B–E
Case-4 (C4)	B–C–D–A–E

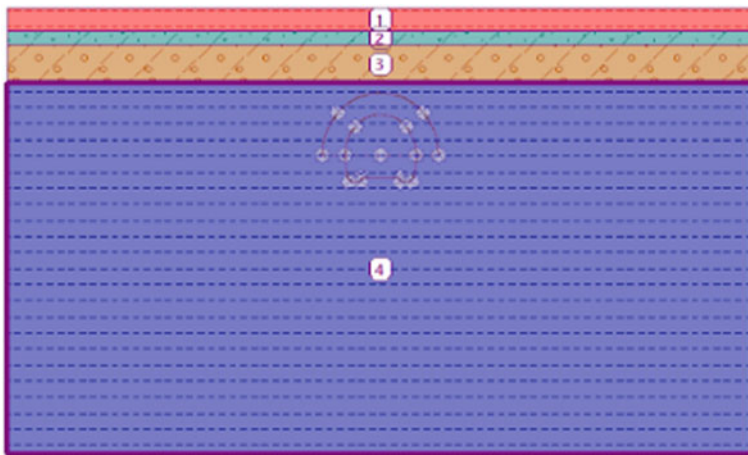


**Fig. 3** Stratification arrangement considered in numerical models

different points, including 1 (P1), 2 (P2) and 3(P3) as per shown in Fig. 1. The typical FEM tunnel model for case-1 is shown in Fig. 4.

The stresses and displacement under static load and equivalent dynamic vibration are studied. The stress counters are studied for the critical load case. Figure 5 shows the stress distribution contours for the loads. The stress at the top and subsequent lays is the combination of geostatic and induced stresses. At the top of the tunnel (at crown level) its showing stresses magnitude about 150 mPa and it increases tremendously

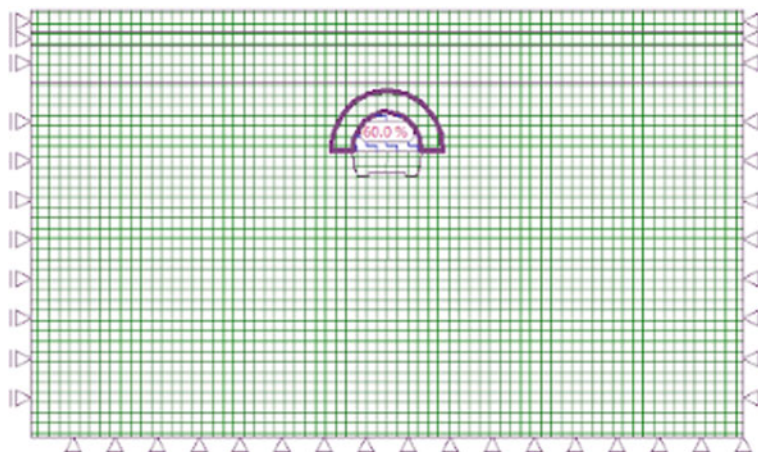


Fig. 4 Typical FEM model for tunnel within heterogenous soil condition

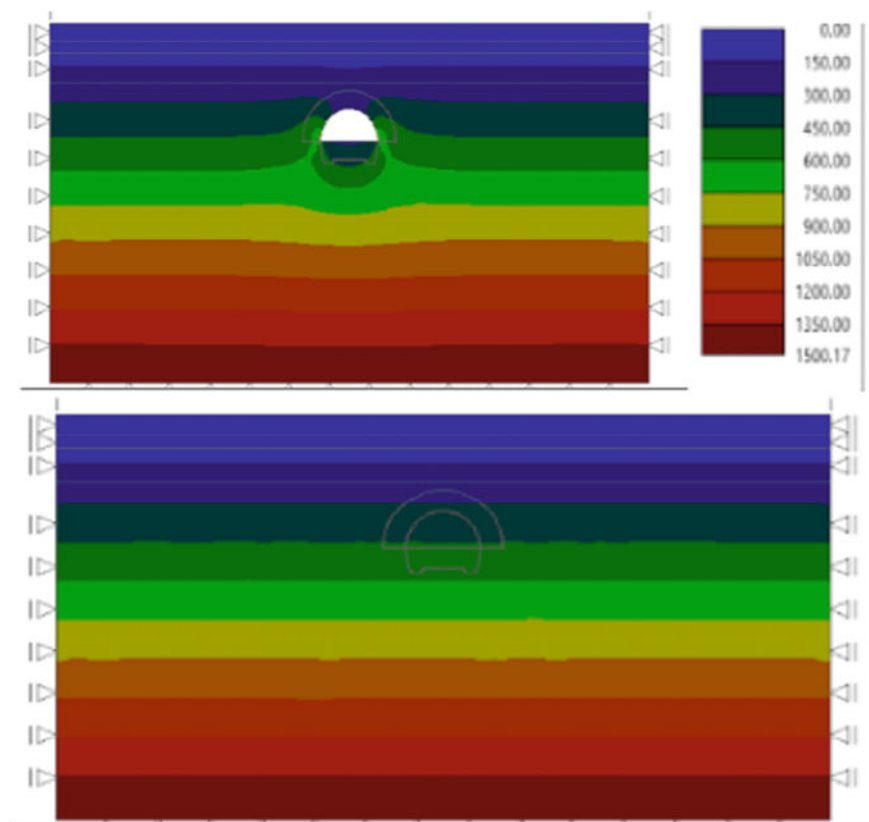


Fig. 5 Static stress condition for tunnel in stratified soil for Case-1

at the lower subsequent layers to the 600 mPa. Also naturally as we go away from the ground, the geostatic stresses will be taking dominating effect.

Also, it is very important to understand the displacement demand of the construction for the critical load condition. The typical settlement contours are shown in Fig. 6 for Case-1. It has been observed that the 1.8 cm is at the bottom, which is considered as the vertical settlement due to geostatic loading condition. Also, it is very interesting to observe that the high settlement zone is created immediately below the ground surface and the top of the tunnel where it is needed to take care to prevent the settlement (Fig. 6).

Also, the stresses and settlements studied for a critical loading condition for different stratification sequences are mentioned in Table 2 at different points, including P1 (Crown Point), P2 and P3 (left and right bottom of tunnel) (Fig. 7).

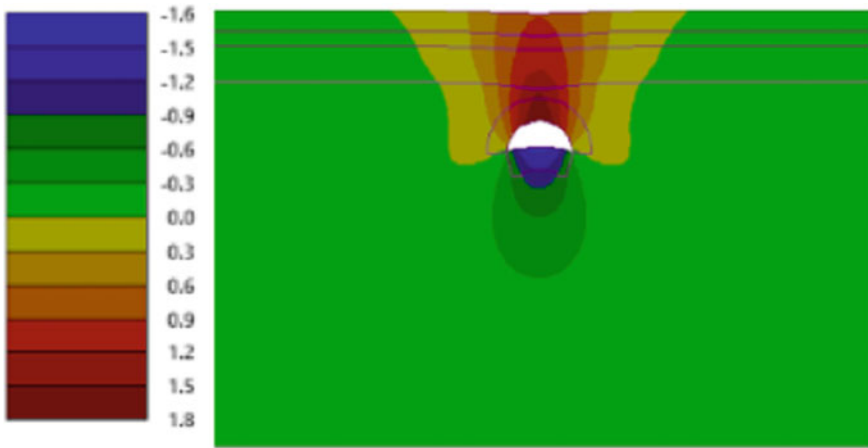
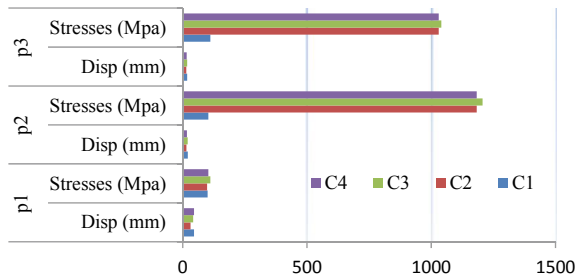


Fig. 6 Settlement for tunnel in stratified soil for Case-1

Fig. 7 Displacement and stresses different cases of stratification



## 4 Conclusion

The displacement is found to be greater at top of the tunnel than the bottom, but the scenario is reversed in case of stresses due to the geostatic stress effect at the bottom points. To study the effect of stratification on displacement and stresses is compared to the different stratification sequence, and it is observed that the combination 2, i.e. slate at the top followed by silt and gravel offers the lesser displacement and stresses. This combination gives around 21% (avg.) less displacements than the other stratification combinations. Thus, combination 2 is the recommended stratification sequence for this study.

## References

1. Anagnostou, G., & Kovári, K. (1996). Face stability conditions with earth pressure balanced shields. *Journal Tunnelling and Underground Space Technology*, 11, 165–173.
2. Anagnostou, G., & Kovári, K. (1994). The face stability of slurry-shield driven tunnels. *Journal Tunneling and Underground Space Technology*, 9, 165–174.
3. Broere, W. (2015). On the face support of Microtunnelling TBMs. *Journal Tunneling and Underground Space Technology*, 46, 12–17.
4. Chen, R. P., Tang, L. J., Ling, D. S., & Chen, Y. M. (2011). Face stability analysis of shallow shield tunnels in dry sandy ground using the discrete element method. *Journal Computers and Geotechnics*, 38, 187–195.
5. Graziani, A., Capata, A., & Romualdi, P. (2007). Analysis of Rock-TBM-lining interaction in squeezing rock. *Felsbau Magazine*, 25, 23–31.
6. Hasanpour, R. (2014). Advance numerical simulation of tunneling by using a double shield TBM. *Journal Computers and Geotechnics*, 57, 37–52.
7. Khezri, N., Mohamad, H., & Fatahi, B. (2016). Stability assessment of tunnel face in a layered soil using upper bound theorem of limit analysis. *Geomechanics and Engineering*, 11, 471–492.
8. Lee, I. M., Lee, J. S., & Nam, S. W. (2004). Effect of seepage force on tunnel face stability reinforced with multi-step pipe grouting. *Journal Tunneling and Underground Space Technology*, 19, 551–565.
9. Liu, H. L., Li, P., & Liu, J. Y. (2004). Numerical investigation of underlying tunnel heave during a new tunnel construction. *Journal Tunnelling and Underground Space Technology*, 26, 276–283.
10. Leca, E., Leblais, Y., & Kuhnhenh K. (2000). Underground works in soils and soft rock tunneling. In *International Conference on GeoEng2000*. Melbourne, Key note lecture.
11. Mair, R. J., & Taylor, R. N. (1997). Bored tunnelling in the urban environment: State of the art report. In *Proceedings of 14th ICSMFE*, Hamburg. Balkema.
12. Mair, R. J., Taylor, R. N., & Burland, J. B. (1996). Prediction of ground movements and assessment of risk of building damage due to bored tunneling. In: *International Conference Geotechnical Aspects of Underground Construction in Soft Ground* (pp. 713–718). London, Balkema).
13. Mestat, Ph, Bourgeois, E., & Riou, Y. (2004). Numerical modelling of embankments and underground works. *Computers and Geotechnics*, 31, 227–236.
14. Peck, R. B., Hendron, A. J., Mohraz, B. (1972). State of the art in soft ground tunneling. In *The Proceedings of the Rapid Excavation and Tunneling Conference* (pp. 259–286). New York, NY: American Institute of Mining, Metallurgical, and Petroleum Engineers.
15. Zhang, Z. X., Hu, X. Y., & Scott, K. D. (2011). Discrete numerical approach for modeling face stability in slurry shield tunnelling in soft soils. *Computers and Geotechnics*, 38, 94–104.
16. Zhang, C. P., Han, K. H., & Zhang, D. L. (2015). Face stability analysis of shallow circular tunnels in cohesive–frictional soils. *Tunnelling and Underground Space Technology*, 50, 345–357.

# Effect of Interference on Ultimate Bearing Capacity of Strip Footings Resting on Reinforced Clay Overlying Sand



Chandra Sekhar Jonnagiri, Venkata Balaiah Kami  
and Rabi Narayan Behera

**Abstract** The prevailing studies on the bearing capacity of shallow foundations show the tendency of relying on a hypothesis of an isolated footing resting in a homogeneous soil mass. In practice, the soil is seldom homogeneous, and heterogeneity increases with the area of consideration. In addition to the non-homogeneous nature of the soil, the footing also may not be isolated due to various reasons like very rare availability of good construction sites and rapid urbanization coupled with the shortage of land. However, these studies are ineffective when the closely placed footings encountered at shallow depths of a multi-layered soil mass. In the present study, a numerical investigation is carried out to evaluate the effect of interference on the ultimate bearing capacity of two closely placed identical surface strip footings resting over two-layered soil (weak soil overlying on a strong soil) mass subjected to a vertical concentric load using the finite element package, PLAXIS 3D. The granular soil (sand with relatively higher stiffness) is considered as strong soil, whereas the soft soil is considered as a weak soil. The analysis is carried out for various ratios of clear spacing to the footing width ( $s/B$ ) ranging from 0.5 to 6 by varying first layer thickness ( $H$ ) as  $B-5B @ B$ . Based on the analyses of results, the critical spacing ( $s_{cr}$ ) and significant depths ( $H_s$ ) were observed as  $3B$  and  $2B$ . The increment in ultimate bearing capacity ceases after these spacing and depth for weak soil overlying strong soil mass system. Also, with the inclusion of reinforcement, the critical spacing ( $s_{cr}$ ) was observed as  $1.5B$ .

**Keywords** Interference · Strip footings · Ultimate bearing capacity · Multi-layered soil · Reinforcement · Numerical analysis

---

C. S. Jonnagiri · V. B. Kami · R. N. Behera (✉)  
Department of Civil Engineering, National Institute of Technology Rourkela, Rourkela, India  
e-mail: [rnbehera82@gmail.com](mailto:rnbehera82@gmail.com)

C. S. Jonnagiri  
e-mail: [chandra.2052@gmail.com](mailto:chandra.2052@gmail.com)

V. B. Kami  
e-mail: [balu.k1200@gmail.com](mailto:balu.k1200@gmail.com)

© Springer Nature Singapore Pte Ltd. 2020  
S. Saride et al. (eds.), *Advances in Geotechnical and Transportation Engineering*,  
Lecture Notes in Civil Engineering 71,  
[https://doi.org/10.1007/978-981-15-3662-5\\_27](https://doi.org/10.1007/978-981-15-3662-5_27)

## 1 Introduction

The interference concept is observed when two or more number of footings are placed closely. The interference phenomenon was first coined by Stuart [1]. Stuart [1] examined the closely spaced strip footings laying on the surface. Stuart [1] observed a difference in the ultimate bearing capacity and settlement of isolated footings when they placed close. Finally, Stuart [1] concluded that the overlapping of pressure bulbs has a significant impact on the bearing capacity and settlement behavior of the isolated footings. Numerous researches have been carried out to determine the interference effect on the ultimate bearing capacity of various types of footings resting over homogeneous soil mass. Stuart [1] reported that the bearing capacity of interfering footings increases as the spacing between the footings decreases and it attains a peak magnitude at a spacing known as *critical spacing* ( $s_{cr}$ ). The similar findings were observed by Ghazavi and Lavasan [2], Srinivasan and Ghosh [3], Elthohamy and Zidan [4], Pusadkar et al. [5]. From the literature, the critical spacing is observed in the range of  $0.6B$  [4] to  $2B$  [2]. It is also noted that the interference effect becomes insignificant after a certain spacing. This spacing is reported in the range of  $3B$  [6] to  $6B$  [7] for two identical square footings resting over sandy soil. West and Stuart [8] observed the increase in bearing capacity of parallel spaced strip footing considering the effect of eccentricity and inclination of soil reaction. Kumar and Saran [9] reported non dimensional charts for pressure ratio calculation of adjacent rectangular footing. The interference effect of strip footing on single layer uniaxial sand bed was presented by [10]. The response of a number of identically spaced multiple strip footing was presented in [11]. A Fast Lagrangian Analysis of Continua algorithm for studying the effect of interference was presented by [12]. Daud [13] reported that, response of multiple strip footing is similar to that of single footing for distance greater than four times the width of footing. Noorzad and Manavirad [14] found that increasing the number of reinforcement layer does not have significant effect beyond the threshold value. Interference of strip footing was presented, using Hoek–Brown failure criterion in [15]. The performance of ring footing on multilayered reinforced soil was reported by [16]. The interference effect in the case of square footing was presented in [17]. The decrease in ultimate bearing capacity due to the effect of interference was observed by [18]. They found that, the ultimate bearing capacity reduces irrespective of the spacing between the footings. The literature showed that the increase in stiffness of reinforcement beyond a threshold value does not affect the bearing capacity of interfering footings. However, very limited literature is available to determine the effect of interference on the ultimate bearing capacity of footings resting over multilayered reinforced soil. The current research focused on the effect of interference on the ultimate bearing capacity of two surface strip footings resting on clay overlying sand in both unreinforced and reinforced conditions.



## 2 Materials Used

### 2.1 Soil

Two soils, namely soft clay (cohesive soil) and dry sand (cohesionless soil), together represent the multi-layered soil mass system considered in the present study. The soils are assumed to behave as elastic-perfectly plastic material and hence considered Mohr–Coulomb failure criterion. A cubical soil volume of  $2 \text{ m} \times 0.37 \text{ m} \times 0.5 \text{ m}$  ( $L \times B \times H$ ) is simulated to resemble the full soil geometry. The geometry of soil volume for the case of  $H/B = 3$  cases is shown in Fig. 1. The full 3D soil geometry with two nearby strip footings resting on two-layered soil mass with the associated parameters  $b$ ,  $l$ ,  $u$ ,  $h$ ,  $s$ ,  $B$  and  $N$  representing width of reinforcement layer, length of reinforcement layer, depth of first reinforcement layer from bottom of the footing, vertical spacing of reinforcement, clear distance between the footings, width of footings and the number of reinforcement layers, respectively, and is shown in Fig. 2.

The undrained type of behavior is adapted to the clay for which the shear strength parameters are incorporated in terms of undrained shear strength and drained behavior is adopted for the sand. The mechanical properties of soils are presented in Table 1.

The undrained character of the clay preferred to include in the analysis is to simulate the field conditions. The drained behavior of sand is undertaken in the study to represent the very quick dissipation of pore water pressures from voids immediately after the application of load in practice.

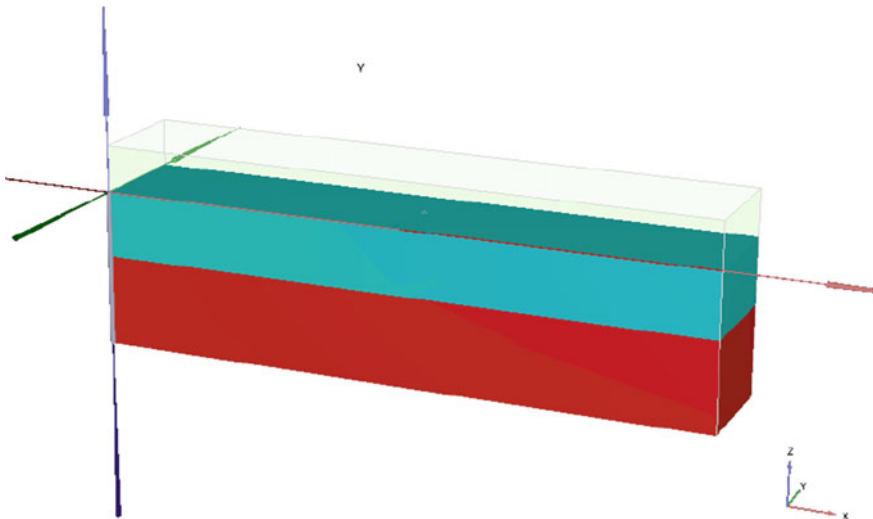


**Fig. 1** The geometry of soil volume for  $H/B = 3$  case

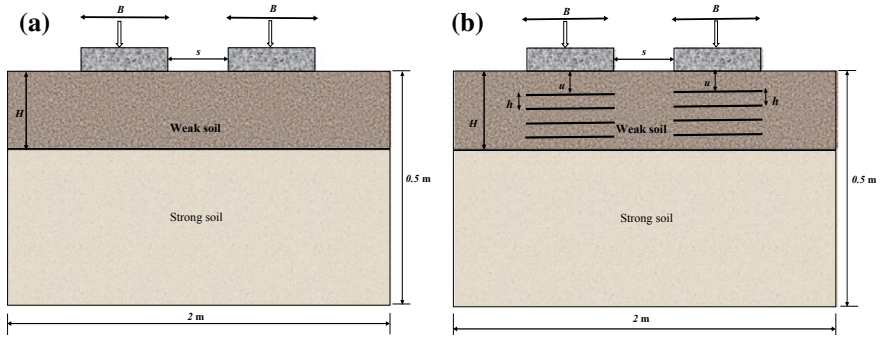


Fig. 2 Weak soil overlying relatively strong soil, (a) unreinforced case and (b) reinforced case

Table 1 Mechanical properties of soils

Property	Model/value	Model/value
Model type	Mohr–Coulomb	Mohr–Coulomb
Soil type	SP	CL
Drainage type	Drained	Undrained
$\gamma_{dry}$ (kN/m <sup>3</sup> )	16.2	17.5
$\gamma_{sat}$ (kN/m <sup>3</sup> )	18.0	19.5
$D_{60}$ (mm)	0.75	–
$D_{30}$ (mm)	0.37	–
$D_{10}$ (mm)	0.20	–
$C_u$	3.75	–
$C_c$	0.91	–
Effective cohesion $c'$ (kPa)	0.1	–
Undrained shear strength $S_u$ (kPa)	–	30
Effective angle of internal friction $\phi'$ (°)	37.4	0
Modulus of elasticity $E$ (kPa)	35,000	5000
Poisson’s ratio, $\mu$	0.25	0.3
Relative density $R_D$ (%)	67	–
$k_X$ (m/day)	0.6	$0.05E^{-3}$
$k_Y$ (m/day)	0.6	$0.05E^{-3}$
$k_Z$ (m/day)	0.6	$0.05E^{-3}$

**Table 2** Mechanical properties of footing and test box

Property	Footing	Test box
Modeled as	Plate	Plate
Model type	Linear-elastic	Linear-elastic
Thickness (m)	0.025	0.025
$\gamma$ (kN/m <sup>3</sup> )	78.5	78.5
Width, $B$ (m)	0.07	0.37
Modulus of elasticity, $E$ (kPa)	$200 \times 10^6$	$200 \times 10^6$
Poisson's ratio, $\mu$	0.25	0.25

## 2.2 Footing and Test Box

A semi-rigid strip footing with the dimensions of  $0.36 \text{ m} \times 0.07 \text{ m}$  ( $L \times B$ ) is simulated to represent footing for the numerical analysis. The footing is modeled by a steel plate of thickness 0.03 m. The steel plate is relatively stiff enough compared to the stiffness of soils used in the current study to assume it as a semi-rigid footing. Two such identical symmetrical footings are used to determine the interference effect on the ultimate bearing capacity of footings in the two-layered soil mass. Linear-elastic nature is adopted for the footing used in the numerical analysis. Table 2 lists the mechanical properties of the footing and test box.

## 2.3 Reinforcement

Reinforcement layers were modeled using geogrids option in PLAXIS 3D which represents a structural tensile element with unit thickness and tensile strength. The biaxial geogrid elements are placed at a specified depth and at specified regular vertical intervals below the bottom of the footing. No slip between the soil and reinforcement is assumed, and hence, no interface elements are used in the current study. The geogrid behaves as an elastic material which can have only tensile resistance but no compressive and flexural resistance. The tensile strength of geogrid is incorporated in terms of the axial stiffness per meter length of the geogrid. The magnitude of the tensile strength of the geogrid used for the numerical analysis has been adopted from the majorly illustrated literature. The mechanical properties of the reinforcement element are tabulated in Table 3.

**Table 3** Mechanical properties of reinforcement

Property	Model/value
Reinforcement type	Geogrid
Model type	Elastic-isotropic
Axial stiffness, $EA_1$ (kN/m)	40
Axial stiffness, $EA_2$ (kN/m)	40

### 3 Methodology

#### 3.1 Schematic Explanation of Modeling

In the current study, a finite element program PLAXS 3D is employed to model interfering surface strip footings resting on two-layered soil system without reinforcement and with reinforcement. In broad, the procedure consists of the determination of the optimum top layer thickness for the unreinforced case and then the continuation of the similar study with reinforcement for the optimum top layer thickness.

The stress-controlled approach is adopted by applying the load till the failure of the soil mass occurs. It is assumed that no groundwater table exists below the footing, and hence, it is simulated by applying groundwater well below the footings, so that it does not affect the ultimate bearing capacity of the footings in dry condition. The whole soil volume is enclosed in a steel tank to represent the laboratory conditions used for the similar kind of experimental investigations carried out by Kumar and Bhoi [19]. Validation study also has been carried out in the test box of dimensions as specified by Kumar and Bhoi [19]. 15 noded elements are used to generate the meshing. The staged construction mode has been adopted to simulate the procedure of construction practices. The vertical concentric point loads are applied to make the calculations easy and time-effective.

The whole analysis is presented in two cases, unreinforced and reinforced, as shown in Fig. 2. The most common problems are addressed by considering both stages, which is the most reliable pattern of analysis. In addition, all possible cases are considered by the means of different parameters which includes significant depth or the top layer thickness, critical spacing and the optimum number of reinforcement layers. Failure patterns also are shown in the present study to support numerical analysis. Both isolated and interfering footings of optimum cases are also compared by taking assistance from the failure patterns. In the present study, the inclusion of reinforcement is done by considering the deep slab mechanism explained by Huang and Menq [20].

### 4 Numerical Modeling

The procedure of modeling the geometry, simulating the experimental conditions and generation of mesh and the calculations are elaborated with the help of respective PLAXIS 3D images. Two cases, unreinforced and reinforced of weak soil, overlying relatively strong soil are simulated and analyzed. The number of reinforcement layers is varied from one to four in both cases. The interference effect is determined in various terminology defined by the various researchers in literature. The terminology related to this interference effect used in the current study is explained as below.

Various terminology related to interference effect used in the current study:

$$\xi = \frac{(q_{u,int})}{(q_{u,single})} \text{ for homogeneous soil mass} \tag{1}$$

$$E_f = \frac{(q_{u,int})}{(q_{u,single})} \text{ for multi-layered unreinforced soil mass} \tag{2}$$

$$E'_f = \frac{(q_{u,int})}{(q_{u,single})} \text{ for multi-layered reinforced soil mass} \tag{3}$$

where  $\xi$ ,  $E_f$  and  $E'_f$  are efficiency factors in respective conditions and  $(q_{u,int})$  and  $(q_{u,single})$  are the ultimate bearing capacities of interfering footing and single footing, respectively. For all the cases, the geometry of the model and the material properties used are kept unchanged as the observing variables only change accordingly. The procedure employed to reach the output is also kept constant throughout the analysis. All the analyses are performed to reach the ultimate failure of the soil mass and the corresponding bearing resistance is determined from the graphs plotted as load intensity ( $q_u$ ) versus settlement curves. The ultimate bearing capacity is determined by using the double tangent method. The procedure adopted to model and analyzing the problem is clearly explained in the preceding sections. First, the unreinforced case is carried out for isolated and interfering footing by varying first (top) layer thickness from the bottom of the footing ( $H$ ) with the thickness equal to one time of the footing width to five times of the footing width. From these unreinforced cases ( $H = B, 2B, 3B, 4B$  and  $5B$ ), the optimum thickness of the top layer is obtained in terms of maximum ultimate bearing capacity and the reinforcement layers ( $N = 1, 2, 3, 4$ ) are being incorporated to evaluate the optimum reinforcement depth. The optimum case is selected based on the highest ultimate bearing capacity observed among all the unreinforced cases and this case is utilized to carry the reinforced cases by varying the number of reinforcement layers ( $N$ ) from one to four. The geometry of the model, structural elements and generated mesh of the optimum case ( $H/B = 3$ ) are shown in Figs. 3, 4 and 5, respectively, for both isolated and interference footings. The analysis of interference of strip footings is preceded further to the reinforced case for the optimum top layer thickness by varying the number of reinforcement layers. The four number of reinforcement layers are introduced at a vertical spacing of ( $h/B =$

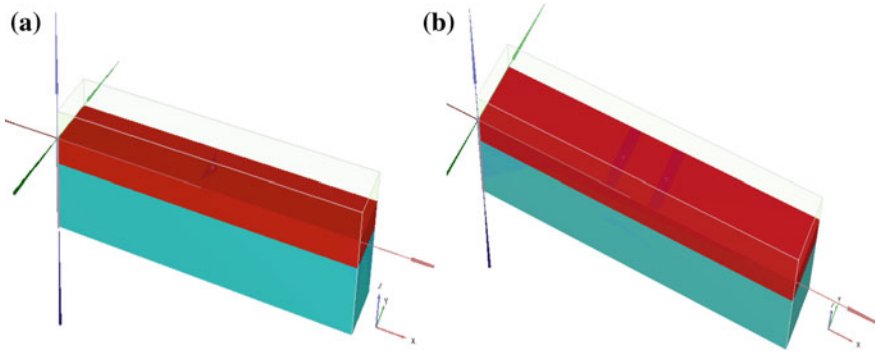


**Fig. 3** The geometry of soil volume for  $H/B = 2$  cases, (a) isolated footing and (b) interfering footings, clay overlying sand

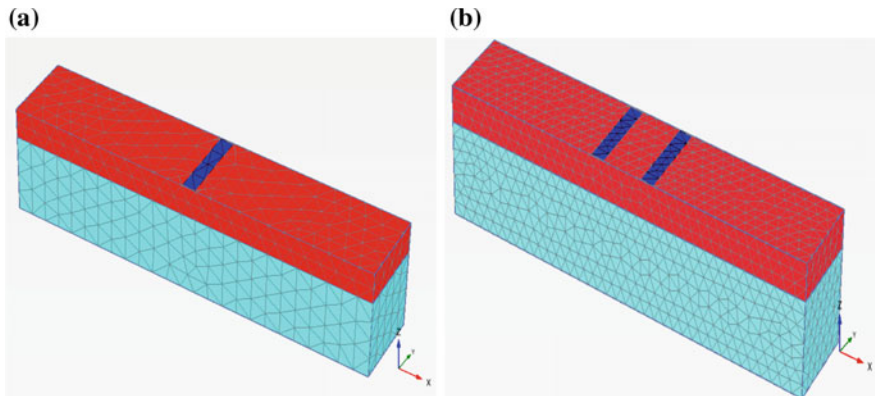


**Fig. 4** Meshing for  $H/B = 2$  case (a) isolated footing and (b) interfering footings, clay overlying sand

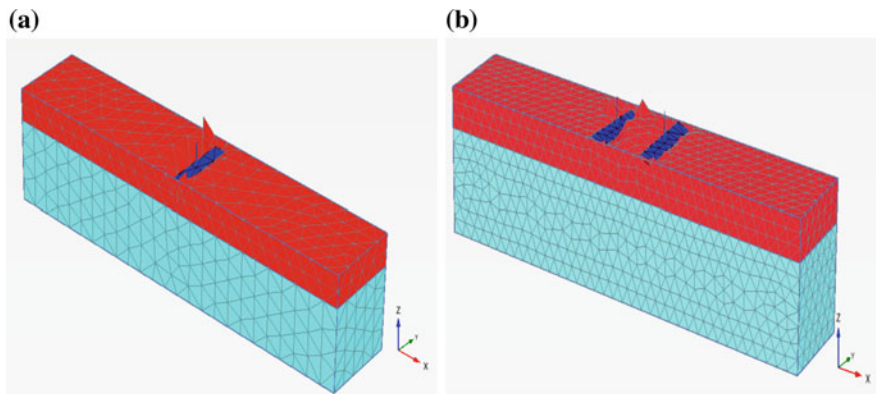


**Fig. 5** The deformed mesh of isolated footing, for  $H/B = 2$  case (a) Isolated footing and (b) interfering footings, clay overlying sand

0.25) with the depth of first or top reinforcement layer from the bottom of the footings as ( $u/B = 0.35$ ). The use of geogrid as reinforcement in geotechnical applications become unique advantage program especially in foundations overlying weak soils or the soils with very low bearing capacity. The soil–reinforcement interface friction is the key factor which derives additional shear strength to the original soil.

It is well established that the inclusion of reinforcement in soils make them stronger, stiffer and durable, and hence, the application of reinforcement become quite common in geotechnical engineering applications.

## 5 Validation

In the present study, validation has been carried out with the experimental investigation of a similar study in the homogeneous soil.

The numerical results obtained from PLAXIS 3D are compared with the experimental investigation carried out by Kumar and Bhoi [19]. In which, the effect of interference of footing on ultimate bearing capacity in terms of efficiency factor ( $\xi$ ) at ultimate failure for a dry density of  $16.2 \text{ kN/m}^3$  in homogeneous soil mass has been presented. The geometrical model adopted in the current study is clearly shown in Fig. 6.

From the validation study, it is found that both finite element software and experimental investigation of Kumar and Bhoi [19] yielded similar results. The results obtained from numerical analysis are very well agreed with experimental results presented by Kumar and Bhoi [19] as shown in Fig. 7.

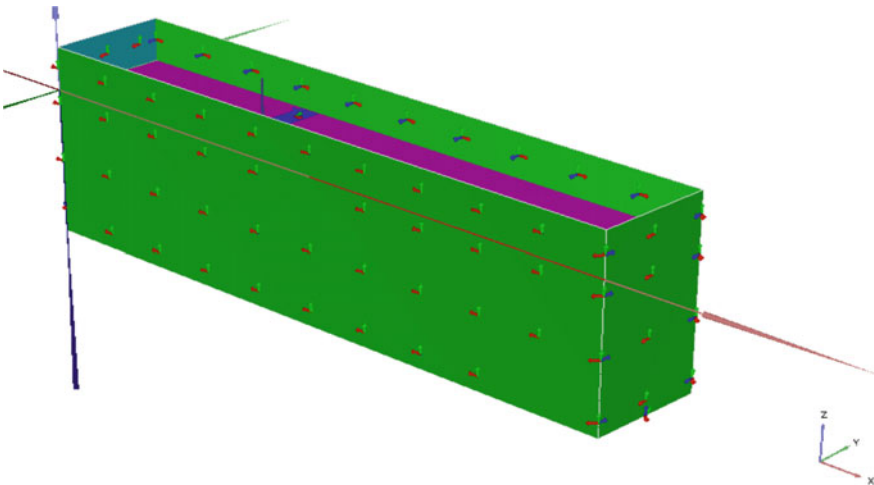


**Fig. 6** The geometrical model generated in PLAXIS 3D for validation

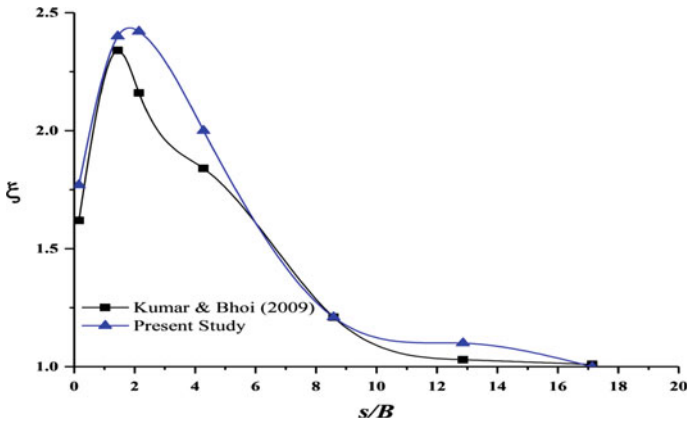


Fig. 7 Validation of present study with Kumar and Bhoi [19]

## 6 Results and Discussion

### 6.1 Clay Overlying Sand Without Reinforcement

The analysis of weak soil overlying strong soil has been carried out. As an initial step, the analysis was carried out without reinforcement to find the optimum clay layer thickness. Later, the study is continued by reinforcing the clay layer with a different number of reinforcement layers. The interference effect of the footings on ultimate bearing capacity in terms of efficiency factor has shown in Fig. 8. From Fig. 8, it is clearly observed that there is an increment of bearing capacity in terms of efficiency factor ( $E_f$ ) up to  $s/B = 3$  and descends till  $s/B = 5$  for all the case of  $H/B$ . It is also observed that the efficiency factor ( $E_f$ ) is increased up to a top layer thickness of  $2B$  and decreases till  $5B$ . So,  $s/B = 3$  and  $H/B = 2$  are found to be optimum spacing and optimum thickness, respectively, after which the interference effect is minimal.

Further, the study is continued with the inclusion of a different number of reinforcement layers for the optimum case ( $H/B = 2$ ). The failure patterns of the optimum case ( $H/B = 2$ ) for both isolated and interfering footings of  $s/B = 3$  are as shown in Figs. 9 and 10, respectively.

### 6.2 Clay Overlying Sand with Reinforcement

The analysis of interference of strip footings is proceeded further to the reinforced case for the optimum top layer thickness ( $H = 2B$ ) by varying the number of reinforcement layers. The four number of reinforcement layers are introduced at a vertical spacing of ( $h/B = 0.25$ ) with the depth of first or top reinforcement layer from the



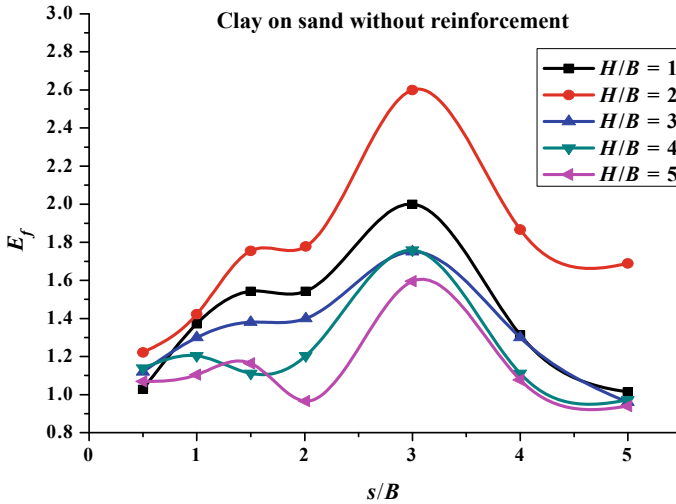


Fig. 8 Interference factor versus  $s/B$  with a variation of top layer thickness

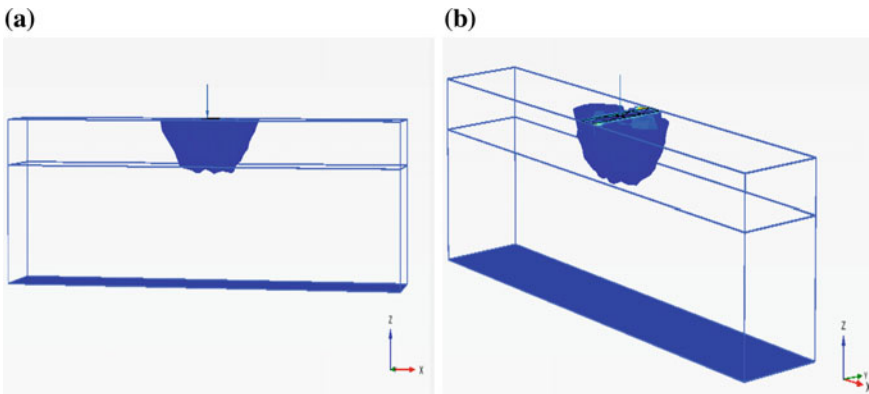


Fig. 9 Failure pattern of isolated footing, for  $H/B = 2$  case (a) front view and (b) isometric view

bottom of the footings as ( $u/B = 0.35$ ). Figure 11 shows the variation of the ultimate bearing capacity of interfering footings in terms of efficiency factor with the number of reinforcement layers. In the reinforced case, the efficiency factor is designated as  $E_f'$  to differentiate it from the unreinforced case. From Fig. 11, it is observed that as the number of reinforcement layers increased, the interference effect also increased. It is also noted that the optimum interference effect on ultimate bearing capacity observed for  $N_{opt} = 3$ .

Figure 12 depicts the failure patterns of three and four number of reinforcement layers of the top layer thickness ( $H$ ) of  $2B$  for the clear spacing ( $s$ ) of  $1.5B$ , respectively.

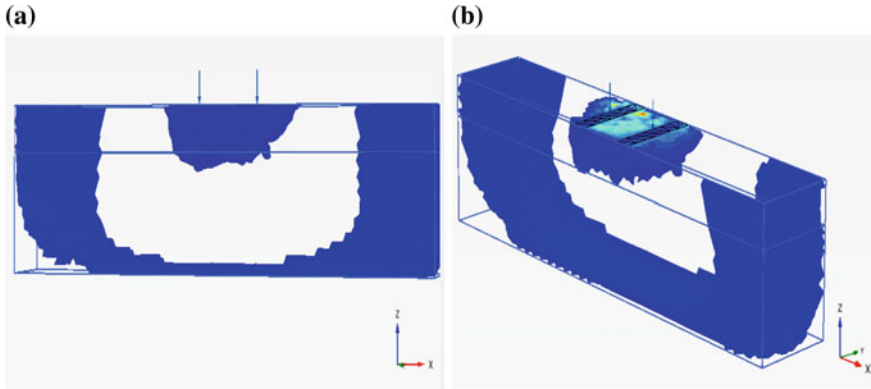


Fig. 10 Failure pattern of interfering footing ( $s/B = 3$ ), for  $H/B = 2$  case (a) front view and (b) isometric view

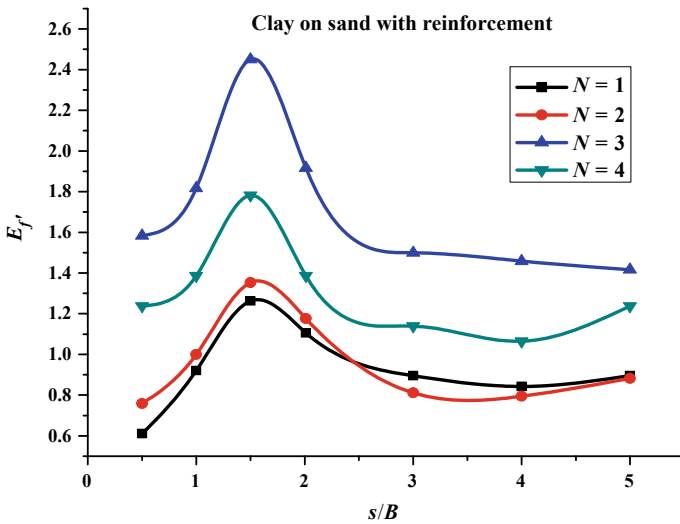
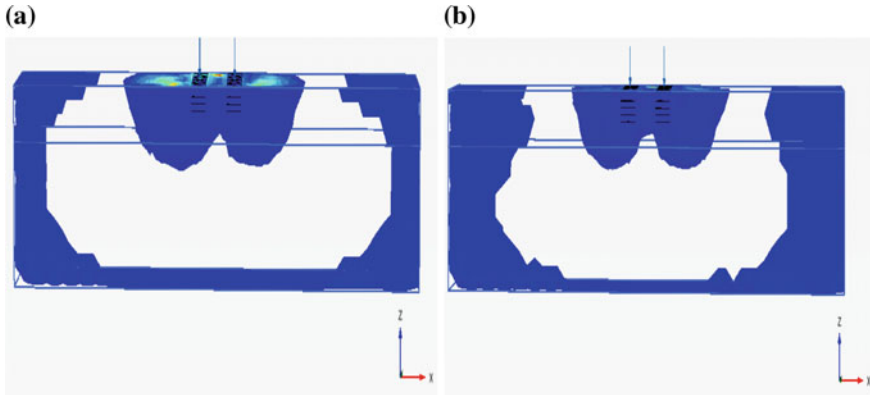


Fig. 11 Interference factor versus  $s/B$  with a variation of number of reinforcement layers

## 7 Conclusions

In the present study, the effect of clear spacing between two closely spaced footings, effect of reinforcement, effect of top layer thickness on ultimate bearing capacity ( $q_u$ ) of interfering footings resting over two-layered soil (weak soil overlying on a strong soil) with and without reinforcement have been analyzed, and the results are presented in the form of critical spacing ( $s_{cr}$ ), significant depth ( $H_s$ ) and optimum number of reinforcement layers ( $N_{opt}$ ).



**Fig. 12** Failure pattern of (a) three reinforcement layers and (b) four reinforcement layers of  $H/B = 2$  case

In the unreinforced soil system,

- The critical spacing ( $s_{cr}$ ) is observed as  $3B$ .
- The critical depth ( $H_{cr}$ ) is observed as  $2B$ .

In the reinforced soil system,

- The critical spacing ( $s_{cr}$ ) is observed as  $1.5B$ .
- The optimum number of reinforcement layers ( $N_{opt}$ ) is observed as 3.

## References

1. Stuart, J. (1962). Interference between foundations, with special reference to surface footings in the sand. *Geo-technique*, 12(1), 15–22.
2. Ghazavi, M., & Lavasan, A. A. (2008). Interference effect of shallow foundations constructed on sand reinforced with geosynthetics. *Geotextiles and Geomembranes*, 26(5), 404–415.
3. Srinivasan, V., & Ghosh, P. (2013). Experimental investigation on interaction problem of two nearby circular footings on layered cohesionless soil. *Geomechanics and Geoengineering*, 8(2), 97–106.
4. Eltohamy, A. M., & Zidan, A. F. (2013). Performance of interfering strip footings resting on reinforced sand under uniform and non-uniform load-experimental and numerical study. *Journal of American Science*, 9(1), 421–430.
5. Pusadkar, S., Gupta, M. R., & Soni, M. K. (2013). Influence of interference of symmetrical footings on bearing capacity of the soil. *International Journal of Engineering Inventions e-ISSN*, 22–25.
6. Lee, J., & Eun, J. (2009). Estimation of bearing capacity for multiple footings in the sand. *Computers and Geotechnics*, 36(6), 1000–1008.
7. Reddy, E. S., Borzooei, S., & Reddy, G. N. (2012). Interference between adjacent footings on sand. *International Journal of Advanced Engineering Research and Studies*, 1(4), 95–98.
8. West, J., & Stuart, J. (1965). Oblique loading resulting from interference between surface footings on sand. In *Proceedings, 6th International Conference of Soil Mechanics and Foundation Engineering* (vol. 2, pp. 214–217).

9. Kumar, A., & Saran, S. (2004). Closely spaced rectangular footings on reinforced sand. *Geotechnical and Geological Engineering*, 22(4), 497–524.
10. Ghosh, P., & Kumar, P. (2009). Interference effect of two nearby strip footings on reinforced sand. *Contemporary Engineering Sciences*, 2(12), 577–592.
11. Kumar, J., & Bhattacharya, P. (2010). Bearing capacity of interfering multiple strip footings by using lower bound finite elements limit analysis. *Computers and Geotechnics*, 37(5), 731–736.
12. Mabrouki, A., Benmeddour, D., Frank, R., & Mellas, M. (2010). Numerical study of the bearing capacity for two interfering strip footings on sands. *Computers and Geotechnics*, 37(4), 431–439.
13. Daud, K. A. (2012). Interference of shallow multiple strip footings on sand. *The Iraqi Journal for Mechanical and Material Engineering*, 12(3), 492–507.
14. Noorzad, R., & Manavirad, E. (2014). Bearing capacity of two close strip footings on soft clay reinforced with geotextile. *Arabian Journal of Geosciences*, 7(2), 623–639.
15. Javid, A., Fahimifar, A., Imani, M., et al. (2015). Numerical studies on the bearing capacity of two interfering strip footings based on Hoek–brown materials. In *13th ISRM International Congress of Rock Mechanics, International Society for Rock Mechanics* (vol. 13, issues 5, pp. 625–634).
16. Dhattrak, A., & Mishra, P. (2016). Performance of ring footing resting on reinforced multilayered soil using plaxis 2d. *International Journal of Research in Engineering and Technology*, 7(4), 103–114.
17. Pusadkar, S., & Ninghot, K. (2016). Interference of square footing on layered soil subjected to vertical load. *SSRG International Journal of Civil Engineering (SSRG-IJCE) e-ISSN*, 3(6), 9–13.
18. Subhan, M. (2017). Interference of symmetrical footings on bearing capacity of the soil. *SSRG International Journal of Civil Engineering (SSRG-IJCE) e-ISSN*, 4(5), 14–17.
19. Kumar, J., & Bhoi, M. K. (2009). Interference of two closely spaced strip footings on sand using model tests. *Journal of Geotechnical and Geoenvironmental Engineering, ASCE*, 135(4), 595–604.
20. Huang, C. C., & Menq, F. Y. (1997). Deep-footing and wide-slab effects in reinforced sandy ground. *Journal of Geotechnical and Geoenvironmental Engineering, ASCE*, 123(1), 30.

# Feasible Study for Allocation of Nodal Demands Through WaterGEMS



Chekka V. S. S. Sudheer, Maddamsetty Ramesh  
and Gedela Venkata Ramana 

**Abstract** Demand for potable water is an increase on continual basis with a corresponding increase in population and livelihood activities. The ever increasing demand can be fulfilled by designing efficient water distribution networks based on advance computing systems include modern hydraulic modeling and designing softwares, such as WaterGEMS, EPANET, LOOP, WaterCAD, InfoWater and KY pipes. The above-said softwares can stimulate real networks under the given circumstances independent of its size. Besides, these hydraulics simulation softwares yield results precisely and accurately within a considerable time. In parallel, one should emphasize on the relevant method for assigning the base demands through various methods, even though the difference is too low but still, it is important where precision becomes first criteria for designing a pipeline network. In this paper, authors highlight a comparative study about the hydraulic analysis outputs of pipeline network between different base demand allocation methods using WaterGEMS software with the main motive to model a feasible pipeline of water distribution network based on appropriate methods using demand control center for Bodhan town. The present system of distribution for Bodhan (study area) is adopted with an intermittent supply with the distribution network of total length of 89 km. Keeping in view of increasing population and changing demands of living beings, existing network has to be investigated for its steadiness for supplying water. Therefore, analysis was carried by simulating existing water network through WaterGEMS software. The examination was carried out based on inputs assigned to objects present in the network such as nodes, pipes and tanks. Design of network using simulation for assumed design period will make the municipality be aware of the changes in rate of increase in the

---

C. V. S. S. Sudheer (✉) · M. Ramesh  
Department of Civil Engineering, GITAM Institute of Technology, GITAM University,  
Visakhapatnam, Andhra Pradesh, India  
e-mail: [royal.chsudheer@gmail.com](mailto:royal.chsudheer@gmail.com)

M. Ramesh  
e-mail: [ramesh.maddamsetty@gitam.edu](mailto:ramesh.maddamsetty@gitam.edu)

G. V. Ramana  
Department of Civil Engineering, St. Martin's Engineering College, Hyderabad, Telangana, India  
e-mail: [ramanakethana2017@gmail.com](mailto:ramanakethana2017@gmail.com)

demands, its validity based on pressure and other parameters. From the comparative results, the feasible method of base demand allocation is adopted for the design of water distribution network.

**Keywords** Demand control center · Hydraulic simulation softwares · WaterGEMS · Intermittent water supply · Demand allocation

## 1 Introduction

Water distribution networks (WDN) are the social infrastructures which range from simple to complex in size depending upon various parameters such as population and size of the study area. The main role of a typical WDN is that to transfer the potable water to the required end user in sufficient quantities with appropriate quality. Public infrastructural buildings like schools, hospitals, public parks and large buildings are considered to be very crucial junctions in the WDN [1, 2]. Besides, allocation of demands to nodes/junctions through demand control center plays a very key role while designing water supply system (WSS). Allocation Assigning of calculated base demands to the existing nodes in the network through WaterGEMS software is consisting of several methods base on the following criteria [3, 4].

- Point load data
- Area load data
- Population/Land use data.

The methodology involved in assigning of nodal demands is explained in the following sections.

### 1.1 Point Load Data

Point load data is generally referred to junctions/ nodes, which again consists of three subcategories, namely billing meter aggregation, nearest node connected to the pipes and nearest pipe to the nearby junction [5, 6].

- Billing meter aggregation is the method in which it assigns the demands to all the nodes confined within the service polygon. This method involves a detailed household survey in order to find the exact number of billing meters within the service polygon.
- Nearest node is the method in which it assigns the demands to all nodes within the network which are close to the nearby node.
- Nearest pipe in the method in which it assigns the demand to all the junctions in the network confined to the nearest pipe [7, 8].

## 1.2 Area Load Data

This method mainly refers to the corresponding area influenced by the node within the given network. It was subcategorized as equal flow distribution, proportional distribution by area, proportional distribution by population and unit line method [9, 10].

- The first method in area load data is equal flow distribution which explains that the distribution of demand to the node within the network distributes equally confined within the polygon/boundary. Equation to estimate the nodal demand through this method was shown in Eq. 1. This method is practically applicable in the areas where the distribution of population is uniform and the type of network is well defined [8].

$$q_j = \frac{Q}{N} \quad (1)$$

where

$q_j$  Demand of  $j$ th node in the network

$Q$  Total demand of the network calculated based on the given conditions

$N$  Total number of nodes in the boundary/polygon.

- The allocation of demands to nodes by proportional distribution by area is based on the ratio of total area of boundary to area of nodes in the network or confined to the polygon. This technique is applicable when the study area is classified homogenously such as public places, schools, hospitals and recreational areas [11].
- Another method in area load data is that proportional distribution by population plays a key role and practically applicable to most of the study areas where the demands to the nodes in the network are assigned by creating the influence diagrams or Thiessen polygons to the corresponding nodes [12].
- The last method in the area load data is that unit line method, where it involves two methods while assigning the nodal demands like known demand and unknown demand. Known demand involves the demand obtained through billing metered data and unknown demand involves leakage and unmeasured demands through various pipes in the network. This method is practically feasible only if the population occupies both sides of the pipe.

## 1.3 Population/Land Use Data

The demand allocation to the nodes in the given network through this method is subcategorized into two methods, such as projection by land use and load estimation by population [13].

- In the first method, projection by land use, the demands are assigned to nodes in the network based on the classification of land use. In this method, density per land use for each zone shall be calculated and then assigned to these nodes.
- The second method, load estimation by population demands, is calculated by user predefined instructions between per capita demand and population data [6].

In this paper, the author mainly enlightens the methods used described in area load data method such as: equal distribution method, proportional distribution by population and unit line method, in order to find the feasible method for allocating the demands to the nodes in the network through WaterGEMS simulation software. The reason behind for not choosing other methods is that due to unavailability of data like billing meter data, nearest node and pipe, land use classification, etc.

### ***1.4 Role of WaterGEMS in Hydraulic Simulation***

Simulation is defined as the process of generating or producing a computer-based model, for the purpose of detailed study and analysis. Various tools (freeware and proprietary) are readily available in the market for the hydraulic simulation of typical water distribution networks. The basic advantage of these simulation softwares is that, irrespective to the size of the network, a detailed study or the behaviors of the network can be made simple with accurate results in a considerable period of time. Some of the tools which were mentioned above are EPANET, WaterGEMS, WaterCAD, LOOP and KY pipes. These modeling softwares contrast in numerous features which include their functionality, compatibility to different computational systems and requirements, graphical user interface (GUI), and operational algorithms etc. A brief review of the modeling softwares used for hydraulic simulation was discussed below [5, 13].

#### **EPANET**

A hydraulic software tool developed by the US Environmental Protection Agency's Water Supply and Water Resource Division named under—Environmental Protection Agency Network (EPANET)—which is an open tool developed to design any sort of network with the given input bounds. It is capable of performing extended period simulation within the pressurized pipe networks. The main drawback with the use of this software is that it was not most user-friendly compared to those other softwares, and the modules of GIS were not integrated.

#### **WaterGEMS**

Water Geospatial Engineering Modeling System (WaterGEMS) is a versatile tool for the simulation of a typical water distribution system. It has wide range of capabilities which performs different types of calculations for the given network under different sets of combination based on the user inputs. Following are the advantages of this software is that: it identifies weak links and evaluates the suitability of isolation



valves, assesses the weak zones of fire protection in water distribution network which enables to improvise the sizing and location of pipes and other hydraulic components in order to meet the fire flow requirements, identifies the leakages in pipes and ranks the pipe links for replacement or repair based on their criticality index. [5, 14]

### **KYPipe**

Hydraulic simulation software for the analysis of the water distribution network can be applied to any type of the liquids. It is also capable of performing the extended period simulation when compared to other simulation softwares. It has a strong computational algorithm for the design and analysis of various hydraulic components in the distribution system. It is most user-friendly for designing and optimization of distribution networks. It is also companionable with Geographical Information Systems (GIS) with extended type of extension formats for the analysis of the network [5, 15].

Of all the above available simulation software tools in the market, by considering the advantages of WaterGEMS software, authors choose for the analysis and optimal design of the distribution network in the study area.

## **2 Study Area**

Bodhan is one of the major towns in the Nizamabad district. It is located at 18° 39' 47.7" N E. It is at a distance of 29 km from the district headquarters. The main crops that are grown in this area are paddy and sugarcane. The satellite view of the Bodhan town is shown in Fig. 1. It is a grade II municipality with an extent of 21.36 km<sup>2</sup>. The total population of the study area is about 77,639 numbers according to 2011 census. According to the water supply details, the entire town is divided into nine zones. In this study, two zones were considered of all the nine zones since the data is sufficiently available. The population for these two zones was observed as 30,488 numbers according to 2011 census. Besides, following information was obtained from the officials of Bodhan municipality which were considered as inputs in this analysis.

- The source of water supply for the town is from Bellal reservoir with a capacity of 346 Million Cubic Feet (MCFT).
- Daily 10 MLD of drinking water is drawn from Bellal reservoir
- Water treatment plant having capacity 12.22 MLD is existing at Rakasipet.
- Before supply, the water is treated by aeration, alum, sedimentation and addition of chlorine gas.
- The zone 1 and zone 2 consist of two existing water tanks named Shankar nagar tank and Housing board tank with a volume of capacity 1364 KL and 800 KL, respectively.
- Daily demand of water is considered as 110 L per capita per day (lpcd).

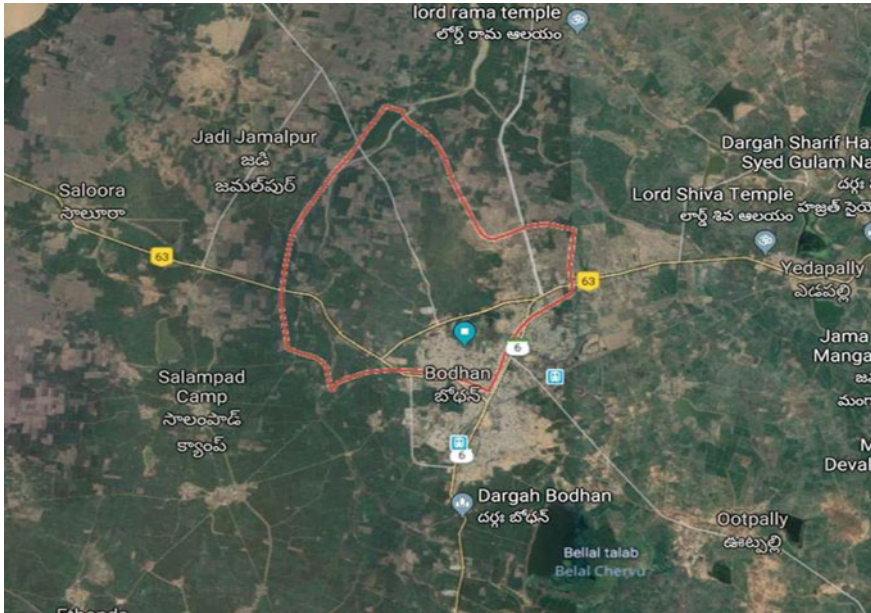


**Fig. 1** Satellite view of Bohdan town

Based on the street view of the study area, base map with historical places for zones—1 and 2—was created using Auto CAD tool which was shown in Fig. 2. Besides, the data was considered as an input for designing the given network.

### 3 Methodology

The preliminary data that was obtained from various sources is quite helpful which proceeds further to run the network within the stipulated period of time. Following methodology was adopted in this paper which was in Fig. 3 to find the feasible method for the estimation of nodal demands through WaterGEMS simulation software.

On the other hand, a detailed scheme design was prepared to find the ultimate population with corresponding ultimate demand for which the existing system needs to sustain for a period of three decades. Correspondingly, final capacity of the service reservoir was also calculated using this scheme design which was shown in Table 1. Besides, floating population, losses in the network and firefighting services were also considered to the maximum of 10% of total volume of the tank during the analysis. With all the above considerations, the total volume of Elevated Service Reservoir (ELSR) for the ultimate year 2040 is approximately 240 KL with total height of 30.5 m from the ground level. Moreover, as the preliminary data collected from

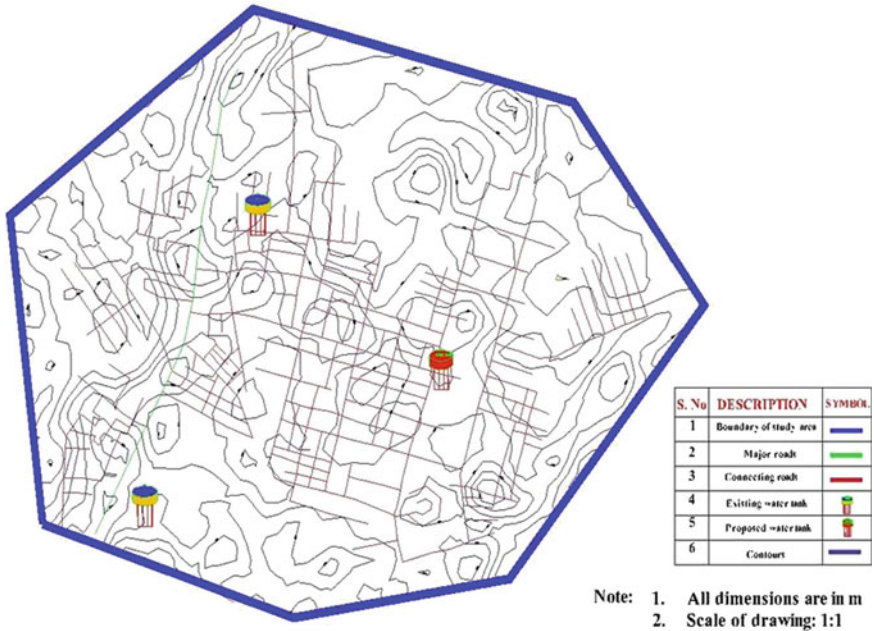


Fig. 2 Base map of the study area overlaid with contours

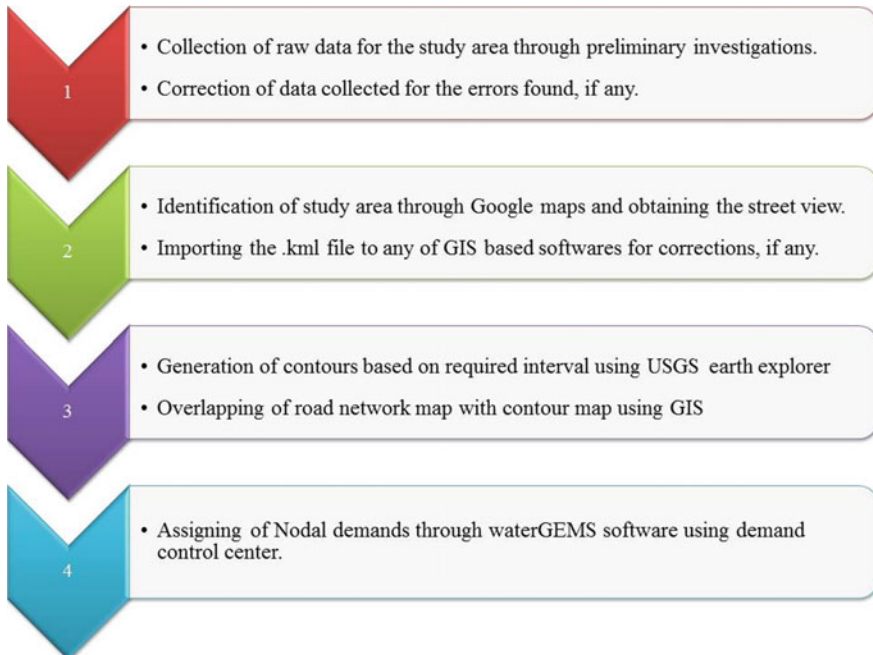


Fig. 3 Methodology to run the network through WaterGEMS software

**Table 1** Scheme design

1	Population as per 2011 census	30,488	No's
2	Base year of the scheme, i.e., completion of the scheme	2020	
3	No. of households	6098	No's
4	Growth of population proposed (P)	9.4%	
	By the method of arithmetical increase method, population for prospective year (2030) and ultimate year (2040) is forecasted as with the help of formulae as shown here: $P_n = P + nC$		
5	Base year population (2020)	33,461	No's
6	Prospective population (2030)	36,434	No's
7	Ultimate population (2040)	39,406	No's
8	Per capita supply (including losses)	110	lpcd
9	Pumping hours	24	hrs
10	Storage capacity (GLSR)	50%	Of ultimate demand
11	Demand for year 2020—(Base year)	3,680,710	lpd
		2556.05	lpm
12	Prospective demand for the year 2030	4,007,740	lpd
	Prospective LPM	2783.15	lpm
13	Ultimate demand for the year 2040	4,334,660	lpd
	Ultimate LPM	3010.18	lpm
		49.76	lps
14	<i>Infrastructure</i>		
15	Source	lake	
16	Storage capacity of OHSR	2,167,330	L
	Assuming fire and other emergency services; therefore, assume 10% excess of the total capacity of the total volume of the tank		
	10% total capacity	216,733	L
	Therefore total capacity of tank to be provided as	2,384,063	L
	Rounding off to the nearest value, provide tank capacity as	2,400,000	L
	Capacity of existing ELSR near to proposed ELSR	2,164,000	L
17	Hence, finally provide tank capacity as	236,000	L
		236	KL
	Therefore, provide a ELSR of capacity 240 KL for the—Zones 1 and 2 (Study area) with a diameter of 7.5 m and height of 5.5 m		
18	R.L of GL at proposed ELSR	367.9	m
19	Highest GL in distribution network	379.02	m

(continued)

**Table 1** (continued)

20	Provide minimum residual head	3	m
21	Head loss in distribution network minimum head of service reservoir required	11.12	m
22	Minimum head of service reservoir required	393.14	m
23	Therefore staging of GLSR required	25.24	m
	Finally, propose 240 KL capacity GLSR with	25	m
24	GL at ELSR	367.9	m
25	LWL of GLSR	392.9	m
26	MWL of GLSR (LWL + 5.5 M)	398.4	m

various sources seems to be not sufficient for successful run of the network, the authors made some assumptions for smooth processing which are as follows: [9]

- The material of the pipe is assumed to be high-density polyethylene (HDPE).
- Since the pipes are old, the value of roughness coefficient ( $C$ ) is assumed as 90.
- For the initial run of the network, the inner diameters of the pipes in the network are assumed to be constant with a value of 110 mm.
- Contours are generated using DEM for the study area with an interval of 1 m.

The above figure describes the methodology involved in the generation of pipe network along with all required input data such as (length of pipe, elevation at junction, diameter of pipe, and roughness coefficient of pipes) [6, 9]. Besides, a detailed scheme design was prepared in order to get the clear for the total population, demand and capacity of service reservoir to be provided for the ultimate year (2040) which was shown below in table.

Table 1 describes in detail about the demand of water for the base year (2020), perspective year (2030), and ultimate year (2040) and corresponding volume of service reservoir to be provided with it minimum water level (MWL), maximum water level (MWL), etc. Further, the methodologies adopted for calculation of base demands by using various methods available in demand control center of WaterGEMS software shall be discussed briefly, which explains the detailed methodology and assumptions made in successful run of the network.

### ***3.1 Methodology Adopted for Calculation of Nodal Demand Through Equal Distribution Method***

As mentioned in earlier sections, in this division, authors discuss briefly the detailed procedure for the estimation of demands at nodes in the given network through equal distribution method shall be estimated as follows:

- Calculate the total demand for the ultimate year population which can be observed from Table 1 as 49.76 lps.

- Calculate the total number of nodes in the network from the WaterGEMS software. In this network, the number of nodes is 293. The number of nodes completely varies from network to network which depends on various parameters.
- The ratio to total ultimate demand for ultimate year and total number of nodes in the network gives the demand at each and individual node. The demand at each node was observed to be as 0.169 lps.
- The demand thus obtained in the above step shall be assigned to the nodes through the option demand control center provided in WaterGEMS software.

### ***3.2 Methodology Adopted for Calculation of Nodal Demands Through Proportional Distribution by Population Method***

In this method, influence diagrams or Thiessen polygons for all nodes in the network are drawn the option available in WaterGEMS software. The procedure is as follows:

- Consider the total demand for the ultimate year population (2040) from Table 1.
- Ensure that the input parameters were assigned to all objects in network such as length of pipe, diameter of pipe, roughness coefficient of pipe, elevation at nodes, diameter, lowest water level (LWL) and maximum water level (MWL) for the service reservoir.
- Create the Thiessen polygons for each and individual nodes in the network by using the option provided in the WaterGEMS software.
- On the other hand, calculate the population density of the network, i.e.,  $\frac{\text{Total number of population for Ultimate year}}{\text{Total area of the network}}$ .
- Assign the demands at nodes by multiplying the population density with corresponding area of Thiessen polygon.
- The method of assigning the demands at nodes is very accurate through this method.

### ***3.3 Methodology Adopted for Calculation of Nodal Demands Through Unit Line Method***

- This method requires a detailed survey, which involves the number of houses and corresponding number of persons living in the houses is essential. On the other hand with some basic assumptions, the calculations involving the base demand can be estimated by using simple Excel sheets also. In this method, it was assumed that the houses are occupied along both the sides of pipe.
- The nodal demands obtained through this method give inaccurate values, where the houses are not being occupied at the outskirts of village or where the land is occupied with agricultural fields or any wastelands.

- The results of nodal demands that were obtained through the above three methods were shown below in Table 2. These shall be considered as input values for the given network and thus requires for smooth and successful analysis of the network.

From the above table, it can be clearly observed that values of nodal demand obtained by Thiessen polygon method seem to be more appropriate when compared to other two methods because of the following reasons. Values of the base demand obtained by three methods for the study area were not shown in detail due to constraint of space.

- Generation of Thiessen polygon diagrams which are also known as Voronoi diagrams or influence diagrams is used to assign space to the nearest node/junction and also essential for the analysis and proximity and neighborhood.
- The distribution of demand is distributed based on population density only. Therefore, the demand will be assigned proportionately based on the population.
- The process of assigning demands to all nodes in the network does not require a detailed survey, more assumptions compared to other two methods.
- Values of demands shall be obtained within short period of time rather the other two.

**Table 2** Output for nodal demand values obtained through WaterGEMS

Label	Elevation (m)	Demand by unit pipe length method in lps	Demand by Thiessen polygon method in lps	Demand by equal distribution method in lps
J-1	362.00	0.108	0.028	0.169
J-2	361.93	0.098	0.028	0.169
J-3	364.65	0.201	0.055	0.169
J-4	364.63	0.096	0.055	0.169
J-5	360.89	0.043	0.028	0.169
J-6	360.63	0.074	0.028	0.169
J-7	364.70	0.078	0.028	0.169
J-8	360.61	0.159	0.028	0.169
J-9	362.82	0.129	0.028	0.169
J-10	363.38	0.278	0.111	0.169
J-11	365.25	0.174	0.055	0.169
J-12	365.79	0.126	0.055	0.169
J-14	364.70	0.043	0.028	0.169
J-18	367.66	0.139	0.028	0.169
⋮	⋮	⋮	⋮	⋮
⋮	⋮	⋮	⋮	⋮
J-293	364.71	0.010	0.028	0.169

## 4 Results and Analysis

WaterGEMS is a very powerful, user-friendly tool having very broad options compared to all other simulation softwares which also has a wide-ranging capability to merge with GIS. After successful run of the network with all the input values assigned, results were obtained for various hydraulic parameters such as demands at nodes, pressure at nodes and flow in pipes. The results thus plotted on a graph using MS-Excel tool for better visualization in order to compare the feasible method for assigning the demands to the nodes.

### 4.1 Comparison of Nodal Demands

The values of demands obtained through all three stated methods were plotted on a graph and shown in Fig. 4. It can be observed that the demands obtained by Thiessen polygon were appropriate and accurate. This mainly depends on the area of the influence diagram of the corresponding node. From the graph, near the nodes/junctions J—228, 256–292, the value of demands at the corresponding nodes increases due to the main reason that the density of population is high in these two zones. Besides, the demand obtained through unit pipeline method and equal distribution method does not give accurate values due to some erroneous assumptions made while assigning the nodal demands.

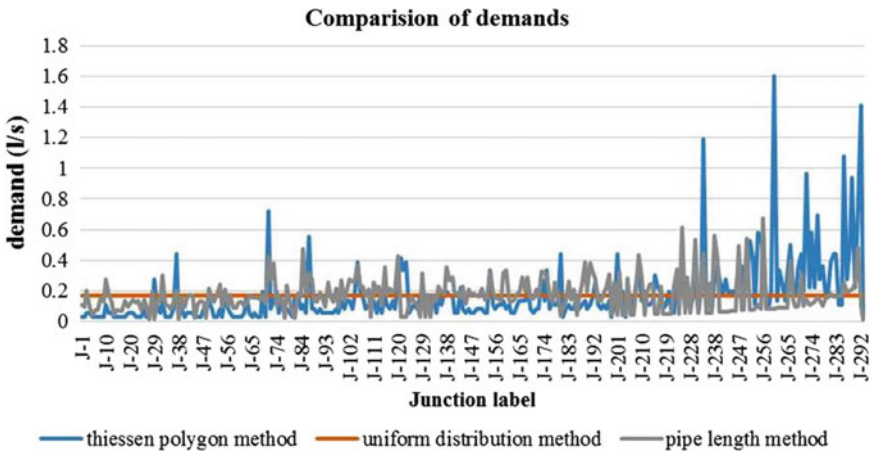


Fig. 4 Comparison of nodal demands obtained through three methods using WaterGEMS



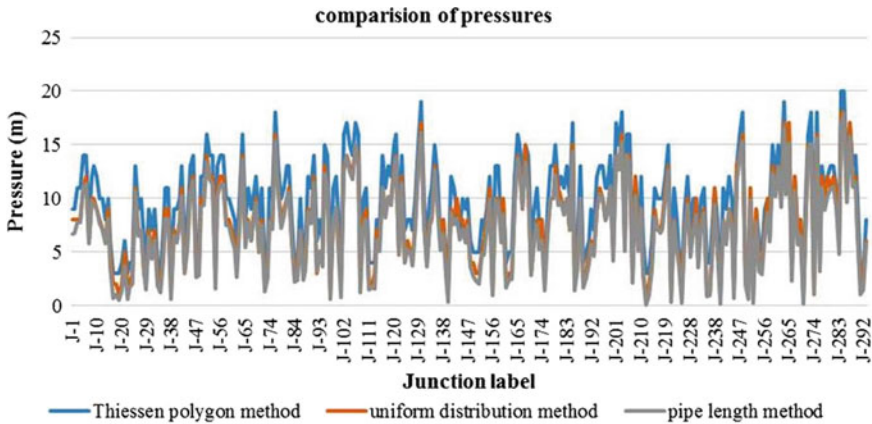


Fig. 5 Comparison of pressure heads obtained through three methods

### 4.2 Comparison of Pressure Heads

The other important hydraulic parameter in any typical water distribution network is pressure head. Therefore, the values of pressure head measured in terms of water obtained through three methods were plotted using MS-Excel and shown in Fig. 5. It can be clearly observed that irrespective of the method used to assign the node demands, pressure head values completely depend on the ground elevation at that junction, residual head provided (3.00 m) and the ground elevation at service reservoir. Since the altitude of the study area varies from 360.25 to 379.02 m, the pressure head also varies corresponding to the elevation at junction.

## 5 Conclusions

Some of the following conclusions were drawn through this research after successful run of the network.

- Thiessen polygon or Voronoi polygon or influence diagram for the nodes is generated irrespective of topographical features of the study area.
- Demands to the nodes are assigned purely based on the population density, which shows the proportional distribution to the living habitants in the study area.
- Demands assigned by equal method of distribution give inaccurate results and not suitable for irregular or uneven distribution of population.
- Unit line method and equal distribution methods are highly suitable for the areas which are well-defined land use classification, since the demand by the habitants in those areas varies accordingly.

- Therefore, allocation of demands to the node by Thiessen polygon method is accurate and efficient when compared to that of unit pipe length method and uniform distribution method due to factors discussed above.
- All the hydraulic parameters like flow, velocity and pressure are fairly sufficient for the adequate supply of water and within the permissible limits.
- An Elevated Service Reservoir of capacity of 236 KL is proposed to meet the future demands for the year 2040.

## References

1. Alperovits, E., & Shamir, U. (1977). Design of optimal water distribution systems. *Water Resources Research*, 13(6), 885–900; Gheisi, A., & Forsyth M. (2015). Water distribution systems reliability.
2. Adeniran, A. E., & Oyelowo, M. A. (2013). An EPANET analysis of water distribution network of the University of Lagos, Nigeria. *Journal of Engineering Research*, 18(2), 69–83.
3. Dilip Babubhai, P. (2017). Analyzing the existing water distribution system of Surat using Bentley WaterGems.
4. Mays, L. W. (2000). *Water distribution system handbook* (pp. 409–482). New York: McGraw Hill.
5. Sonaje, N. P., & Joshi, M. G. (2015). A review of modeling and application of Water Distribution Networks (WDN) softwares. *International Journal of Technical Research and Applications*, 3(5):174–178.
6. Pathan, S. S., & Kahalekar, U. J. (2013). Design of optimal water distribution system and its water quality analysis by using WaterGEMS.
7. Cross, H. (1936). Analysis of flow in networks of conduits or Conductors. Engineering Experiment Station, University of Illinois, Bulletin No. 286.
8. Ingeduld, P., & Svitak, Z. (2006). Modelling intermittent water supply systems with EPANET. In *The Proceedings of Eighth Annual Water Distribution Systems Analysis Symposium (WDSA)*, August 27–30, 2006.
9. Ramana, G. V., Sudheer, V. S. S., & Rajashekar, B. (2015). Network analysis of water distribution system in rural areas using EPANET. In *13th Computer Control for Water Industry Conference, CCWI*. Elsevier.
10. Swamee, P. K., & Sharma, A. K. (2008). Design of water supply pipe networks (pp 44–75). New York: Wiley.
11. Saminu, A., Abubakar, N., & Sagir, L.: Design of NDA water distribution network using EPANET. *International Journal of Emerging Science and Engineering (IJESE)*, 1(9), 5–9.
12. Sumithra, R. P., Nethaji Mariappan V. E., & Amaranath, J. (2013). Feasibility analysis and design of WDS for Tirunelveli Corporation using loop and water gems softwares.
13. Shinde, P. B. (2017). Feasibility analysis of water distribution system for Yavatmal city using water gems software.
14. [www.bentley.com/WaterGEMS-Spec](http://www.bentley.com/WaterGEMS-Spec) as visited on March 28, 2016.
15. <http://kypipe.com/pipe-2018-features/> visited on December 15, 2018.